



TUM School of Engineering and Design
der Technischen Universität München

Estimation Methods for Sensor Fault-Tolerant Control of Reluctance Synchronous Machines

Matthias Laumann

Vollständiger Abdruck der von der TUM School of Engineering and Design der
Technischen Universität München zur Erlangung des akademischen Grades eines

Doktors der Ingenieurwissenschaften (Dr.-Ing.)

genehmigten Dissertation.

Vorsitz: Prof. Dr.-Ing. habil. Gerhard Rigoll

Prüfer*innen der Dissertation:

1. Prof. Dr.-Ing. Dr. h. c. Ralph M. Kennel
2. Prof. Dr.-Ing. Christian Weiner

Die Dissertation wurde am 17.11.2022 bei der Technischen Universität München
eingereicht und durch die TUM School of Engineering and Design am 14.03.2023
angenommen.

Preface

The present dissertation arose from a cooperative project between the Institute for High-Power Converter Systems (formerly the Institute for Electrical Drive Systems and Power Electronics) at the Technical University of Munich and the Darmstadt University of Applied Sciences. The work is dedicated to estimation methods for sensor fault-tolerant control of reluctance synchronous machines, primarily aiming to contribute to a safer drive system.

The opportunity for a dissertation at the Technical University of Munich required faith in me from the former chair of the institute. Dear Prof. Dr.-Ing. Dr. h. c. Ralph M. Kennel, I would like to express my sincere thanks for this opportunity, although I was not a former student at TUM. Thank you for enabling many great experiences, such as the research stay in Stellenbosch and the participation in three ALM symposia.

Dear Prof. Dr. Christian Weiner, I am obliged for the most profound thanks. You opened the entire project by providing contact with Prof. Kennel and our industry partner. Thank you for supporting me over what has been a long road by any measure. Your pleasant-natured personality instilled assurance, even in the difficult times of this project.

Dear Prof. Maarten Kamper, my special thanks for the great opportunity of a research stay at Stellenbosch University in the spring of 2018. I learned a lot at your institute, and I look back with fond memories.

I would particularly like to thank the whole team of our industry partner, Linde Material Handling GmbH. Thank you, Jochen, Stefan, Peter, and Heiko, for supporting me from the beginning of my master's thesis.

Thanks to my doctoral colleagues Tobias and Eyke for the lively exchange, the sports challenges, and the pleasant togetherness, which made this time even more enjoyable.

The realization of such a project is time-consuming and affects private life over a long period. Therefore, I want to thank my friends and close ones, especially Christine, for the understanding they showed me many times.

Matthias Laumann
Darmstadt, October 2022

Contents

1	Introduction	1
1.1	Problem formulation	3
1.2	Contributions	6
1.3	Outline	7
2	Fundamentals	9
2.1	Nomenclature	9
2.1.1	Dimensions	10
2.1.2	Time variance and invariance	10
2.1.3	Superscripts	10
2.1.4	Subscripts	11
2.1.5	Accents	12
2.2	Coordinate transformations	12
2.2.1	Space vectors and Clarke transformation	12
2.2.2	Park transformation	15
2.3	Machine model	16
2.3.1	Electrical model	17
2.3.2	Mechanical model	22
2.3.3	Simulation model	23
2.4	Voltage average model of the two-level VSI	25
3	Setup of the drive system	27
3.1	Inverter	28
3.2	Processing unit with timing structure and control settings	29
3.3	Machine	32
4	Redundancy in the event of an encoder fault	35
4.1	Extended electromotive-force-based encoderless control	36

4.2	Injection-based encoderless control	41
4.2.1	Anisotropy detection - Arbitrary Injection	42
4.2.2	Conventional rotor position assignment	49
4.2.3	Overload capability problem	52
4.2.3.1	Alternative injection-based models	56
	A. Conventional Arbitrary Injection	56
	B. Alternating Injection	57
	C. HF-EEMF model	60
	D. Method of the unique assignment of the admittance or inductivity to the rotor location	62
4.2.3.2	Empirical investigation of the injection-based model's overload capability	67
4.2.3.3	Novel convergence criterion	70
4.2.3.4	Verification of the convergence criterion	74
4.2.3.5	Conclusion about the overload capability issue	79
4.3	Hybrid encoderless control scheme	80
4.4	Empirical verification of the hybrid encoderless control scheme	82
5	Redundancy in the event of a DC-link voltage sensor fault	87
5.1	Relationship between DC-link voltage and machine voltages	88
5.1.1	Derivation for the idealized VSI	89
5.1.2	Extension by the interlock time	91
5.2	Estimation at medium to high speeds	92
5.3	Estimation at low speeds	93
5.4	Hybrid DC-link-voltage-sensorless control	95
5.5	Empirical verification	96
6	Redundancy in the event of current sensor faults	103
6.1	State-space model	104
6.2	Observability of the state-space model	106
6.3	Extended Kalman filter-based current sensorless control	112
6.3.1	Jacobian matrices	114
6.3.2	Covariance tuning	121
6.4	Empirical verification	124
7	Sensor fault-tolerant control approach	133
7.1	The ambiguity of residua	138

7.2	Hybrid sensor fault detection	140
7.3	Empirical verification during supply voltage fault	142
7.3.1	DC-link voltage sensor fault	143
7.3.2	Incremental encoder fault	145
7.3.3	Fault of the current sensors	147
7.4	Conclusion to fault-tolerant control	151
8	Conclusion	153
8.1	Summary	154
8.2	Limitations and outlook	157
	Appendix	161
A.1	Abbreviations	161
A.2	List of publications	163
A.3	Determination of the phase inductances	164
	List of Figures	165
	List of Tables	169
	List of Symbols	171
	Bibliography	179

Chapter 1

Introduction

The electrification of established technologies based on fossil fuels is becoming more and more important to counter climate change. This can be seen in the number of electric vehicles, which is increasing rapidly [1, p.15]. Electrification is not only important for road transport but also for many other areas where electrical drive systems add an advantage. Electrical drive systems are highly efficient and produce fewer CO₂ emissions than conventional systems based on fossil fuels. Besides this, electrical drive systems have become even more flexible in terms of operational behavior ever since suitable power electronic components became available. The trend of using electrical drives continues in industrial traction drive applications, e.g., for use in forklifts, which require high safety to prevent accidents by malfunction.

With the rising number of electrical drive systems, they are increasingly being used in applications where their fault could be critical for life and limb. Thus, the safety¹ of electrical drive systems is becoming more important.

The electrical drive system consists of many parts, with the main components being the power supply, power electronics, electrical machine, and control unit. The power electronic and machine are controlled by the control unit, which executes the control software to achieve high efficiency, performance, and reliability of the system. Without an operational control unit, no advanced drive system works. The control unit relies on control feedback from the electrical machine and the power electronics to adequately react to system changes and verify whether the intended states are being met. The required feedback from the machine and the power electronics are measured

¹In the field of reliability, different terminologies with distinct meanings are used [2, p.12]. Safety: The probability that a catastrophic event is avoided. Availability: The probability that a system functions at time t .

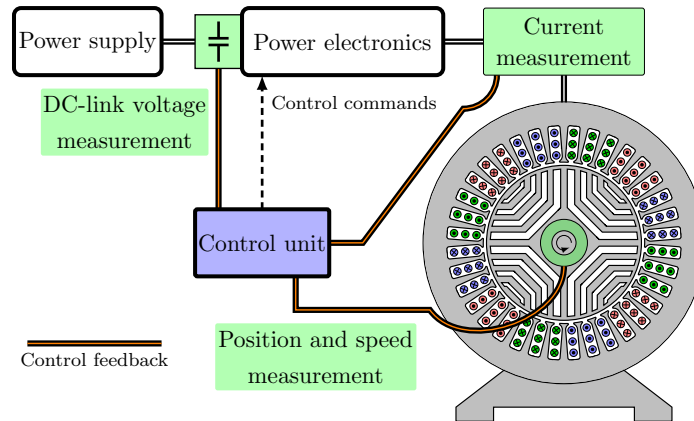


Figure 1.1: System overview with control feedback measurements.

by sensors and sent to the control unit. A system overview with the required control feedback (measurements) is shown in Fig. 1.1. In a conventional drive system, the direct current (DC)-link voltage of the power electronics, the machine phase currents, machine rotor position, and/or machine rotor speed are measured. Information on the rotor position and phase currents are required to set the desired torque and for the position control. Most control strategies require the speed measurement for speed control and to determine the electromotive-force (EMF) of the machine (feed-forward of the current controllers). Information on the DC-link voltage is required to apply the desired voltages to the machine. A failure in one of these measurement devices is critical and might result in a loss of control capability. Depending on the application and situation, such failures might potentially be critical for life and limb. A fault of the DC-link voltage sensor is less critical and might be compensatable, yet, a fault of the current sensors or the position and speed encoder inevitably results in a loss of control capability. There are many root causes for feedback failures, including failures in the power supply, connectors, or the sensors themselves, and they all result in erroneous control feedback. Although the feedback chain contains many potential root causes for feedback failures, the probability of such events is low. The probability differs from drive system to drive system and depends on many factors, with the final, overall, failure probability of the feedback chain being the result of the addition of the single failure probabilities of each potential failure source. This overall failure probability might be small but cannot be disregarded due to the potentially catastrophic consequences of such a scenario. With the increasing number of drive systems and their use in safety-critical applications, such events will become even more probable in the future.

The present dissertation is dedicated to increasing the reliability (first and foremost,

the safety) of industrial drive systems by developing and investigating methods to estimate the required control feedback signals. The methods provide estimations, which are employed to detect failures in the control feedback and to replace defective sensor signals. The methods should not increase the system costs, and, thus, should not rely on additional hardware. Furthermore, the algorithms must be executable on a standard microcontroller without high computational power used in industrial drive applications today. However, using an industrial microcontroller aggravates the development of algorithms throughout this work. The investigations are representatively conducted for a synchronous reluctance machine (RSM), which has become more popular in the last decade in industrial applications due to its robustness, low price, and high efficiency compared to induction machines (IMs). The RSM has its nominal operating point in deep magnetic saturation, making this machine highly nonlinear and challenging for estimation methods.

1.1 Problem formulation

The potential consequence of erroneous control feedback due to defective components in the measurement circuitry was briefly discussed in the introduction. A safer and more reliable drive system would be established if control feedback faults could be detected and compensated for. Estimating the control feedback through physical models of the system is an evident approach to realizing such a detection and compensation structure. Estimation methods used to estimate sensor information are already part of science and industry. However, available methods are subject to certain drawbacks and limitations, which are discussed in the next pages. Furthermore, most of these estimation methods have been primarily developed to reduce costs and space.

The existing literature and the overall problem formulation can be divided into four research topics, of which three are concerned with the estimation methods to estimate the sensor feedback, and one is concerned with the objective of detecting control feedback faults. The first topic concerns the popular methods of *encoderless control*, which are dedicated to control without a position or speed encoder. The field of encoderless control has been a research interest for more than three decades. The second topic is so-called *current sensorless control*, which is concerned with control under a partial or full relinquishment of current sensors. This technique is barely investigated. The third topic is control without a DC-link voltage sensor, called *DC-link-voltage-sensorless control*. There is currently no research history regarding DC-link-voltage-sensorless control for drive systems. These three research topics are all concerned with the esti-

mation of the sensor data. The fourth topic is so-called *sensor fault-tolerant control*, which is concerned with detecting and compensating for sensor and control feedback faults. This technique can be realized by the three estimation methods explained above. The research activities in this field have been quite limited so far.

The state of the art of the four topics comprises several restrictions, drawbacks, and incompleteness. The most relevant open issues are briefly summarized below. A more detailed description of the state of the art is provided in the specific chapters.

Encoderless control

Encoderless control is a well-known technique and has extensively been researched for a long time. Hence, many research questions about this technique have already been answered. In the last couple of years, the research effort in this field has declined significantly. Nonetheless, there are still open research questions in this field:

- (1) **Accuracy** – The accuracy of these methods is still limited compared to that of a high-resolution position encoder. Hence, these methods are excluded from applications requiring very precise position information.
- (2) **Convergence issue** – The approaches in the category of so-called injection-based encoderless control algorithms suffer stability problems when the electrical machine is driven into deep magnetic saturation. The cause of the convergence issue has not been satisfactorily investigated but does form part of current research activities. The limitation in the achievable current magnitude excludes the use of these algorithms in many applications.

Current sensorless control

Current sensorless control methods have been significantly less researched than encoderless techniques. There are several open research questions that can be summarized as follows:

- (3) **Magnetic saturation** – The effect of magnetic saturation is inadequately considered in existing current sensorless schemes due to the use of simplified machine models. This can lead to limited performance when operating highly nonlinear machines.
- (4) **Harmonics** – Current sensorless control methods for machines with strong harmonic anisotropies have not been developed yet. Existing algorithms are restricted to machines with low harmonics, e.g., to those with distributed windings.

- (5) **System feedback** – Almost all the research literature proposes approaches based on open-loop observers, which fully rely on an approximated model running on the control unit. Open-loop observers do not employ feedback from the remaining sensors and hence, do not take advantage of the actual system state to correct the estimations. The use of the remaining feedback is expected to increase estimation performance and reliability.

DC-link-voltage-sensorless control

There is no research history regarding DC-link-voltage-sensorless control for a drive system. This results in the following open subject:

- (6) **Approaches** – DC-link-voltage-sensorless methods for drive systems have not been developed yet. Hence, entirely new algorithms must be developed to enable estimation.

Sensor fault detection and compensation

All control feedback must be estimable to ensure reliable sensor fault-tolerant control in every system condition. The restrictions of the estimation methods above result in limitations for existing sensor fault-tolerant control approaches. The open research questions are summarized below:

- (7) **Generality** – Existing sensor fault-tolerant control methods are based on deterministic approaches employing system-dependent thresholds to detect sensor faults. Thus, these approaches must be adapted from drive system to drive system resulting in limited transferability. Furthermore, deterministic approaches are implemented for a limited number of fault scenarios, which leads to uncertainty about whether all possible fault scenarios are detectable.
- (8) **Restrictions** – The restrictions of the estimation methods lead to limitations for existing sensor fault-tolerant control approaches. Not all control feedback is estimable, and some feedback signals can only be estimated in a limited operating range. Hence, it is not possible to detect and compensate for control feedback faults in all operating conditions of the system. Solving this issue will significantly increase safety in the respective applications.

1.2 Contributions

This dissertation aims to contribute to a safer drive system by improving and extending the properties of sensor fault-tolerant control. Thereby, the focus is on the restrictions (8) of existing approaches. As mentioned above, these restrictions result in patchy coverage by the fault detection and compensation with respect to the operating area of the machine (insofar as an estimation method is even available). This work aims to improve the coverage of the fault detection and compensation with the constraint of limited computational power and without additional hardware. Thereby, the proposed algorithms should be employable by most industrial drive systems. From the previous sentences, it is evident that the focus is on investigating and improving the estimation methods and less on the actual fault detection (7). However, the investigation and improvement of the estimations methods is the foundation for solving (7) in the future. Solving (8) requires this thesis to deal with subjects (2), (3), (5), and (6). Issue (4) is not subjected due to the use of an RSM with weak harmonic anisotropies.

The investigation of the convergence issue (2) of encoderless control algorithms is a major contribution of this work. The research concerns so-called injection-based algorithms but allows general conclusions about how the structure of estimation algorithms affects stability properties. The aim is to find the cause of the convergence problem by empirically investigating existing injection-based algorithms and reinforcing the findings with a novel convergence criterion. The investigations reveal the cause of the convergence issue. The new insights help improve encoderless algorithms in terms of stability and can be transferred to estimation algorithms in general.

Subjects (3) and (5) are addressed by developing a novel current sensorless control approach employing extended Kalman filter (EKF)-based state estimation. The effect of magnetic saturation is accommodated throughout the entire derivation process, and the remaining feedback (speed) is employed. The comprehensive equations (computationally costly due to the consideration of magnetic saturation) are simplified without a significant loss in estimation quality.

Approaches to overcome subject (6) (DC-link voltage estimation) are proposed. These approaches follow the example of encoderless control by combining injection-based estimation used at/or close to a standstill with another technique for the medium to high-speed range. The injection-based scheme also estimates the voltage drop across the power electronics with a novel online estimation approach without depending on a model of the voltage source inverter (VSI).

The validity of the approaches and investigations for (2), (3), (5), and (6) is demon-

strated with a fault-detection and compensation approach, which is based on the preliminary work. The fault-detection approach is not the focus of this dissertation and works for a limited number of possible fault scenarios. However, it shows the future possibilities in this field if suitable sensor data estimation algorithms are employed.

Besides the major contributions above, this work also contains less significant findings. Here, the improvement of the so-called extended electromotive force (EEMF)-based encoderless model must be emphasized, which was extended by the effect of cross-saturation.

The pre-publications originated on the way to this work are listed in Appendix A.2. They can be recognized by the letters in brackets following the citation number, for example, [33][LWK]. The letters refer to the involved authors' last names.

One philosophy of this work is to primarily present measurement results to confirm the theories introduced. Hence, simulation results are only presented if they provide a surplus to measurements.

1.3 Outline

The structure of this work is as follows. After the introduction, fundamental knowledge in the control of drives is presented in Chapter 2. Here, the focus is on coordinate transformations, models of the electrical machine, and models of the power electronics. The fundamentals are followed by Chapter 3, where the drive system and the control structure are presented. Chapter 4 introduces conventional encoderless control models, discusses the convergence issue, and generally deals with the topic of encoderless control. Chapter 5 proposes a new method to estimate the DC-link voltage. The novel current sensorless control approach is proposed and tested in Chapter 6. Chapter 7 demonstrates the effectiveness of the estimation methods for fault detection and compensation purposes by proposing a deterministic fault-tolerant control approach. The fault-tolerant control approach is verified empirically by a realistic supply voltage fault scenario. Finally, the work is concluded in Chapter 8, and an outlook for possible future works and improvements is given.

Chapter 2

Fundamentals

The following chapter introduces the fundamental theories and mathematical conventions repeatedly resorted throughout this work. The presented information can be regarded as textbook knowledge in the control of electrical drives.

The chapter starts with a brief description of the nomenclature and the conventions applied to the mathematical symbols. Fundamental coordinate transformations are introduced, which are essential for controlling electrical drives. These transformations are known as Clarke and Park transformations. Afterward, the non-linear electrical machine model of the [RSM](#) is derived from a three-phase representation, and a detailed derivation of the magnetic anisotropy is carried out. The mechanical fundamentals follow the electrical derivations, which are then incorporated with the electrical theories in a simulation model. At the end of the chapter, the influence of the [VSI](#) interlock time is described and modeled.

2.1 Nomenclature

The nomenclature used within this thesis has been chosen to be informative and compact simultaneously and follows typical conventions used in the research literature. A list of all symbols is attached at the end of this work, in the List of Symbols [A.3](#).

This section introduces the nomenclature to help understand and interpret the mathematical equations. The denotation of the most common sub- and superscripts is explained. It is described how dimensions are distinguished and time variance and invariance are denoted. Finally, the meaning of the accents is introduced.

2.1.1 Dimensions

The symbols for different dimensions are listed in Tab. 2.1. The subscript of the unity matrix determines its dimension.

<i>Dimensions</i>			
Symbol	Description	Notation	Dimension
X, x	scalar	capital or small regular letter	1
\mathbf{x}	vector	small bold letter	n
\mathbf{X}	matrix	capital bold letter	$m \times n$
\mathbf{I}_i	unity matrix	upright capital bold I	$\mathbf{I}_i \in \mathbb{R}^i \quad (i \in \mathbb{N}^*)$

Table 2.1: Nomenclature for different dimensions.

2.1.2 Time variance and invariance

A clear distinction between time-variant and invariant mathematical variables, dimensions, or subscripts is made within this work. Time-variant symbols are written in italics, whereas time-invariant symbols are written upright. Note, in some cases, the variable is time-variant, whereas the subscript is not. The basic convention regarding time variance and invariance is listed in Tab. 2.2.

<i>Indication of time invariance and variance</i>		
Symbol	Description	Notation
$X, x, \mathbf{X}, \mathbf{x}$	time-invariant symbolism	upright letters
x_s, X_s	time-invariant subscript	upright subscripts
$X, x, \mathbf{X}, \mathbf{x}$	time-variant symbolism	italics letters
x_s	time-variant subscript	italics subscripts

Table 2.2: Nomenclature of time-variant and invariant symbols.

2.1.3 Superscripts

Superscripts either indicate the reference frame in which a variable is presented or mathematical operations as depicted in Tab. 2.3.

Superscripts

Symbol	Description
t	quantity in three-phase stator fixed coordinates
s	quantity in two-phase stator fixed coordinates
r	quantity in rotor fixed coordinates
-1	inverse matrix, reversed function, or reciprocal
+	pseudo-inverse of a matrix
T	transposed matrix or vector
*	reference value

*Table 2.3: List of the most used superscripts.***2.1.4 Subscripts**

Subscripts indicate the components of a reference frame or act as an additional identifier to differentiate between variables with the same base symbol. Tab. 2.4 lists the most frequently used subscripts. Subscripts not listed in Tab. 2.4 are introduced within the thesis or can be found in the List of Symbols A.3.

Subscripts

Symbol	Description
s	stator-related quantity
a, b, c	components of the three stator winding's
α, β	abscissa and ordinate in stator coordinates
d, q	abscissa and ordinate in rotor coordinates
el	quantity in electrical units
m	quantity in mechanical units
Σ, Δ	mean and delta component
n	nominal value
DC	DC-Link
L	parameter which acts as a load
A	variable related to the magnetic anisotropy
δ	deviation due to cross-saturation
dt	dead time
ctr.	controller-related (purely software) variable

Table 2.4: Frequently used subscripts.

2.1.5 Accents

Accents are used to further differentiate between variables with the same symbolism but different meanings. For example, the real rotor angle is depicted as θ_{el} , whereas the estimated rotor angle is $\hat{\theta}_{\text{el}}$. Accents are a compact and directly recognizable way to mark such differences. The accents used are listed in Tab. 2.5.

<i>Accents</i>	
Symbol	Description
\dot{L}	differential inductance
\hat{x}	estimated parameter which might contain an error
\bar{x}	mean value

Table 2.5: List of accents.

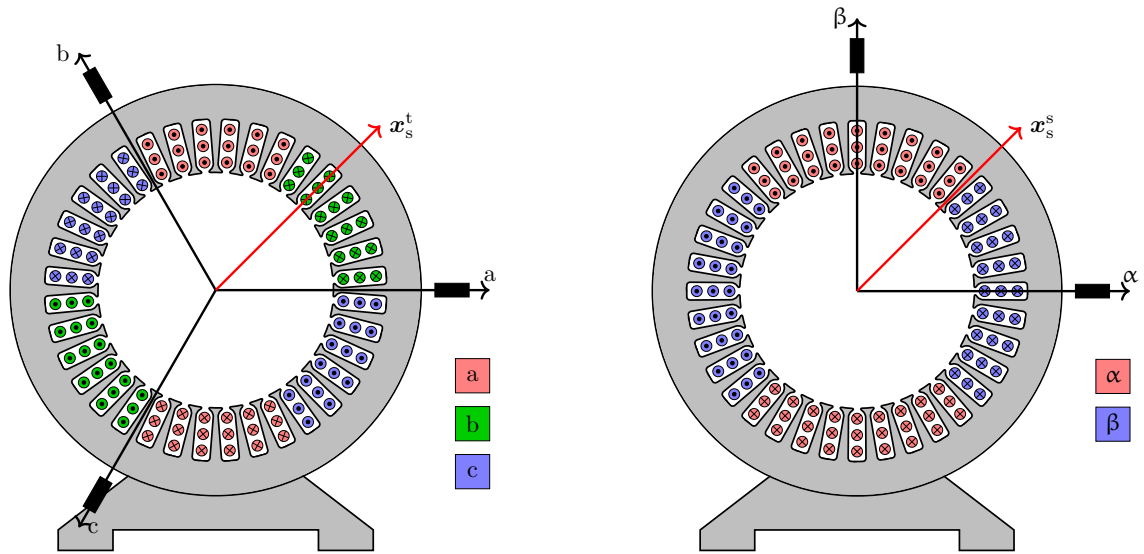
2.2 Coordinate transformations

Coordinate transformations are a standard tool in the control of electrical machines. The transformations are used to transform the actual signals of the system into fictive signals. The fictive signals simplify the mathematical equations and hence, the control algorithms. The most used transformations, Clarke and Park transformations, are based on space vectors. This section introduces the principles of space vectors and these transformations.

2.2.1 Space vectors and Clarke transformation

The basic principle of space vector theory is the temporal and spatial assignment of the signals in a three-phase² electrical system [3, p.405]. In the case of an electrical machine, the currents and voltages have no spatial assignment, but they are time-variant. The spatial assignment of the signals results from the spatial assignment of the phase coils. The composition of all coils and their spatial and temporal (due to the time-variant signal) assignment is then unified in a time-dependent vector called a space vector. The space vector can be interpreted as a pointer viewed from the rotor shaft perspective as shown in Fig. 2.1 a).

²Three phases is the most common case. However, the theory can also be applied to other numbers of phases.



a) Real stator with the three-phase coil system.

b) Illustration of the fictive stator with the two-phase coil system.

Figure 2.1: Examples of a stator with one pole pair.

If the machine is assumed to be Y-connected with an isolated neutral point, it constitutes a two-dimensional system³. Therefore, the system has only two degrees of freedom [4, p.12]. This can be verified if Kirchhoff's current law is applied to the equivalent circuit of a Y-connected machine, as shown in Fig. 2.2. The result is equation (2.1), which confirms the two degrees of freedom.

$$0 = i_a + i_b + i_c \quad (2.1)$$

However, if the machine is only a two-dimensional system, it can also be described by two components, e.g., α , β . This principle is illustrated in Fig. 2.1 b). The transformation from the stator fixed abc reference frame to the stator fixed $\alpha\beta$ reference frame is referred to as the Clarke transformation ($\alpha\beta$ Transformation) [5, p.308]. There are different mathematical ways to perform this transformation. However, only two are commonly used. The first kind of description is based on space phasors [5, p.4] using complex numbers. The analysis with complex numbers is simpler in the case of steady-state and purely sinusoidal signals [6, p.171], but less useful for the analysis in the dynamic nonsinusoidal case [4, p.12]. The second possibility of describing space vectors is based on vector notation and is more efficient for dynamic systems and the

³This two-dimensionality also applies to machines in Delta-connection, which are mathematically transformed into an equivalent Y-connected machine.

derivation of a state-space model, as depicted in [7, p. 85]. The vector notation is often used in control theory and also used within this thesis.

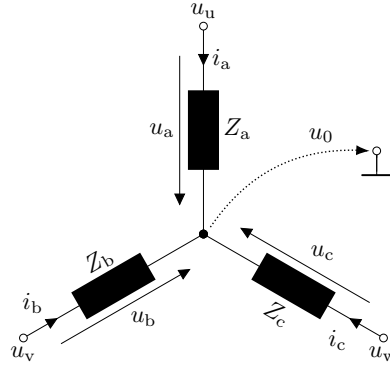


Figure 2.2: Star-connected three-phase machine.

The so-called *amplitude invariant* Clarke transformation, also referred to as the *power variant* transformation, is used within this work. Hence, the amplitudes (purely sinusoidal signals assumed) of the currents and voltages remain the same after the transformation. However, a scaling factor of $3/2$ needs to be considered in the torque equation and with power-related quantities to be energetically correct, which is detailed discussed in [8, p.1005]. The transformation is textbook knowledge and therefore not derived in the following, it is referred to [5][9, p. 8] for a more extensive view.

The amplitude invariant Clarke transformation, denoted by the transformation matrix $\mathbf{C} \in \mathbb{R}^{2 \times 3}$, can be used for the transformation of current and voltage-related signals and is defined as follows:

$$\mathbf{x}_s^s = \begin{bmatrix} x_\alpha \\ x_\beta \end{bmatrix} = \frac{2}{3} \begin{bmatrix} 1 & -\frac{1}{2} & -\frac{1}{2} \\ 0 & \frac{\sqrt{3}}{2} & -\frac{\sqrt{3}}{2} \end{bmatrix} \begin{bmatrix} x_a \\ x_b \\ x_c \end{bmatrix} = \mathbf{C} \mathbf{x}_s^t \quad (2.2)$$

Matrix \mathbf{C} has only a pseudoinverse to back transform to the abc reference frame. The reverse transformation can be conducted using the pseudoinverse $\mathbf{C}^+ \in \mathbb{R}^{3 \times 2}$, which is known as the inverse Clarke transformation:

$$\mathbf{x}_s^t = \begin{bmatrix} x_a \\ x_b \\ x_c \end{bmatrix} = \begin{bmatrix} 1 & 0 \\ -\frac{1}{2} & \frac{\sqrt{3}}{2} \\ -\frac{1}{2} & -\frac{\sqrt{3}}{2} \end{bmatrix} \begin{bmatrix} x_\alpha \\ x_\beta \end{bmatrix} = \mathbf{C}^+ \mathbf{x}_s^s \quad (2.3)$$

2.2.2 Park transformation

The Clarke transformation enables the first simplification of a three-phase system. However, the resulting signals are still alternating current (AC) signals. As the analysis and control of a system with AC signals is more complex than with DC signals, the control and analysis are significantly simplified if the signals are transformed into DC signals. This can be realized by introducing a third reference frame, which rotates with the frequency of the rotor (in electrical units).

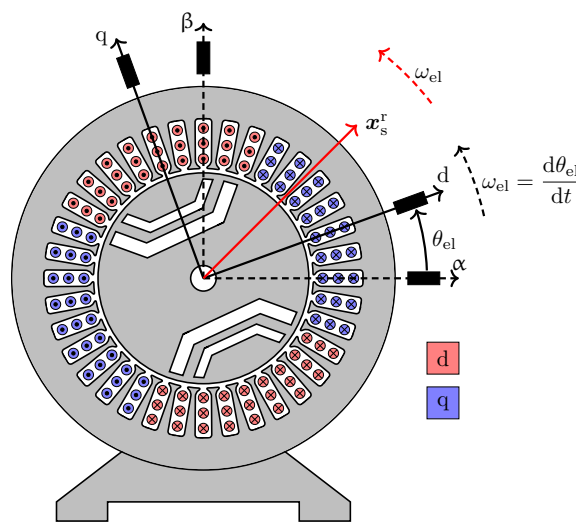


Figure 2.3: Reluctance synchronous machine with one pole pair.

The principle is illustrated in Fig. 2.3. In the case of Fig. 2.3, the angle between an exemplary chosen vector \mathbf{x}_s^r and the abscissa of the new reference frame is constant⁴ if purely sinusoidal signals are considered. Thus, the components d and q of the new vector are constants in the case of sinusoidal original signals. The transformation to the new reference frame can be realized by a clockwise rotation⁵ of the vector, which is realized by the time-variant rotational matrix $\mathbf{P} \in \mathbb{R}^2$ [10, p.192]. The rotational transformation is referred to as Park transformation⁶ or as dq transformation [11] in

⁴This applies for synchronous machines only. In the case of the induction machine, care has to be taken due to the difference in frequency between the stator and rotor field.

⁵Note that the positive mathematical direction of rotation (counter-clockwise) is opposite to the positive mechanical direction of rotation (clockwise).

⁶The original Park transformation transforms directly from abc quantities to dq quantities and, thus, includes the Clarke transformation. However, in the literature, it is common to denote the rotational transformation as the Park transformation.

this context.

$$\mathbf{x}_s^r = \begin{bmatrix} x_d \\ x_q \end{bmatrix} = \begin{bmatrix} \cos(\theta_{el}) & \sin(\theta_{el}) \\ -\sin(\theta_{el}) & \cos(\theta_{el}) \end{bmatrix} \begin{bmatrix} x_\alpha \\ x_\beta \end{bmatrix} = \mathbf{P} \mathbf{x}_s^s \quad (2.4)$$

A counter-clockwise rotation can be realized by the inverse or by the transpose of \mathbf{P} . This operation is called the inverse Park transformation. It is used to transform from the rotor fixed reference frame back to the two-phase stator fixed reference frame⁷.

$$\mathbf{x}_s^s = \begin{bmatrix} x_\alpha \\ x_\beta \end{bmatrix} = \begin{bmatrix} \cos(\theta_{el}) & -\sin(\theta_{el}) \\ \sin(\theta_{el}) & \cos(\theta_{el}) \end{bmatrix} \begin{bmatrix} x_d \\ x_q \end{bmatrix} = \mathbf{P}^{-1} \mathbf{x}_s^r \quad (2.5)$$

$$= \mathbf{P}^\top \mathbf{x}_s^r = \mathbf{P}(-\theta_{el}) \mathbf{x}_s^r \quad (2.6)$$

A rotation by 90° is an ordinary operation in conjunction with the dq transformation and denoted by the matrix:

$$\mathbf{J} := \mathbf{P}^{-1} \left(\frac{\pi}{2} \right) = \begin{bmatrix} 0 & -1 \\ 1 & 0 \end{bmatrix} \quad (2.7)$$

The time derivatives of the transformation matrices need to be calculated frequently; their result is:

$$\frac{d\mathbf{P}}{dt} = \frac{d\theta_{el}}{dt} \begin{bmatrix} -\sin(\theta_{el}) & \cos(\theta_{el}) \\ -\cos(\theta_{el}) & -\sin(\theta_{el}) \end{bmatrix} = -\omega_{el} \mathbf{J} \mathbf{P} \quad (2.8)$$

$$\frac{d\mathbf{P}^{-1}}{dt} = \frac{d\theta_{el}}{dt} \begin{bmatrix} -\sin(\theta_{el}) & -\cos(\theta_{el}) \\ \cos(\theta_{el}) & -\sin(\theta_{el}) \end{bmatrix} = \omega_{el} \mathbf{J} \mathbf{P}^{-1} \quad (2.9)$$

2.3 Machine model

A mathematical model aims to emulate the actual behavior of a system and forms the basis of developments in engineering. It can be used to analyze and predict the behavior of a system. Thereby, the quality of the results depends strongly on how much detail was used to build the model and how many effects were considered. The

⁷The denotation of the transformation is mostly contrariwise in the literature, e.g., the Park transformation is denoted by the term \mathbf{P}^{-1} . However, the author has decided to denote the Park transformation by \mathbf{P} , so that the mathematical denotation is in harmony with the terminology.

effort to develop and analyze a model increases significantly with the number of effects considered. Hence, it is appropriate to only consider the effects expected to be relevant. This section aims to derive a model of the electrical machine, one of the most important components of the drive system. The section starts with the derivation of the electrical model of the [RSM](#), followed by the derivation of the mechanical equations. Finally, the simulation model is introduced, which is based on the derived equations.

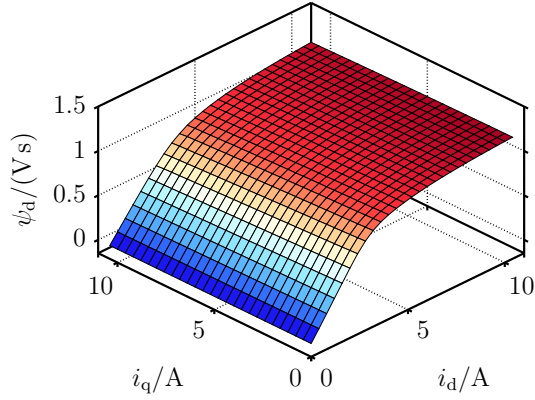
2.3.1 Electrical model

The fundamental electrical equations of the [RSM](#) are derived in this subsection. The derivation is based on a few simplifying assumptions regarding the machine, which are listed in the following:

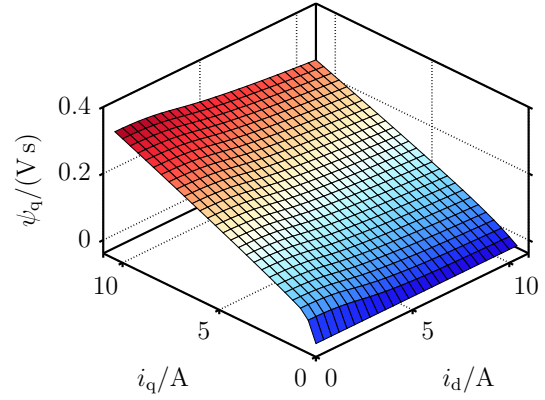
- The effective air gap between the stator and rotor is sinusoidally distributed. Hence, there is no stator-fixed anisotropy ($\frac{\partial \psi_s^r}{\partial \theta_{el}} = 0$).
- The stator windings are perfectly sinusoidally distributed, without higher space harmonics. Thus, the flux linkages in the rotor fixed reference frame are not rotor-angle-dependent ($\frac{\partial \psi_s^r}{\partial \theta_{el}} = 0$).
- The capacitive behavior of the machine is neglected.
- Eddy currents, skin and hysteresis effects are not considered.
- The effect of leakage inductances is assumed to be small and therefore neglected.
- The stator related flux linkages $\psi_s^x, \forall x \in \{t, s, r\}$ are continuously differentiable functions⁸ $\psi_s^x \in \mathcal{C}^1(\mathbb{R}^{2,3}; \mathbb{R}^{2,3})$ of the stator currents i_s^x [[3](#), p. 916].

Synchronous reluctance machines are designed to have their nominal operating point in magnetic saturation. [Fig. 2.4](#) shows some fundamental measurements of the synchronous reluctance machine, which confirm the highly non-linear characteristic due to magnetic saturation. Therefore, it is essential to derive a non-linear model of the machine for the best possible results. In order to incorporate the effect of magnetic saturation, all the inductances must be considered to be functions of the currents. Consequently, there arises a difference between the absolute inductances L and the differential inductances \acute{L} , which are marked with an acute accent.

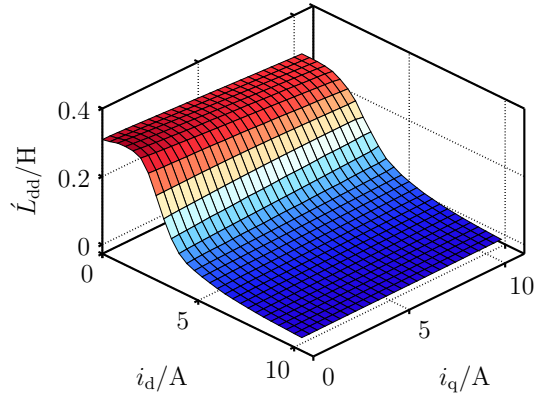
⁸ \mathcal{C}^n is the subspace of the n -times continuously differentiable functions. In this case it either maps from \mathbb{R}^2 to \mathbb{R}^2 or from \mathbb{R}^3 to \mathbb{R}^3 .



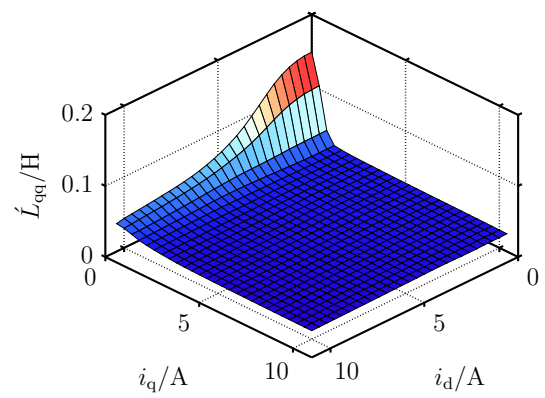
a) Flux linkage of the d-axis.



b) Flux linkage of the q-axis.



c) Differential inductance of the d-axis.



d) Differential inductance of the q-axis.

Figure 2.4: Measured magnetic quantities of the RSM.

The terminal voltage of an AC Machine consists of an ohmic voltage drop caused by the winding resistance superimposed with the time derivative of the flux linkage according to Maxwell's third equation. Thus, the terminal voltage can be described by the following vector equation

$$\mathbf{u}_s^t := R_s \mathbf{i}_s^t + \frac{d\boldsymbol{\psi}_s^t}{dt} \quad (2.10)$$

with voltage vector $\mathbf{u}_s^t \in \mathbb{R}^3$, current vector $\mathbf{i}_s^t \in \mathbb{R}^3$, flux linkage vector $\boldsymbol{\psi}_s^t \in \mathbb{R}^3$, and stator winding resistance $R_s \in \mathbb{R}$. The component representation of the vectors is as follows

$$\mathbf{u}_s^t := [u_a \quad u_b \quad u_c]^\top \quad \mathbf{i}_s^t := [i_a \quad i_b \quad i_c]^\top \quad \boldsymbol{\psi}_s^t := [\psi_a \quad \psi_b \quad \psi_c]^\top \quad (2.11)$$

whereas the flux linkage vector in the coils can be expressed by equation (2.12) using the rotor angle $\theta_{el} \in \mathbb{R}$, and current-vector-dependent absolute inductance matrix \mathbf{L}_s^t . The current dependency is not denoted for clarity in the rest of the derivation.

$$\boldsymbol{\psi}_s^t := \mathbf{L}_s^t(\theta_{el}, \mathbf{i}_s^t) \mathbf{i}_s^t \quad (2.12)$$

The inductance matrix is analytically described by (2.14). It contains an isotropic non-rotor-angle-dependent term scaling with the absolute mean inductance $L_\Sigma \in \mathbb{R}^+$ and an anisotropic rotor-angle-dependent part scaling with the absolute delta inductance $L_\Delta \in \mathbb{R}$. This matrix can be derived geometrically as demonstrated in Appendix A.3 or analytically [12, p. 48]. The matrix is symmetric ($\mathbf{L}_s^t = \mathbf{L}_s^{t\top}$), as are all inductance matrices due to the reciprocity theorem [13], and positive semi-definite, since all eigenvalues are equal or greater than zero ($\mathbf{x}^\top \mathbf{L}_s^t \mathbf{x} \geq 0, \forall \mathbf{x} \in \mathbb{R}^3$). Consequently, the mutual inductances are equal to their counterpart mirrored on the main diagonal.

$$\mathbf{L}_s^t := \begin{bmatrix} L_{aa} & L_{ab} & L_{ac} \\ L_{ba} & L_{bb} & L_{bc} \\ L_{ca} & L_{cb} & L_{cc} \end{bmatrix} \quad (2.13)$$

$$= \frac{2}{3} L_\Sigma \begin{bmatrix} 1 & -0.5 & -0.5 \\ -0.5 & 1 & -0.5 \\ -0.5 & -0.5 & 1 \end{bmatrix} + \frac{2}{3} L_\Delta \begin{bmatrix} \cos(2\theta_{el}) & \cos(2\theta_{el} - 120^\circ) & \cos(2\theta_{el} + 120^\circ) \\ \cos(2\theta_{el} - 120^\circ) & \cos(2\theta_{el} + 120^\circ) & \cos(2\theta_{el}) \\ \cos(2\theta_{el} + 120^\circ) & \cos(2\theta_{el}) & \cos(2\theta_{el} - 120^\circ) \end{bmatrix} \quad (2.14)$$

The transformation of (2.12) with the Clarke transformation (2.2) results in the flux linkage vector in the two-phase stator fixed reference frame:

$$\boldsymbol{\psi}_s^s = \mathbf{C} \mathbf{L}_s^t \mathbf{C}^+ \mathbf{i}_s^s = \mathbf{L}_s^s \mathbf{i}_s^s \quad (2.15)$$

$$= \left(L_\Sigma \begin{bmatrix} 1 & 0 \\ 0 & 1 \end{bmatrix} + L_\Delta \begin{bmatrix} \cos(2\theta_{el}) & \sin(2\theta_{el}) \\ \sin(2\theta_{el}) & -\cos(2\theta_{el}) \end{bmatrix} \right) \mathbf{i}_s^s \quad (2.16)$$

Equation (2.16) can be further simplified employing the Park transformation (2.4). It results in the flux linkage vector in rotor fixed coordinates:

$$\boldsymbol{\psi}_s^r = \mathbf{P} \mathbf{L}_s^s \mathbf{P}^{-1} \mathbf{i}_s^r = \mathbf{P} \mathbf{C} \mathbf{L}_s^t \mathbf{C}^+ \mathbf{P}^{-1} \mathbf{i}_s^r = \mathbf{L}_s^r \mathbf{i}_s^r \quad (2.17)$$

$$= \begin{bmatrix} L_\Sigma + L_\Delta & 0 \\ 0 & L_\Sigma - L_\Delta \end{bmatrix} \mathbf{i}_s^r =: \begin{bmatrix} L_d & 0 \\ 0 & L_q \end{bmatrix} \mathbf{i}_s^r \quad (2.18)$$

The comparison of the matrices entries of equation (2.18) allows for the following equations:

$$L_{\Sigma} = \frac{L_d + L_q}{2} \quad L_{\Delta} = \frac{L_d - L_q}{2} \quad (2.19)$$

Equation (2.18) can be used to determine the voltage equation of the rotor fixed reference frame. It can be derived from the voltage equation (2.10), which is first transformed into two-phase stator fixed coordinates (not presented here) and after that into rotor fixed coordinates, which yields:

$$\mathbf{P}\mathbf{u}_s^s = R_s \mathbf{P}\mathbf{i}_s^s + \mathbf{P} \frac{d\mathbf{P}^{-1}\mathbf{L}_s^r \mathbf{i}_s^r}{dt} \quad (2.20)$$

resulting in the following voltage equation in dq coordinates with consideration of magnetic saturation:

$$\mathbf{u}_s^r = R_s \mathbf{i}_s^r + \begin{bmatrix} L_d + i_d \frac{\partial L_d}{\partial i_d} & i_d \frac{\partial L_d}{\partial i_q} \\ i_q \frac{\partial L_q}{\partial i_d} & L_q + i_q \frac{\partial L_q}{\partial i_q} \end{bmatrix} \frac{d\mathbf{i}_s^r}{dt} + \omega_{el} \mathbf{J} \boldsymbol{\psi}_s^r \quad (2.21)$$

$$= R_s \mathbf{i}_s^r + \begin{bmatrix} \frac{\partial \psi_d}{\partial i_d} & \frac{\partial \psi_d}{\partial i_q} \\ \frac{\partial \psi_q}{\partial i_d} & \frac{\partial \psi_q}{\partial i_q} \end{bmatrix} \frac{d\mathbf{i}_s^r}{dt} + \omega_{el} \mathbf{J} \boldsymbol{\psi}_s^r \quad (2.22)$$

$$= R_s \mathbf{i}_s^r + \begin{bmatrix} \dot{L}_{dd} & \dot{L}_{dq} \\ \dot{L}_{qd} & \dot{L}_{qq} \end{bmatrix} \frac{d\mathbf{i}_s^r}{dt} + \omega_{el} \mathbf{J} \boldsymbol{\psi}_s^r \quad (2.23)$$

The difference between the absolute (fundamental) and differential (incremental) inductances becomes evident from the three equations (2.21)-(2.23). It can be seen that the differential cross-saturation inductances \dot{L}_{dq} , \dot{L}_{qd} are due to iron saturation. The differential inductance matrix is denoted with $\dot{\mathbf{L}}_s^r$ and has the properties ($\dot{\mathbf{L}}_s^r = \dot{\mathbf{L}}_s^{r\top}$; $\mathbf{x}^\top \dot{\mathbf{L}}_s^r \mathbf{x} \geq 0, \forall \mathbf{x} \in \mathbb{R}^2$), resulting in the voltage equation in rotor fixed coordinates:

$$\mathbf{u}_s^r = R_s \mathbf{i}_s^r + \dot{\mathbf{L}}_s^r \frac{d\mathbf{i}_s^r}{dt} + \omega_{el} \mathbf{J} \boldsymbol{\psi}_s^r \quad (2.24)$$

For some tasks, especially in the field of encoderless control, it is more valuable to start a derivation with the voltage equations in two-phase stator fixed coordinates. Hence, the voltage equation in alpha-beta coordinates is derived using the inverse Park

transformation. The inverse Park transformation is applied to (2.24), which yields:

$$\mathbf{P}^{-1}\mathbf{u}_s^r = R_s \mathbf{P}^{-1}\mathbf{i}_s^r + \mathbf{P}^{-1}\dot{\mathbf{L}}_s^r \frac{d\mathbf{P}\mathbf{i}_s^s}{dt} + \omega_{el}\mathbf{J}\mathbf{P}^{-1}\boldsymbol{\psi}_s^r \quad (2.25)$$

$$\mathbf{u}_s^s = R_s \mathbf{i}_s^s + \mathbf{P}^{-1}\dot{\mathbf{L}}_s^r \mathbf{P} \frac{d\mathbf{i}_s^s}{dt} - \omega_{el}\mathbf{P}^{-1}\dot{\mathbf{L}}_s^r \mathbf{P}\mathbf{J}\mathbf{i}_s^s + \omega_{el}\mathbf{J}\boldsymbol{\psi}_s^s \quad (2.26)$$

$$= R_s \mathbf{i}_s^s + \dot{\mathbf{L}}_s^s \frac{d\mathbf{i}_s^s}{dt} + \omega_{el} (\mathbf{J}\boldsymbol{\psi}_s^s - \dot{\mathbf{L}}_s^s \mathbf{J}\mathbf{i}_s^s) \quad (2.27)$$

Some investigations in this work rely on a detailed description of the differential inductance matrix in two-phase stator-fixed coordinates. It can be deduced from the differential inductance matrix in rotor fixed coordinates, as shown by the second term of equation (2.26).

$$\dot{\mathbf{L}}_s^s = \begin{bmatrix} \frac{\partial \psi_\alpha}{\partial i_\alpha} & \frac{\partial \psi_\alpha}{\partial i_\beta} \\ \frac{\partial \psi_\beta}{\partial i_\alpha} & \frac{\partial \psi_\beta}{\partial i_\beta} \end{bmatrix} = \begin{bmatrix} \dot{L}_{\alpha\alpha} & \dot{L}_{\alpha\beta} \\ \dot{L}_{\beta\alpha} & \dot{L}_{\beta\beta} \end{bmatrix} = \mathbf{P}^{-1}\dot{\mathbf{L}}_s^r \mathbf{P} \quad (2.28)$$

$$= \begin{bmatrix} \dot{L}_{dd} \cos^2(\theta_{el}) + \dot{L}_{qq} \sin^2(\theta_{el}) - \dot{L}_{dq} \sin(2\theta_{el}) & \dot{L}_{dq} \cos(2\theta_{el}) \\ \dot{L}_{dq} \cos(2\theta_{el}) & \dot{L}_{dd} \cos^2(\theta_{el}) + \dot{L}_{qq} \sin^2(\theta_{el}) + \dot{L}_{dq} \sin(2\theta_{el}) \end{bmatrix} \quad (2.29)$$

$$= \frac{\dot{L}_{dd} + \dot{L}_{qq}}{2} \begin{bmatrix} 1 & 0 \\ 0 & 1 \end{bmatrix} + \frac{\dot{L}_{dd} - \dot{L}_{qq}}{2} \begin{bmatrix} \cos(2\theta_{el}) & \sin(2\theta_{el}) \\ \sin(2\theta_{el}) & -\cos(2\theta_{el}) \end{bmatrix} + \dot{L}_{dq} \begin{bmatrix} -\sin(2\theta_{el}) & \cos(2\theta_{el}) \\ \cos(2\theta_{el}) & \sin(2\theta_{el}) \end{bmatrix} \quad (2.30)$$

The equation can be further compacted by introducing the rotational matrix $\mathbf{S}(\theta_{el})$, the differential mean inductance \dot{L}_Σ as well as the differential delta inductance \dot{L}_Δ :

$$\mathbf{S}(\theta_{el}) := \begin{bmatrix} \cos(2\theta_{el}) & \sin(2\theta_{el}) \\ \sin(2\theta_{el}) & -\cos(2\theta_{el}) \end{bmatrix} \quad (2.31)$$

$$\dot{L}_\Sigma := \frac{\dot{L}_{dd} + \dot{L}_{qq}}{2} \quad (2.32)$$

$$\dot{L}_\Delta := \frac{\dot{L}_{dd} - \dot{L}_{qq}}{2} \quad (2.33)$$

which yields:

$$\dot{\mathbf{L}}_s^s = \dot{L}_\Sigma \mathbf{I}_2 + \dot{L}_\Delta \mathbf{S}(\theta_{el}) + \dot{L}_{dq} \mathbf{J}\mathbf{S}(\theta_{el}) \quad (2.34)$$

The two rotational terms of equation (2.34) can be simplified into one rotational term employing the harmonic addition theorem. The result is:

$$\dot{\mathbf{L}}_s^s = \dot{L}_\Sigma \mathbf{I}_2 + \dot{L}_A \mathbf{S}(\theta_A) \quad (2.35)$$

$$\dot{L}_A := \sqrt{\dot{L}_\Delta^2 + \dot{L}_{dq}^2} \quad (2.36)$$

$$\theta_A := \theta_{el} + \frac{1}{2} \arctan\left(\frac{\dot{L}_{dq}}{\dot{L}_\Delta}\right) = \theta_{el} + \theta_\delta \quad (2.37)$$

Equation (2.35) shows that the differential inductance matrix contains one isotropic and one anisotropic term, similar to the absolute inductance matrix in three-phase representation. However, it also indicates that the orientation of the anisotropy is not always aligned with the rotor angle but shifted due to the differential mutual inductance, which causes the misalignment angle θ_δ . This angle superimposed with the rotor angle θ_{el} gives the so-called anisotropy angle θ_A . Note that the orientation of the anisotropy is operating-point-dependent due to the operating-point-dependent inductances.

2.3.2 Mechanical model

Fundamental mechanical relationships are derived in the following to describe the machine as an electromechanical energy converter. One of the characteristic quantities of the machine is the electromagnetic torque M_{el} . The torque equation can be derived from a power balance of the machine by multiplying the voltage equation (2.24) with the current and considering the factor of 3/2, as discussed in Subsection 2.2.1.

$$S_{tot} := \frac{3}{2} \mathbf{i}_s^{r\top} \mathbf{u}_s^r = \frac{3}{2} \mathbf{i}_s^{r\top} \left(R_s \mathbf{i}_s^r + \dot{\mathbf{L}}_s^r \frac{d\mathbf{i}_s^r}{dt} + \omega_{el} \mathbf{J} \boldsymbol{\psi}_s^r \right) \quad (2.38)$$

The mechanical rotational power is expressed by equation (2.39) if friction torque is neglected.

$$P_m := M_{el} \omega_m = M_{el} \frac{\omega_{el}}{p} \quad (2.39)$$

Here, p is the number of pole pairs. From (2.38) and (2.39) it is evident that the term scaling with ω_{el} in (2.38) must be related to the mechanical power of the machine.

Thus, the mechanical power is rewritten to

$$M_{\text{el}} \frac{\omega_{\text{el}}}{p} = \frac{3}{2} \mathbf{i}_s^{\text{T}} \omega_{\text{el}} \mathbf{J} \boldsymbol{\psi}_s^{\text{r}} \quad (2.40)$$

which can be solved for the electromechanical torque:

$$M_{\text{el}} = \frac{3p}{2} \mathbf{i}_s^{\text{T}} \mathbf{J} \boldsymbol{\psi}_s^{\text{r}} = \frac{3p}{2} \det(\boldsymbol{\psi}_s^{\text{r}}, \mathbf{i}_s^{\text{r}}) \quad (2.41)$$

The result is analogously for two-phase stator fixed quantities:

$$M_{\text{el}} = \frac{3p}{2} \mathbf{i}_s^{\text{sT}} \mathbf{J} \boldsymbol{\psi}_s^{\text{s}} = \frac{3p}{2} \det(\boldsymbol{\psi}_s^{\text{s}}, \mathbf{i}_s^{\text{s}}) \quad (2.42)$$

Up to this point, the derivation neglected the impact of the friction torque M_{f} , which might be insufficient for some consideration of this work. Therefore, the friction torque is considered in the state equation of the mechanical speed. Different approaches are available to model the friction torque as discussed in [14]. However, the friction torque is speed-dependent and can generally be described by the following dependency:

$$M_{\text{f}}(\omega_{\text{m}}) \quad (2.43)$$

The angular acceleration of the machine is expressed by (2.44), with M_{L} being the load torque and J the mass moment of inertia:

$$\frac{d\omega_{\text{m}}}{dt} := \frac{1}{J} (M_{\text{el}} - M_{\text{L}} - M_{\text{f}}) \quad (2.44)$$

The mechanical rotor angle can be obtained by integrating the angular velocity:

$$\theta_{\text{m}} := \int \omega_{\text{m}} dt + \theta_{\text{m}0} \quad (2.45)$$

2.3.3 Simulation model

Simulations are an essential tool in all kinds of engineering. Simulations can help to understand the behavior of a system and can be a great support in developing new algorithms. It is common practice to simulate new ideas before trying them on an actual system.

The simulation model used in this work is shown in Fig. 2.5. It is based on the theory introduced in Subsection 2.3.1 and 2.3.2 with the electrical and mechanical equations.

The electrical behavior is modeled in the rotor fixed reference frame. The key element of the simulation model is the consideration of iron saturation using the dependency $i_s^r(\psi_s^r)$, which can be deduced by inverting the flux linkage maps of Fig. 2.4. The resulting two current maps i_d and i_q are stored in two 2D lookup tables (LUTs). Rotor angle dependencies due to higher harmonics in the current and the flux linkage are not considered. Hence, higher harmonic anisotropies are not included in the simulation. Effects like the inverter interlock time or iron losses are considered if required and are further discussed if corresponding simulation results are presented.

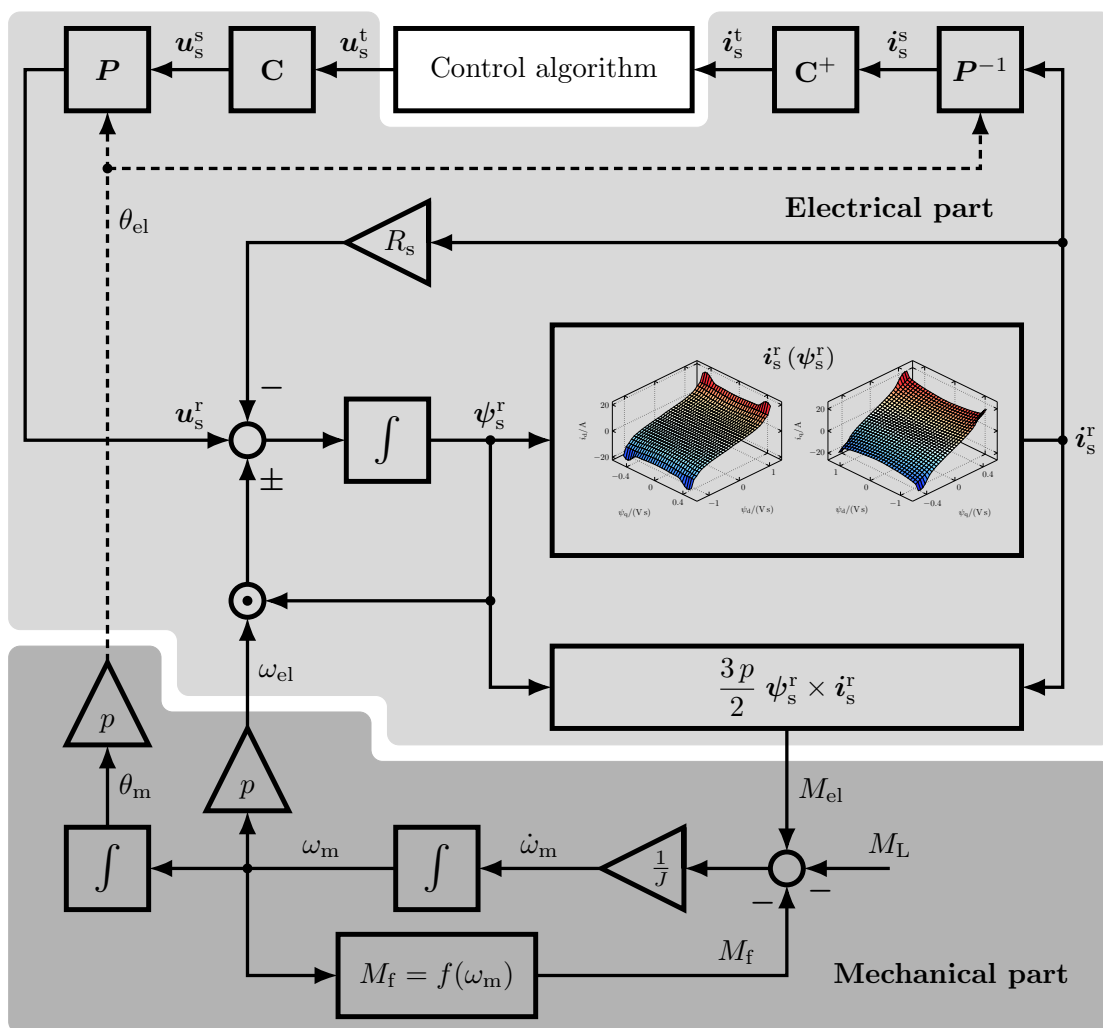


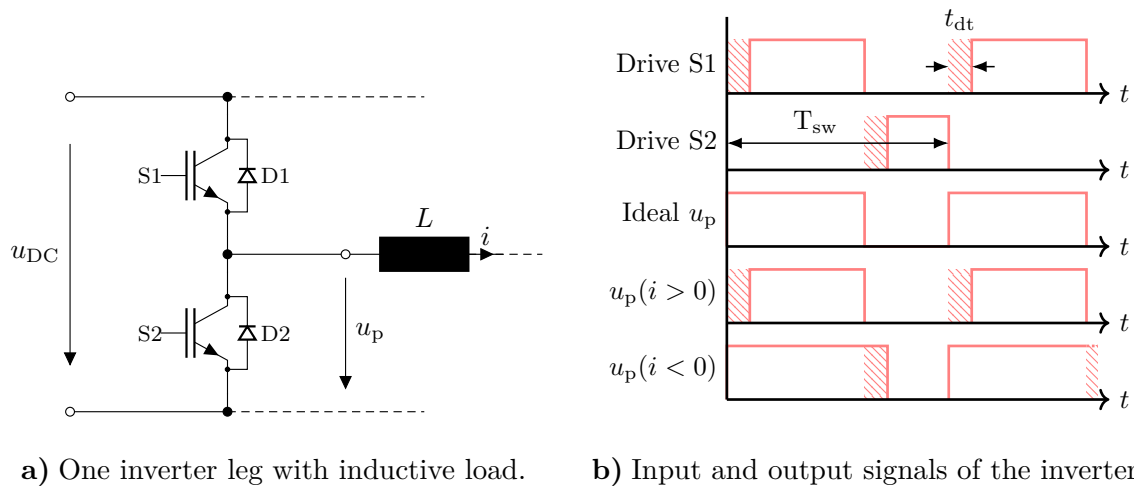
Figure 2.5: Schematic of the fundamental simulation model.

The control algorithms are executed in the block *Control algorithm*, which outputs a three-phase voltage. The voltage from the *Control algorithm* is the input of the machine model, which determines the three-phase currents subsequently fed back to

the *Control algorithm*. Besides the currents, the *Control algorithm* is provided with the machine's rotor angle and rotor speed, which is not depicted in the illustration to remain the clarity. The simulation is carried out with the tool ©MATLAB/Simulink.

2.4 Voltage average model of the two-level VSI

The two-level VSI is the second key element of the drive system. It has the task of converting the logical signals from the pulse width modulation (PWM) module to analog voltages requested by the control algorithm. The VSI is a non-ideal element, which distorts the requested voltage from the control algorithm due to multiple effects. One of these effects is caused by the VSI interlock time, which has a non-neglectable impact and must be considered for the estimation algorithms investigated in this work.



a) One inverter leg with inductive load. b) Input and output signals of the inverter.

Figure 2.6: Effect of the VSI interlock time.

The interlock time of an inverter, also called dead time, is used to avoid a low ohmic path through the high and low-side semiconductor switches during the transition phase. After one switch of a leg is turned off, a certain time t_{dt} is waited until the other switch is turned on. This introduced dead time prevents the switches from being destroyed in the worst-case scenario. The dead time ranges typically from a couple of hundred nanoseconds to a few microseconds. However, recently [15] it has been shown that the interlock time can significantly be decreased compared to standards for insulated-gate-bipolar-transistor (IGBT)-based inverters without destructing the semiconductors. The drawback of the introduced dead time is a voltage deviation compared to that of the voltage commands requested by the control unit. This voltage

deviation is not constant but changes with the respective current sign when an inductive load is connected. Therefore, a case analysis is necessary to describe this effect.

The two cases of a positive and a negative current are studied based on Fig. 2.6. The semiconductor switches and diodes are assumed to be ideal, though in reality the parasitic elements, the driver circuitry, and the voltage drops of the devices also influence the voltage deviation [16].

- $i > 0$: If it is assumed that the state of switch S1 is changing from closed to open, the inductance forces the current to flow out of the terminal, resulting in a current path closed via diode D2. The terminal voltage follows the ideal one in this case perfectly. However, if S2 is switched off, the inductance still forces the current to flow through diode D2 until the dead time t_{dt} is over and S1 is switched on. This results in a voltage-time loss over one switching period T_{sw} compared to that of the ideal requested signal u_p .
- $i < 0$: It is vice versa in this case. If the state of switch S1 is assumed to change from closed to open, the inductance forces the current to flow into the terminal, resulting in a current path closed via diode D1. The terminal is, therefore, still connected to the positive rail of the DC-link voltage until the dead time t_{dt} is over, and S2 is switched on. This results in a voltage-time gain over one switching period T_{sw} compared to that of the ideal requested signal u_p .

It is evident that this behavior causes significant estimation errors in estimation schemes [17, 18, 19] if uncompensated. Hence, this effect should be considered when deriving voltage-based estimators. The mean phase voltage deviation over one switching cycle, caused by the interlock time, can be described by the following equation in the three-phase stator fixed reference frame.

$$\mathbf{u}_{dt}^t := \frac{t_{dt}}{T_{sw}} u_{DC} \cdot \text{sgn}(\mathbf{i}_s^t) \quad (2.46)$$

It is worth mentioning that the requested ideal controller output voltage of the different reference frames, \mathbf{u}_{ctr}^x with $x \in \{t, s, r\}$, consists of the machine terminal voltage \mathbf{u}_s^x superimposed with the voltage deviation caused by the interlock time \mathbf{u}_{dt}^x .

$$\mathbf{u}_{ctr}^x := \mathbf{u}_s^x + \mathbf{u}_{dt}^x \quad x \in \{t, s, r\} \quad (2.47)$$

Chapter 3

Setup of the drive system

The drive system setup, with its substantial limitations in terms of computational power, is described in this chapter for a better classification of the results achieved.

An overview of the test bench is given at the beginning of this chapter. Afterward, the inverter system is described, which is followed by the description of the processing unit with the timing and control structure. Finally, data on the [RSM](#) is provided, and the construction of the machine is briefly depicted.

Fig. 3.1 shows the test bench with the test machine (gold) on the left and the load machine (blue) on the right-hand side. Both machines are [RSMs](#) from the company KSB SE & Co. KGaA ([KSB](#)). The load machine has a higher nominal power rating to guarantee proper control of the test machine. Both machines are mechanically coupled via a torque transducer type KTR Dataflex 16/30 and fed by two modified [VSIs](#) from the company SEW-Eurodrive GmbH & Co KG ([SEW](#)). The measured torque is indicated by the variable M_{KTR} for the provided measurements. The [DC](#)-link circuits of both inverters are connected. Thus, only the internal system losses need to be compensated by the supply. The supply is ensured by the rectified grid voltages. Therefore, the [DC](#)-link voltage is superimposed by a 300 Hz component caused by the rectification of the grid voltages. The rotor position and speed are measured with an incremental encoder type Kuebler 8.5020.2842.3600, which can achieve a theoretical resolution of 0.025° mechanical. All three stator currents of the machine are measured by type CMS3005 current sensors from Sensitec GmbH. The inverter provides an internal [DC](#)-link voltage measurement, and a microcontroller manages all data. The data from the microcontroller can be converted by digital-to-analog converters ([DACs](#)) and be transmitted to the scope (in the middle of the rear wall), using Bayonet Neill-Concelman ([BNC](#)) connectors.

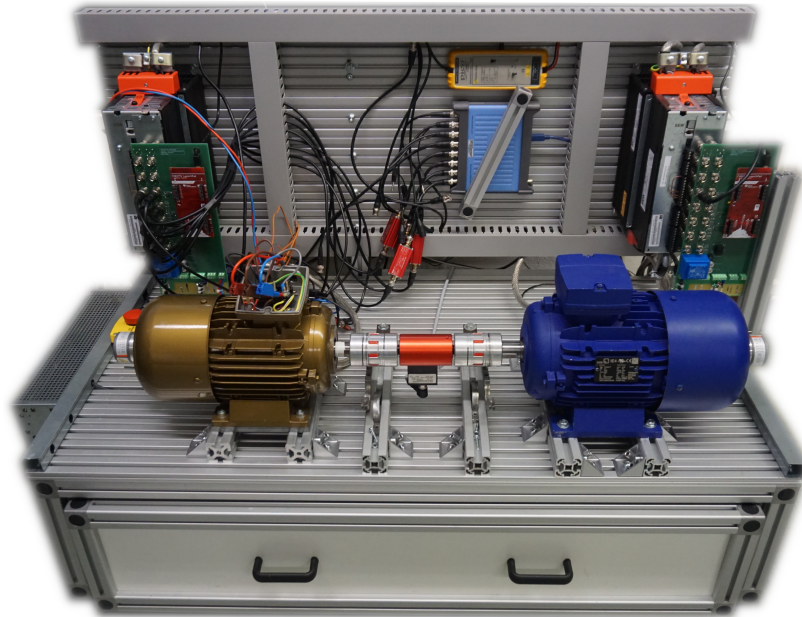


Figure 3.1: Test bench.

3.1 Inverter

The VSI (part at the back) and the control unit (red) are shown in Fig. 3.2. Both are connected via an adapter board (green), which also contains the power supply for the microcontroller and external sensors. The microcontroller board is also connected to a personal computer (PC), from where the software is installed, and control commands are sent.



Figure 3.2: VSI with microcontroller.

Type MDX61B0110-5A3-4-0T

Description	Symbol	Value
Nominal power	$P_{\text{vsi.}}$	11 kW
Nominal current	$I_{\text{vsi.}}$	24 A
DC-link voltage	$U_{\text{DC,vsi.}}$	563 V
Fixed dead time	$t_{\text{dt,vsi.}}$	800 ns

Table 3.1: SEW inverter data.

The basis of the [VSI](#) is a serial product from [SEW](#). However, [SEW](#) has modified the product so that the input of the [IGBT](#) drivers and different measurements are accessible via [BNC](#) connectors. Therefore, the control of the machine can be performed on a separate control unit. The most important inverter data is shown in [Tab. 3.1](#). Note that the rated current of the [VSI](#) amounts to multiple times the rated current of the test machine. Hence, the test machine can be driven into deep magnetic saturation, which is required for some experiments in this thesis.

3.2 Processing unit with timing structure and control settings

The control unit is the control center of the entire drive system and is responsible for executing the algorithms. It outputs the signals for the driver circuitry of the inverter and reads in the required analog and digital signals. The control platform used in this work is based on a Texas Instruments ([TI](#)) microcontroller evaluation board. The performance of the platform is comparable to most systems in today's industry, where more performant controllers, like field-programmable gate arrays ([FPGAs](#)), are often withheld for specific tasks. The selection of the performance-limited control platform was done consciously to develop algorithms, which can also be executed on a standardized microcontroller available in industry. Algorithms like the one introduced in [\[20\]](#), which require a high computational effort, are not applicable, therefore. The control unit introduces an intended constraint regarding the computational power for the entire dissertation. This should be considered when classifying the results.

The TMS320F2837xS 32 Bit floating-point controller has a clock frequency of $f_{cl} = 200$ MHz and a flash memory of 1024 kB. All the control algorithms are developed with the aid of [©MATLAB/Simulink](#) and its graphical interface, making the development more simple, illustrative, and fast. The final C code, required for the microcontroller, is generated from the [©MATLAB/Simulink](#) model using the code generation tool [©TargetLink](#) from the company [dSPACE GmbH](#).

The correct timing within the control unit is important. It is crucial to time the sampling of the current measurements properly to the switching period [\[3, p.671\]](#). Thus, synchronous current sampling ([SCS](#)) is used. This sampling technique makes sure that the current sampling is carried out in the middle of the zero voltage vector to avoid measuring during voltage and current transients. This technique is usable as long as the [PWM](#) is operating in the linear range [\[3, p.670\]](#). The measured cur-

rent sample then corresponds to the mean current over one switching period (if no additional voltage injection is used) if the current evolves linearly over a time interval with constant voltage. However, this assumption is only valid if the sampling period is sufficiently small compared to the electrical time constant of the machine [21][4, p. 56]. In [4, p. 62-67] it is shown that the current evolves nonlinearly in reality due to cable recharging, machine recharging, and eddy current effects. However, these effects are more important if intensive current oversampling is used and can be neglected in this work.

Fig. 3.3 shows the timing structure used. The structure was proposed in [22] but is applied slightly differently in the present work. This approach employs synchronous current sampling (SCS) but calls the control algorithm less frequently than the sampling and PWM task.

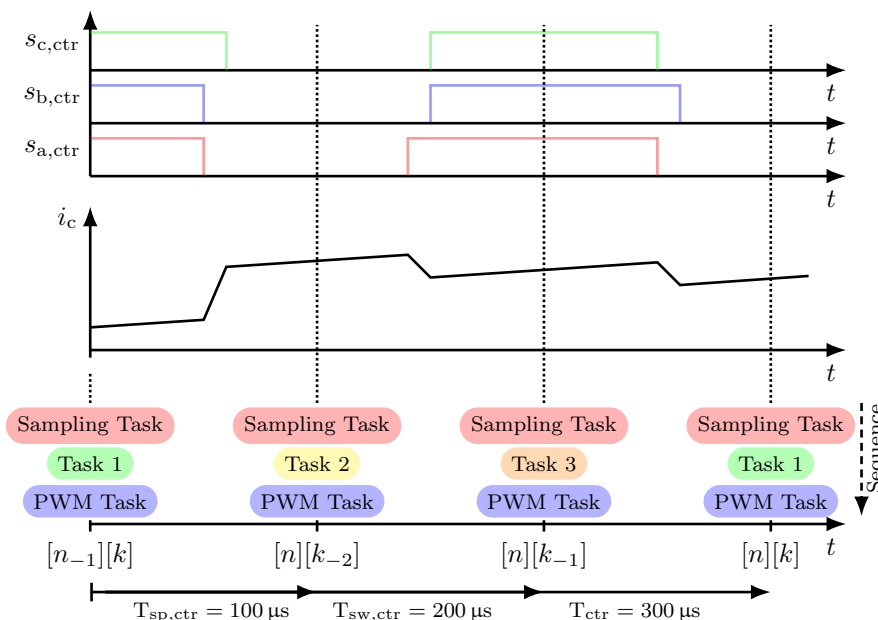


Figure 3.3: Setup of the timing structure.

The approach has the benefit that the PWM and measurement sampling frequencies can be higher than the achievable ones when all algorithms must be executed within one sampling instance. This is due to the available time window $T_{sp,ctr}$, which might not be long enough to execute all of the algorithms used in this work. However, the execution within the available time window must be ensured for a reliable operation, resulting in a lower switching frequency necessary for conventional SCS. Furthermore, the higher number of available current measurements, as compared to that of a common SCS structure, enables new possibilities for the online estimation of parameters, e.g.,

as employed by the DC-link voltage estimator. Different from the original approach of [22], where only one sampling window seems to be used to execute the algorithms, all of the three available windows are used here. The different algorithms are separated into the different Tasks (1, 2, 3) so that the available time window $T_{sp,ctr}$ is sufficiently long for each of the separated algorithms. The periods set are shown at the bottom of Fig. 3.3. Hence, the switching frequency is $f_{sw} = 5$ kHz while the voltage commands and the measurements are updated at $f_{sp,ctr} = 10$ kHz. The tasks for the algorithms (1-3) are called at $f_{ctr} = 3.\bar{3}$ kHz. Due to the different time periods, it must be distinguished between instances n and k as shown in the illustration. The instance n is the integer multiplier of the algorithm execution time T_{ctr} while k is the integer multiplier of the sampling period $T_{sp,ctr}$.

The external signals are sampled with 12 Bit analog-to-digital converters (ADCs). However, four samples of each signal are taken consecutively when the sampling task is called. Those four samples are used to increase the resolution to 13 Bit by means of the *oversampling and decimation* principle [23].

The primary control technique used in this thesis is typical field-oriented control (FOC) [24, 25], which was introduced at the end of the sixties by K. Hasse and F. Blaschke independently. It is carried out in Task 1 as shown in Fig. 3.3. The schematic of the control structure can be found in Fig. 3.4.

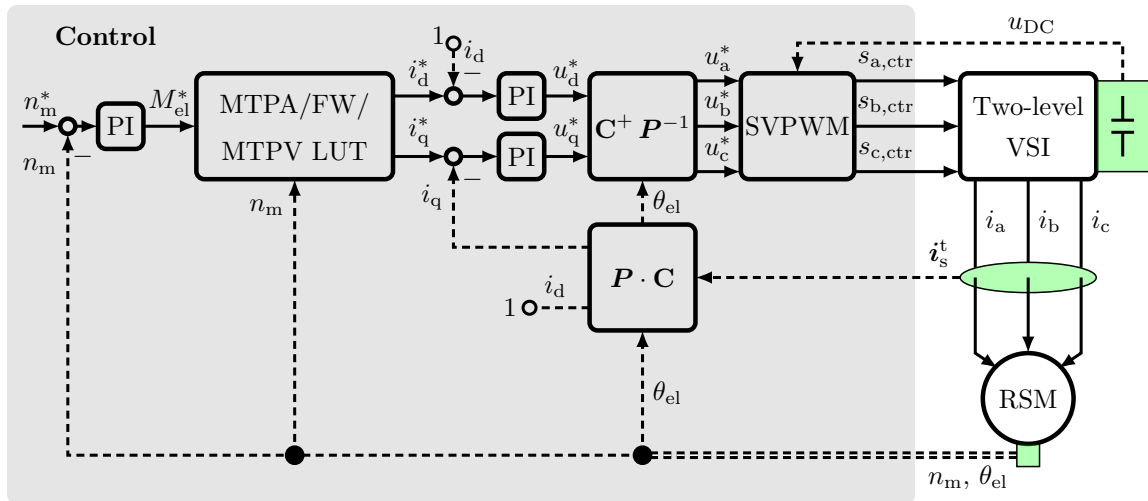


Figure 3.4: Schematic of the control structure.

An outer speed control loop superimposes the current control loops. The control of the current control loop is performed by two proportional integral (PI) controllers. The time constants of the resulting first-order elements (time constant of the machine is

compensated operating-point-dependent [3, p. 933]) are set to the same fixed time constant of $\tau_{cc} = 2$ ms for each axis. The speed control is realized by a PI controller as well, which is tuned according to the theory of the symmetrical optimum as described in [3, p. 65]. The quotient of controller reset time to the time constant of the current control plant is chosen to be $a_{SO} = 3$. These controller settings are used for all experiments unless stated otherwise. The reference currents are generated from the reference torque and the actual speed to operate along the maximum torque per ampere (MTPA) [26], the field weakening (FW), or the maximum torque per voltage (MTPV) trajectories. The necessary dependencies $i_d^*(M_{el}^*, n_m)$ and $i_q^*(M_{el}^*, n_m)$ are pre-calculated and stored in two LUTs. Space vector modulation is used for optimized utilization of the DC-link voltage.

3.3 Machine

The working principle of the synchronous reluctance machine (RSM) was known a long time ago [27] but faded into obscurity due to the missing power electronic components necessary to operate this type of machine as desired. A couple of years ago, interest in this type of machine grew again due to modern semiconductors, which can be used to drive this machine with high efficiency.

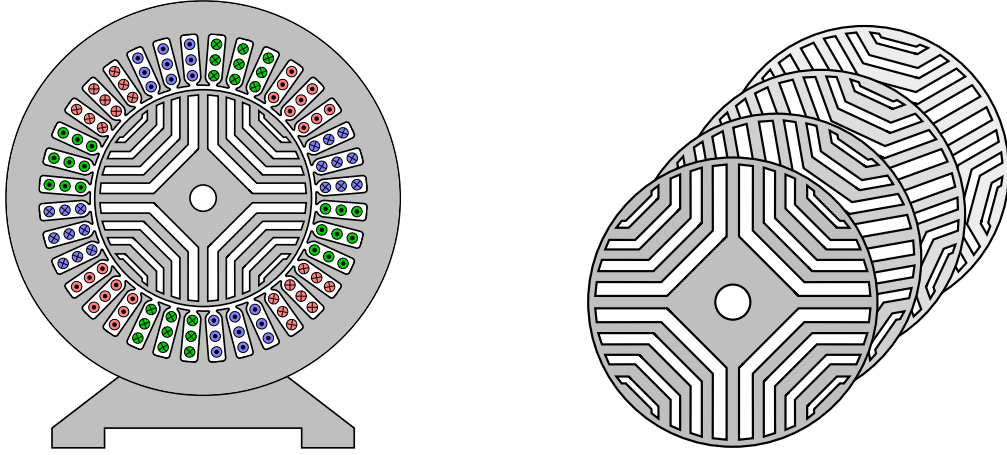
The benefit of the machine is its comparatively high efficiency (compared to IMs) without the use of any permanent magnets (PMs). Also, the simple and robust structure without any rotor coils makes the machine easy to build, reliable, and comparably cheap. The drawback of the machine is its decreased power factor (PF), resulting in a required higher current rating of the inverter compared to IMs.

The RSM used in this thesis is built and sold by the manufacturer KSB SE & Co. KGaA (KSB) and indented for use in pump applications. KSB was one of the first companies which established the RSM in industry.

The machine's rotor is continuously skewed to reduce torque ripple, which is present due to the stator teeth. The skewing of the rotor needs to be considered when creating a finite element method (FEM) model of the machine to achieve correct results. The principal geometry of the RSM with its distributed windings is shown in Fig. 3.5. The most important data is listed in Tab. 3.2.

It is important to mention that standard measurement procedures performed to obtain the model parameters of the machine (e.g., Fig. 2.4) are not conclusively explained in this thesis. Many works in the past provided approaches to determine parameters such as flux linkages and inductances. For an extensive view, it is referred to the

works [28, 29], which were the basis for most measurements presented in this thesis. However, a measurement procedure is described if it is novel, not explained in former publications, and necessary to obtain unconventional parameters.



a) Schematic of the stator and rotor.

b) Sketch of the skewed rotor layers.

Figure 3.5: Geometry of the RSM.

Type KSB 01633731

Description	Symbol	Value
Nominal power	$P_{m,n}$	1.5 kW
Nominal speed	$n_{m,n}$	1500 rpm
Nominal torque	$M_{m,n}$	9.6 Nm
Nominal current	I_n	4 A
Stator resistance	R_s	2.85Ω
Total inertia	J	$6.33 \times 10^{-3} \text{ kg m}^2$
Number of pole pairs	p	2
Number of stator teeth	N_{teeth}	36
Saliency ratio ⁹	$\dot{L}_A / \dot{L}_\Sigma$	0 % to 79 %

Additional information: RSM, distributed windings, continuously skewed rotor

Table 3.2: Parameters of the KSB test machine.

⁹The saliency ratio is a measure for the rate of the anisotropic to the isotropic behavior of the machine. The higher the saliency ratio, the easier it is to isolate the anisotropic behavior of the machine by an anisotropy-based encoderless method. RSMs naturally have a high maximum saliency ratio due to the distinctive rotor geometry. However, their saliency ratio can reach zero when the machine is unsaturated. Thus, a certain presaturation of the q-axis is necessary to apply an anisotropy-based encoderless method, even if no torque is requested.

Chapter 4

Redundancy in the event of an encoder fault

Encoders are used to measure rotor angle and rotor speed, which is required to operate the machine efficiently. In the case of synchronous machines (SMs), the rotor speed is mainly required for the speed control and the EMF feed-forward of the current controllers. The rotor position is needed to precisely set the intended current angle and, thus, electromagnetic torque. In the event of a failure, the encoder or its supply can become disrupted either by external or internal occurrences. In the event of such a failure, it is evident to use an encoderless control method as a backup algorithm. Encoderless control algorithms estimate rotor position and speed using information extracted from the current and voltage.

This chapter is dedicated to the area of encoderless control. Many different algorithms for estimating rotor angle and speed are available in today's research literature. Therefore, no novel encoderless control algorithm is proposed in the following. Existing methods are analyzed, applied, and compared. Hereby, the considerations are restricted to encoderless methods for SMs.

The area of encoderless control has quite a long research history of more than 30 years. For a long time, less attention was given to the stability and reliability issues of these methods. For example, the so-called injection-based methods, used around a standstill, are less reliable when the machine is driven into deep magnetic saturation. Conventional injection-based methods tend to become unstable at certain current amplitudes and can, therefore, only be used up to a certain torque. This issue, which is often denoted by the terminologies *convergence problem*, *stability problem*, or *overload problem*, needs to be investigated further to ensure reliable sensor fault detection and

compensation in the event of an encoder fault.

The main contribution to the field of encoderless control is the investigation of the behavior of injection-based encoderless methods in deep magnetic saturation. The investigation aims to understand and predict the behavior of the existing methods to find the most reliable algorithm. This investigation constitutes a significant part of this dissertation.

The chapter starts with the derivation of the **EMF**-based method, which is used for the estimation in the medium to high-speed region of the machine. The anisotropy detection algorithm applied around zero speed is introduced afterwards and followed by the introduction of the rotor position assignment algorithm. Afterward, alternative injection-based algorithms are presented and investigated regarding the overload capability problem. The investigation is carried out employing a novel convergence criterion. Based on the investigation and comparison, a final encoderless control setup is chosen and verified by measurements.

4.1 Extended electromotive-force-based encoderless control

The extended electromotive force (**EEMF**) model belongs to the category of so-called **EMF** models, typically used at speeds unequal to zero. The basic principle of the **EEMF** model was introduced by [30, 31] for an interior permanent magnet synchronous machine (**IPMSM**). The motivation for the development of the **EEMF** model was a drawback of common **EMF** methods, which appears when operating synchronous machines with buried permanent magnets. The drawback appears when the ordinary voltage equation in rotor fixed coordinates, similar to (2.24), is transformed to two-phase stator fixed coordinates. After the transformation, two rotor-angle-dependent terms appear. One of the terms rotates with the electrical frequency (mainly caused by the permanent magnets), whereas the second term varies with twice the angular speed (caused by the saliency). Therefore, direct demodulation via the arctan function is not possible. Also, the demodulation with a phase-locked loop (**PLL**) is only stable as long as one of the terms is dominant [32]. This is not the case when operating an **IPMSM** [32]. The authors of [30, 31] solved this problem by introducing the aforementioned **EEMF** model, which results from a shrewdly mathematical rearranging in the rotor fixed reference frame. The aim of the rearranging is to eliminate the term, which is rotating with twice the angular frequency in the two-phase stator fixed reference frame.

This can be achieved by manipulating the inductance matrices in rotor coordinates in a way that they hold the following two properties

- The elements on the major diagonal are equal.
- The elements of the side diagonal are equal according to amount but differ in the sign.

Alternatively, the matrices can be skew-symmetrical ($\mathbf{L}^\top = -\mathbf{L}$). The effect of these manipulations is shown in the following derivation of the EEMF model with the consideration of cross-saturation. The novel EEMF model introduced next considers the effect of the cross-saturation inductance. The cross-saturation effect was neglected ($\dot{L}_{dq} = 0$) by corresponding publications with the exception of the pre-publication [33][LWK]. A few publications [34, 35] compensated for the angle error due to cross-saturation using an FEM-based approach. However, no improved model was derived in these works. The main steps of the following derivation are analog to those conducted in [30, 31].

The derivation starts with the voltage equation in rotor coordinates (2.24). The use of equation (2.24) implies that only the effects of Subsection 2.3.1 are considered. Equations (4.1) and (4.2) are the voltage equations in rotor coordinates.

$$\mathbf{u}_s^r = R_s \mathbf{i}_s^r + \dot{\mathbf{L}}_s^r \frac{d\mathbf{i}_s^r}{dt} + \omega_{el} \mathbf{J} \boldsymbol{\psi}_s^r \quad (4.1)$$

$$= R_s \mathbf{i}_s^r + \begin{bmatrix} \dot{L}_{dd} & \dot{L}_{dq} \\ \dot{L}_{dq} & \dot{L}_{qq} \end{bmatrix} \frac{d\mathbf{i}_s^r}{dt} + \omega_{el} \begin{bmatrix} -L_q i_q \\ L_d i_d \end{bmatrix} \quad (4.2)$$

Equation (4.2) is rearranged to (4.3) to meet the above-described properties for the matrices.

$$\mathbf{u}_s^r = R_s \mathbf{i}_s^r + \begin{bmatrix} \dot{L}_{qq} & -\dot{L}_{dq} \\ \dot{L}_{dq} & \dot{L}_{qq} \end{bmatrix} \frac{d\mathbf{i}_s^r}{dt} + \omega_{el} \begin{bmatrix} 0 & -L_d \\ L_d & 0 \end{bmatrix} \mathbf{i}_s^r + \begin{bmatrix} e_{\text{EEMF}} \\ 0 \end{bmatrix} \quad (4.3)$$

$$= R_s \mathbf{i}_s^r + \dot{\mathbf{L}}_{s,\text{EEMF}}^r \frac{d\mathbf{i}_s^r}{dt} + \omega_{el} \mathbf{L}_{s,\text{EEMF}}^r \mathbf{i}_s^r + \begin{bmatrix} e_{\text{EEMF}} \\ 0 \end{bmatrix} \quad (4.4)$$

It can be seen that all the inductance matrices meet the requirements and that an additional quantity, e_{EEMF} appears. The name EEMF arises from this quantity, which

is described by equation (4.5).

$$e_{\text{EEMF}} := \omega_{\text{el}} i_{\text{q}} (L_{\text{d}} - L_{\text{q}}) + \frac{di_{\text{d}}}{dt} (\dot{L}_{\text{dd}} - \dot{L}_{\text{qq}}) + 2\dot{L}_{\text{dq}} \frac{di_{\text{q}}}{dt} \quad (4.5)$$

Now, equation (4.4) is transformed into two-phase stator fixed coordinates using the inverse Park transformation:

$$\mathbf{u}_{\text{s}}^{\text{s}} = R_{\text{s}} \mathbf{i}_{\text{s}}^{\text{s}} + \mathbf{P}^{-1} \dot{\mathbf{L}}_{\text{s,EEMF}}^{\text{r}} \frac{d\mathbf{P}\mathbf{i}_{\text{s}}^{\text{s}}}{dt} + \omega_{\text{el}} \mathbf{P}^{-1} \mathbf{L}_{\text{s,EEMF}}^{\text{r}} \mathbf{P}\mathbf{i}_{\text{s}}^{\text{s}} + \mathbf{P}^{-1} \begin{bmatrix} e_{\text{EEMF}} \\ 0 \end{bmatrix} \quad (4.6)$$

$$= R_{\text{s}} \mathbf{i}_{\text{s}}^{\text{s}} - \omega_{\text{el}} \dot{\mathbf{L}}_{\text{s,EEMF}}^{\text{s}} \mathbf{J}\mathbf{i}_{\text{s}}^{\text{s}} + \dot{\mathbf{L}}_{\text{s,EEMF}}^{\text{s}} \frac{d\mathbf{i}_{\text{s}}^{\text{s}}}{dt} + \omega_{\text{el}} \mathbf{L}_{\text{s,EEMF}}^{\text{s}} \mathbf{i}_{\text{s}}^{\text{s}} + \mathbf{P}^{-1} \begin{bmatrix} e_{\text{EEMF}} \\ 0 \end{bmatrix} \quad (4.7)$$

with the new inductance matrices in stator coordinates being:

$$\dot{\mathbf{L}}_{\text{s,EEMF}}^{\text{s}} := \mathbf{P}^{-1} \dot{\mathbf{L}}_{\text{s,EEMF}}^{\text{r}} \mathbf{P} = \dot{\mathbf{L}}_{\text{s,EEMF}}^{\text{r}} \quad (4.8)$$

$$\mathbf{L}_{\text{s,EEMF}}^{\text{s}} := \mathbf{P}^{-1} \mathbf{L}_{\text{s,EEMF}}^{\text{r}} \mathbf{P} = \mathbf{L}_{\text{s,EEMF}}^{\text{r}} \quad (4.9)$$

The advantage of the manipulations done in rotor coordinates is discernible now. The inductance matrices in stator and rotor coordinates are equal, and no additional rotor-angle-dependent term appears. Only one term rotating at the electrical frequency is present. This term, rotating at the electrical frequency, can be demodulated by an arctan function or a PLL. Equation (4.7) can be consolidated to the voltage equation (4.10).

$$\mathbf{u}_{\text{s}}^{\text{s}} = R_{\text{s}} \mathbf{i}_{\text{s}}^{\text{s}} + \dot{\mathbf{L}}_{\text{s,EEMF}}^{\text{s}} \frac{d\mathbf{i}_{\text{s}}^{\text{s}}}{dt} + \omega_{\text{el}} \left(\mathbf{L}_{\text{s,EEMF}}^{\text{s}} - \dot{\mathbf{L}}_{\text{s,EEMF}}^{\text{s}} \mathbf{J} \right) \mathbf{i}_{\text{s}}^{\text{s}} + \underbrace{e_{\text{EEMF}} \begin{bmatrix} \cos(\theta_{\text{el}}) \\ \sin(\theta_{\text{el}}) \end{bmatrix}}_{=:\mathbf{e}_{\text{s,EEMF}}^{\text{s}}} \quad (4.10)$$

In its expanded and rearranged form, it can be given as follows:

$$\begin{aligned} \mathbf{u}_{\text{s}}^{\text{s}} = & \underbrace{R_{\text{s}} \mathbf{i}_{\text{s}}^{\text{s}} + \begin{bmatrix} \dot{L}_{\text{qq}} & 0 \\ 0 & \dot{L}_{\text{qq}} \end{bmatrix} \frac{d\mathbf{i}_{\text{s}}^{\text{s}}}{dt} + \omega_{\text{el}} \begin{bmatrix} 0 & (\dot{L}_{\text{qq}} - L_{\text{d}}) \\ -(\dot{L}_{\text{qq}} - L_{\text{d}}) & 0 \end{bmatrix} \mathbf{i}_{\text{s}}^{\text{s}} + e_{\text{EEMF}} \begin{bmatrix} \cos(\theta_{\text{el}}) \\ \sin(\theta_{\text{el}}) \end{bmatrix}}_{\text{EEMF model according to current literature}} \dots \\ & \dots + \underbrace{\begin{bmatrix} 0 & -\dot{L}_{\text{dq}} \\ \dot{L}_{\text{dq}} & 0 \end{bmatrix} \frac{d\mathbf{i}_{\text{s}}^{\text{s}}}{dt} + \omega_{\text{el}} \begin{bmatrix} \dot{L}_{\text{dq}} & 0 \\ 0 & \dot{L}_{\text{dq}} \end{bmatrix} \mathbf{i}_{\text{s}}^{\text{s}}}_{\text{New additional terms due to cross-saturation}} \end{aligned} \quad (4.11)$$

An examination of equation (4.5) shows that the rotor-angle-dependent term is not only present in the case of an angular speed unequal to zero, but also if current derivatives in the d- or q-axis appear. This property is useful to apply encoderless control around zero speed [36, 37, 38].

The new model with consideration of cross-saturation (4.10) and (4.11), might explain the inaccuracies during torque transients which have been frequently reported [39, 40, 41]. These publications did not consider the effect of cross-saturation in their model, which leads to estimation errors. However, further investigation regarding this effect does not form part of this work.

The rotor position-dependent term of (4.10) must be isolated for the rotor position estimation. The term can be isolated by employing a disturbance observer, which is derived in the following. The rotor-angle-dependent term $\mathbf{e}_{s,\text{EEMF}}^s$ of (4.10) is considered to be the disturbance, since it contains the desired rotor position information. Equation (4.10) is used to estimate the disturbance $\hat{\mathbf{e}}_{s,\text{EEMF}}^s$ using the estimated angular frequency $\hat{\omega}_{\text{el}}$ as feedback. After the discretization for the sampling instance k with the explicit Euler method [42], and with the assumption of constant inductance matrices during the sampling interval, the estimated disturbance is given by:

$$\hat{\mathbf{e}}_{s,\text{EEMF}}^s[n][k-1] = \hat{e}_{\text{EEMF}}[n][k-1] \begin{bmatrix} \cos(\hat{\theta}_{\text{el}}[n][k-1]) \\ \sin(\hat{\theta}_{\text{el}}[n][k-1]) \end{bmatrix} = \begin{bmatrix} \hat{e}_{\alpha,\text{EEMF}}[n][k-1] \\ \hat{e}_{\beta,\text{EEMF}}[n][k-1] \end{bmatrix} \quad (4.12)$$

$$\begin{aligned} &= \mathbf{u}_s^s[n][k-1] - R_s \mathbf{i}_s^s[n][k-1] - \hat{\mathbf{L}}_{s,\text{EEMF}}^s[n][k-1] \frac{\Delta \mathbf{i}_s^s[n][k]}{T_{\text{sp,ctr}}} \dots \\ &\dots - \hat{\omega}_{\text{el}}[n][k-1] \left(\mathbf{L}_{s,\text{EEMF}}^s[n][k-1] - \hat{\mathbf{L}}_{s,\text{EEMF}}^s[n][k-1] \mathbf{J} \right) \mathbf{i}_s^s[n][k-1] \end{aligned} \quad (4.13)$$

$$= \mathbf{u}_s^s[n][k-1] - \hat{\mathbf{u}}_{s,\text{mod}}^s[n][k-1] \quad (4.14)$$

However, a rotor position estimation based on this model causes significant estimation errors in practice due to the neglected effect of the inverter's interlock time, as reported by [17, 18, 19]. Thus, the model of the idealized disturbance observer (4.14) is extended by the model of the VSI (2.46) according to equation (2.47) by substituting $\mathbf{u}_s^s = \mathbf{u}_{\text{ctr.}}^s - \mathbf{u}_{\text{dt.}}^s$. This yields to:

$$\hat{\mathbf{e}}_{s,\text{EEMF}}^s[n][k-1] = \mathbf{u}_{\text{ctr.}}^s[n][k-1] - \mathbf{u}_{\text{dt.}}^s[n][k-1] - \hat{\mathbf{u}}_{s,\text{mod}}^s[n][k-1] \quad (4.15)$$

The schematic of the disturbance observer is shown in Fig. 4.1. The rotor angle can be estimated as shown in (4.16) using the arctan2 function, getting the full range from

$-\pi$ to π . Equation (4.16) assumes that the rotor angle varies only slowly during one sampling interval. This assumption is appropriate due to the sufficient high sampling frequency. With the substitution $\hat{\theta}_{\text{el,EEMF}} := \hat{\theta}_{\text{el}}$ it follows:

$$\hat{\theta}_{\text{el,EEMF}}[n][k] \approx \hat{\theta}_{\text{el}}[n][k-1] = \arctan2(\hat{e}_{\beta,\text{EEMF}}[n][k-1], \hat{e}_{\alpha,\text{EEMF}}[n][k-1]) \quad (4.16)$$

Alternatively, the estimated angle can be passed through a PLL, for filter purposes, as described later in Section 4.3.

The benefits of using the EEMF model are summarized below to make the decision for this model more comprehensible:

- The method can be applied to many different synchronous machines with only minor modifications.
- The model does not rely on an integration of the voltage and therefore avoids the known offset drift problem [43, 44] of flux-linkage-based models.
- The model can be used at a standstill with minor accommodations, where most of the other EMF-based methods do not work.

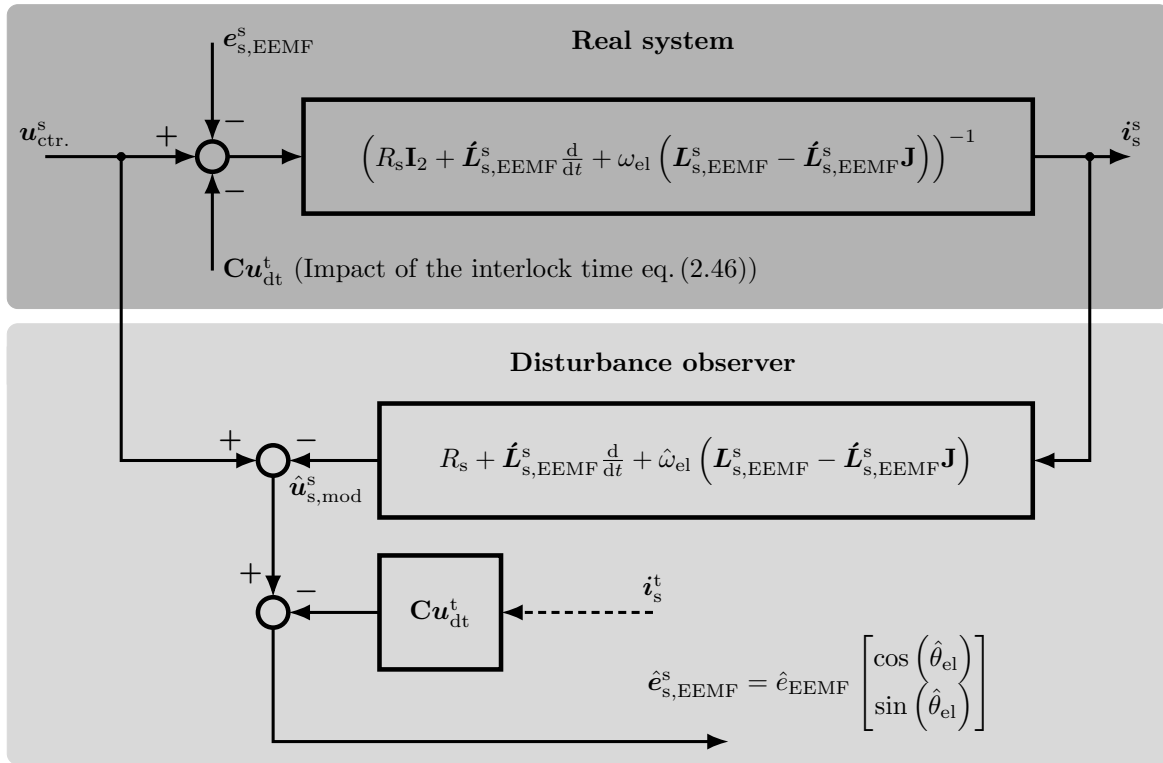


Figure 4.1: Schematic of the disturbance observer with compensation for the inverter's interlock time.

4.2 Injection-based encoderless control

Algorithms in the category of [EMF](#)-based encoderless control algorithms were the first developed in the history of encoderless control. Commonly these methods suffer from a bad signal-to-noise ratio ([SNR](#)) of the induced voltage close to zero speed so that the rotor position cannot be estimated around a standstill. To cover the low-speed region also, so-called injection-based methods were developed, often referred to as anisotropy-based methods. These methods commonly employ an additional voltage or current injection. Such an injection-based method is derived later in this section. But first, the question arises about why a second algorithm is used, as the formerly presented [EEMF](#) scheme was advertised working around zero speed with some modifications. The reasons to use an additional injection-based algorithm for the low-speed region are the following:

- The injection-based method introduced in the following relies on very few parameters as compared to the [EEMF](#) model.
- Injection-based methods are less sensitive to voltage errors or even independent. This is because injection-based methods use mainly relative voltages (voltage differences) contrary to the [EEMF](#)-based approach, which uses absolute voltages. Thus, the injection-based method has a higher [SNR](#) in the low-speed region, resulting in a more accurate and reliable rotor position estimation.

Anisotropy-based methods, which are strictly speaking only a part of the entire injection-based estimation structure, make use of the anisotropic behavior of the machine. The anisotropy is caused by rotor-position-dependent inductances as described by equation (2.35). A saliency may not only be due to the geometry of the rotor but can also be caused by saturation due to the permanent magnets. The terminology “anisotropy-based method” comes from the property that these methods commonly at first estimate the so-called anisotropy angle as shown in (2.36) and not the real rotor angle. As discussed later, the real rotor angle is demodulated by a second algorithm, which is also a part of the entire injection-based estimation structure.

The theory of anisotropy-based methods uses several different definitions of angles. For a better understanding, the different definitions are listed in the following:

- θ_{el} is the electrical rotor angle. Each encoderless method aims to estimate this quantity as precisely as possible.

- θ_A is the so-called anisotropy angle. The anisotropy angle is estimated at first (before demodulating the actual rotor angle) by most conventional injection-based methods. It differs from the electrical rotor angle due to magnetic saturation and higher space harmonics. Its mathematical definition has already been derived (2.37) and is given by $\theta_A = \theta_{el} + \theta_\delta$.
- θ_δ is called the misalignment angle, and it describes the displacement angle between the actual rotor angle and the anisotropy angle due to magnetic saturation. It is commonly compensated for with a second algorithm inside the injection-based estimation structure. This second algorithm is called the rotor position assignment algorithm. The mathematical definition of the misalignment angle has already been derived (2.37) and is given by $\theta_\delta = \frac{1}{2} \arctan\left(\frac{L_{dq}}{L_\Delta}\right)$.
- $\Delta\theta_{el}$ is named the rotor position estimation error. This angle describes the deviation between the final (after the compensation for the misalignment angle) estimated electrical rotor angle $\hat{\theta}_{el}$ and the actual electrical rotor angle. It is defined as follows $\Delta\theta_{el} := \hat{\theta}_{el} - \theta_{el}$.

4.2.1 Anisotropy detection - Arbitrary Injection

A variety of methods exist to estimate the anisotropy of the machine, too many to present each. Therefore, only the method used within this work is presented. The method is the so-called “Arbitrary Injection” [45, 46, 47]. It was developed with the intention of being able to inject arbitrary voltage waveforms. Prior methods relied on a defined shape of the voltage injection, which reduces the flexibility in many points. Examples for prior methods are the Rotational Injection [48], the Alternating Injection [49, 50], and the indirect flux detection by online reactance measurement (INFORM) method [51].

One great benefit of using arbitrary voltage vectors is that no additional voltage injection is required under idealized conditions. The current controllers automatically cause a small voltage injection to keep the currents at their reference values. Furthermore, the PWM can also cause a sufficient large injection and current ripple. The authors of [4, 45, 52] demonstrated operation even without additional voltage injection successfully.

The Arbitrary Injection model is derived in the following. The starting point is the state equation of the current in the two-phase stator fixed reference frame deduced

from (2.27). The result is:

$$\frac{d\mathbf{i}_s^s}{dt} = \left(\dot{\mathbf{L}}_s^s\right)^{-1} \left(\mathbf{u}_s^s - R_s \mathbf{i}_s^s - \omega_{el} \left(\mathbf{J}\boldsymbol{\psi}_s^s - \dot{\mathbf{L}}_s^s \mathbf{J}\mathbf{i}_s^s\right)\right) \quad (4.17)$$

The derivation requires the discretized form of equation (4.17). It is discretized using the explicit Euler method [42] employing the sampling interval of the currents $T_{\text{sp,ctr}}$. If the discretized form of (4.17) is directly solved for the current difference between two consecutive sampling points it yields equation (4.18). Note that the integer multiplier of the algorithm execution time n is not denoted for the clarity of the equations. The entire derivation refers to the instance n .

$$\Delta\mathbf{i}_s^s[k] := \frac{T_{\text{sp,ctr}}}{\left(\dot{\mathbf{L}}_s^s[k_{-1}]\right)} \left(\mathbf{u}_s^s[k_{-1}] - R_s \mathbf{i}_s^s[k_{-1}] - \omega_{el}[k_{-1}] \left(\mathbf{J}\boldsymbol{\psi}_s^s[k_{-1}] - \dot{\mathbf{L}}_s^s[k_{-1}] \mathbf{J}\mathbf{i}_s^s[k_{-1}]\right)\right) \quad (4.18)$$

It is appropriate to assume that the applied voltage varies significantly faster than the current due to the inductive character of the machine. Therefore, the right-hand side of equation (4.18) can be interpreted as a superposition of a fast-changing current difference $\Delta\mathbf{i}_{s,\text{HF}}^s[k]$ (high-frequency (HF) component) and slowly changing current difference $\Delta\mathbf{i}_{s,\text{LF}}^s[k]$ (low-frequency component)

$$\Delta\mathbf{i}_s^s[k] = \Delta\mathbf{i}_{s,\text{HF}}^s[k] - \Delta\mathbf{i}_{s,\text{LF}}^s[k] \quad (4.19)$$

with the HF component (ohmic voltage drop neglected)

$$\Delta\mathbf{i}_{s,\text{HF}}^s[k] := T_{\text{sp,ctr}} \left(\dot{\mathbf{L}}_s^s[k_{-1}]\right)^{-1} \mathbf{u}_s^s[k_{-1}] \quad (4.20)$$

and the low-frequency component

$$\Delta\mathbf{i}_{s,\text{LF}}^s[k] := T_{\text{sp,ctr}} \left(\dot{\mathbf{L}}_s^s[k_{-1}]\right)^{-1} \left(R_s \mathbf{i}_s^s[k_{-1}] + \omega_{el}[k_{-1}] \left(\mathbf{J}\boldsymbol{\psi}_s^s[k_{-1}] - \dot{\mathbf{L}}_s^s[k_{-1}] \mathbf{J}\mathbf{i}_s^s[k_{-1}]\right)\right) \quad (4.21)$$

It can be seen, that both components, (4.20) and (4.21), include position information hidden in the differential inductance matrix. The high-frequency component includes only one angle-dependent term, whereas the slowly changing component includes several terms which are more sophisticated to demodulate. Hence, the fast-changing part $\Delta\mathbf{i}_{s,\text{HF}}^s[k]$ must be isolated from the total current difference $\Delta\mathbf{i}_s^s[k]$, to achieve the position information easily. A filtering approach [53] seems to be the most simple way

to eliminate the low-frequency part in (4.19). However, filtering needs to be tuned and results in a limited bandwidth of the rotor angle estimation. Furthermore, it causes estimation errors as shown in [53]. To avoid these drawbacks, the authors of [54, 55], [47, p. 36] developed the so-called Δ -scheme, where the slow-changing part of (4.19) is assumed to be constant over two consecutive sampling periods. As long as the speed is low, this is a valid assumption due to the sufficiently high sampling frequency. The low-frequency part $\Delta \mathbf{i}_{s,\text{LF}}^s$ can then be eliminated when subtracting the past current difference $\Delta \mathbf{i}_s^s[k-1]$ from the actual current difference $\Delta \mathbf{i}_s^s[k]$, without any filtering. However, an error appears at higher speeds [47, p. 46] since $\Delta \mathbf{i}_{s,\text{LF}}^s$ is not constant anymore. Therefore, the so-called Δ^2 -scheme was introduced by [56] and [47, p. 39] with an improved behavior at higher speeds.

This Δ^2 -Scheme is derived in the following and used as a so-called anisotropy-based (high-frequency) method. The Δ^2 -scheme assumes a linear change $\Lambda_{s,\text{LF}}^s$ of $\Delta \mathbf{i}_{s,\text{LF}}^s$, over two¹⁰ consecutive sampling periods of the current difference to isolate the high-frequency component. The differential inductance matrix $\hat{\mathbf{L}}_s^s$ is assumed to be constant over the three consecutive sampling periods $T_{\text{sp,ctr}}$, or over one control period T_{ctr} respectively. Therefore, it applies $\hat{\mathbf{L}}_s^s[k] = \hat{\mathbf{L}}_s^s[k-1] = \hat{\mathbf{L}}_s^s[k-2] = \hat{\mathbf{L}}_s^s[k-3]$. The underlying assumption of the Δ^2 -scheme is shown in Fig. 4.2, exemplary for the α -component.

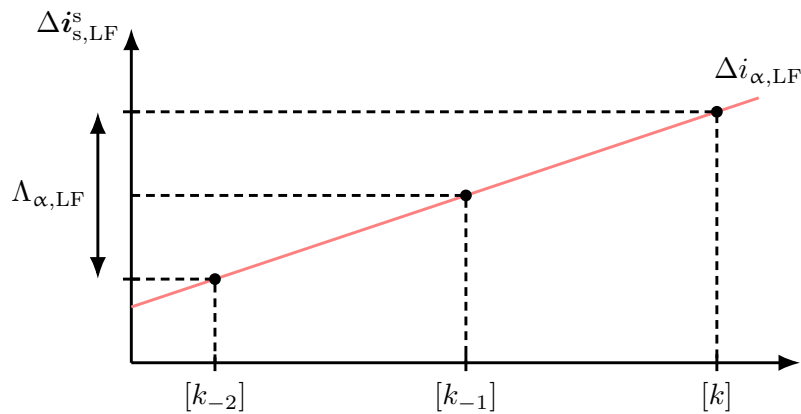


Figure 4.2: Illustration of the low-frequency current difference when a linear change over two consecutive sampling periods of the current difference is assumed.

The low-frequency part can be eliminated by employing the abovementioned assumption if three sampling instances of $\Delta \mathbf{i}_s^s$ are subtracted as follows (Δ^2 is an identifier

¹⁰Note: Two sampling periods of the current difference correspond to three sampling points in time of the current difference. This constitutes three sampling periods of the current and four sampling points in time of the current.

and no mathematical operation):

$$\Delta^2 \mathbf{i}_s^s[k] := \Delta \mathbf{i}_s^s[k] - 2\Delta \mathbf{i}_s^s[k-1] + \Delta \mathbf{i}_s^s[k-2] \quad (4.22)$$

$$= (\mathbf{i}_s^s[k] - \mathbf{i}_s^s[k-1]) - 2(\mathbf{i}_s^s[k-1] - \mathbf{i}_s^s[k-2]) + (\mathbf{i}_s^s[k-2] - \mathbf{i}_s^s[k-3]) \quad (4.23)$$

Inserting (4.19) in (4.22) and using the assumption of a linearly changing low-frequency component results in the isolation of the squared high-frequency current difference:

$$\begin{aligned} \Delta^2 \mathbf{i}_s^s[k] &= \Delta \mathbf{i}_{s,\text{HF}}^s[k] - \Delta \mathbf{i}_{s,\text{LF}}^s[k] - 2(\Delta \mathbf{i}_{s,\text{HF}}^s[k-1] - \Delta \mathbf{i}_{s,\text{LF}}^s[k-1]) + \dots \\ &\dots \Delta \mathbf{i}_{s,\text{HF}}^s[k-2] - \Delta \mathbf{i}_{s,\text{LF}}^s[k-2] \end{aligned} \quad (4.24)$$

$$\begin{aligned} &= \Delta \mathbf{i}_{s,\text{HF}}^s[k] - \Delta \mathbf{i}_{s,\text{LF}}^s[k] - 2(\Delta \mathbf{i}_{s,\text{HF}}^s[k-1] - (\Delta \mathbf{i}_{s,\text{LF}}^s[k] - 0.5\mathbf{\Lambda}_{s,\text{LF}}^s)) + \dots \\ &\dots \Delta \mathbf{i}_{s,\text{HF}}^s[k-2] - (\Delta \mathbf{i}_{s,\text{LF}}^s[k] - \mathbf{\Lambda}_{s,\text{LF}}^s) \end{aligned} \quad (4.25)$$

$$= \Delta \mathbf{i}_{s,\text{HF}}^s[k] - 2\Delta \mathbf{i}_{s,\text{HF}}^s[k-1] + \Delta \mathbf{i}_{s,\text{HF}}^s[k-2] \quad (4.26)$$

The high-frequency components on the right-hand side of equation (4.26) can be substituted using (4.20):

$$\Delta^2 \mathbf{i}_s^s[k] = \mathbf{T}_{\text{sp,ctr}} (\dot{\mathbf{L}}_s^s[k])^{-1} \underbrace{(\mathbf{u}_s^s[k-1] - 2\mathbf{u}_s^s[k-2] + \mathbf{u}_s^s[k-3])}_{\Delta^2 \mathbf{u}_s^s[k-1]} \quad (4.27)$$

With the definition of the differential inductance matrix (2.35) and its inverse, equations (4.28) to (4.30) are derived. A new physical quantity Y called the admittance with the unit A/(Vs) is introduced. It is commonly used in the area of encoderless control and was introduced in [55] to shorten the terms of the inverse inductance. The admittance multiplied by the voltage-time area, applied over the sampling period $\mathbf{T}_{\text{sp,ctr}}$, results in the rise of the current. The rise is often assumed to be linear. Hence, $\mathbf{T}_{\text{sp,ctr}} \ll \tau_{\text{min}}$ must apply, with τ_{min} being the smallest electrical time constant of the machine [4, p. 56]. The terminologies of the different admittances are as follows, \mathbf{Y}_s^s is the admittance matrix, \mathbf{Y}_Σ is the mean admittance, and \mathbf{Y}_A is named the anisotropy admittance.

$$\Delta^2 \mathbf{i}_s^s[k] = T_{\text{sp,ctr}} \left(\underbrace{\frac{-\dot{L}_\Sigma[k]}{\dot{L}_A[k]^2 - \dot{L}_\Sigma[k]^2}}_{\dot{Y}_\Sigma[k]} \mathbf{I}_2 + \underbrace{\frac{\dot{L}_A[k]}{\dot{L}_A[k]^2 - \dot{L}_\Sigma[k]^2}}_{\dot{Y}_A[k]} \mathbf{S}(\theta_A[k]) \right) \Delta^2 \mathbf{u}_s^s[k_{-1}] \quad (4.28)$$

$$= T_{\text{sp,ctr}} \underbrace{\left(\dot{Y}_\Sigma[k] \mathbf{I}_2 + \dot{Y}_A[k] \mathbf{S}(\theta_A[k]) \right)}_{\dot{Y}_s^s[k]} \Delta^2 \mathbf{u}_s^s[k_{-1}] \quad (4.29)$$

$$=: \Delta^2 \mathbf{i}_{s,\Sigma}^s[k] + \Delta^2 \mathbf{i}_{s,\Delta}^s[k] \quad (4.30)$$

The mean admittance can be expressed by the differential inductances of the rotor fixed reference frame, which yields:

$$\dot{Y}_\Sigma[k] = \frac{-\dot{L}_\Sigma[k]}{\dot{L}_A[k]^2 - \dot{L}_\Sigma[k]^2} = \frac{\dot{L}_{\text{dd}}[k] + \dot{L}_{\text{qq}}[k]}{2\dot{L}_{\text{dd}}[k]\dot{L}_{\text{qq}}[k] - 2\dot{L}_{\text{dq}}[k]^2} \quad (4.31)$$

It can be seen that (4.29) consists of an isotropic term scaling with the mean admittance and an anisotropic term containing the position information in terms of the anisotropy angle in the admittance matrix. Hence, the anisotropic part $\Delta^2 \mathbf{i}_{s,\Delta}^s[k]$ can only be separated if the mean admittance is known. The mean admittance can either be predetermined by measurements and stored in a LUT, or it can be estimated online during operation [57, 53]. Assuming that an estimation of \hat{Y}_Σ is provided, the isotropic part can be estimated as follows:

$$\Delta^2 \hat{\mathbf{i}}_{s,\Sigma}^s[k] = T_{\text{sp,ctr}} \hat{Y}_\Sigma[k] \mathbf{I}_2 \Delta^2 \mathbf{u}_s^s[k_{-1}] = T_{\text{sp,ctr}} \hat{Y}_\Sigma[k] \Delta^2 \mathbf{u}_s^s[k_{-1}] \quad (4.32)$$

Equation (4.32) is then subtracted from (4.29) to achieve the estimated anisotropic part:

$$\Delta^2 \hat{\mathbf{i}}_{s,\Delta}^s[k] = \Delta^2 \mathbf{i}_s^s[k] - \Delta^2 \hat{\mathbf{i}}_{s,\Sigma}^s[k] \quad (4.33)$$

$$= T_{\text{sp,ctr}} \hat{Y}_A[k] \mathbf{S}(\hat{\theta}_A[k]) \Delta^2 \mathbf{u}_s^s[k_{-1}] \quad (4.34)$$

Equation (4.34) consists of two equations (vector with two components) with two unknowns and can be solved for the estimated anisotropy angle. Hence, (4.34) needs

to be expressed by its alpha and beta component. After some rearranging, a model error related vector (4.35)-(4.37) is derived, which can be demodulated by a PLL or by an arctan2 function. As mentioned initially, it constitutes the estimation at the sampling instances $[n][k]$.

$$\hat{\mathbf{e}}_{s, \text{AI}}^s[n][k] = \begin{bmatrix} \hat{e}_{\alpha, \text{AI}}[n][k] \\ \hat{e}_{\beta, \text{AI}}[n][k] \end{bmatrix} \quad (4.35)$$

$$= \begin{bmatrix} T_{\text{sp,ctr}} \hat{Y}_A[k] \left(\Delta^2 u_\alpha^2[n][k_{-1}] + \Delta^2 u_\beta^2[n][k_{-1}] \right) \cos \left(2\hat{\theta}_A[n][k] \right) \\ T_{\text{sp,ctr}} \hat{Y}_A[k] \left(\Delta^2 u_\alpha^2[n][k_{-1}] + \Delta^2 u_\beta^2[n][k_{-1}] \right) \sin \left(2\hat{\theta}_A[n][k] \right) \end{bmatrix} \quad (4.36)$$

$$= \begin{bmatrix} \Delta^2 \hat{i}_{\alpha, \Delta}[n][k] \cdot \Delta^2 u_\alpha[n][k_{-1}] - \Delta^2 \hat{i}_{\beta, \Delta}[n][k] \cdot \Delta^2 u_\beta[n][k_{-1}] \\ \Delta^2 \hat{i}_{\alpha, \Delta}[n][k] \cdot \Delta^2 u_\beta[n][k_{-1}] + \Delta^2 \hat{i}_{\beta, \Delta}[n][k] \cdot \Delta^2 u_\alpha[n][k_{-1}] \end{bmatrix} \quad (4.37)$$

The demodulation with an arctan2 function would look as follows:

$$\hat{\theta}_A[n][k] = \frac{1}{2} \arctan2 \left(\hat{e}_{\beta, \text{AI}}[n][k], \hat{e}_{\alpha, \text{AI}}[n][k] \right) \quad (4.38)$$

To make the decision for the Arbitrary Injection more comprehensible, its most important advantages are briefly summarized below:

- The method is independent of the shape of the voltage injection if the mean admittance is known [3, p. 1161]. This creates more flexibility than other methods have.
- The voltage drop caused by the inverter's interlock time has no effect due to the use of relative voltages.
- An extended version of the introduced Δ^2 -scheme, called the Δ^2 -scheme for flexible intervals [47, p. 55], can be used without additional signal injection.
- High bandwidths can be achieved because no filtering must be applied.
- Online estimation algorithms [57, 53] for the mean admittance \hat{Y}_Σ can be used, which allows parameter-free estimation of the anisotropy angle.

However, the method requires that the high-frequency squared current difference (4.26) is unequal to zero. Thus, a high-frequency current difference must be present over two dedicated sampling periods. To ensure this, the injected voltage must contain a

frequency component that is equal to the frequency of the sampling interval [47, p. 41].

The block diagram of the Arbitrary Injection Δ^2 -scheme, shown in Fig. 4.3, states the simplicity in implementation. The $1/z$ block is called unit delay; it holds and delays its input by one sampling period.

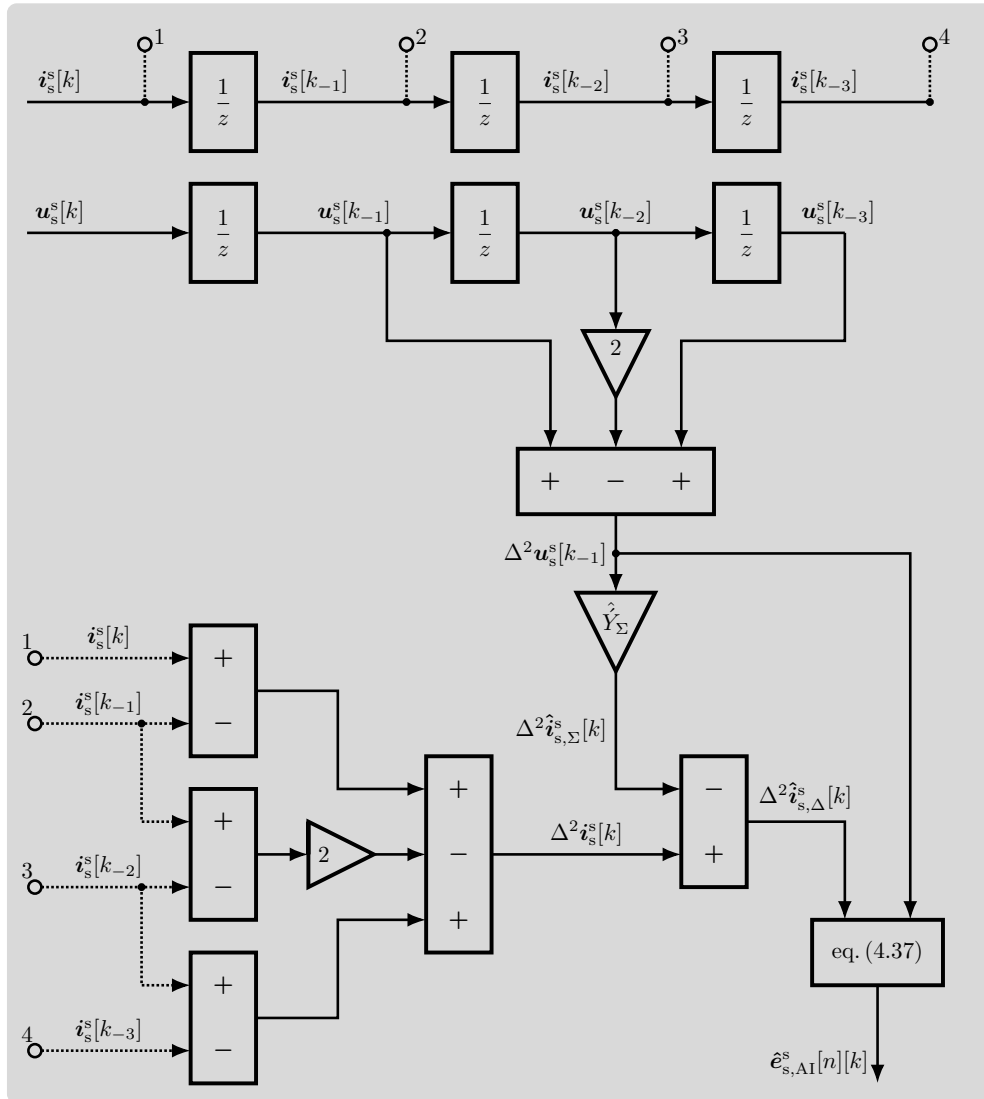


Figure 4.3: Schematic of the Arbitrary Injection Δ^2 -scheme.

The Arbitrary Injection-based anisotropy detection allows a high degree of freedom with regard to the shape and frequency of the injected voltage. The voltage injection used within this work is shown in Fig. 4.4. This type of injection is called triangular injection [46] and provides linearly independent voltage vectors, which are required for some of the approaches to estimating the mean admittance online. This type of injection causes the voltage commands and the current ripple as shown in Fig. 3.3. The

amplitude of the voltage vector is set to $|u_{inj}| = 75 \text{ V}$ within this work which conforms to 13% of the DC-link voltage. This is a typical value in the research literature.

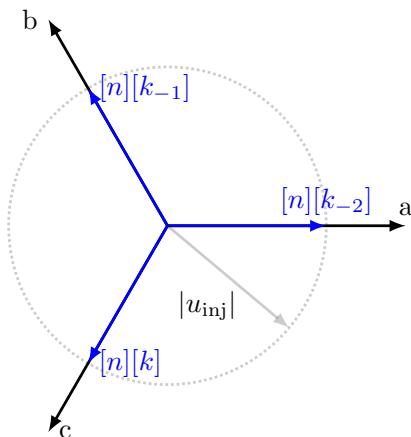


Figure 4.4: Voltage injection sequence of the Arbitrary Injection.

4.2.2 Conventional rotor position assignment

The derivation in the previous subsection has shown that anisotropy-based encoderless algorithms determine the magnetic anisotropy or the anisotropy angle, respectively. However, the actual aim is to estimate the rotor angle of the machine. Using the anisotropy angle [49, 48] in the FOC would cause a significant loss in efficiency due to the misalignment angle and operation next to the MTPA trajectory. In the case of strong harmonic anisotropies, the anisotropy angle might even be completely useless.

The compensation of the deviations due to cross-saturation and harmonic anisotropies is the task of the so-called rotor position assignment algorithm. The rotor position assignment algorithm determines the estimated rotor angle with a second model considering the effects of cross-saturation and harmonic anisotropies.

For an RSM, the deviation between the anisotropy angle and the rotor angle is mainly due to the misalignment angle caused by cross-saturation. Due to the distributed windings in the stator, only weak space harmonics are present, which can be neglected. The influence of the misalignment angle θ_δ can be compensated for using the currents of the rotor fixed reference frame as inputs for a LUT, which contains the data of the determined misalignment angle. Fig. 4.5 shows the measured misalignment angle of the machine and the intended MTPA trajectory (green). It can be seen that the misalignment angle can reach values up to 15° along the MTPA trajectory. The reference q-axis current of the MTPA is set to a minimum of 3 A to ensure pre-saturation and

the saliency of the machine (2.36), otherwise, $\dot{L}_A = 0$ applies.

The substantial drop in the misalignment angle at about $i_d = 8$ A and $i_q = 0$ A is because the q-axis differential inductance becomes bigger than that of the d-axis, causing a 90° rotation according to (2.37).

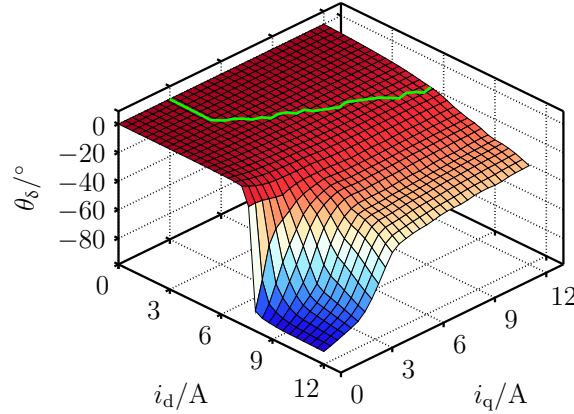


Figure 4.5: Measured misalignment angle with *MTPA* trajectory in green.

The authors of [58] proposed the first rotor position assignment algorithm. Since then, several approaches have been proposed, e.g., [59, 60], to compensate also for deviations due to higher space harmonics. Most of these approaches are based on a modified PLL structure. However, these approaches function up to a certain anisotropy ratio¹¹ only. Thus, the authors of [56] have developed the approach so-called multidimensional exploitation of the harmonics, which can cope with higher anisotropy ratios. It is known that this approach still suffers from stability issues at anisotropy ratios where the anisotropy trajectories are not strictly monotone and thus do not change with the rotor position.

As aforementioned, the impact of harmonic anisotropies is neglectable for the machine used and not considered in the rotor position assignment algorithm. The misalignment angle is only compensated dependent on the currents, based on the measurement shown in Fig. 4.5. To save memory and computational resources the actual compensation $\theta_{\delta, \text{comp.}}$ is restricted to the *MTPA* trajectory (4.39), with a 1D LUT.

$$\theta_{\delta, \text{comp.}} (\|\mathbf{i}_s^s\|) := \theta_{\delta} \left(\mathbf{i}_s^r \Big|_{\text{MTPA}} \right) \quad (4.39)$$

¹¹The anisotropy ratio is an intensity measure of the negative two-times harmonic anisotropy compared to the fundamental anisotropy. Often, the negative two-times harmonic has the second strongest influence after the fundamental one or is even stronger than the fundamental anisotropy; therefore, it is considered in the anisotropy ratio. The negative rotating harmonic is stator fixed and can cause significant estimation errors if uncompensated.

The compensation term is stored with respect to the current amplitude and is mirrored in the software using the current signs to cover all four quadrants. This mirroring is valid because of the symmetry of the differential cross-saturation inductance [13] for RSMs.

It is intuitive to directly subtract the compensation term $\theta_{\delta,comp.}$ from the detected anisotropy angle (4.38) to estimate the rotor angle $\hat{\theta}_{el} = \hat{\theta}_A - \theta_{\delta,comp.}$. However, it is recommended to filter both angles $\hat{\theta}_A$ and $\theta_{\delta,comp.}$ first to reduce the noise caused by the current measurements. Hence, a modified PLL structure is used to filter and demodulate the estimated rotor position. This structure of the PLL is called the scalar compensation approach in the field of encoderless control and was proposed by [59]. Its structure is shown in Fig. 4.6. The algorithm reconstructs the anisotropy angle $\theta_{A,comp.} = \hat{\theta}_{el} + \theta_{\delta,comp.}$ in the feedback of the PLL and compares it with the estimated angle $\hat{\theta}_A$ from the Arbitrary Injection. The resulting deviation is fed to the PI controller with a subsequent integrator to extract the estimated rotor position. This demodulation principle is widely used for rotor position assignment but is restricted to synchronous machines.

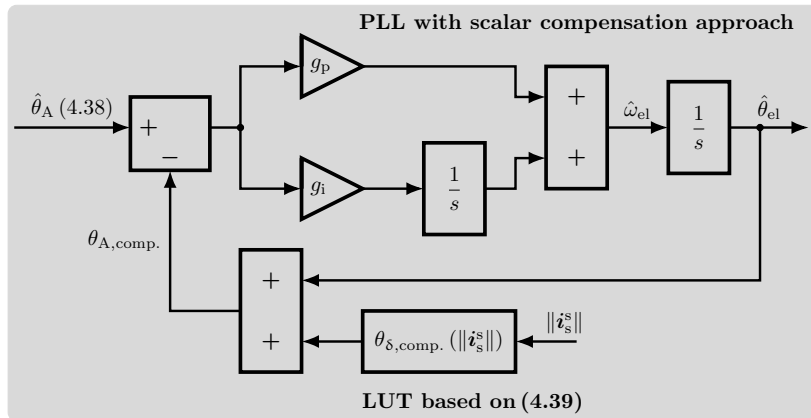


Figure 4.6: PLL combined with the rotor position assignment.

It should be mentioned that the actual misalignment angle θ_δ is unknown when operating encoderless. This is due to the use of the estimated currents \hat{i}_d and \hat{i}_q to determine the misalignment angle. The currents are estimations because the Park transformation uses the estimated rotor position while operating encoderless. Also, in the case when the misalignment angle is not calculated from the two estimated currents \hat{i}_d and \hat{i}_q and instead from the current amplitude as shown in Fig. 4.6, it remains an estimation. It is an estimation since it is stored along the intended MTPA trajectory and can, therefore, not follow any actual operating point next to the stored trajectory.

It is important to summarize that conventional rotor position assignment algorithms depend on the machine's estimated operating point and constitute an estimation as well. This property is especially important when the overload capability problem is investigated.

4.2.3 Overload capability problem

One of the major contributions of this work is the investigation of the so-called *overload capability problem*, often denoted by the terminologies *convergence problem* or *stability problem*. The overload capability problem describes the phenomenon that most injection-based encoderless control algorithms lose their capability of tracking the rotor position in deep magnetic saturation resulting in a diverging position error. The stable region is therefore often called the convergence region of the method. The stability issue prevents the injection-based methods from being widely used in applications, where the machine is operated in deep magnetic saturation, e.g., in the automotive sector. In addition, it is difficult to predict the operating points where the algorithms lose their capability to track the rotor position. Hence, unpredictable and unacceptable behavior is the result. Therefore, the phenomenon is investigated in the following subsections with three primary aims. The first aim is to predict the phenomenon to avoid unstable operating points or to set a current limitation alternatively. This prediction should be applicable to different injection-based encoderless algorithms. The second aim is to determine which existing algorithm achieves the highest current amplitude and torque to cover the maximum possible operating area. The third aim is to understand the cause of the problem and to define improving properties of algorithms that help overcoming the issue. It should be mentioned that these issues were investigated detailed in the pre-publication [33][LWK], which arose during this Ph.D. project.

The overload capability problem has been present since the first use of injection-based encoderless algorithms. However, for a long time, the main research focus was on improving acoustic noise and accuracy, so the overload capability problem with its “invisible” property was less considered. Nevertheless, in recent years it has more intensively been researched.

One of the first who dealt with the overload phenomenon were the authors of [61, 62]. It has been recognized that the rotor position can become nonobservable at specific operating points, which is also confirmed by other works, e.g., [63, p. 85]. The investigations were without the consideration of higher space harmonics. The outcome of

[61, 62] and [63, p. 85] is the criterion given in inequation (4.40).

$$\dot{L}_A = \sqrt{\dot{L}_\Delta^2 + \dot{L}_{dq}^2} \stackrel{!}{>} 0 \quad (4.40)$$

The fulfillment of the criterion guarantees that the saliency of the machine is present, which is a necessary condition for encoderless control. In practice, \dot{L}_A must exceed a certain inductance limit greater than zero, depending on the quality of the current measurement and the voltage injection. However, the criterion is automatically fulfilled for the present work due to the minimum provided q-axis current as described in Subsection 4.2.2. Based on the criterion (4.40) the authors of [61, 62] were the first who optimized a synchronous machine with respect to observability. This was achieved by optimizing the machine parameters so that nonobservable operating points are not at or close to the MTPA trajectory. However, such an optimization leads to disadvantages of other parameters such as efficiency and power-to-weight ratio. Even though these drawbacks are known, the optimization of the electrical machine is still one of the focuses of today's research [64, 65, 66, 67]. The aforementioned works have three points in common. These are with regards to observability according to inequation (4.40). The impact of higher space harmonics is neglected, and only one specific injection-based algorithm is investigated. Hence, it cannot be expected that the results are valid for all the other injection-based algorithms.

Indeed, the criterion (4.40) is not sufficient to guarantee stable injection-based encoderless control. It has been experienced that the control can become unstable even if the criterion is fulfilled. Hence, the authors of [68] further investigated the phenomenon with the consideration of higher harmonic anisotropies. The outcome of this work is a set of three criteria, which should guarantee stable injection-based encoderless control. The first criterion of [68] is equal to inequation (4.40). The second criterion introduced by W. Hammel [68] is as follows

$$\frac{\partial \theta_A}{\partial \theta_{el}} \stackrel{!}{>} 0 \quad (4.41)$$

and guarantees that the anisotropy angle is reversible over the rotor angle (strictly monotone) when the criterion is fulfilled. It ensures a clear assignment of the anisotropy angle to the rotor angle by the rotor position assignment algorithm. This assignment is not always possible, especially for machines with strong harmonic anisotropies. It is a necessary condition when direct demodulation (arctangent function) of the anisotropy angle is intended. However, it can be overcome even if not fulfilled (for a specific

point but not for an area) [56] for certain anisotropy ratios using sophisticated observer structures. For machines with distributed windings, it can be assumed that the criterion (4.41) is always fulfilled due to the low harmonic content in the anisotropy. This is assumed henceforth.

Over the years, it has been experienced that these two criteria are still not sufficient to guarantee stability in every condition. Therefore, the authors of [68] have proposed a third criterion in addition to (4.40) and (4.41). While (4.40) and (4.41) concern the observability of the machine, the new criterion is intended to guarantee the stability of the rotor position assignment algorithm in the event of estimation errors. The theory of [68] takes the impact of estimation errors $\Delta\theta_{el} = \hat{\theta}_{el} - \theta_{el}$ on the rotor position assignment algorithm into account. Estimation errors frequently appear due to inaccuracies in the model, parameter variations, or measurement inaccuracies. These estimation errors lead to a wrongly rotated voltage vector due to the dq transformation and subsequently to a misaligned current vector (time-transient process). The misaligned current vector changes the saturation of the machine, which leads to a change in the magnetic anisotropy according to (2.37). This process can result in convergence or divergence of the estimation error. The third criterion of [68] given by inequation (4.42) assesses this process, but only regarding the rotor position assignment algorithm and not for the entire injection-based structure. Furthermore, in [68] it was assumed that the convergence region (where the third criterion (4.42) is fulfilled) is a property of the machine and hence equal for all injection-based algorithms. The statement that stability (convergence) is a property of the machine will be verified and assessed later.

$$\frac{\partial\theta_A}{\partial\theta_{el}} - \frac{\partial\theta_A}{\partial\Delta\theta_{el}} \stackrel{!}{>} 0 \quad (4.42)$$

Besides the three criteria, W. Hammel [68] recommended modeling the inductance or admittance matrix in dependency on the estimation error $\Delta\theta_{el}$. This additional dependency was taken advantage of by [69, 70, 71, 72, 73] to derive a new category of injection-based models. The new models show an enlarged convergence region compared to conventional models that neglect the estimation error dependency. Most of these new models take advantage of the saturation effects due to estimation errors by linearizing the machine's model with respect to the estimation error. However, this linearization might become inaccurate for larger estimation errors, leading to the algorithm's instability at some extended limit. The model parameters used by these algorithms rely on the estimated rotor position. Hence, the model parameters are estimations and no actual parameters during encoderless operation. The use of estimated

parameters is an important property of an algorithm and becomes important when interpreting the results.

The currently most promising algorithms concerning the convergence issue are briefly discussed in the following. The model of [70] takes advantage of the injection direction to maximize the extractable rotor position information and hence the convergence region. However, the model relies on estimated parameters.

The approach presented in the patent [74] by Landsmann, Paulus, and Kuehl pursues a novel approach. The renewals concern the rotor position assignment algorithm. The novel rotor position assignment algorithm is independent of the estimated operating point of the machine, as employed by conventional rotor position assignment algorithms (Subsection 4.2.2). The difference is that the rotor position assignment algorithm is based on the measurable and therefore known currents of the two-phase stator fixed reference frame. Hence, the correction term of the rotor position assignment algorithm is not an estimation. This novel approach is derived later and forms part of the investigated injection-based methods.

W. Hammel and H. Wolf also invented an approach that decouples the model parameters from unknown input variables in their patent [75]. The method is different from [74] but is expected to achieve similar results as [74]. However, the approach of [75] is not investigated within this work.

Despite the abovementioned research effort, the overload capability problem still raises questions that must be answered. The questions are briefly listed below to summarize the current research state of the convergence problem.

- The present state of research does not clarify whether the convergence region is a machine property, as stated by [68, 64, 65, 66, 67]. There are justified assumptions that the injection-based model also has an influence.
- The previous point implicates a comparison of different injection-based algorithms, which is not available in the current research literature.
- No existing convergence criterion can predict the convergence region for several injection-based algorithms, only for one specific. Thus, the aim is to derive a new criterion appropriate for various injection-based models.
- The authors of [74] expect parameters stored according to an unknown reference frame (when operating encoderless) to be the cause of the stability problem.

However, there is no proof of this expectation. The aim is to verify this expectation and to reveal the cause of the overload problem.

These open questions are aimed to be answered on the following pages, which are organized into sections for a better overview. The first section briefly discusses alternative injection-based models besides the Arbitrary Injection 4.2.1. These models and the Arbitrary Injection are subsequently analyzed regarding the overload capability problem. In the next section, the principle tendency of the convergence region is investigated empirically. From these empirical results, first conclusions are drawn, which are employed to derive a novel convergence criterion. The new criterion is used to predict the convergence region, which is verified by measurements. Finally, conclusions about the overload capability problem are drawn.

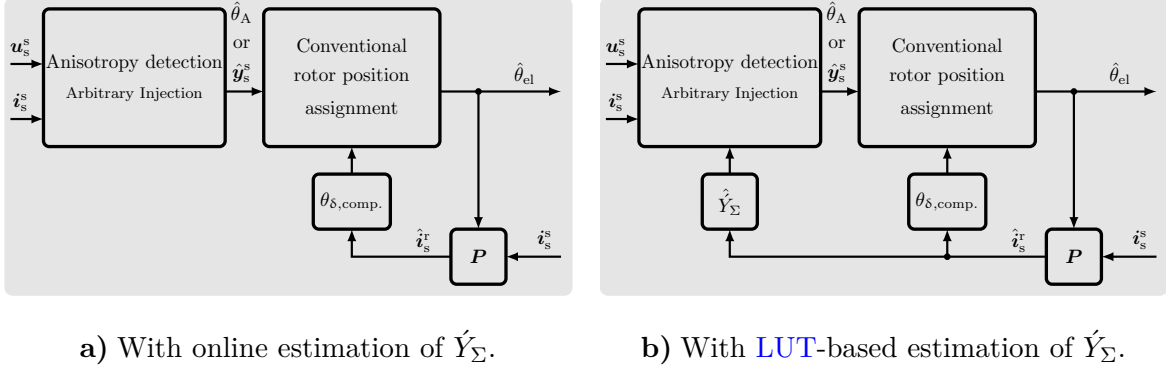
4.2.3.1 Alternative injection-based models

The injection-based models investigated on the overload capability problem are briefly described in the following so that the operation principles become clear and the results can be interpreted. The research literature provides many different injection-based algorithms. However, only a selection is investigated within this work. The selected algorithms are very different among themselves. This helps to find the cause of the overload capability issue. A simplified structural diagram of each algorithm is provided, which aids in understanding the root cause of the overload capability problem.

A. Conventional Arbitrary Injection

The conventional Arbitrary Injection model of Subsection 4.2.1 is one of the investigated models. The terminology “conventional” is used to indicate that it is combined with a conventional rotor position assignment algorithm as described in Subsection 4.2.2. This differentiation in the terminology is important since Arbitrary Injection (with minor modifications) can also be combined with the new approach for the rotor position assignment algorithm proposed by [74]. The mathematical equations of conventional Arbitrary Injection were derived and defined in Subsection 4.2.1. Therefore, only the simplified structural diagrams are given below. It should be mentioned that conventional Arbitrary Injection will be investigated for two different implementations for estimating the mean admittance \hat{Y}_{Σ} . Once for the case that \hat{Y}_{Σ} is stored in a LUT and once for the online estimation approach proposed in [57, 53]. The two diagrams are shown below. It can be noticed that both diagrams are slightly different

in terms of control feedback. In the case of the online estimation, feedback is due to the compensation for the misalignment angle that requires the Park transformation.



a) With online estimation of \hat{Y}_Σ .

b) With LUT-based estimation of \hat{Y}_Σ .

Figure 4.7: Simplified structural diagrams of conventional Arbitrary Injection.

This structural diagram also applies if the position assignment algorithm is implemented as shown in Fig. 4.6 along with the MTPA trajectory and without employing the Park transformation. The feedback is still present since $\theta_{\delta,comp.}$ relies on the estimated and not on the actual operating point of the machine. Thus, the structural diagram of Fig. 4.6 can be assumed as shown in Fig. 4.7 a), if an online estimation of the mean admittance is conducted. The online estimation of the mean admittance is assumed to be ideal. Hence, no feedback path towards the anisotropy detection is present.

Fig. 4.7 b) shows that a second feedback loop appears when a LUT is used for the estimation of the mean admittance. This is required for the LUT (storage of \hat{Y}_Σ), which relies on the currents of the rotor fixed reference frame.

B. Alternating Injection

The so-called Alternating Injection method was first proposed by [49]. The method injects a “high-frequency” sinusoidal voltage into the estimated anisotropy d-axis and measures the “high-frequency” current response in the anisotropy q-axis. From that response, an anisotropy angle error-related signal can be extracted which is fed into a PLL. The PLL adjusts the estimated anisotropy angle in a way that the anisotropy q-axis current response disappears. The derivation of the Alternating Injection relies on a mathematical description in so-called anisotropy coordinates. Quantities in anisotropy coordinates are derived by transforming the two-phase stator fixed related quantities. The transformation is carried out using the Park and inverse Park transformation but with the anisotropy angle θ_A as the argument of the trigonometric functions. Hence,

the inductance matrix in anisotropy coordinates can be determined by transforming (2.35) as shown in (4.43). It should be mentioned that the following derivation is based on [3, p. 1155].

$$\hat{\mathbf{L}}_s^a := \mathbf{P}(\theta_A) \hat{\mathbf{L}}_s^s \mathbf{P}^{-1}(\theta_A) = \begin{bmatrix} \dot{L}_\Sigma + \dot{L}_A & 0 \\ 0 & \dot{L}_\Sigma - \dot{L}_A \end{bmatrix} \quad (4.43)$$

A sinusoidal voltage is injected in the estimated anisotropy d-axis. It results in the following high-frequency flux-linkage vector in estimated anisotropy coordinates (denoted with a circumflex $\hat{\boldsymbol{\psi}}_{\text{car}}^a$):

$$\hat{\boldsymbol{\psi}}_{\text{car}}^a := \int \underbrace{u_{\text{car}} \cos(\omega_{\text{car}} t)}_{=:\hat{\mathbf{u}}_{\text{car}}^a} \begin{bmatrix} 1 \\ 0 \end{bmatrix} dt = \begin{bmatrix} \frac{u_{\text{car}} \sin(\omega_{\text{car}} t)}{\omega_{\text{car}}} \\ 0 \end{bmatrix} \quad (4.44)$$

where u_{car} and ω_{car} are the injection amplitude and frequency. However, due to potential estimation errors in the estimated anisotropy angle, the actual high-frequency flux-linkage vector is dependent on the anisotropy estimation error $\Delta\theta_A = \hat{\theta}_A - \theta_A$. Equation (4.45) follows for the actual high-frequency flux linkage

$$\boldsymbol{\psi}_{\text{car}}^a := \mathbf{P}^{-1}(\Delta\theta_A) \hat{\boldsymbol{\psi}}_{\text{car}}^a = \begin{bmatrix} \frac{u_{\text{car}} \sin(\omega_{\text{car}} t) \cos(\Delta\theta_A)}{\omega_{\text{car}}} \\ \frac{u_{\text{car}} \sin(\omega_{\text{car}} t) \sin(\Delta\theta_A)}{\omega_{\text{car}}} \end{bmatrix} \quad (4.45)$$

which can be used to determine the high-frequency current response from the machine (4.46). It is assumed that the injected frequency is chosen sufficiently high so that the inductive voltage drop of the machine dominates.

$$\mathbf{i}_{\text{car}}^a := \left(\hat{\mathbf{L}}_s^a\right)^{-1} \boldsymbol{\psi}_{\text{car}}^a = \begin{bmatrix} \frac{u_{\text{car}} \sin(\omega_{\text{car}} t) \cos(\Delta\theta_A)}{\omega_{\text{car}} (\dot{L}_\Sigma + \dot{L}_A)} \\ \frac{u_{\text{car}} \sin(\omega_{\text{car}} t) \sin(\Delta\theta_A)}{\omega_{\text{car}} (\dot{L}_\Sigma - \dot{L}_A)} \end{bmatrix} \quad (4.46)$$

However, this current response is unknown due to the unknown actual anisotropy angle. The known, estimated, current response can be determined by transforming

(4.46) into estimated anisotropy coordinates:

$$\hat{\mathbf{i}}_{\text{car}}^{\text{a}} := \mathbf{P}(\Delta\theta_{\text{A}}) \mathbf{i}_{\text{car}}^{\text{a}} = \begin{bmatrix} \frac{u_{\text{car}} \sin(\omega_{\text{car}} t) (\dot{L}_{\Sigma} - \dot{L}_{\text{A}} \cos(\Delta\theta_{\text{A}}))}{\omega_{\text{car}} (\dot{L}_{\text{A}}^2 - \dot{L}_{\Sigma}^2)} \\ -\frac{\dot{L}_{\text{A}} u_{\text{car}} \sin(\omega_{\text{car}} t) \sin(\Delta\theta_{\text{A}})}{\omega_{\text{car}} (\dot{L}_{\text{A}}^2 - \dot{L}_{\Sigma}^2)} \end{bmatrix} =: \begin{bmatrix} \hat{i}_{\text{A},\text{d}} \\ \hat{i}_{\text{A},\text{q}} \end{bmatrix} \quad (4.47)$$

Only the q-axis component of (4.47) is of interest since it is demodulated and used as input for the PLL. When the anisotropy angle is estimated correctly, the signal demodulated from the q-axis component is zero. The demodulated signal, which is finally used to feed the PLL is determined by multiplying the q-axis component by $\sin(\omega_{\text{car}} t)$ before applying a low-pass filter (LPF) with cut-off frequency $\omega_{\text{g,LP}}$. Hence, the error signal for the PLL is given by:

$$i_{\text{A},\text{q,PLL}} := \text{LPF}(\hat{i}_{\text{A},\text{q}} \sin(\omega_{\text{car}} t)) = \text{LPF}\left(\frac{\dot{L}_{\text{A}} u_{\text{car}} \sin(\Delta\theta_{\text{A}}) (\cos(2\omega_{\text{car}} t) - 1)}{2\omega_{\text{car}} (\dot{L}_{\text{A}}^2 - \dot{L}_{\Sigma}^2)}\right) \quad (4.48)$$

$$\omega_{\text{g,LP}} \ll 2\omega_{\text{car}} \approx \frac{-\dot{L}_{\text{A}} u_{\text{car}} \sin(\Delta\theta_{\text{A}})}{2\omega_{\text{car}} (\dot{L}_{\text{A}}^2 - \dot{L}_{\Sigma}^2)} \sin(\Delta\theta_{\text{A}}) \approx \Delta\theta_{\text{A}} \approx \frac{-\dot{L}_{\text{A}} u_{\text{car}} \Delta\theta_{\text{A}}}{2\omega_{\text{car}} (\dot{L}_{\text{A}}^2 - \dot{L}_{\Sigma}^2)} \quad (4.49)$$

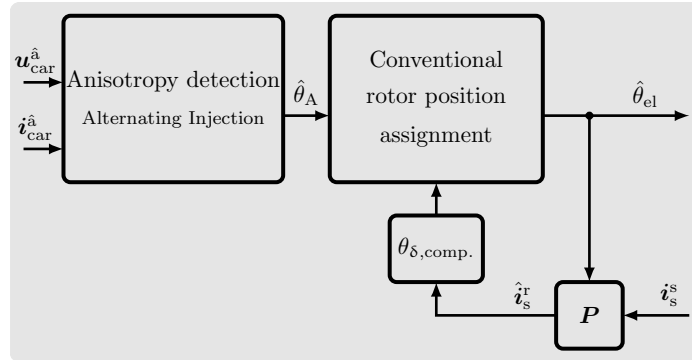


Figure 4.8: Simplified structural diagram of the Alternating Injection.

The Alternating Injection has the benefit that it is independent on parameters for the determination of the anisotropy angle. Therefore, the estimated anisotropy angle always converges towards the actual one. The drawback of this method is that the error signal for the PLL, $i_{\text{A},\text{q,PLL}}$, is operating-point-dependent, which complicates the tuning of the PLL. The injection frequency and amplitude were set to $\omega_{\text{car}} = 2\pi 300$ Hz

and $u_{\text{car}} = 30 \text{ V}$ for the investigations performed later. These are typical values used in the research literature. Fig. 4.8 shows the simplified structure of the Alternating Injection. Note that feedback only appears towards the rotor position assignment algorithm.

C. HF-EEMF model

In Subsection 4.1 was mentioned that the EEMF method could be used at a standstill after some modifications. The authors of [36, 37] were the first to recognize this and proposed the EEMF method with an additional current injection. Equation (4.5) shows that either axes, d or q, can be used for the injection. In the following, a sinusoidal current injection in the estimated d-axis is used, given by equation (4.50).

$$\hat{\mathbf{i}}_{\text{car,EEMF}}^{\text{r}} := i_{\text{car,EEMF}} \sin(\omega_{\text{car,EEMF}} t) \begin{bmatrix} 1 \\ 0 \end{bmatrix} \quad (4.50)$$

Due to potential estimation errors, the actual current injection vector of the machine is:

$$\mathbf{i}_{\text{car,EEMF}}^{\text{r}} := \mathbf{P}^{-1}(\Delta\theta_{\text{el}}) \hat{\mathbf{i}}_{\text{car,EEMF}}^{\text{r}} \quad (4.51)$$

$$= \begin{bmatrix} i_{\text{car,EEMF}} \sin(\omega_{\text{car,EEMF}} t) \cos(\Delta\theta_{\text{el}}) \\ i_{\text{car,EEMF}} \sin(\omega_{\text{car,EEMF}} t) \sin(\Delta\theta_{\text{el}}) \end{bmatrix} =: \begin{bmatrix} i_{\text{cd}} \\ i_{\text{cq}} \end{bmatrix} \quad (4.52)$$

These two injection components i_{cd} and i_{cq} are inserted in equation (4.5), resulting in the EEMF vector $\mathbf{e}_{\text{s,EEMF}}^{\text{s}}$ below (4.54). For equations (4.53) and (4.54) it is assumed that the angular velocity is small $\omega_{\text{el}} \approx 0$ and that the estimation error $\frac{d\Delta\theta_{\text{el}}}{dt} \approx 0$ is varying slowly.

$$\mathbf{e}_{\text{s,EEMF}}^{\text{s}} = \begin{pmatrix} \frac{di_{\text{cd}}}{dt} (\dot{L}_{\text{dd}} - \dot{L}_{\text{qq}}) + 2\dot{L}_{\text{dq}} \frac{di_{\text{cq}}}{dt} \\ \dots \end{pmatrix} \begin{bmatrix} \cos(\theta_{\text{el}}) \\ \sin(\theta_{\text{el}}) \end{bmatrix} \quad (4.53)$$

$$= \begin{bmatrix} \cos(\theta_{\text{el}}) \\ \sin(\theta_{\text{el}}) \end{bmatrix} i_{\text{car,EEMF}} \omega_{\text{car,EEMF}} \cos(\omega_{\text{car,EEMF}} t) \dots \\ \dots \underbrace{\left((\dot{L}_{\text{dd}} - \dot{L}_{\text{qq}}) \cos(\Delta\theta_{\text{el}}) + 2\dot{L}_{\text{dq}} \sin(\Delta\theta_{\text{el}}) \right)}_{=:\dot{L}_{\text{HF,EEMF}}} \quad (4.54)$$

It can be seen that the inductance $\dot{L}_{\text{HF,EEMF}}$ is unequal to zero for small estimation errors in the case of a salient machine, which allows rotor position estimation. Equa-

tion (4.54) is multiplied by $\cos(\omega_{\text{car,EEMF}} t)$, similar to the procedure for Alternating Injection, which results in a constant component in the amplitude of $\mathbf{e}_{\text{dem,EEMF}}^s$.

$$\mathbf{e}_{\text{dem,EEMF}}^s := \begin{bmatrix} \cos(\theta_{\text{el}}) \\ \sin(\theta_{\text{el}}) \end{bmatrix} i_{\text{car,EEMF}} \omega_{\text{car,EEMF}} \frac{1}{2} (1 + \cos(2\omega_{\text{car,EEMF}} t)) \dot{L}_{\text{HF,EEMF}} \quad (4.55)$$

Equation (4.55) is then low-pass filtered (cut-off frequency $\omega_{\text{g,LP}}$) analogous to the Alternating Injection, which yields to:

$$\text{LPF}(\mathbf{e}_{\text{dem,EEMF}}^s) \stackrel{\omega_{\text{el}} \ll \omega_{\text{g,LP}} \ll 2\omega_{\text{car,EEMF}}}{\approx} \frac{1}{2} i_{\text{car,EEMF}} \omega_{\text{car,EEMF}} \dot{L}_{\text{HF,EEMF}} \begin{bmatrix} \cos(\theta_{\text{el}}) \\ \sin(\theta_{\text{el}}) \end{bmatrix} \quad (4.56)$$

It should be mentioned that equation (4.54) is estimated using a disturbance observer similar to (4.13). Therefore, it relies on various estimated inductance parameters. The rotor position can be extracted directly from (4.56) using the arctangent function analogous to (4.16). Thus, this method does not rely on a rotor position assignment algorithm and has an entirely different structural diagram compared to the other injection-based methods. This specific attribute might be helpful to further isolate the cause of the overload capability issue. For the tests later, the reference injection amplitude was set to $i_{\text{car,EEMF}}^* = 0.7 \text{ A}$ ¹² and the frequency to $\omega_{\text{car,EEMF}} = 2\pi 300 \text{ Hz}$, which are typical values in the related literature. The simplified structural diagram with the multiple feedback is shown in Fig. 4.9.

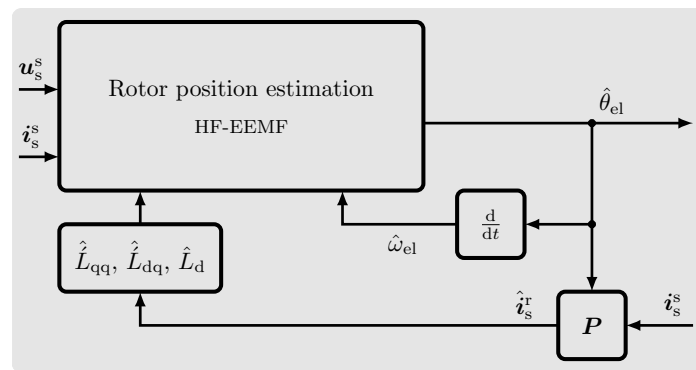


Figure 4.9: Simplified structural diagram of the *HF-EEMF* method.

¹²The actual current amplitude is lower due to the damping of the current control loop but still large enough to be measured by the current measurement unit.

D. UARP

The following pages are dedicated to the approach proposed in the patent [74] and referred to as the method of the unique assignment of the admittance or inductivity to the rotor location (UARP). This approach aims to modify the rotor position assignment algorithm so that all employed parameters are independent of estimated or assumed input variables. The authors of [74] developed the rotor position assignment algorithm based on the currents in the two-phase stator fixed reference frame, as they are directly measurable and therefore known. The model is derived in the following based on [74].

The conventional approach in encoderless-related literature is to model and measure the admittance vector \mathbf{y}_s^s dependent on the currents of the rotor fixed reference frame \mathbf{i}_s^r . This leads to a dependency as shown in (4.57).

$$\mathbf{y}_s^s(\mathbf{i}_s^r, \theta_{el}) \quad (4.57)$$

The admittance vector \mathbf{y}_s^s constitutes the vector that contains at least two linear combinations of the admittance matrix $\hat{\mathbf{Y}}_s^s$ (4.29). The admittance matrix is given as follows in its general form:

$$\hat{\mathbf{Y}}_s^s := \begin{bmatrix} \hat{Y}_{\alpha\alpha} & \hat{Y}_{\alpha\beta} \\ \hat{Y}_{\beta\alpha} & \hat{Y}_{\beta\beta} \end{bmatrix} \quad (4.58)$$

The entries of the admittance matrix $\hat{Y}_{\alpha\alpha}$, $\hat{Y}_{\beta\beta}$, $\hat{Y}_{\alpha\beta}$, and $\hat{Y}_{\beta\alpha}$ are measured by a suitable anisotropy-based method. In the present work, the Arbitrary Injection from Subsection 4.2.1 in combination with an online estimation of \hat{Y}_Σ [57, 53] is used for the estimation of the admittance components¹³. The admittance components determined by the Arbitrary Injection contain all influences caused by the nonsinusoidal arrangement of the machine. Thus, the effects caused by higher space harmonics are automatically considered by this approach.

Within the present work, the following two linear combinations are used to construct the admittance vector:

$$\mathbf{y}_s^s := \frac{1}{2} \begin{bmatrix} \hat{Y}_{\alpha\alpha} - \hat{Y}_{\beta\beta} \\ \hat{Y}_{\alpha\beta} + \hat{Y}_{\beta\alpha} \end{bmatrix} =: \begin{bmatrix} y_A \\ y_B \end{bmatrix} \quad (4.59)$$

¹³The Arbitrary Injection is only used up to the point where the admittance components can be determined from the voltages and currents, up to equation (4.29). The anisotropy angle is not used.

The first innovation of [74] is to describe this admittance vector in dependence on the two-phase stator fixed current vector (4.60) and not in dependency on the rotor fixed current vector as shown in (4.57). This yields the following dependency:

$$\mathbf{y}_s^s(\mathbf{i}_s^s, \theta_{el}) \quad (4.60)$$

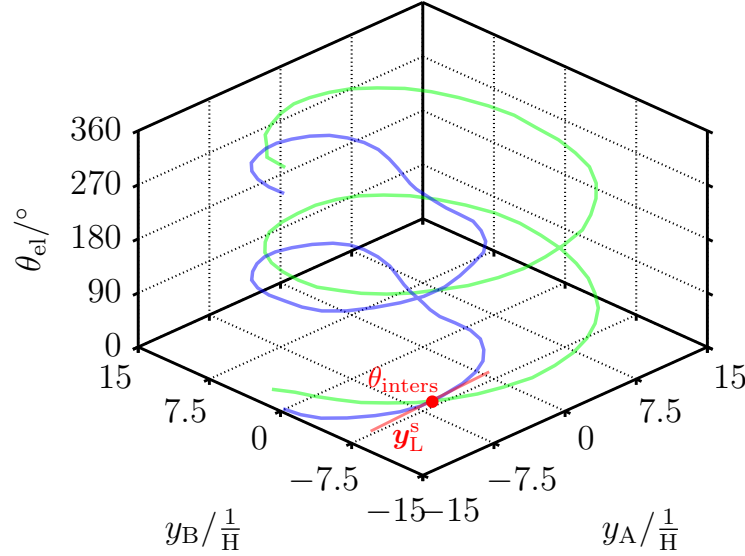


Figure 4.10: Measured trajectories at $\|\mathbf{i}_s^s\| = 8$ A. The current angle in the alpha-beta reference was fixed at $\theta_{i,\alpha\beta} = 90^\circ$. The trajectory for a constant current vector in the rotor fixed reference frame is depicted in green and the trajectory for a stator fixed current vector in blue. The linearization approach is depicted in red.

The dependency (4.60) of the admittance vector can be measured by applying constant currents in the stator fixed reference frame while changing the rotor position with a load machine. The admittance vector is measured throughout the process by an anisotropy-based method, e.g., with Arbitrary Injection. An exemplary trajectory of such a measurement is shown in Fig. 4.10 (blue) for a current amplitude of $\|\mathbf{i}_s^s\| = 8$ A and a current angle of $\theta_{i,\alpha\beta} = 90^\circ$ in the alpha-beta reference frame. The green trajectory of Fig. 4.10 shows the conventional measurement in dependency on a constant current vector in dq coordinates with $\|\mathbf{i}_s^s\| = 8$ A and with respect to the MTPA trajectory.

The second innovation of [74] is to obtain a reversed version of equation (4.60) so that the rotor angle can be found as a function of the admittance vector and the current vector of the two-phase stator fixed reference frame.

$$\theta_{el}(\mathbf{i}_s^s, \mathbf{y}_s^s) \quad (4.61)$$

However, it would result in large LUTs with a high demand of memory space if each of those reversed trajectories (Fig. 4.10) are stored in their total extend over all possible rotor angles. To reduce the memory requirements, the authors of [74] introduced a simplification by employing that the current operating points are at or close to that of the MTPA trajectory. They proposed to linearize the admittance vector $\mathbf{y}_s^s(i_s^s, \theta_{el})$ in the position of intersection $\theta_{inters.}$ ¹⁴ between the trajectory measured at a constant current vector in dq coordinates with that measured at a constant current vector in alpha-beta coordinates. This is exemplarily illustrated by the straight red line of Fig. 4.10 and is described by the linearized admittance vector \mathbf{y}_L^s .

Mathematically, the linearized admittance vector can be described by a first-order Taylor polynomial:

$$\mathbf{y}_L^s(i_s^s, \theta_{el}) := \mathbf{y}_s^s \Big|_{\theta_{inters.}} + (\theta_{el} - \theta_{inters.}) \frac{\partial \mathbf{y}_s^s}{\partial \theta_{el}} \Big|_{\theta_{inters.}} \quad (4.62)$$

$$=: \mathbf{y}_{L,0}^s + (\theta_{el} - \theta_{inters.}) \mathbf{m} =: \mathbf{y}_{L,0}^s + \theta_L \mathbf{m} \quad (4.63)$$

$$=: \begin{bmatrix} m_A \theta_L + y_{A,0} \\ m_B \theta_L + y_{B,0} \end{bmatrix} \quad (4.64)$$

It is important to notice that the slope vector $\mathbf{m}(i_s^s)$ and the admittance vector in the point of intersection $\mathbf{y}_{L,0}^s(i_s^s)$ are functions of the current vector in two-phase stator fixed coordinates. Basically, the approach is to store the data of the linearized admittance vector and then calculate them with the measured admittance components from the anisotropy detection.

However, the admittance vector estimated by the Arbitrary Injection $\hat{\mathbf{y}}_s^s$ might slightly deviate to the pre-measured linearized version \mathbf{y}_L^s , whose data is stored on the control unit. The deviation could be caused by measurement inaccuracies, for example. This is exemplarily shown in Fig. 4.11.

¹⁴The positions of intersection conform to an operation along the MTPA trajectory [74]. E.g., $\theta_{inters.} = 30^\circ$ in Fig. 4.10. This is meaningful for $\theta_{i,\alpha\beta} = 90^\circ$ since it results in a current angle (dq) of 60° , which is in the expected range for an RSM.

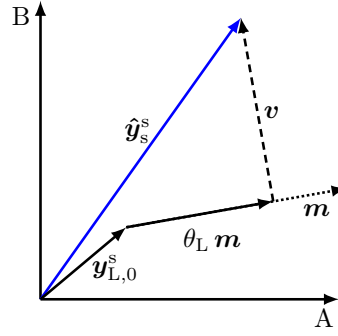


Figure 4.11: Illustration of the vector projection.

However, θ_L and the estimated rotor angle θ_{el} , respectively, could be chosen to minimize the distance between $\mathbf{y}_L^s = \mathbf{y}_{L,0}^s + \theta_L \mathbf{m}$ and $\hat{\mathbf{y}}_s^s$. The minimized distance is described by the vector \mathbf{v} , which is orthogonal to the slope vector $\mathbf{v} \perp \mathbf{m}$. Hence, the scalar product of both vectors is zero $\langle \mathbf{v}, \mathbf{m} \rangle = 0$, which yields to:

$$\mathbf{v}^\top \mathbf{m} = (\hat{\mathbf{y}}_s^s - \mathbf{y}_{L,0}^s - \theta_L \mathbf{m})^\top \mathbf{m} = (\hat{\mathbf{y}}_s^s - \mathbf{y}_{L,0}^s)^\top \mathbf{m} - \|\mathbf{m}\|^2 (\hat{\theta}_{el} - \theta_{inters.}) = 0 \quad (4.65)$$

This scalar equation can be used to determine the estimated rotor position $\hat{\theta}_{el}$ so that the distance between $\hat{\mathbf{y}}_s^s$ and \mathbf{y}_L^s is minimized. The result is:

$$\hat{\theta}_{el} = \frac{(\hat{\mathbf{y}}_s^s - \mathbf{y}_{L,0}^s)^\top \cdot \mathbf{m}}{\|\mathbf{m}\|^2} + \theta_{inters.} \quad (4.66)$$

Equation (4.66) can be illustrated in its expanded form by the entries of the linearized admittance vector \mathbf{y}_L^s . The results are shown in (4.67) and (4.68) with the substitution $\hat{\theta}_{el,UARP} := \hat{\theta}_{el}$.

$$\hat{\theta}_{el,UARP} = \hat{y}_A \frac{m_A}{m_A^2 + m_B^2} + \hat{y}_B \frac{m_B}{m_A^2 + m_B^2} - \frac{y_{A,0} m_A + y_{B,0} m_B}{m_A^2 + m_B^2} + \theta_{inters.} \quad (4.67)$$

$$= \hat{y}_A L_{k,A}(\mathbf{i}_s^s) + \hat{y}_B L_{k,B}(\mathbf{i}_s^s) + \theta_0(\mathbf{i}_s^s) \quad (4.68)$$

Here, \hat{y}_A and \hat{y}_B are the estimated admittance vector components from the Arbitrary Injection (anisotropy detection). The coefficients $L_{k,A}$, $L_{k,B}$, and θ_0 are pre-determined and stored in LUTs for different current angles $\theta_{i,\alpha\beta}$, and current amplitudes $\|\mathbf{i}_s^s\|$. Once these coefficients have been determined offline, the actual online computational effort is low. The computation of (4.68) requires only a few additions and multiplications as well as the searching algorithms for the three LUTs.

The measured coefficients are shown in Fig. 4.12. The measurement procedure used to determine these coefficients does not form part of this dissertation. However, the procedure can be derived from the illustrations in Fig. 4.10.

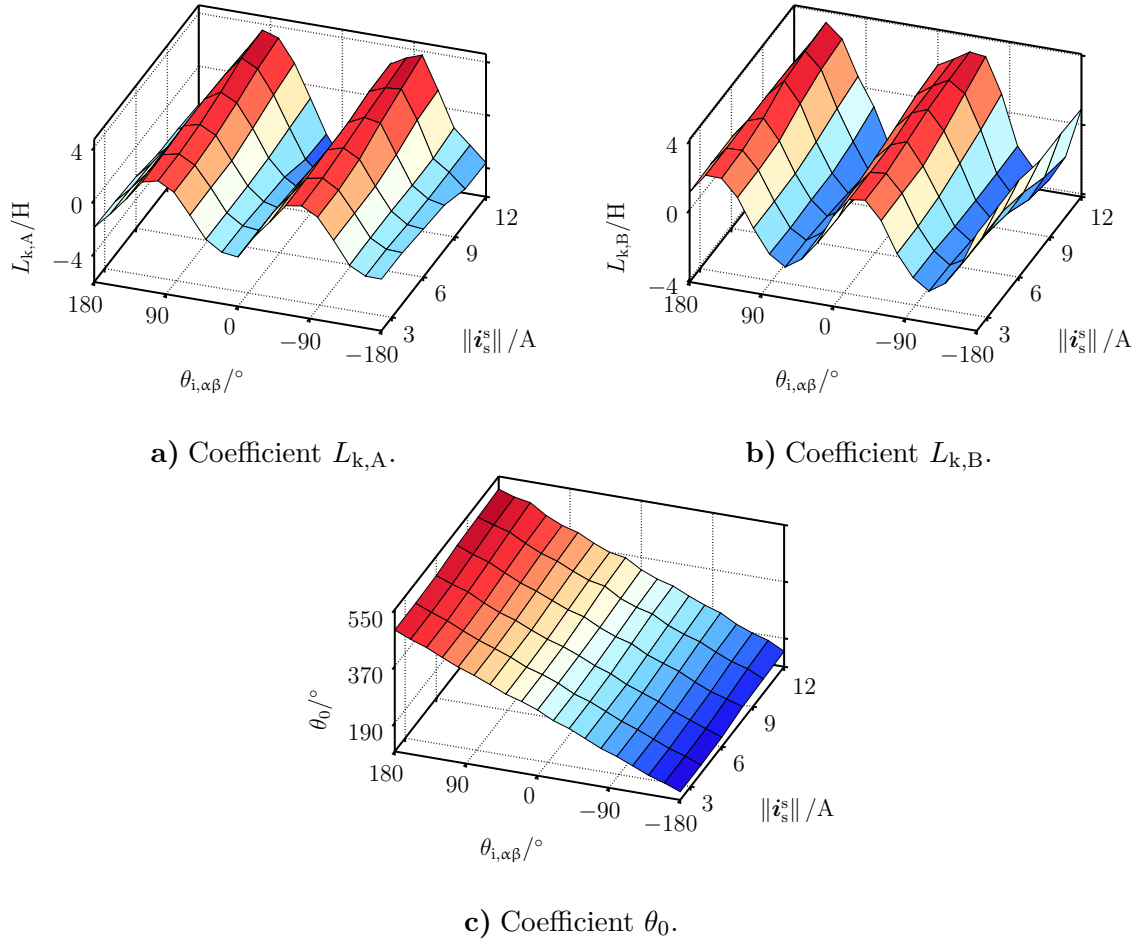


Figure 4.12: Measured coefficients of the *UARP* approach.

It should be mentioned that the inventors of [74] also proposed the transformation of these coefficients with a measurable angle. The current angle in alpha-beta coordinates is an appropriate choice for this transformation. The transformation reduces the alternating character of the coefficients and, hence, the required number of points stored. However, this simplification was not used within the present work due to sufficient memory capacities of the microcontroller.

The *UARP* method also opens new possibilities for the control of machines with strong harmonic anisotropies. This advantage is not required for the *RSM* under investigation but worth to be mentioned. That is because the trajectories of the ad-

mittance vector as described in (4.60) are more often monotone¹⁵ [74] compared to that of the conventional description (4.57). Furthermore, the admittance vector can be constructed by more than two linear combinations, which further improves the monotony of the admittance vector over the rotor position.

Fig. 4.13 shows the simplified structural diagram of the UARP method. It can be seen that no feedback of estimated quantities is present, and all blocks are dependent on measurable currents only.

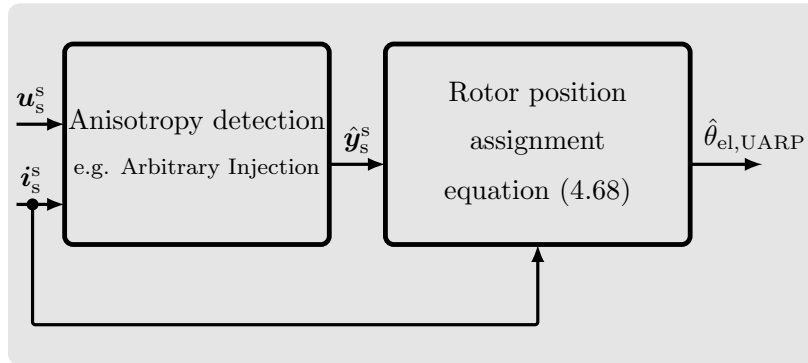


Figure 4.13: Simplified structural diagram of the UARP method according to [74].

4.2.3.2 Empirical investigation of the injection-based model's overload capability

The following pages are aimed to investigate the overload capability of the five¹⁶ injection-based encoderless control algorithms described before. The empirical investigation should show whether the injection-based model influences the overload capability or whether it is only a property of the machine as assumed in [68, 64, 65, 66, 67] and hence, widely independent of the algorithm. Furthermore, this test is performed to learn more about the overload capability problem and the influence of the injection-based models. The new perceptions are subsequently employed to derive a novel convergence criterion.

The investigation is carried out as follows. The test machine is operated in closed-loop current control mode using the estimated rotor position and rotor speed. The reference torque is increased ramp-shaped, and the reference currents are set with respect to the MTPA trajectory. The increase of the reference torque is performed in

¹⁵Monotony is strictly required to uniquely assign measured admittance components to a rotor position.

¹⁶Conventional Arbitrary Injection is investigated once with the online estimation of \hat{Y}_Σ and once with \hat{Y}_Σ being stored in a LUT.

small steps to operate close to the **MTPA**. Furthermore, the reference torque steps are timed to apply each reference over the full range of 360° to cover all possible operating points. During the procedure, the load machine keeps the speed constant at $n_m = 50$ rpm. The current magnitude $\|\mathbf{i}_s^s\|$ and estimation error $\Delta\theta_{el}$ are recorded throughout the test and the control is switched off if $|\Delta\theta_{el}| > 25^\circ$ applies. The limit $|\Delta\theta_{el}| > 25^\circ$ is chosen based on experience. Experience has shown that no stable equilibrium can be reestablished if the estimation error exceeds a limit in this order of magnitude. The quality measure for this test is the current amplitude achieved right before the limit $|\Delta\theta_{el}| > 25^\circ$ was exceeded.

The previously described test procedure is conducted for two different settings of the **PLL** for all five injection-based algorithms. Once with a comparably slow setting¹⁷ for the **PLL** with $g_p = 125\text{ s}^{-1}$ and $g_i = 3900\text{ s}^{-2}$ and once with a faster setting which is $g_p = 286\text{ s}^{-1}$, $g_i = 20000\text{ s}^{-2}$. Where, g_p is the proportional and g_i the integral gain of the **PLL**. The test with different **PLL** settings is performed to determine the influence of the **PLL** on the overload capability.

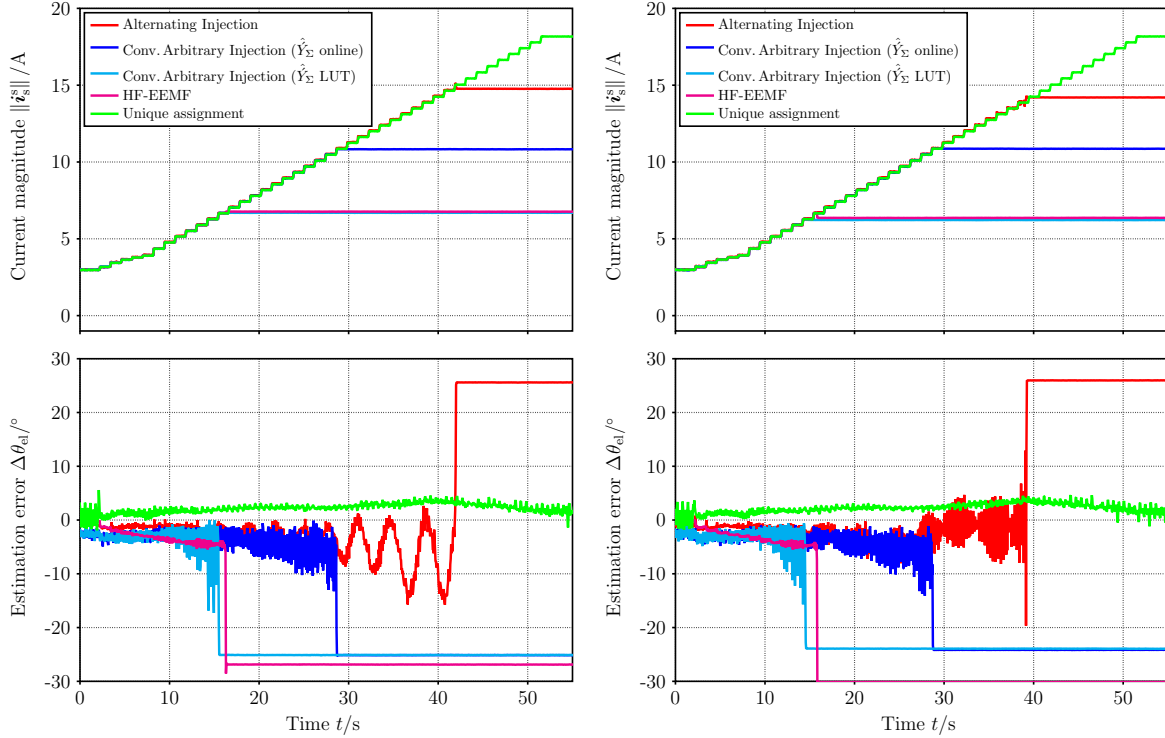
The results of the empirical investigations are shown in Fig. 4.14. They show significant differences in the achievable current magnitude. This could be reproduced by multiple repetitions of the test procedure. However, the repeated measurements are not explicitly presented here.

The **HF-EEMF** model achieved a maximum current amplitude of $\|\mathbf{i}_s^s\|_{\max} = 6.8\text{ A}$ respectively $\|\mathbf{i}_s^s\|_{\max} = 6.7\text{ A}$ for the two **PLL** settings. Thus it can be concluded that the **PLL** has a neglectable influence on the overload capability of this method. The achievable current amplitude is one of the lowest compared to the other methods. The low achievable current amplitude is traceable to using a variety of estimated parameters, leading to an inaccurate model when estimation errors appear. The test shows that the overload capability problem also appears without using a rotor position assignment algorithm.

The conventional Arbitrary Injection model with **LUT**-based estimation of the mean admittance achieved $\|\mathbf{i}_s^s\|_{\max} = 6.7\text{ A}$ and $\|\mathbf{i}_s^s\|_{\max} = 6.3\text{ A}$ for the two **PLL** settings, which is in the range of the **HF-EEMF** model. The **PLL** settings show a minor impact on the achievable current amplitude again. The achievable current amplitude is far below the conventional Arbitrary Injection model with an online estimation of the mean admittance. This is due to the use of the **LUT**, which creates a second feedback loop

¹⁷A precise setting of the **PLL** for Alternating Injection is difficult due to the operating-point-dependent gain of the method (4.49). However, the operating-point-dependent gain is statically compensated with its value at zero reference torque.

as depicted in Fig. 4.7 b). Thus, the model becomes even more inaccurate if estimation errors appear.



a) PLL settings $g_p = 125 \text{ s}^{-1}$, $g_i = 3900 \text{ s}^{-2}$. b) PLL settings $g_p = 286 \text{ s}^{-1}$, $g_i = 20000 \text{ s}^{-2}$.

Figure 4.14: Overload test with reference torque ramp at current control mode and $n_m = 50 \text{ rpm}$ [33][LWK].

The conventional Arbitrary Injection model with online estimation of the mean admittance achieved $\|i_s^s\|_{\max} = 10.8 \text{ A}$ for both PLL settings. Hence, the PLL has no affect on the overload capability during this test. The achievable current amplitude is below that of Alternating Injection. This behavior is not reflected in their structural diagrams (Fig. 4.7 a) and Fig. 4.8) since both have only one feedback loop towards the rotor position assignment algorithm, however, it can be explained as follows. The compensation term of the rotor position assignment algorithm $\theta_{\delta, \text{comp}}$ is pre-measured with respect to the MTPA trajectory and is thus related to a specific trajectory of the mean admittance in the case of the Arbitrary Injection with online estimation. However, when estimation errors appear, the actual mean admittance changes due to magnetic saturation. It is subsequently not the same mean admittance with which the compensation term $\theta_{\delta, \text{comp}}$ was measured. The feedback path in Fig. 4.7 a) is thus affected more by estimation errors compared to the feedback path in Fig. 4.8. Alterna-

tively, the difference could be caused by the different injection directions as they have an effect as well [70].

The Alternating Injection model achieved $\|\mathbf{i}_s^s\|_{\max} = 14.7$ A and $\|\mathbf{i}_s^s\|_{\max} = 14.3$ A for the two PLL settings. The overload capability of this method is, again, hardly influenced by the PLL settings. However, the graphs over time of the estimation errors are different. The operating-point-dependent gain (4.49) is constantly changing during the test. Hence, the transfer function of the position estimation is also changing, resulting in the different graphs of the estimation errors.

The UARP model achieved the maximum possible current amplitude of the test bench for both PLL settings with a good estimation quality. The UARP does not require feedback, leading to the conclusion that feedback paths cause the overload capability problem.

The most important findings derived from the prior conducted empirical investigation are briefly summarized below [33][LWK].

- The PLL settings have shown to be less relevant for the overload capability problem as long as the settings are adapted meaningfully to the system.
- Minor differences in the implementation can cause significant differences in the achievable current amplitude, as the two implementation versions of the conventional Arbitrary Injection have shown.
- The convergence region is less determined by the machine design, which was attempted to be optimized in [68, 64, 65, 66, 67]. The convergence region seems to be mainly a property of the injection-based encoderless algorithm and to be affected by feedback paths, respectively estimated parameters. If the convergence region would be a machine property only, the results should be the same for all algorithms.
- Criteria as they are currently available, e.g., [68], do consider the specificities of a single algorithm. Hence, they cannot predict the convergence region of different injection-based encoderless algorithms as the achievable current amplitudes were different.

4.2.3.3 Novel convergence criterion

The end of the last section stated that existing convergence criteria cannot predict the convergence region for several algorithms reliably. This is aimed to be achieved in the

following by deriving a new criterion based on the previous findings.

The novel convergence criterion aims to analyze the impact of parameter deviations on the estimation error. The parameter deviations are assumed to be due to a difference between the estimated/assumed operating point and the actual operating point of the machine. Since the criterion shall predict the convergence region of different injection-based algorithms reliably, the derivation cannot be based on a specific injection-based algorithm but must be derived in a more general form.

The meaning of the previously mentioned terminology “*operating point*” should be defined more precisely for the understanding of the following derivation. The terminology “*operating point*” is used to denote all variables which influence the model parameters of an injection-based encoderless algorithm. Standard injection-based algorithms use inductance parameters in their model, which can generally be described dependent on three variables. These three variables are the current amplitude $\|\mathbf{i}_s^x\|$ with $x \in \{t, s, r\}$, the current angle $\theta_{i,x}$ with $x \in \{dq, \alpha\beta, abc\}$, and the rotor position θ_{el} . In the following, it is assumed that the inductance parameters are modeled according to a rotating reference frame, which is rotating in coherence with the actual rotor angle¹⁸. In that case, the rotor position dependency of the model parameters only applies to machines with strong harmonic anisotropies. Since the RSM has low harmonic content in the magnetic anisotropy, the inductances are dependent on the current amplitude and angle only; the rotor position is not required. Hence, the terminology “*operating point*” is used representative for a certain current angle and current amplitude (respectively a current vector) in the following.

The components of a current vector are the current amplitude and current angle. However, only the current angle can cause a deviation between the estimated and the actual operating point. The current vector amplitude can be measured and is known, even when operating encoderless. Hence, the operating point deviation, which causes the deviation in the model parameters, can solely be caused by a deviation of the current angle. The current angle deviation can be defined analogous to the rotor position estimation error $\Delta\theta_{el} = \hat{\theta}_{el} - \theta_{el}$ as follows

$$\Delta\theta_i := \hat{\theta}_i - \theta_i \quad (4.69)$$

with $\theta_i \in \mathbb{R}$ being the actual current angle and $\hat{\theta}_i \in \mathbb{R}$ the estimated current angle. By the assumption made above, the current angle deviation can be related to any rotating

¹⁸Commonly, the dq reference frame is used. However, it could also be any other rotating reference frame that relies on knowledge of the rotor position.

reference frame, which depends on the estimated rotor position. It is important to mention that the rotor position estimation error $\Delta\theta_{el}$ and the current angle deviation $\Delta\theta_i$ behave contrary due to the current controllers as illustrated in Fig. 4.15. That means that the current angle deviation becomes negative for a positive rotor position estimation error.

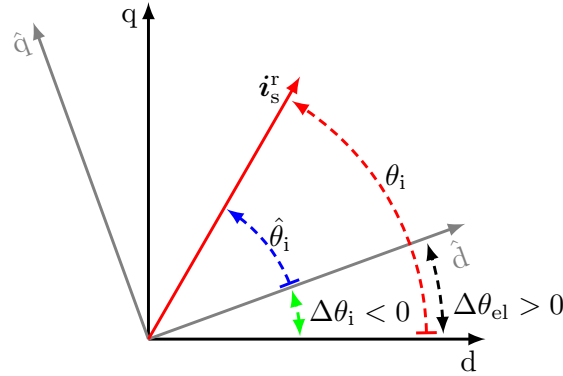


Figure 4.15: Relationship between rotor position estimation error and current angle deviation; exemplarily for a dq rotating reference frame.

A relationship between the rotor position estimation error and the current angle deviation must be derived to verify the effect of parameter deviations on the estimation error. A first-order Maclaurin series can approximate this dependency if the development is conducted around the origin of the current angle deviation. It is required that $\Delta\theta_i$ is small and that $\Delta\theta_{el}$ is in the subspace of the one-time continuously differentiable functions $\Delta\theta_{el} \in \mathcal{C}^1(\mathbb{R}; \mathbb{R})$ of $\Delta\theta_i$. If this applies, the first-order approximation is given as follows:

$$\Delta\theta_{el}(\Delta\theta_i) \approx \Delta\theta_{el} \Big|_{\Delta\theta_i=0^\circ} + \Delta\theta_i \cdot \frac{\partial \Delta\theta_{el}}{\partial \Delta\theta_i} \Big|_{\Delta\theta_i=0^\circ} \quad (4.70)$$

Equation (4.70) can be simplified if it is assumed that no position estimation error is present when operating without current angle deviation. The encoderless model is assumed to be ideal in this case, and it follows that:

$$\Delta\theta_{el} \Big|_{\Delta\theta_i=0^\circ} \approx 0^\circ \quad (4.71)$$

This leads to the simplified relationship between rotor position estimation error and

current angle deviation:

$$\Delta\theta_{\text{el}}(\Delta\theta_i) \approx \Delta\theta_i \cdot \left. \frac{\partial\Delta\theta_{\text{el}}}{\partial\Delta\theta_i} \right|_{\Delta\theta_i=0^\circ} \quad (4.72)$$

Basically, the current angle deviation is a consequence of an estimation error that leads to a rotation of the voltage vector and, subsequently, to a rotated current vector due to the Park transformation. The current vector is not rotated immediately but follows the voltage vector in a time-transient. However, in the following, it is assumed that the current vector immediately rotates when an estimation error appears. This assumption is required to bypass the derivation with the current control transfer function, which would significantly complicate the derivation. A small initial estimation error $\Delta\theta_{\text{el,init}} \in \mathbb{R}$ causing the current angle deviation is assumed in the following, which can be caused by a measurement inaccuracy, for instance. The relationship between the initial estimation error and the current angle deviation can be approximated by (4.73) under the previously mentioned assumption and the coherences of estimation error and current angle deviation as shown in Fig. 4.15.

$$\Delta\theta_{\text{el,init}} \approx -\Delta\theta_i \quad (4.73)$$

Substituting (4.73) in (4.72) yields equation (4.74).

$$\Delta\theta_{\text{el}}(\Delta\theta_{\text{el,init}}) \approx \Delta\theta_{\text{el,init}} \cdot \left. \frac{\partial\Delta\theta_{\text{el}}}{\partial\Delta\theta_{\text{el,init}}} \right|_{\Delta\theta_{\text{el,init}}=0^\circ} \quad (4.74)$$

If the terminology convergence/stability of an encoderless control algorithm is defined as follows

Definition I (convergence/stability): An encoderless control algorithm is in stable equilibrium if an initial estimation error leads subsequently to a lower estimation error. In the case of an initial estimation error leading to a greater estimation error, the algorithm is in an unstable equilibrium¹⁹.

the following (4.75) must be fulfilled in equation (4.74) to fulfill convergence/stability in the sense of ***Definition I***.

¹⁹The definition is inspired and applied analogous to Ljapunow's definition of a stable equilibrium.

$$\Gamma := \frac{\partial \Delta \theta_{\text{el}}}{\partial \Delta \theta_{\text{el,init}}} \Big|_{\Delta \theta_{\text{el,init}}=0^\circ} \stackrel{!}{<} 1 \quad \forall \mathbf{i}_s^r, \theta_{\text{el}} \quad (4.75)$$

However, equation (4.75) is difficult to verify in practice due to the use of $\Delta \theta_{\text{el,init}}$. Therefore, the relationship of equation (4.73) is substituted in equation (4.75) which yields the final convergence criterion:

$$\Gamma = - \frac{\partial \Delta \theta_{\text{el}}}{\partial \Delta \theta_i} \Big|_{\Delta \theta_i=0^\circ} \stackrel{!}{<} 1 \quad \forall \mathbf{i}_s^r, \theta_{\text{el}} \quad (4.76)$$

The criterion assesses the effect of a current angle deviation on the model parameters and hence, on the position estimation error. The convergence criterion requires low effort to be verified in practice. In open-loop operation, a current angle deviation must be introduced, and the resulting estimation error must be recorded to achieve the data for computing the partial derivative.

4.2.3.4 Verification of the convergence criterion

The verification of the novel convergence criterion is carried out in the following. The convergence region is predicted using the measured convergence criterion and compared with the points of divergence/instability that appear when driving into deep magnetic saturation while operating encoderless.

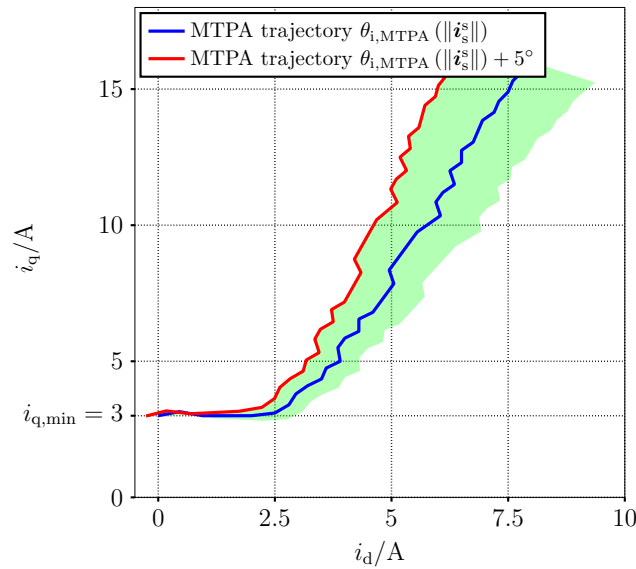


Figure 4.16: Current trajectories for the measurement of the convergence criterion.

The verification is performed as follows and consists of two separate measurement procedures as described in the following. The first measurement procedure is for recording the convergence criterion. The machine is operated in open-loop current control mode using the encoder signal while it is rotated by the load machine at a constant speed of $n_m = 50$ rpm. During the procedure, the machine is operated one-time along the intended **MTPA** trajectory with the current angles $\theta_{i,\text{MTPA}} (\|\mathbf{i}_s^s\|)$, which is shown in blue in Fig. 4.16. A second time, the machine is operated along a rotated **MTPA** trajectory shown in red in Fig. 4.16. The red trajectory appears if a constant angle of 5° is added to the measured encoder signal before using it in the **FOC**. This constitutes a current angle deviation of $\Delta\theta_i = -5^\circ$ if the model parameters and the conventional rotor position assignment algorithm data are stored along the intended blue **MTPA** trajectory. The current amplitude is increased, and the estimation error is recorded throughout the measurements. Thereby, an region around the **MTPA** trajectory is assessed regarding convergence that is indicated by the green area of Fig. 4.16. The convergence factor Γ is approximated from these two measurements using the discretized form of the convergence criterion, which is described by the following equations:

$$\Gamma \approx - \frac{\Delta\theta_{\text{el}}(\Delta\theta_i = 0^\circ) - \Delta\theta_{\text{el}}(\Delta\theta_i = -5^\circ)}{\underbrace{(\theta_{i,\text{MTPA}} - \hat{\theta}_i)}_{\hat{\theta}_i} - \underbrace{(\theta_{i,\text{MTPA}} - \theta_i)}_{\theta_i} - \underbrace{(\theta_{i,\text{MTPA}} - \hat{\theta}_i)}_{\hat{\theta}_i} - \underbrace{(\theta_{i,\text{MTPA}} - (\theta_{i,\text{MTPA}} + 5^\circ))}_{\theta_i}} \Big|_{\Delta\theta_i \approx 0^\circ} \quad (4.77)$$

$$\approx - \frac{\Delta\theta_{\text{el}}(\Delta\theta_i = 0^\circ) - \Delta\theta_{\text{el}}(\Delta\theta_i = -5^\circ)}{5^\circ} \Big|_{\Delta\theta_i \approx 0^\circ} \stackrel{!}{<} 1 \quad \forall \theta_{\text{el}}, \|\mathbf{i}_s^s\| \Big|_{\text{MTPA}} \quad (4.78)$$

The second measurement procedure is conducted to verify whether the prediction of (4.78) is correct. The machine is operated in closed-loop current control mode using the estimated signals. The machine's rotor is mechanically locked in different positions; at least every sixty degrees in electrical units. Then, the reference torque (respectively current) are increased in a ramp up to the point when $|\Delta\theta_{\text{el}}| > 25^\circ$ applies. The maximum achieved current amplitude $\|\mathbf{i}_s^s\|_{\text{max},i}$ is recorded right before $|\Delta\theta_{\text{el}}| > 25^\circ$ and the control is switched off. This second measurement process (i) is repeated four times for each rotor position to guarantee reproducibility. From the four measurements, the mean of the maximum current amplitude is calculated:

$$\overline{\|\mathbf{i}_s^s\|_{\text{max}}} := \frac{\sum_{i=1}^4 \|\mathbf{i}_s^s\|_{\text{max},i}}{4} \quad (4.79)$$

and the sample standard deviation is determined by:

$$s_{\|\mathbf{i}_s^s\|_{\max}} := \sqrt{\frac{\sum_{i=1}^4 \left(\|\mathbf{i}_s^s\|_{\max,i} - \overline{\|\mathbf{i}_s^s\|_{\max}} \right)^2}{4 - 1}} \quad (4.80)$$

Measurement procedure one and measurement procedure two are visualized together in one diagram. The predictions with the convergence criterion (4.78) are depicted as contour plots. The results of the locked rotor test, (4.79) and (4.80), are indicated by green dots, green squares, and green error bars. A green dot indicates that the control became unstable on average at this point with the green error bars depicting the sample standard deviation. A green square indicates that the maximum possible current amplitude of the test bench was reached. The results of the verification are shown in Fig. 4.17.

Fig. 4.17 a) confirms the results from Section 4.2.3.2 of the **UARP** model. The convergence criterion predicts stable equilibrium at all investigated operating points, which is confirmed by the locked rotor test. The convergence factor of the **UARP** has a maximum value of 0.12 and is far from the threshold for an unstable equilibrium. The **UARP** is the only algorithm that remained stable at all investigated operating points.

The results for the two implementation versions of conventional Arbitrary Injection are shown in Fig. 4.17 b) and c). The results are again in accordance with the results from Section 4.2.3.2. The prediction of the convergence criterion is accurate in both cases. The results of the locked rotor test show that there is a very small sample standard deviation in all rotor positions. Hence, the points of instability are highly reproducible. Fig. 4.17 b) shows periodic oscillations, one oscillation with twice the electrical frequency, which is caused by a minor estimation error of \check{Y}_Σ (online estimation method) and, secondly, a sixth periodicity which is caused by the winding arrangement of the machine (minus second harmonic anisotropy [3, p. 1165]). If \check{Y}_Σ is stored in a **LUT** (Fig. 4.17 c)), a strong second harmonic appears, which is caused by a deviation of the mean admittance \check{Y}_Σ and explains the large difference in the overload capability between both implementation versions of conventional Arbitrary Injection.

The results for Alternating Injection shown in Fig. 4.17 d) confirm the results from Section 4.2.3.2. The points of instability are highly reproducible, and the convergence criterion predicts the behavior well. The sixth harmonic is also present (so-called minus second harmonic anisotropy [3, p. 1165]).

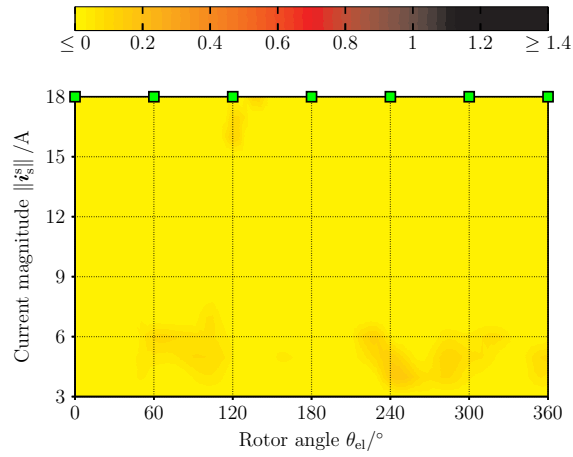
The result for the **HF-EEMF** model are shown in Fig. 4.17 e). The tendencies of the convergence factor and the locked rotor test are in accordance with each other.

However, the prediction is not as precise as for the other algorithms. The first reason for this is that the convergence criterion assumes the operating point of a model to be current angle and current-amplitude-dependent only. However, a look at the simplified structure of the HF-EEMF model in Fig. 4.9 shows that the operating point of the model is also dependent on the estimated speed $\hat{\omega}_{el}$. Another explanation is that the convergence factor was measured at $n_m = 50$ rpm but the locked rotor test was conducted at a standstill. Due to differences in the speed between the measurement procedures, and the speed dependency of the model, deviations in the results are comprehensible.

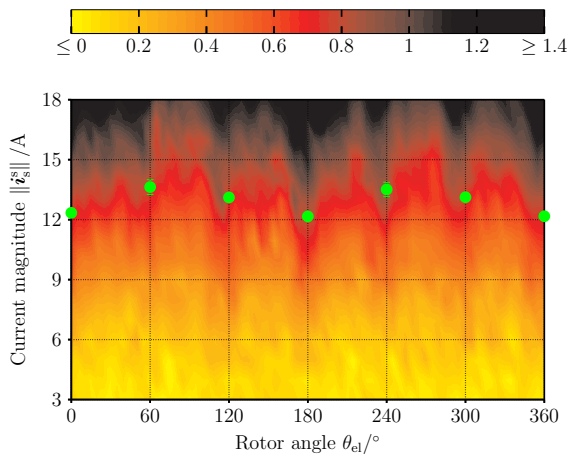
In general, it could be observed that the achieved current amplitudes from the first test conducted in Section 4.2.3.2 are slightly higher than the achieved current amplitudes from Fig. 4.17. This is because the algorithms do not immediately become unstable if the operating point of the machine is located in a small unstable region (when rotating), which is the case if the machine is at a standstill. This effect might be affected by the PLL settings, the electrical speed, and the size of unstable regions over 360° . However, this effect is not investigated further since the worst-case operating condition (standstill) is of interest.

From the results of this verification, it can be concluded that the proposed convergence criterion is appropriate to predict the convergence region for most of the investigated injection-based encoderless models.

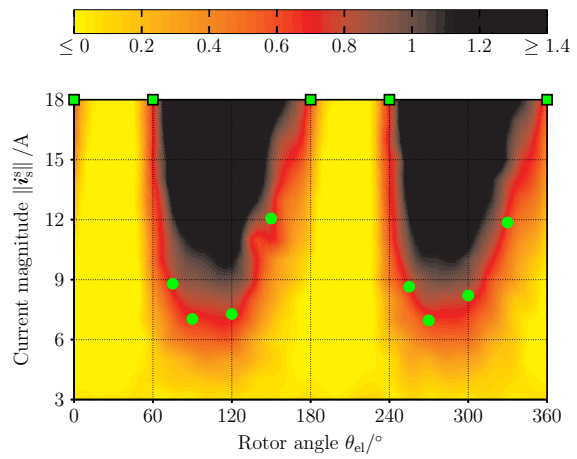
It should be mentioned that the criterion can also be employed to predict the convergence region early in the design stage of the machine based on FEM results as demonstrated in the pre-publication [33][LWK].



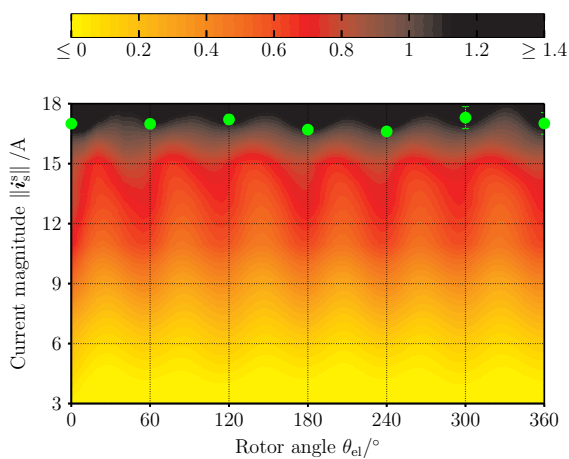
a) UARP model.



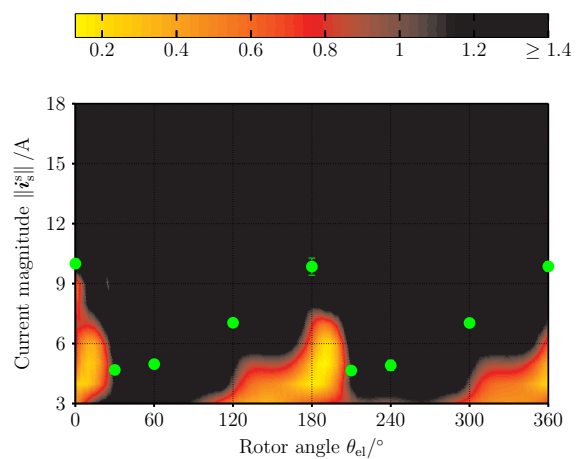
b) Arbitrary Injection online est. of \hat{Y}_Σ .







c) Arbitrary Injection LUT est. of \hat{Y}_Σ .



d) Alternating Injection.



e) HF-EEMF model.

Figure 4.17: Measurement results for the verification of the convergence criterion.  convergence factor.  test bench maximum reached.  mean unstable points.  sample standard deviation of $\|\mathbf{i}_s^s\|_{\max}$.

4.2.3.5 Conclusion about the overload capability issue

The previous section has confirmed the convergence criterion and all the assumptions made during its derivation to be valid. This circumstance allows drawing some important conclusions regarding the overload capability problem and the convergence criterion. These conclusions are listed below and concern the open questions from Section 4.2.3.

- The overload capability problem is less a property of the machine as assumed in [68, 64, 65, 66, 67], but to a great extent a property of the algorithm. Since one of the algorithms did not suffer stability issues, an optimization of the machine with respect to the encoderless overload capability issue is unnecessary.
- The proposed convergence criterion is valid as long as the model relies on a current-dependent operating point. This is the case for almost all injection-based algorithms, enabling the prediction for many different algorithms.
- The expectations of [74] were confirmed. Model parameters stored according to an unknown reference frame (when operating encoderless) are the cause of the stability problem.
- Predicting the convergence region for several algorithms in the early design stage of the machine is possible with the new criterion employing FEM simulation, as shown in [33][LWK].

The overload capability problem can be resolved if all the model parameters are determinable from directly measurable quantities during encoderless operation without relying on estimated quantities. Otherwise, an algorithm will have a stability issue at some operating point.

Hence, it is expected that also the algorithm of W. Hammel and H. Wolf [75] is capable of working at any operating point since it is based on always known model parameters.

It should be mentioned that it is expected that EMF-based encoderless algorithms suffer the same stability issue as they usually also employ estimated parameters. Thus, it cannot be assumed that conventional EMF-based models are unlimited in the current magnitude. However, an investigation of the overload capability problem regarding EMF-based models was not carried out in this dissertation.

Since the sensor-fault-tolerant approach of this dissertation should be reliable in as

many operating points as possible, the decision was taken for the **UARP** approach as an injection-based method for the further investigations.

4.3 Hybrid encoderless control scheme

The previous two sections introduced and analyzed encoderless models for the medium to high-speed²⁰ region and for estimation around standstill. The **EEMF** model of Section 4.1 is used for medium to high speeds, whereas the **UARP** of Section 4.2.3.1 is used for low-speeds. Actually, the **UARP** can be used over the entire speed range with additional voltage injection. However, an additional voltage injection should be avoided when operating close to the **FW** and **MTPV** trajectories for optimal utilization of the **DC-link** voltage. Hence, the **EEMF** model is used when operating close to the **FW** or **MTPV** trajectory.

To cover the entire speed range of the machine, both encoderless methods must be combined. This combination is often referred to as a hybrid encoderless scheme. The transition from one encoderless method to the other is usually done speed-dependent. Some works, e.g., [76, 77], use either an **EMF**-based model or the injection-based model dependent on speed and torque. These approaches only use one of the models at the same time; the switch over between the methods is often discontinuous and realized by a hysteresis switching function. However, an instant switch-over is critical and often causes significant estimation errors, which can lead to stability issues in the drive system [78].

A more appropriate solution is an information fusion where both encoderless models are used, at least partially, simultaneously. Thus, the switch-over between both models can be realized more smoothly based on weighting coefficients, which strongly reduces the possibility of unstable behavior during the switch-over process. In encoderless control, information fusion algorithms have been applied more intensively for about ten years. The information fusion of [4, p. 127] is based on a Kalman filter (**KF**) but most publications regarding information fusion for encoderless control, e.g., [79, 80, 81, 82], employ a modified **PLL** structure.

The information fusion used in the present work is based on a modified **PLL** structure similar to [79] and is named information-fusion-phase-locked-loop (**IFPLL**) in the

²⁰The limit between high and low speed cannot be defined in general; it depends on the specific **SNR** of the angle estimation. However, the low-speed region is often referred to as the region where an injection-based algorithm is applied, whereas in the medium and high-speed region, the **EMF**-based method is used.

following. The central element of the IFPLL is the error signal shown below that feeds a typical PLL structure (Fig. 4.19).

$$e_{\text{pll}} := k_{\text{ani}} \hat{\theta}_{\text{el,UARP}} + (1 - k_{\text{ani}}) \hat{\theta}_{\text{el,EEMF}} - \theta_{\text{el,PLL}} \quad (4.81)$$

The error signal is defined using the weighting coefficient $k_{\text{ani}}(\cdot)$ with $\{k_{\text{ani}} \in \mathbb{R} | 0 \leq k_{\text{ani}} \leq 1\}$. The larger k_{ani} is, the more the estimation from the injection-based model is used since $\hat{\theta}_{\text{el,UARP}}$ is the position estimation from the UARP (equation (4.68)). The smaller k_{ani} the more the EEMF model and its estimation $\hat{\theta}_{\text{el,EEMF}}$ from equation (4.16) is used. The coefficient $k_{\text{ani}}(\cdot)$ can be a function of several variables or it can be determined dependent on the actual SNR [52]. In the following k_{ani} is considered estimated-speed-dependent only as shown in Fig. 4.18. The coefficient k_{inj} with $\{k_{\text{inj}} \in \mathbb{R} | 0 \leq k_{\text{inj}} \leq 1\}$ is used to scale the amplitude of the voltage injection ($k_{\text{inj}} \cdot |u_{\text{inj}}|$). Thus, with $k_{\text{inj}} = 0$, the voltage injection is switched off.

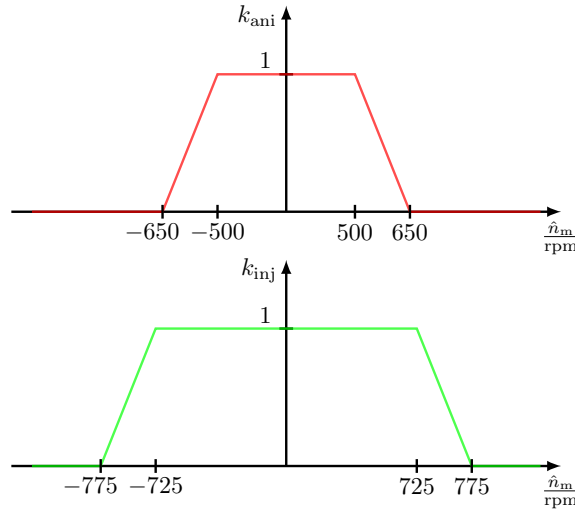


Figure 4.18: Coefficients for the hybrid encoderless control scheme.

This parametrization allows a smooth transition between the low-speed and the medium to high-speed encoderless method. A smooth transition of the voltage injection is also recommended since estimation errors have been experienced with the EEMF model when the voltage injection was switched on or off instantly. The structural diagram of the IFPLL is shown in Fig. 4.19.

Another benefit of the UARP method comes apparent when comparing the structure of the IFPLL in Fig. 4.19 with the PLL structure of Fig. 4.6. The new IFPLL has no gain in the feedback loop of $\theta_{\text{el,PLL}}$ so that no positive feedback can appear, which can

cause limitations for machines with high anisotropy ratios [47, p.106]. This further improves the stability behavior of the entire encoderless control structure.

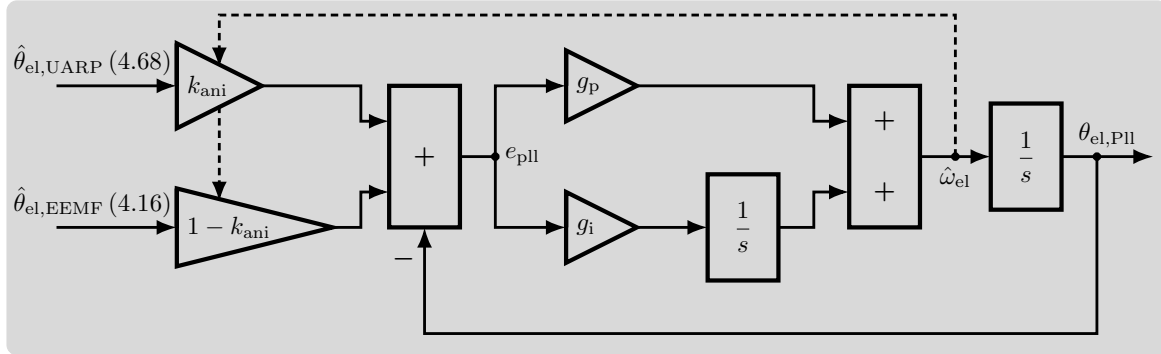


Figure 4.19: Schematic of the information-fusion-phase-locked-loop (IFPLL).

4.4 Empirical verification of the hybrid encoderless control scheme

The last section of this chapter presents the measurement results of the hybrid encoderless control scheme and demonstrates the achievable accuracy. Information about the achievable accuracy is important for implementing sensor fault detection later. The encoderless control is carried out in Task 2 of Fig. 3.3. It must be executed in a separate task due to its computational requirements.

The measurements are conducted in closed-loop speed control mode using the estimated signals. The encoderless speed control is more prone to failure than the current control due to the estimated speed as additional feedback. Thus, the speed control results are a reliable indicator of the performance of an encoderless control scheme (besides the position control).

Due to the filtering of the estimated signals, especially the speed, the settings of the PI speed controller must be adapted for encoderless control. The settings of the speed controller are chosen based on [4, p.137] to guarantee a stable speed control loop. Based on this, the proportional gain is set to $g_{p,n} = 0.1 \text{ Nm s rad}^{-1}$ and the integral gain to $g_{i,n} = 0.5 \text{ Nm rad}^{-1}$. The speed-control bandwidth is comparable to most existing works. However, highly dynamic processes are not the focus of this work, but high reliability is primarily aimed. Indeed, the system would have allowed for higher dynamics, but the limits are not exhausted within this work to guarantee a safety margin to the stability limit. The gains of the IFPLL are set to $g_p = 200 \text{ s}^{-1}$ and $g_i = 10000 \text{ s}^{-2}$.

Fig. 4.20 shows the measurement result of the reference tracking during speed control over a wide speed range. The reference speed is ramped-up and down with the machine operating as a motor and generator. M_{KTR} is the measured torque, and \hat{M}_{el} is the estimated torque based on (2.41) calculated with the estimated currents and flux linkages. The position estimation error is shown with respect to the filtered estimated angle $\theta_{\text{el,PLL}}$ of the IFPLL. The reference speed is tracked accurately, and the position estimation error is low over the entire experiment with a maximum of about $\pm 7^\circ$. The noisy position estimation at a standstill is due to zero reference current of the d-axis and related to the storage of the UARP coefficients. The coefficients of the UARP method shown in Fig. 4.12 were determined for positive reference torques of the MTPA. However, those coefficients must be mirrored²¹ when a negative torque is requested depending on the d-axis current sign. Otherwise, the coefficients must be stored for negative reference torques additionally. Since the sign of the d-axis current is constantly changing during zero reference torque, the mirroring of the coefficients is continually triggered, which causes the noisy shape. However, no expended effort was made to improve this behavior. Furthermore, the effect disappears if a small torque is requested and the sign of the d-axis current remains constant.

Fig. 4.21 shows the measurement result of the disturbance rejection during speed control at a standstill with load steps of ± 4 Nm. The disturbances are compensated for in about 500 ms, and the estimation error is mainly within $\pm 5^\circ$, which is acceptable. It can be seen that no enlarged estimation error appears during the high accelerations. The noise in the angle estimation is due to the same effect discussed above (mirroring of the coefficients) and disappears when torque is requested. Based on k_{ani} , it can be seen that only the UARP method is active during the experiment.

Fig. 4.22 shows the measurement result of the disturbance rejection during speed control at a speed of $n_{\text{m}} = 1000$ rpm with load steps of ± 4 Nm. The disturbances are compensated for in about 500 ms again, and the estimation error attests to a high estimation quality. Only the EEMF method is active during the experiment, as it can be seen on the coefficient k_{ani} . The estimation error is primarily within $\pm 2^\circ$ except during the transients.

The measurement results of the hybrid encoderless control scheme have shown that it can be used as a reliable backup algorithm in the event of an encoder fault. The estimation quality and the achievable dynamics are sufficient for the sensor fault-tolerant

²¹The mirroring (load symmetry is assumed [74]) is a simplification to save memory. Hence, it is an estimation that applies quite well but which it is not 100% correct; that explains the resulting estimation errors when the mirroring is carried out.

approach of this work. The measurements showed an overall stable behavior at the investigated operating points, which is most important. The maximum estimation error was in the range of $\pm 10^\circ$, which needs to be considered later when developing the sensor fault detection strategy.

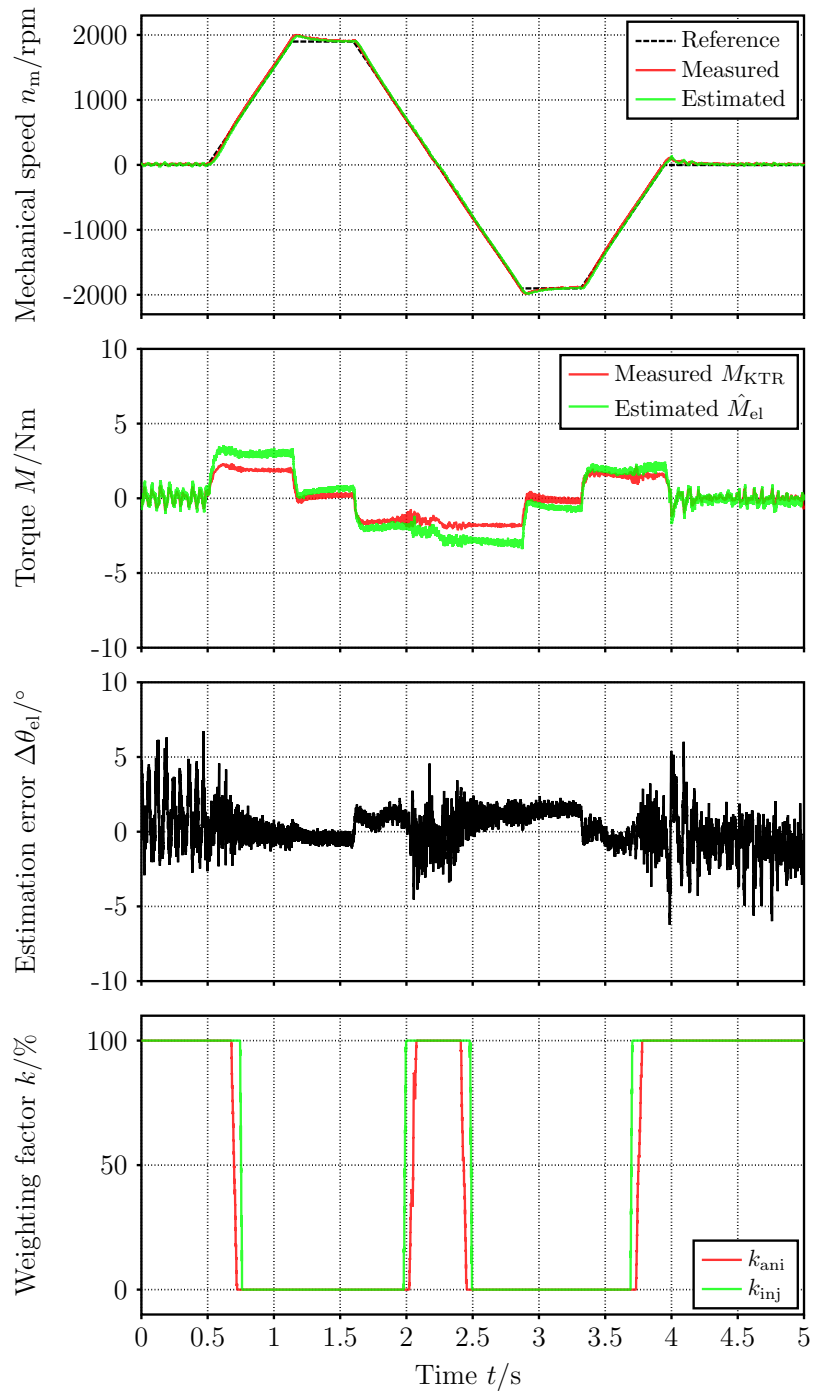


Figure 4.20: Reference tracking during encoderless speed control.

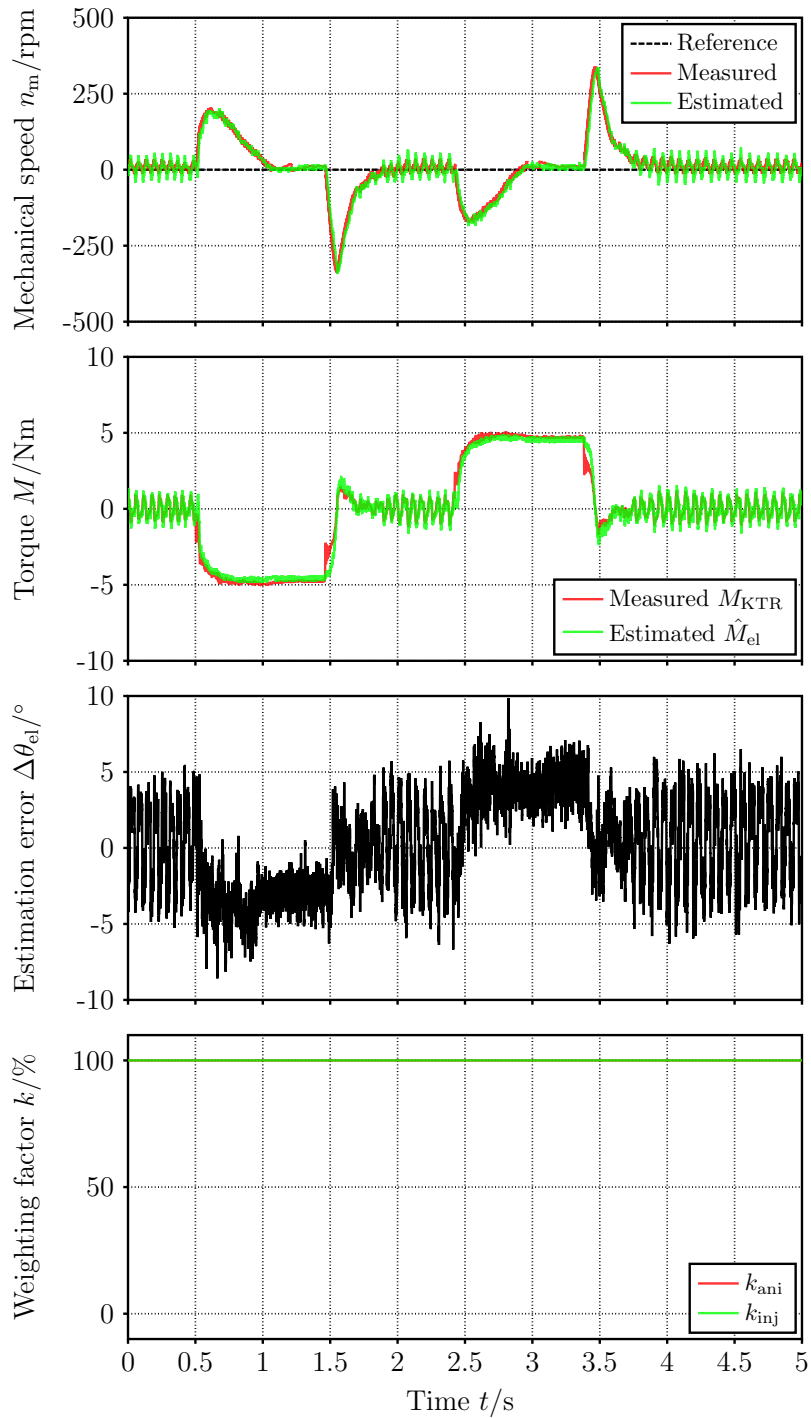


Figure 4.21: Disturbance rejection during encoderless speed control at a standstill.

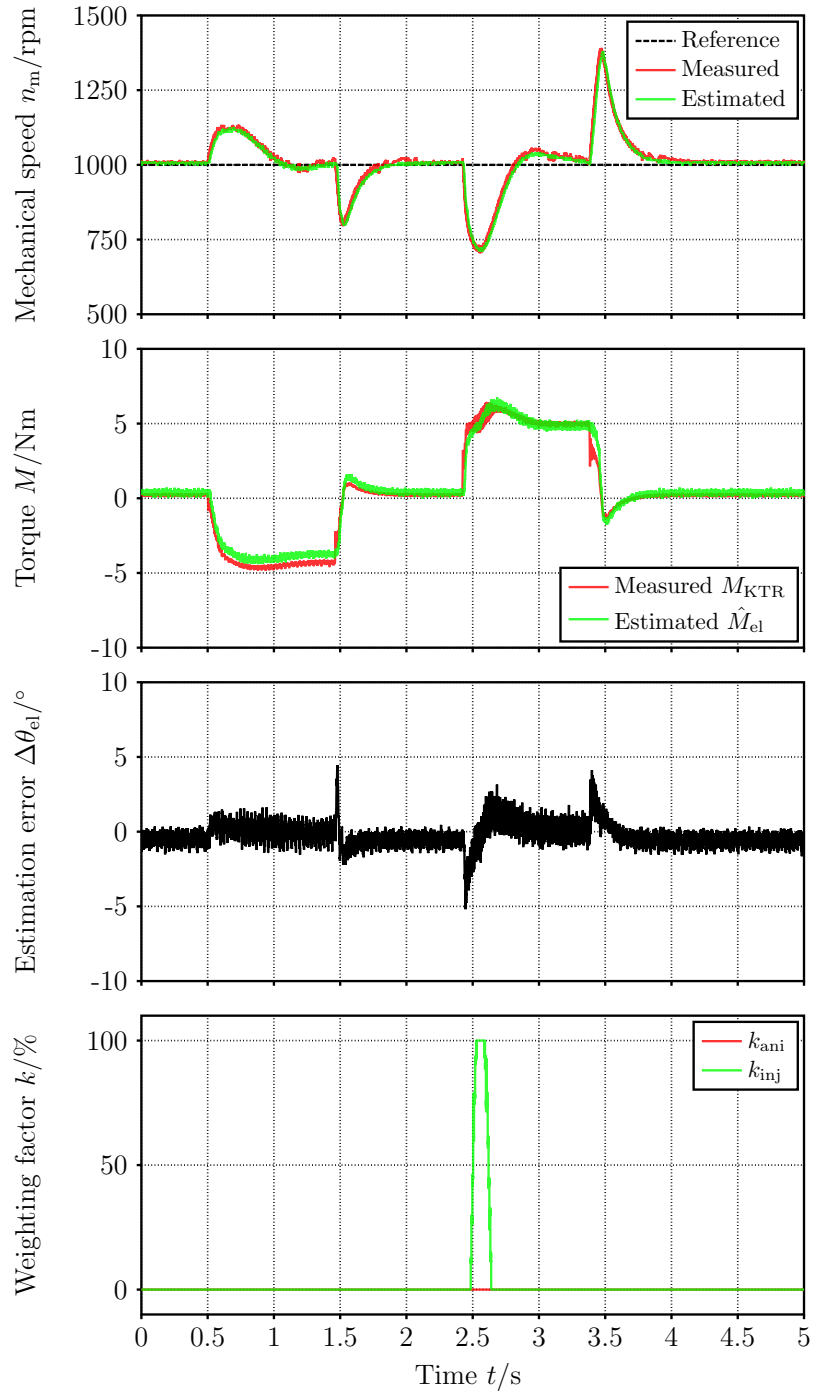


Figure 4.22: Disturbance rejection during encoderless speed control at $n_m = 1000$ rpm.

Chapter 5

Redundancy in the event of a DC-link voltage sensor fault

The DC-link voltage sensor is used to measure the DC-link voltage, which is required for calculating the duty cycles of the semiconductors. Besides this, information of the DC-link voltage is required for the best possible utilization of the available voltage in FW or MTPV operation. As long as the machine is not operated along the FW or MTPV trajectory, a DC-link voltage sensor fault is less critical than a fault of the encoder or the current sensors. The current controllers can compensate for such a fault by adjusting the duty cycles to sustain the currents on their reference values. However, this works only if the deviation of the faulty signal is not too large. Nonetheless, a DC-link voltage sensor fault should be detected to avoid using this erroneous information in a critical operating area. An estimation scheme for the DC-link voltage is an evident approach for a backup algorithm in such an event. The estimation schemes could be employed to detect a DC-link voltage sensor fault and to continue operation. Hence, the following chapter is dedicated to deriving a DC-link-voltage-sensorless control scheme.

The field of encoderless control has been researched for more than thirty years, which has resulted in a comprehensive number of corresponding publications. In contrast, there are no publications on the topic of DC-link-voltage-sensorless control for a drive system, including an estimation of the DC-link voltage. Only for the field of grid-connected converters, e.g. [83], or grid-connected photovoltaic (PV) systems, e.g. [84], a few publications exist that estimate the DC-link voltage. However, the theories behind these works are not related to a drive system and are, hence, not employable. This is because their estimation of the DC-link voltage is commonly based on the

DC/DC converter in their system. The authors of [85] estimated the DC-link voltage for a three-phase boost power factor correction rectifier based on a model of the DC-link capacitor. However, since capacitors can vary significantly in their capacitance over a lifetime, such an approach can become inaccurate. Due to missing estimation approaches in the literature, a completely new method must be developed in the following.

The chapter starts with a section in which the link between the DC-link voltage and machine voltages is derived. The relationship between both voltages can be described by the switching states of the VSI. Based on this relationship, a model for estimating the DC-link voltage in medium to high speeds is derived. After introducing a second estimation model for low speeds, both models are combined in a hybrid method following the example of encoderless control. In the end, the hybrid method is verified empirically.

5.1 Relationship between DC-link voltage and machine voltages

The VSI is the linking element between the DC-link voltage and the machine voltages and is one of the central components for the considerations of this chapter. The two-level VSI is shown in Fig. 5.1. In most applications, the input current i_{B6} is not measured, also when the VSI is connected to a battery. On the test bench, the inverter of the load machine is connected to the same DC-link rail, resulting in one more unknown current i_{vsi2} . Therefore, it is not possible to solve for i_C by means of i_{B6} and i_{vsi2} , which could be used to estimate the DC-link voltage by calculating its time integral. Hence, another estimation approach must be found which does not rely on the currents of the VSI.

The machine currents and encoder signals are available when operating DC-link-voltage-sensorless. The idealized switching states of the VSI are calculated in the control unit, and the machine voltages can be determined/estimated using a current-based machine model. The machine voltages in turn are related to the DC-link voltage via the actual switching states of the VSI. With these information, it is possible to reconstruct the DC-link voltage using the information of the machine voltages and the actual switching states. Therefore, a model is required which describes the relationship between the actual switching states, the DC-link voltage, and the machine voltages. Such a model is derived in this section. The derivation is first conducted for an idealized

VSI, which is afterward extended by the effect of the inverter interlock time. Both models are combined for DC-link-voltage-sensorless control over the entire speed range.

The derivation is based on the following assumptions:

- All switches, also the diodes, are assumed to be ideal. Thus, parasitic effects such as voltage drops, nonlinearities, etc. [16] are neglected.
- Only the impedances drawn in Fig. 5.1 are considered. Other voltage-drop-causing elements are neglected
- The gate driver circuits are assumed to transmit the control commands ideally, leading to an idealized switching behavior of the semiconductors.

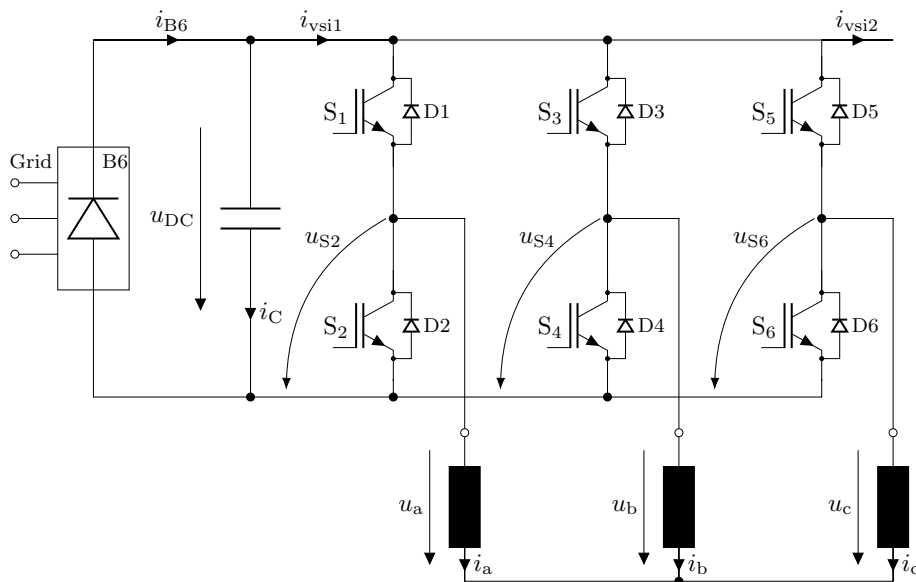


Figure 5.1: Two-level VSI.

5.1.1 Derivation for the idealized VSI

The derivation of this subsection is dedicated to an idealized VSI, which converts the control signals from the control unit undistorted. The derivation starts with the definition of the three voltages $u_{S2,ctr}, u_{S4,ctr}, u_{S6,ctr} \in \mathbb{R}^+$ (no voltage drops across the diodes assumed) across the bottom switches for the idealized VSI²². The voltages can be expressed by the DC-link voltage $u_{DC} \in \mathbb{R}^+$ and the idealized controller switching

²²Variables with the subscript ctr denote idealized quantities, which apply when the VSI converts the control signals undistorted. Hence, some of the variables of Fig. 5.1 have optional the additional identifier ctr (control) in the subscript. These quantities are the reference values from the control unit and are known, therefore.

state functions $s_{x,\text{ctr}} \in \{0, 1\}$, with $x \in \{a, b, c\}$. Hereby, $s_{x,\text{ctr}} = 1$ constitutes that the top switch of the specific leg is closed and that the bottom switch is open. For $s_{x,\text{ctr}} = 0$ it is vice versa. Therefore, the idealized voltages across the bottom switches are:

$$u_{S2,\text{ctr}} := u_{\text{DC}} \cdot s_{a,\text{ctr}} \quad (5.1)$$

$$u_{S4,\text{ctr}} := u_{\text{DC}} \cdot s_{b,\text{ctr}} \quad (5.2)$$

$$u_{S6,\text{ctr}} := u_{\text{DC}} \cdot s_{c,\text{ctr}} \quad (5.3)$$

The PWM modules are configured to apply the reference voltages over one switching period T_{sw} . This is achieved by adjusting the duty cycle. Hence, voltages and switching states used in the control unit are mean values if a modulator-based approach is used. These mean voltages can be discretized with respect to the instance k (instance n is not denoted for the clarity of the equations) and can be expressed using the switch-on times of the top switches $t_{x,\text{ON},\text{ctr}} \in [0, T_{\text{sw}}]$ with $x \in \{a, b, c\}$ and the switching period²³:

$$\bar{u}_{S2,\text{ctr}}[k] := u_{\text{DC}}[k] \cdot \bar{s}_{a,\text{ctr}}[k] = u_{\text{DC}} \frac{t_{a,\text{ON},\text{ctr}}[k]}{T_{\text{sw}}} \quad (5.4)$$

$$\bar{u}_{S4,\text{ctr}}[k] := u_{\text{DC}}[k] \cdot \bar{s}_{b,\text{ctr}}[k] = u_{\text{DC}} \frac{t_{b,\text{ON},\text{ctr}}[k]}{T_{\text{sw}}} \quad (5.5)$$

$$\bar{u}_{S6,\text{ctr}}[k] := u_{\text{DC}}[k] \cdot \bar{s}_{c,\text{ctr}}[k] = u_{\text{DC}} \frac{t_{c,\text{ON},\text{ctr}}[k]}{T_{\text{sw}}} \quad (5.6)$$

Equations (5.4) to (5.6) can be consolidated through vector representation:

$$\bar{\mathbf{u}}_{S246,\text{ctr}}[k] := u_{\text{DC}}[k] \cdot \bar{\mathbf{s}}_{\text{ctr}}[k] \quad (5.7)$$

The next step is to derive a connection between the ideal machine voltages $\bar{u}_{a,\text{ctr}}$, $\bar{u}_{b,\text{ctr}}$, $\bar{u}_{c,\text{ctr}}$ and the bottom switch voltage vector $\bar{\mathbf{u}}_{S246,\text{ctr}}$. This connection can be established with the following system of equations, which is achieved by applying Kirchhoff's voltage law:

$$\underbrace{\begin{bmatrix} 1 & -1 & 0 \\ 0 & 1 & -1 \\ -1 & 0 & 1 \end{bmatrix}}_{=: \mathbf{U}_t} \begin{bmatrix} \bar{u}_{a,\text{ctr}}[k] \\ \bar{u}_{b,\text{ctr}}[k] \\ \bar{u}_{c,\text{ctr}}[k] \end{bmatrix} = u_{\text{DC}}[k] \begin{bmatrix} \bar{s}_{a,\text{ctr}}[k] - \bar{s}_{b,\text{ctr}}[k] \\ \bar{s}_{b,\text{ctr}}[k] - \bar{s}_{c,\text{ctr}}[k] \\ \bar{s}_{c,\text{ctr}}[k] - \bar{s}_{a,\text{ctr}}[k] \end{bmatrix} \quad (5.8)$$

²³The DC-link voltage is assumed to be constant over one switching period T_{sw} .

The matrix \mathbf{U}_t is singular and hence not invertible. Nevertheless, the machine voltages can be determined using the Moore–Penrose inverse \mathbf{U}_t^+ . This yields:

$$\begin{bmatrix} \bar{u}_{a,\text{ctr}}[k] \\ \bar{u}_{b,\text{ctr}}[k] \\ \bar{u}_{c,\text{ctr}}[k] \end{bmatrix} = \frac{u_{\text{DC}}[k]}{3} \underbrace{\begin{bmatrix} 1 & 0 & -1 \\ -1 & 1 & 0 \\ 0 & -1 & 1 \end{bmatrix}}_{=:\mathbf{U}_t^+} \begin{bmatrix} \bar{s}_{a,\text{ctr}}[k] - \bar{s}_{b,\text{ctr}}[k] \\ \bar{s}_{b,\text{ctr}}[k] - \bar{s}_{c,\text{ctr}}[k] \\ \bar{s}_{c,\text{ctr}}[k] - \bar{s}_{a,\text{ctr}}[k] \end{bmatrix} \quad (5.9)$$

Equation (5.9) can be further simplified, resulting in:

$$\bar{\mathbf{u}}_{s,\text{ctr}}^t[k] = \begin{bmatrix} \bar{u}_{a,\text{ctr}}[k] \\ \bar{u}_{b,\text{ctr}}[k] \\ \bar{u}_{c,\text{ctr}}[k] \end{bmatrix} = \frac{u_{\text{DC}}[k]}{3} \underbrace{\begin{bmatrix} 2 & -1 & -1 \\ -1 & 2 & -1 \\ -1 & -1 & 2 \end{bmatrix}}_{=:\mathbf{U}} \begin{bmatrix} \bar{s}_{a,\text{ctr}}[k] \\ \bar{s}_{b,\text{ctr}}[k] \\ \bar{s}_{c,\text{ctr}}[k] \end{bmatrix} = \frac{u_{\text{DC}}[k]}{3} \mathbf{U} \bar{\mathbf{s}}_{\text{ctr}}[k] \quad (5.10)$$

Equation (5.10) describes the relationship between the machine voltages $\bar{\mathbf{u}}_{s,\text{ctr}}^t$ and the DC-link voltage u_{DC} dependent on the ideal switching states $\bar{\mathbf{s}}_{\text{ctr}}$ for an idealized VSI. For some considerations of this work, this model must be extended to incorporate the effect of the inverter interlock time. Hence, the previously derived model is extended in the following.

5.1.2 Extension by the interlock time

The previously introduced model is extended by the model of the inverter interlock time (2.46). The derivation is analogous to the previous derivation and, therefore, not conducted in detail. First, the idealized mean switching state vector $\bar{\mathbf{s}}_{\text{ctr}}$ of equation (5.7) is extended to incorporate the effect of the inverter interlock time described by the switching state vector $\bar{\mathbf{s}}_{\text{dt}} \in \mathbb{R}^3$. Where $\bar{\mathbf{s}}_{\text{dt}}$ is derived from equation (2.46). This results in the new switching state vector $\bar{\mathbf{s}}$:

$$\bar{\mathbf{s}}[k] := \bar{\mathbf{s}}_{\text{ctr}}[k] - \bar{\mathbf{s}}_{\text{dt}}[k] = \begin{bmatrix} \frac{t_{a,\text{ON,ctr}}[k] - t_{\text{dt}} \cdot \text{sgn}(i_a[k])}{T_{\text{sw}}} \\ \frac{t_{b,\text{ON,ctr}}[k] - t_{\text{dt}} \cdot \text{sgn}(i_b[k])}{T_{\text{sw}}} \\ \frac{t_{c,\text{ON,ctr}}[k] - t_{\text{dt}} \cdot \text{sgn}(i_c[k])}{T_{\text{sw}}} \end{bmatrix} =: \begin{bmatrix} \bar{s}_a[k] \\ \bar{s}_b[k] \\ \bar{s}_c[k] \end{bmatrix} \quad (5.11)$$

The $\bar{\mathbf{s}}$ of equation (5.11) substitutes for the $\bar{\mathbf{s}}_{\text{ctr}}$ in equation (5.10), which yields the actual machine voltage ($\bar{\mathbf{u}}_s^t$ substitutes for $\bar{\mathbf{u}}_{s,\text{ctr}}^t$):

$$\bar{\mathbf{u}}_s^t[k] = \frac{u_{\text{DC}}[k]}{3} \mathbf{U} \bar{\mathbf{s}}[k] \quad (5.12)$$

Equation (5.12) describes the relationship between the machine voltages $\bar{\mathbf{u}}_s^t$ and the DC-link voltage u_{DC} in dependence on the switching states $\bar{\mathbf{s}}$ for a VSI with interlock time. This model is used to derive a DC-link voltage estimation for medium to high speeds.

5.2 Estimation at medium to high speeds

The derivation in the previous section provides the basis for estimating the DC-link voltage. A look at equation (5.12) shows that u_{DC} is the only unknown variable that can, hence, be estimated. The estimation approach proposed in this section is intended to be used for medium to high speeds and considers the effect of the inverter interlock time, which has the most significant affect of all inverter nonlinearities in this speed range. The estimation requires that the machine parameters are stored on the control unit to calculate the machine voltages by means of a current-based model.

The estimation scheme is based on quantities of the rotor fixed reference frame. Therefore, equation (5.12) is transformed with the Clarke and Park transformation, which yields the following:

$$\bar{\mathbf{u}}_s^r[k] := \frac{u_{\text{DC}}[k]}{3} \mathbf{P}[k] \underbrace{\mathbf{C} \mathbf{U} \mathbf{C}^+}_{=3 \cdot \mathbf{I}_2} \mathbf{P}^{-1}[k] \bar{\mathbf{s}}^r[k] \quad (5.13)$$

$$:= u_{\text{DC}}[k] \bar{\mathbf{s}}^r[k] \quad (5.14)$$

with:

$$\bar{\mathbf{s}}^r[k] := \mathbf{P}[k] \mathbf{C} \bar{\mathbf{s}}[k] \quad (5.15)$$

The explicit Euler discretization is used to discretize the machine voltage equation of the rotor fixed reference frame (2.24), which is then inserted in equation (5.14) to

estimate the terminal voltages of the machine:

$$\bar{\mathbf{u}}_s^r[k_{-1}] = R_s[k_{-1}] \mathbf{i}_s^r[k_{-1}] + \dot{\mathbf{L}}_s^r[k_{-1}] \frac{\mathbf{i}_s^r[k] - \mathbf{i}_s^r[k_{-1}]}{T_{\text{sp,ctr}}} + \omega_{\text{el}}[k_{-1}] \mathbf{J} \boldsymbol{\psi}_s^r[k_{-1}] \quad (5.16)$$

$$= u_{\text{DC}}[k_{-1}] \bar{\mathbf{s}}^r[k_{-1}] \quad (5.17)$$

Since $u_{\text{DC}} \in \mathbb{R}^+$ applies, the DC-link voltage of the previous sampling instance k is estimated using the magnitudes of the estimated machine voltage vector $\hat{\mathbf{u}}_s^r[k_{-1}]$ and the estimated switching state vector $\hat{\mathbf{s}}^r[k_{-1}]$. This yields the estimated DC-link voltage:

$$\hat{u}_{\text{DC}}[k_{-1}] = \frac{\|\hat{\mathbf{u}}_s^r[k_{-1}]\|}{\|\hat{\mathbf{s}}^r[k_{-1}]\|} \quad (5.18)$$

The timing structure described in Chapter 3 enables an improvement of this estimation. During one instance, n , it is possible to estimate the DC-link voltage three times. This can be used for noise suppression and makes less additional filtering required. If it is assumed that the DC-link voltage is constant over one sampling interval n , it can be estimated by averaging (low-pass filtering) over three sampling instances k . The result constitutes approximately the estimation at the sampling instance n . Note that the following substitution is applied $\hat{u}_{\text{DC, speed}} := \hat{u}_{\text{DC}}$.

$$\hat{u}_{\text{DC, speed}}[n] = \frac{1}{3} \sum_{i=1}^3 \frac{\|\hat{\mathbf{u}}_s^r[k_{-i}]\|}{\|\hat{\mathbf{s}}^r[k_{-i}]\|} \quad (5.19)$$

Equation (5.19) is used to estimate u_{DC} in the medium to high-speed range. Although the model considers the effect of the inverter's interlock time, the estimator is expected to suffer inaccuracies in the low-speed region of the machine. This can be explained by multiple effects (e.g., voltage drops on the semiconductors, non-ideal on and off switching, etc.) introduced by the VSI [16], which were not considered in the derivation and which are more significant at low speeds.

5.3 Estimation at low speeds

In the following, a second estimator is derived for estimation around a standstill. The estimation scheme employs a voltage injection following the example of encoderless control. The same voltage injection as for encoderless control (Fig. 4.4) is used. The

voltage injection enables the online estimation of the unknown voltage drop across the VSI. Again, it is taken advantage of multiple sampling instances k , which are available during one estimation interval n .

The derivation starts with equation (5.10). Equation (5.10) is transformed into rotor coordinates using the Clarke and Park transformation, which yields:

$$\bar{\mathbf{u}}_{s,\text{ctr}}^r[k] := u_{\text{DC}}[k] \bar{\mathbf{s}}_{\text{ctr}}^r[k] \quad (5.20)$$

The actual machine voltage $\bar{\mathbf{u}}_s^r$ results from the superposition of (5.20) with a unknown voltage deviation vector $\Delta\bar{\mathbf{u}}_s^r \in \mathbb{R}^2$ caused by the inverters nonlinearities:

$$\bar{\mathbf{u}}_s^r[k] = u_{\text{DC}}[k] \bar{\mathbf{s}}_{\text{ctr}}^r[k] - \Delta\bar{\mathbf{u}}_s^r[k] \quad (5.21)$$

The unknown voltage deviation vector describes the voltage drop across the VSI and is approximated by a polynomial function (5.22) ($p_{\text{deg}}, i \in \mathbb{N}_0$). Equation (5.22) requires that the voltage deviation is low-frequency compared to the additional voltage injection [22].

$$\Delta\bar{\mathbf{u}}_s^r[n][k] := \sum_{i=0}^{p_{\text{deg}}} \left(k^i \begin{bmatrix} \Delta a_{d,i}[n] \\ \Delta a_{q,i}[n] \end{bmatrix} \right) \quad (5.22)$$

The following linear system of equations can be derived from (5.21) and (5.22) using different time instances k . This approach is inspired by the method proposed in [22] for encoderless control. For (5.23), it is assumed that u_{DC} is constant over one sampling interval n . Furthermore, the definition $\hat{u}_{\text{DC},\text{inj}} := \hat{u}_{\text{DC}}$ is used.

$$\underbrace{\begin{bmatrix} \bar{u}_d[n][0] \\ \bar{u}_q[n][0] \\ \vdots \\ \bar{u}_d[n][k] \\ \bar{u}_q[n][k] \end{bmatrix}}_{\bar{\mathbf{u}}_s^r[n]} = \underbrace{\begin{bmatrix} -1 & 0 & \dots & -0^{p_{\text{deg}}} & 0 & \bar{s}_{d,\text{ctr}}[n][0] \\ 0 & -1 & \dots & 0 & -0^{p_{\text{deg}}} & \bar{s}_{q,\text{ctr}}[n][0] \\ \vdots & \vdots & & \vdots & \vdots & \vdots \\ -k^0 & 0 & \dots & -k^{p_{\text{deg}}} & 0 & \bar{s}_{d,\text{ctr}}[n][k] \\ 0 & -k^0 & \dots & 0 & -k^{p_{\text{deg}}} & \bar{s}_{q,\text{ctr}}[n][k] \end{bmatrix}}_{=:T[n]} \underbrace{\begin{bmatrix} \Delta a_{d,0}[n] \\ \Delta a_{q,0}[n] \\ \vdots \\ \Delta a_{d,p_{\text{deg}}}[n] \\ \Delta a_{q,p_{\text{deg}}}[n] \\ \hat{u}_{\text{DC},\text{inj}}[n] \end{bmatrix}}_{=: \boldsymbol{\xi}_s^r[n]} \quad (5.23)$$

Here \mathbf{T} and $\bar{\mathbf{u}}_s^r$ are known. The voltage vector $\bar{\mathbf{u}}_s^r$ is estimated using a current-based machine model, whereas the entries of \mathbf{T} are either constant or set by the control unit. The unknown vector $\boldsymbol{\xi}_s^r$ can only be estimated if \mathbf{T} is of full rank or alternatively by its pseudo-inverse. The full rank can be ensured by suitably choosing the number of current measurements, the polynomial degree p_{deg} , and the injection sequence. If the pseudo-inverse is used, the Gauß-Markow theorem must be fulfilled [86]. If these requirements are accomplished, $\boldsymbol{\xi}_s^r$ can be estimated either by \mathbf{T}^{-1} or by applying an ordinary least squares method (pseudo-inverse of \mathbf{T}). For the solution with the pseudo-inverse matrix, it follows:

$$\boldsymbol{\xi}_s^r[n] = \mathbf{T}^+[n] \hat{\mathbf{u}}_s^r[n] \quad (5.24)$$

To reduce the computational effort of the estimation, it is appropriate to calculate only the last row of equation (5.24). The polynomial coefficients of the voltage deviation vector are not of interest in this context.

The timing structure used in this work limits the polynomial degree to a maximum of $p_{\text{deg}} = 2$ to ensure a full rank of \mathbf{T} . This limitation arises from the limited number of current measurements within one estimation interval n . However, the polynomial order is set to $p_{\text{deg}} = 0$ (constant) in the following to reduce the computational effort.

5.4 Hybrid DC-link-voltage-sensorless control

A hybrid DC-link-voltage-sensorless control scheme is proposed in the following. It follows the example of encoderless control (Section 4.3). All sensorless methods (encoderless, DC-link-voltage-sensorless, and current sensorless) must be executed simultaneously on the control unit. Hence, each method must work in accordance with the other sensorless schemes, which also applies to the additional voltage injection. Therefore, a similar hybrid approach with the same weighting coefficients and injection is used as proposed for encoderless control (Section 4.3), resulting in the following hybrid estimation equation:

$$\hat{u}_{\text{DC}} := k_{\text{ani}} \hat{u}_{\text{DC},\text{inj}} + (1 - k_{\text{ani}}) \hat{u}_{\text{DC},\text{speed}} \quad (5.25)$$

The coefficient k_{ani} is used to weigh the outputs from the two estimators. The coefficient k_{inj} , used to scale the voltage injection, is already implemented by the encoderless control method. Fig. 5.2 shows the block diagram of the hybrid DC-link-voltage-

sensorless control scheme.

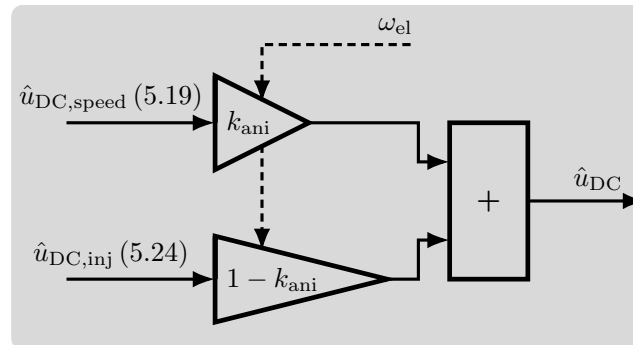


Figure 5.2: Hybrid *DC*-link-voltage-sensorless scheme.

5.5 Empirical verification

The hybrid *DC*-link-voltage-sensorless control scheme is verified in this section. Besides the demonstration of functionality, information about the achievable accuracy is aimed. The information about the achievable accuracy is important for implementing the sensor fault detection at the end. Therefore, a row of tests is conducted. In the first test, the *DC*-link-voltage-sensorless control scheme is verified at steady-state conditions. Afterward, it is tested in a dynamic test drive in motor and generator mode. Finally, the scheme is tested while driving the system into the voltage saturation of the *VSI*. This is expected to be the most critical operating condition of *DC*-link-voltage-sensorless control, since precise information of u_{DC} is strictly required. The tests are conducted in speed control mode if not stated otherwise. The algorithms are carried out in Task 3, depicted in Fig. 3.3.

The settings of the speed controller are the same as for encoderless control. The gain factors remain at $g_{p,n} = 0.1 \text{ Nm s rad}^{-1}$ and $g_{i,n} = 0.5 \text{ Nm rad}^{-1}$. The speed controller setting remains to ensure stability in the event of an encoder failure, resulting in a limited bandwidth of the speed control loop for all estimation methods. This could be improved by adapting the speed controller, dependent on the fault scenario. However, for simplicity this is not implemented within the present work. Instead, the slowest required speed controller setting (encoderless control) is used for all other sensorless methods.

The conventional encoderless control methods showed stability issues when parameter deviations appeared. Such a behavior is not expected for the proposed *DC*-link-voltage-sensorless control since all model parameters are based on measured currents

and encoder signals without relying on estimations.

Some quantities presented in the measurement results have not been introduced yet. One of these quantities is the magnitude of the current controller output voltage vector $\|\mathbf{u}_s^{r*}\|$, which is not allowed to exceed the maximum voltage magnitude of $\|\mathbf{u}_s^{r*}\|_{\max} := u_{\text{DC}}/\sqrt{3}$ to ensure sinusoidal modulation. Note that the anti-windup schemes use the estimated maximum voltage magnitude $\|\hat{\mathbf{u}}_s^{r*}\|_{\max} := \hat{u}_{\text{DC}}/\sqrt{3}$ as reference when operating DC-link-voltage-sensorless, which might cause issues in the current controllers. The estimation error is presented in terms of the relative error, which is calculated as follows

$$f(u_{\text{DC}}) := \frac{\text{LPF}(\hat{u}_{\text{DC}}) - u_{\text{DC}}}{u_{\text{DC}}} \quad (5.26)$$

where the estimated DC-link voltage is first-order low-pass filtered with a time constant of 10 ms before using the estimation in the FOC and for the calculation of (5.26).

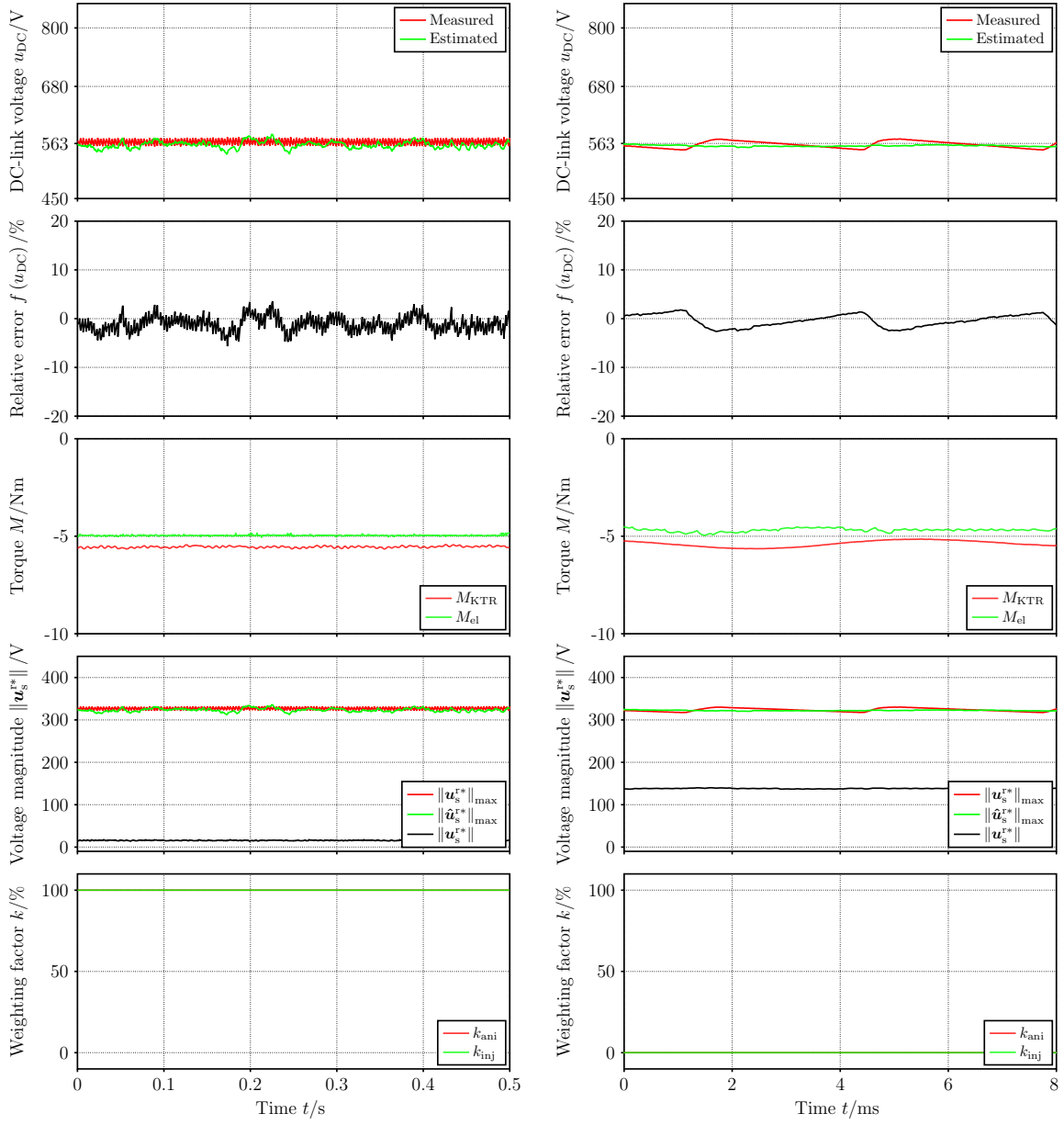
Fig. 5.3 shows the test results at steady-state conditions with 5 Nm of load torque. The left side shows the results in the low-speed area when the model of Section 5.3 is used. The right side shows the results when the medium to high-speed method of Section 5.2 is employed. The maximum relative error remains below $\pm 4\%$ for both measurements. This result implies that the injection-based method can estimate the voltage drop across the VSI online. Otherwise, the estimation would not be that close to the actual value. A 300 Hz component is recognizable in the relative estimation error of Fig. 5.3 b) caused by the B6 rectifier. The estimation bandwidth is not high enough to follow this 300 Hz voltage ripple. This is due to the low-pass filtering and comparably large estimation interval of the algorithm (300 μs). If the filter time constant is reduced and the sampling frequency of the estimation is increased, it should be possible to follow the voltage ripple more precisely.

Fig. 5.4 shows the measurement results for reference speed tracking in motor and generator mode. The relative estimation error reaches $\pm 11\%$ during the speed transients. The injection-based method shows considerably better accuracy than the medium to the high-speed method. The most significant estimation errors appear when the medium to high-speed method is used and a low torque is requested (Fig. 5.4 a)). With low torque requested, primarily a q-axis current is present. As the model parameters have a high gradient along the q-axis, this leads to slight errors in the model parameters determined from the LUTs. This explanation is reasonable when assessing the results of Fig. 5.4 b), where the average estimation error is less than in Fig. 5.4 a), and a d-axis current is always applied. However, also a difference between motor and generator

operating modes can be recognized. The estimation is less accurate during generator mode, which might be caused by the neglected iron loss effects. The injection-based method achieves an accuracy within $\pm 8\%$, confirming that the online estimation of the VSI voltage drop is working appropriately.

The results of the last measurement are shown in Fig. 5.5. The measurement is conducted in the current control mode. The reference currents are applied at a standstill and refer to a reference torque of 17 Nm. Then, the speed is increased in a ramp via the load machine so that the VSI starts to saturate. This is expected to be the most critical operation for DC-link-voltage-sensorless control. In this event, knowledge of the actual DC-link voltage is strictly required to guarantee FW and MTPV operation. It can be seen that the estimated voltage is slightly higher than the reference during the operation in voltage saturation. A weak oscillation appears in the torque (currents) and voltage. This effect is explainable by the anti-windup schemes of the current controllers. The anti-windup schemes cannot work appropriately if the value of the estimated voltage is higher than the actual DC-link voltage. In this case, the reference voltages from the anti-windup schemes cannot be applied to the machine due to the saturated VSI. This disturbs the current control and subsequently leads to oscillations in the currents and in current-dependent quantities. Nonetheless, the control remains stable, and the performance is appropriate to backup a DC-link voltage sensor fault.

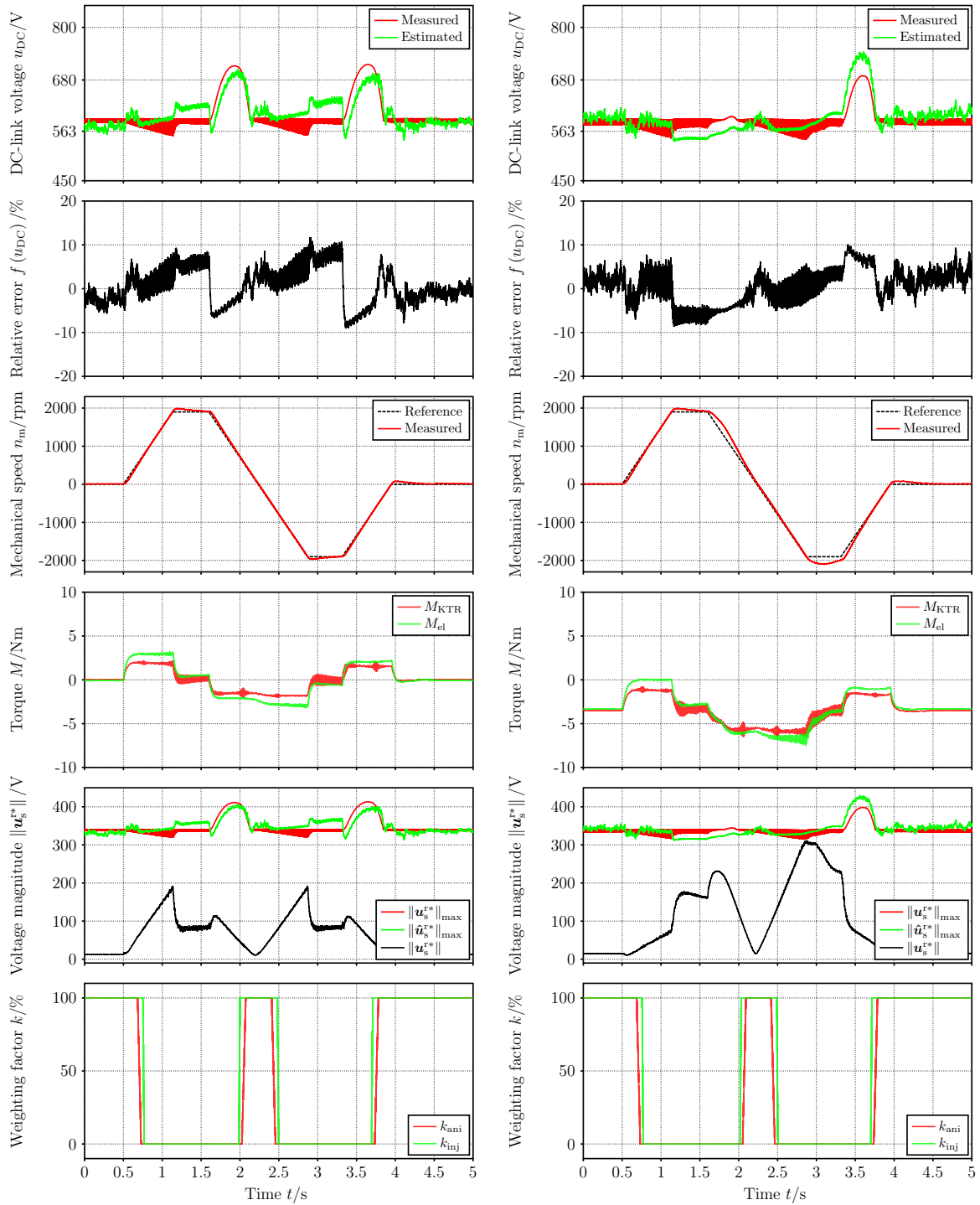
This chapter has introduced a new sensorless control scheme to operate without a DC-link voltage sensor. Comparable schemes do not exist in the current research literature. It can be concluded that the DC-link-voltage-sensorless control approach is a reliable method and will be helpful in implementing the sensor fault-tolerant control algorithm later. The maximum estimation error was in the range of $\pm 11\%$, which needs to be considered when implementing the sensor fault detection.



a) At a speed of $n_m = 50$ rpm.

b) At a speed of $n_m = 1000$ rpm.

Figure 5.3: Steady-state measurements at a load torque of 5 Nm.



a) At zero load torque.

b) At a load torque of 4 Nm.

Figure 5.4: Reference speed tracking during DC-link-voltage-sensorless control.

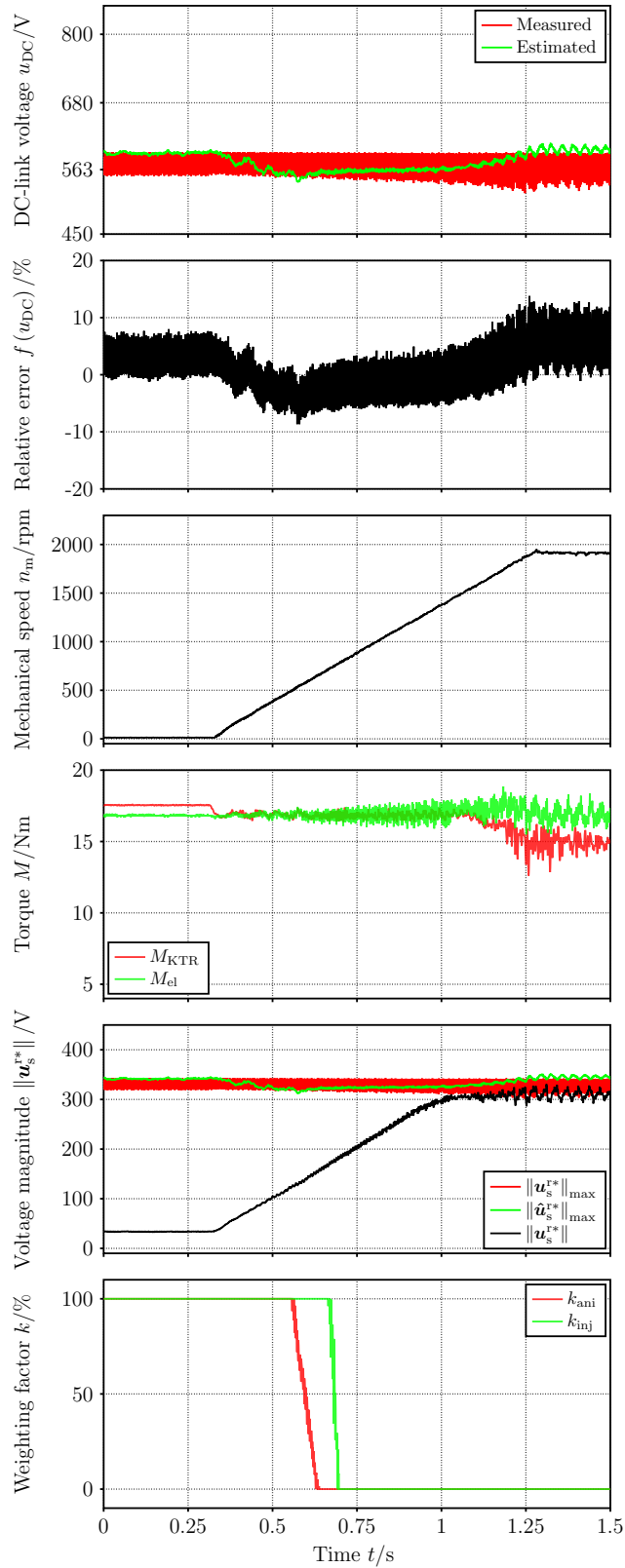


Figure 5.5: Test drive into the voltage saturation of the VSI.

Chapter 6

Redundancy in the event of current sensor faults

The current sensors in an electrical drive system are used to measure the machine's phase currents. The information on the phase currents is required as control feedback for the current control loop in order to adjust the electromagnetic torque of the machine. At least two of the three phase currents²⁴ need to be measured. In a conventional drive system without safety architecture, a fault of the current sensors inevitably leads to the loss of the control capability. A current estimation method, following the example of encoderless control and DC-link-voltage-sensorless control, is an evident approach to compensate for current sensor faults.

In the field of current sensorless control, significantly less research has been conducted as compared to the area of encoderless control. The state-of-the-art can be outlined as follows. Basically, methods that rely on a single current sensor are more in the focus than those without any current sensor. The authors of [87] proposed the control with a single current sensor in the DC-link branch by reconstructing the phase currents employing the switching states of the VSI. The authors of [88] suggested measuring one phase current and one current of an inverter leg with the same current sensor. The information from the single measurement is employed to reconstruct the phase currents. However, also methods that completely omit the current sensors were proposed. In [89], a current sensorless method is proposed, which analytically determines the reference voltages from the actual speed and torque without using current sensors and controllers. However, the method does not provide an estimate of the currents and

²⁴The number of measurements is higher for machines with more than three phases.

is, therefore, not usable within the present work. Other approaches [90, 91, 92] for the IPMSM, IM, and RSM constitute open-loop observers, which do not take advantage of the remaining feedback (e.g. of the speed) to correct the estimations. Furthermore, the effect of magnetic saturation on the machine model is not adequately considered in these approaches. An EKF-based current estimation for a permanent magnet synchronous machine (PMSM) is proposed in [93]. Here, the influence of the load torque and the impact of magnetic saturation is neglected.

The previously mentioned methods, which are the current state-of-the-art in this area, are not entirely satisfying for use in the present work. This is either because remaining feedback (speed) is not used (open-loop observers) to correct the estimates or because of the simplified models that do not consider the effect of magnetic saturation in detail. The simplifications of the effects of magnetic saturation make these approaches less appropriate for highly nonlinear machines, e.g., for the RSM. The open-loop observer-based approaches have another drawback. The existing observer structure must be modified entirely to a closed-loop observer if it is aimed to take advantage of the remaining current sensors (for the case that not all the sensors fail). Due to the mentioned drawbacks, a novel current sensorless scheme is proposed in this chapter. The estimation of the currents is based on an extended Kalman filter (EKF), considering the impact of magnetic saturation in detail. The EKF is aimed to work without a current sensor and should take advantage of the speed as remaining feedback. The speed feedback links the observer to the actual physical system and should improve the estimation quality. The work [94][LWK] can be considered a pre-publication to the following chapter. However, the approach of [94][LWK] is improved with an extended machine model and by considering the VSI voltage drop directly in the state-space model.

6.1 State-space model

The Kalman filter (KF) aimed to estimate the stator currents requires an appropriate state-space model. The required state-space model will be nonlinear, as shown later. According to [95, p. 2], a nonlinear state-space model can generally be described by a set of vector differential equations of the following form:

$$\begin{aligned}\dot{\mathbf{x}} &:= \mathbf{f}(\mathbf{x}, \mathbf{u}) & \mathbf{x}(t=0) &=: \mathbf{x}_0 \\ \mathbf{y} &:= \mathbf{g}(\mathbf{x}, \mathbf{u})\end{aligned}\tag{6.1}$$

where $\mathbf{u} \in \mathbb{R}^i$ with $i \in \mathbb{N}$ is the input vector, $\mathbf{x} \in \mathbb{R}^j$ with $j \in \mathbb{N}$ is the state vector, and $\mathbf{f} \in \mathbb{R}^j$ is the vector function of the system. The vector $\mathbf{y} \in \mathbb{R}^r$ with $r \in \mathbb{N}$ is called the output vector, and $\mathbf{g} \in \mathbb{R}^r$ is the output vector function.

The nonlinear state-space model used to estimate the currents of the machine can be derived from the voltage equation (2.24) of the machine superimposed with a model of the VSI voltage drop and from the state equation of the speed (2.44). The voltage drop of the VSI in rotor fixed coordinates is generally expressed as follows.

$$\mathbf{u}_{\text{vsi}}^r := \begin{bmatrix} u_{\text{d,vsi}} \\ u_{\text{q,vsi}} \end{bmatrix} = \mathbf{P} \mathbf{C} \mathbf{u}_{\text{vsi}}^t \quad (6.2)$$

Therefore, the dependency $\mathbf{u}_{\text{vsi}}^r(i_d, i_q, \theta)$ applies. A more detailed model of the VSI voltage drop is introduced later in the derivation. The state vector is shown in equation (6.3), it contains the states to be estimated. Hence, the currents i_d, i_q are contained. The angular velocity is contained and acts as the output of the state-space model. The speed is required to optimize the Kalman gain by comparing the speed estimation with the measurement (speed feedback). The unknown step-shaped load torque $M_{L,s}$ is considered to achieve stationary accuracy of the observer in the presence of load torques.

$$\mathbf{x} = [i_d \quad i_q \quad \omega_m \quad M_{L,s}]^\top \quad (6.3)$$

The nonlinear state-space model of the state vector \mathbf{x} is described by (6.4), where the vector function \mathbf{f} of the system is derived by the time differentiation of \mathbf{x} .

$$\mathbf{f}(\mathbf{x}, \mathbf{u}) = \begin{bmatrix} \frac{u_{\text{d,ctr.}}}{\dot{L}_{\text{dd}}} - \frac{u_{\text{d,vsi}}}{\dot{L}_{\text{dd}}} - \frac{R_s i_d}{\dot{L}_{\text{dd}}} - \frac{\dot{L}_{\text{dq}}}{\dot{L}_{\text{dd}}} \frac{di_q}{dt} + \frac{\omega_m p \psi_q}{\dot{L}_{\text{dd}}} \\ \frac{u_{\text{q,ctr.}}}{\dot{L}_{\text{qq}}} - \frac{u_{\text{q,vsi}}}{\dot{L}_{\text{qq}}} - \frac{R_s i_q}{\dot{L}_{\text{qq}}} - \frac{\dot{L}_{\text{dq}}}{\dot{L}_{\text{qq}}} \frac{di_d}{dt} - \frac{\omega_m p \psi_d}{\dot{L}_{\text{qq}}} \\ K_T (\psi_d i_q - \psi_q i_d) - \frac{M_{L,s}}{J} - \frac{M_f}{J} \\ 0 \end{bmatrix} \quad (6.4)$$

$$\mathbf{y} = \mathbf{g}(\mathbf{x}, \mathbf{u}) := \omega_m \quad \mathbf{u} := [u_{\text{d,ctr.}} \quad u_{\text{q,ctr.}}]^\top \quad K_T := \frac{3p}{2J}$$

The quantities \mathbf{y} and \mathbf{g} are one-dimensional ($r = 1$) since the EKF is aimed to work with only the speed as feedback. The currents are not employed as feedback to perform estimation without a single current sensor²⁵. State vector \mathbf{x} and the vector function \mathbf{f} are four-dimensional ($j = 4$) whereas \mathbf{u} is two-dimensional ($i = 2$).

Due to magnetic saturation, all inductances $\dot{L}_x, \forall x \in \{\text{dd}, \text{qq}, \text{dq}\}$ and flux linkages $\psi_x, \forall x \in \{\text{d}, \text{q}\}$ are functions of the currents i_d and i_q even if not denoted explicitly.

6.2 Observability of the state-space model

Before deriving the observer, it is to be verified whether the state-space model is generally observable. Criteria for assessing the observability of linear state-space systems are widely used and well discussed in textbooks, e.g., [96, p. 93]. Criteria for verifying the observability of nonlinear state-space systems are considerably less discussed but can still be found in textbooks dealing with nonlinear control theory. The proof of observability for nonlinear systems typically requires more effort than for linear systems. The authors of [97, 95] discuss the topic of nonlinear observability thoroughly. A detailed view of the theory of observability of nonlinear systems is beyond the scope of this dissertation. Hence, the theory is only applied in the following.

The theory of nonlinear observability distinguishes between two categories of observability. The first category is called *global observability*. If a system is globally observable, the initial state can be reconstructed using the input vector and the output vector no matter how “far” the actual state is apart from the initial state. The second kind of observability is called *local observability*, sometimes referred to as *weak observability*. The fulfillment of local observability ensures constrained observability compared to global observability and only holds for a specific “area” of the total state-space. If a system is locally observable, it is guaranteed that the initial state can be reconstructed using the input vector and the output vector only for a state that is at a limited “distance” from the initial state.

According to [95, p. 527], most nonlinear systems are globally observable if they are locally observable; this statement is always true for linear systems. Often, it is only possible to assess local observability, which also applies to the state-space system used here (6.4). This is because the state-space system was not described throughout analytically in the entire state-space, which is needed to assess global observability. The

²⁵The state-space model could be extended by current outputs as well. However, such a state-space model does not work if all current sensors fail simultaneously, but could improve the estimation accuracy if some of the current sensors still work.

throughout analytical description would require an analytical description of the flux linkages considering magnetic saturation, such as provided by [98]. Hence, only local observability is assessed in the following.

According to [95, p. 527], local observability is generally defined as follows

Definition 2 (local observability): A nonlinear system as defined in (6.1) with $\mathbf{x} \subseteq \mathbb{R}^j$ and $\mathbf{u} \subseteq \mathcal{C}^{j-1}$ is locally observable in an environment

$$E = \{\mathbf{x}_0 \in \mathbb{R}^j \mid \|\mathbf{x}_0 - \mathbf{x}_p\| < \rho\}$$

of a point $\mathbf{x}_p \subseteq \mathbb{R}^j$, if $\mathbf{x}_0 \subseteq \mathbb{R}^j$ is unequivocally determinable with knowledge of $\mathbf{u}(t)$ and $\mathbf{y}(t)$ in the time interval $[t_0, t_1 < \infty]$ and that for all possible $\mathbf{x}_p \subseteq \mathbb{R}^j$.

and can be assessed by the following criterion [95, p. 534]

Criterion for local observability: A nonlinear system as defined in (6.1) and Definition 2 is locally observable if the following criterion is fulfilled:

$$j \stackrel{!}{=} \text{rank} \begin{bmatrix} \frac{\partial g(\mathbf{x}, \mathbf{u})}{\partial \mathbf{x}} \\ \frac{\partial h_1(\mathbf{x}, \mathbf{u}, \dot{\mathbf{u}})}{\partial \mathbf{x}} \\ \frac{\partial h_2(\mathbf{x}, \mathbf{u}, \dot{\mathbf{u}}, \ddot{\mathbf{u}})}{\partial \mathbf{x}} \\ \vdots \\ \frac{\partial h_{j-1}(\mathbf{x}, \mathbf{u}, \dot{\mathbf{u}}, \dots, \mathbf{u}^{(j-1)})}{\partial \mathbf{x}} \end{bmatrix} \quad (6.5)$$

whereas the functions denoted with an h are the $(j-1)$ total time derivatives and are defined as follows:

$$h_{j-1} := \frac{\partial h_{j-2}}{\partial \mathbf{x}} \mathbf{f}(\mathbf{x}, \mathbf{u}) + \sum_{l=1}^{j-1} \frac{\partial h_{j-2}}{\partial \mathbf{u}^{(l-1)}} \mathbf{u}^{(l)} \quad (6.6)$$

The criterion (6.5) must be assessed at as many operating points as possible to guarantee local observability in a wide area of the state-space. However, it is not possible to evaluate this criterion at all possible operating points due to the exponential growth of possible constellations with considered dependencies. Hence, the criterion is verified for certain parameters and state constellations only.

The parameters/states included in the state-space system ((6.3), (6.4)) are real numbers ($\in \mathbb{R}$) or element of the subset of the real numbers. The probability that the

rank of the observability matrix (6.5) is unequal to j (nonobservable) is largest if some of these parameters/states are equal to zero. Zero parameter/states can easily result in zero rows or columns, which would cause a non-fulfillment of (6.5). Therefore, the criterion is only verified for constellations where parameters or states are either zero $= 0$ or $\in \mathbb{R}^*$. Since some of the parameters/states are dependent on each other²⁶, the number of possible constellations can be further reduced. An overview of the ranges of values of the parameters/states is depicted in Table 6.1. A checkmark \checkmark indicates that the parameter/state is an element of the range of values, while a cross \times marks that it is not.

Number	state/param.	zero (= 0)	$\in \mathbb{R}^*$
1	p	\times	\checkmark
2	J	\times	\checkmark
3	K_T	\times	\checkmark
4	R_s	\times	\checkmark
5	\dot{L}_{dd}	\times	\checkmark
6	\dot{L}_{qq}	\times	\checkmark
7	\dot{L}_{dq}	\checkmark	\checkmark
8	$u_{d,ctr.}$	\checkmark	\checkmark
9	$u_{q,ctr.}$	\checkmark	\checkmark
10	u_{d,vs_i}	\checkmark	\checkmark
11	u_{q,vs_i}	\checkmark	\checkmark
12	i_d, ψ_d	\checkmark	\checkmark
13	i_q, ψ_q	\checkmark	\checkmark
14	\dot{i}_d	\checkmark	\checkmark
15	\dot{i}_q	\checkmark	\checkmark
16	$M_{L,s}$	\checkmark	\checkmark
17	ω_m, M_f	\checkmark	\checkmark

Table 6.1: Possible ranges of values of the parameters and states.

Eleven of the 17 parameters/states can be either equal or unequal to zero. This gives

$$2^{11} = 2048$$

possible combinations. Not all of these 2048 combinations are physically meaningful;

²⁶E.g., if $i_d > 0$ applies, also $\psi_d > 0$ applies in the case of an [RSM](#).

the number could be further reduced by considering particular parameter/state dependencies. However, all 2048 combinations are assessed regarding observability, and afterward, it is verified whether critical constellations are physically possible or not. The rank calculation and the repetitive process are carried out using a ©Matlab script with symbolic variables.

The rank verification has shown that the observability criterion (6.5) is not fulfilled at 67 of the 2048 constellations. The constellations involved are shown in Table 6.2 and Table 6.3. However, only one of the 67 constellations is physically meaningful and can appear in reality. This critical combination can be found in row 65. The other 66 combinations, marked with different colors, are physically not meaningful because of the following:

- ■ The marked orange rows indicate physically not possible combinations due to the symmetry of the mutual inductance \dot{L}_{dq} for RSMs [13].
- ■ The green-colored rows indicate physically not possible combinations since no currents can be present without any feeding voltage in the system (RSM).
- ■ The marked yellow rows indicate physically not possible combinations because the time derivatives of the current cannot exist for these parameter constellations. For example, in row 53, current derivatives appear without any voltage and current in the system.
- ■ In the red-colored rows, the relationship between torque and angular velocity does not obey the laws of mechanics.
- ■ The marked blue rows are regarding the occurrence of the voltages $u_{d,vs1}$ and $u_{q,vs1}$ caused by the inverter interlock time. It is not possible that these voltages appear in these combinations. For example, in row 28, where both voltages are zero in the presence of a current. This is not reasonable due to the orthogonality of the reference frame and the dependency of the voltages on the currents (2.46).

The remaining locally nonobservable combination in row 65 can be excluded as well. This is because the reference q-axis current is set to a minimum of 3 A, as shown in Fig. 4.16. Hence, a current and voltage must be present, and the combination cannot appear.

Nevertheless, it must be mentioned that the investigated combinations cannot guarantee observability in the whole state-space. The entire state-space was only investigated on the basis of samples. However, since the investigated points were observable,

from here on, it is assumed that the state-space model is generally observable, allowing for applying an [EKF](#).

Ranges of values of the parameters/states

Number	\dot{L}_{dq}	$u_{d,ctr.}$	$u_{q,ctr.}$	$u_{d,vs1}$	$u_{q,vs1}$	i_d, ψ_d	i_q, ψ_q	\dot{i}_d	\dot{i}_q	$M_{L,s}$	ω_m, M_f
1	$\in \mathbb{R}^*$	$\in \mathbb{R}^*$	0	$\in \mathbb{R}^*$	0	$\in \mathbb{R}^*$	0	0	$\in \mathbb{R}^*$	0	0
2	$\in \mathbb{R}^*$	$\in \mathbb{R}^*$	0	$\in \mathbb{R}^*$	0	$\in \mathbb{R}^*$	0	0	0	0	0
3	$\in \mathbb{R}^*$	$\in \mathbb{R}^*$	0	0	0	$\in \mathbb{R}^*$	0	0	$\in \mathbb{R}^*$	0	0
4	$\in \mathbb{R}^*$	$\in \mathbb{R}^*$	0	0	0	$\in \mathbb{R}^*$	0	0	0	0	0
5	$\in \mathbb{R}^*$	0	$\in \mathbb{R}^*$	0	$\in \mathbb{R}^*$	0	$\in \mathbb{R}^*$	$\in \mathbb{R}^*$	0	0	0
6	$\in \mathbb{R}^*$	0	$\in \mathbb{R}^*$	0	$\in \mathbb{R}^*$	0	$\in \mathbb{R}^*$	0	0	0	0
7	$\in \mathbb{R}^*$	0	$\in \mathbb{R}^*$	0	0	0	$\in \mathbb{R}^*$	$\in \mathbb{R}^*$	0	0	0
8	$\in \mathbb{R}^*$	0	$\in \mathbb{R}^*$	0	0	0	$\in \mathbb{R}^*$	0	0	0	0
9	$\in \mathbb{R}^*$	0	0	$\in \mathbb{R}^*$	0	$\in \mathbb{R}^*$	0	0	$\in \mathbb{R}^*$	0	0
10	$\in \mathbb{R}^*$	0	0	$\in \mathbb{R}^*$	0	$\in \mathbb{R}^*$	0	0	0	0	0
11	$\in \mathbb{R}^*$	0	0	0	$\in \mathbb{R}^*$	0	$\in \mathbb{R}^*$	$\in \mathbb{R}^*$	0	0	0
12	$\in \mathbb{R}^*$	0	0	0	$\in \mathbb{R}^*$	0	$\in \mathbb{R}^*$	0	0	0	0
13	$\in \mathbb{R}^*$	0	0	0	0	$\in \mathbb{R}^*$	0	0	$\in \mathbb{R}^*$	0	0
14	$\in \mathbb{R}^*$	0	0	0	0	$\in \mathbb{R}^*$	0	0	0	0	0
15	$\in \mathbb{R}^*$	0	0	0	0	0	$\in \mathbb{R}^*$	$\in \mathbb{R}^*$	0	0	0
16	$\in \mathbb{R}^*$	0	0	0	0	0	$\in \mathbb{R}^*$	0	0	0	0
17	$\in \mathbb{R}^*$	0	0	0	0	0	0	0	0	$\in \mathbb{R}^*$	$\in \mathbb{R}^*$
18	$\in \mathbb{R}^*$	0	0	0	0	0	0	0	0	$\in \mathbb{R}^*$	0
19	$\in \mathbb{R}^*$	0	0	0	0	0	0	0	0	0	$\in \mathbb{R}^*$
20	$\in \mathbb{R}^*$	0	0	0	0	0	0	0	0	0	0
21	0	$\in \mathbb{R}^*$	0	$\in \mathbb{R}^*$	0	$\in \mathbb{R}^*$	0	$\in \mathbb{R}^*$	$\in \mathbb{R}^*$	0	0
22	0	$\in \mathbb{R}^*$	0	$\in \mathbb{R}^*$	0	$\in \mathbb{R}^*$	0	$\in \mathbb{R}^*$	0	0	0
23	0	$\in \mathbb{R}^*$	0	$\in \mathbb{R}^*$	0	$\in \mathbb{R}^*$	0	0	$\in \mathbb{R}^*$	0	0
24	0	$\in \mathbb{R}^*$	0	$\in \mathbb{R}^*$	0	$\in \mathbb{R}^*$	0	0	0	0	0
25	0	$\in \mathbb{R}^*$	0	0	0	$\in \mathbb{R}^*$	0	$\in \mathbb{R}^*$	$\in \mathbb{R}^*$	0	0
26	0	$\in \mathbb{R}^*$	0	0	0	$\in \mathbb{R}^*$	0	$\in \mathbb{R}^*$	0	0	0
27	0	$\in \mathbb{R}^*$	0	0	0	$\in \mathbb{R}^*$	0	0	$\in \mathbb{R}^*$	0	0
28	0	$\in \mathbb{R}^*$	0	0	0	$\in \mathbb{R}^*$	0	0	0	0	0
29	0	0	$\in \mathbb{R}^*$	0	$\in \mathbb{R}^*$	0	$\in \mathbb{R}^*$	$\in \mathbb{R}^*$	$\in \mathbb{R}^*$	0	0
30	0	0	$\in \mathbb{R}^*$	0	$\in \mathbb{R}^*$	0	$\in \mathbb{R}^*$	$\in \mathbb{R}^*$	0	0	0

Table 6.2: Constellations where the criterion for local observability is not fulfilled (part 1).

Ranges of values of the parameters/states

Number	\dot{I}_{dq}	$u_{d,ctr.}$	$u_{q,ctr.}$	$u_{d,vs1}$	$u_{q,vs1}$	i_d, ψ_d	i_q, ψ_q	\dot{i}_d	\dot{i}_q	$M_{L,s}$	ω_m, M_f
31	0	0	$\in \mathbb{R}^*$	0	$\in \mathbb{R}^*$	0	$\in \mathbb{R}^*$	0	$\in \mathbb{R}^*$	0	0
32	0	0	$\in \mathbb{R}^*$	0	$\in \mathbb{R}^*$	0	$\in \mathbb{R}^*$	0	0	0	0
33	0	0	$\in \mathbb{R}^*$	0	0	0	$\in \mathbb{R}^*$	$\in \mathbb{R}^*$	$\in \mathbb{R}^*$	0	0
34	0	0	$\in \mathbb{R}^*$	0	0	0	$\in \mathbb{R}^*$	$\in \mathbb{R}^*$	0	0	0
35	0	0	$\in \mathbb{R}^*$	0	0	0	$\in \mathbb{R}^*$	0	$\in \mathbb{R}^*$	0	0
36	0	0	$\in \mathbb{R}^*$	0	0	0	$\in \mathbb{R}^*$	0	0	0	0
37	0	0	0	$\in \mathbb{R}^*$	0	$\in \mathbb{R}^*$	0	$\in \mathbb{R}^*$	$\in \mathbb{R}^*$	0	0
38	0	0	0	$\in \mathbb{R}^*$	0	$\in \mathbb{R}^*$	0	$\in \mathbb{R}^*$	0	0	0
39	0	0	0	$\in \mathbb{R}^*$	0	$\in \mathbb{R}^*$	0	0	$\in \mathbb{R}^*$	0	0
40	0	0	0	$\in \mathbb{R}^*$	0	$\in \mathbb{R}^*$	0	0	0	0	0
41	0	0	0	0	$\in \mathbb{R}^*$	0	$\in \mathbb{R}^*$	$\in \mathbb{R}^*$	$\in \mathbb{R}^*$	0	0
42	0	0	0	0	$\in \mathbb{R}^*$	0	$\in \mathbb{R}^*$	$\in \mathbb{R}^*$	0	0	0
43	0	0	0	0	$\in \mathbb{R}^*$	0	$\in \mathbb{R}^*$	0	$\in \mathbb{R}^*$	0	0
44	0	0	0	0	$\in \mathbb{R}^*$	0	$\in \mathbb{R}^*$	0	0	0	0
45	0	0	0	0	0	$\in \mathbb{R}^*$	0	$\in \mathbb{R}^*$	$\in \mathbb{R}^*$	0	0
46	0	0	0	0	0	$\in \mathbb{R}^*$	0	$\in \mathbb{R}^*$	0	0	0
47	0	0	0	0	0	$\in \mathbb{R}^*$	0	0	$\in \mathbb{R}^*$	0	0
48	0	0	0	0	0	$\in \mathbb{R}^*$	0	0	0	0	0
49	0	0	0	0	0	0	$\in \mathbb{R}^*$	$\in \mathbb{R}^*$	$\in \mathbb{R}^*$	0	0
50	0	0	0	0	0	0	$\in \mathbb{R}^*$	$\in \mathbb{R}^*$	0	0	0
51	0	0	0	0	0	0	$\in \mathbb{R}^*$	0	$\in \mathbb{R}^*$	0	0
52	0	0	0	0	0	0	$\in \mathbb{R}^*$	0	0	0	0
53	0	0	0	0	0	0	0	$\in \mathbb{R}^*$	$\in \mathbb{R}^*$	$\in \mathbb{R}^*$	$\in \mathbb{R}^*$
54	0	0	0	0	0	0	0	$\in \mathbb{R}^*$	$\in \mathbb{R}^*$	$\in \mathbb{R}^*$	0
55	0	0	0	0	0	0	0	$\in \mathbb{R}^*$	$\in \mathbb{R}^*$	0	$\in \mathbb{R}^*$
56	0	0	0	0	0	0	0	$\in \mathbb{R}^*$	$\in \mathbb{R}^*$	0	0
57	0	0	0	0	0	0	0	$\in \mathbb{R}^*$	0	$\in \mathbb{R}^*$	$\in \mathbb{R}^*$
58	0	0	0	0	0	0	0	$\in \mathbb{R}^*$	0	$\in \mathbb{R}^*$	0
59	0	0	0	0	0	0	0	$\in \mathbb{R}^*$	0	0	$\in \mathbb{R}^*$
60	0	0	0	0	0	0	0	$\in \mathbb{R}^*$	0	0	0
61	0	0	0	0	0	0	0	0	$\in \mathbb{R}^*$	$\in \mathbb{R}^*$	$\in \mathbb{R}^*$
62	0	0	0	0	0	0	0	0	$\in \mathbb{R}^*$	$\in \mathbb{R}^*$	0
63	0	0	0	0	0	0	0	0	$\in \mathbb{R}^*$	0	$\in \mathbb{R}^*$
64	0	0	0	0	0	0	0	0	$\in \mathbb{R}^*$	0	0
65	0	0	0	0	0	0	0	0	0	$\in \mathbb{R}^*$	$\in \mathbb{R}^*$
66	0	0	0	0	0	0	0	0	0	$\in \mathbb{R}^*$	0
67	0	0	0	0	0	0	0	0	0	0	$\in \mathbb{R}^*$

Table 6.3: Constellations where the criterion for local observability is not fulfilled (part 2).

6.3 Extended Kalman filter-based current sensor-less control

The Kalman filter [99] is a widely used method to estimate the states of a system that are either not desired or not possible to measure. The Kalman filter reconstructs the unknown states using the information of the system's inputs, outputs, and a mathematical model of the process. The Kalman filter was introduced for linear systems and differs from the Luenberger observer [100] only in the choice of the feedback matrix \mathbf{K} . Both filters in their initial proposed structure are intended for linear systems but can be extended to nonlinear systems.

The so-called extended Kalman filter (EKF) constitutes the KF for nonlinear systems. The approach is to linearize the nonlinear system so that the principles of the conventional KF are applicable. The first practical uses of the EKF took place in the 1960s, e.g., [101, 102, 103]. Today, the EKF is extensively used, also for multiple tasks in the field of control of drives, e.g., [104, 105]. The theory of the EKF is comprehensive but well presented in several textbooks, e.g., in [95, p. 553]. Hence, the theory is not repeated within this dissertation in detail.

The theory of the Kalman filter assumes that the deterministic system, which is aimed to be observed, is disturbed by normally distributed white noise processes with zero means. The noise processes $\boldsymbol{\rho} \in \mathbb{R}^j$ of the measurements and the noise processes of the states (system) $\boldsymbol{\mu} \in \mathbb{R}^j$ are assumed to be uncorrelated. With these assumptions, the previously introduced state-space system ((6.3), (6.4)) is transformed from a deterministic model into a stochastic model of the following form:

$$\begin{aligned}\dot{\mathbf{x}} &:= \mathbf{f}(\mathbf{x}, \mathbf{u}) + \boldsymbol{\mu} \\ \mathbf{y} &:= \mathbf{g}(\mathbf{x}, \mathbf{u}) + \boldsymbol{\rho}\end{aligned}\tag{6.7}$$

State vector and output vector are consequently stochastic variables. Thus, the Kalman filter does not estimate the actual states of the system, but the expectancy-value (first moment) of the states by adjusting the Kalman gain \mathbf{K} in a way that the sum of the estimated least-squares of the estimation errors expectancy-values is minimized [106]. The estimation equation of the observer is defined analogous to that of linear observers, except that the feedback matrix \mathbf{K} is time-variant.

$$\hat{\dot{\mathbf{x}}} := \mathbf{f}(\hat{\mathbf{x}}, \mathbf{u}) + \mathbf{K}(t)(\mathbf{y} - \mathbf{g}(\hat{\mathbf{x}}))\tag{6.8}$$

The estimation based on equation (6.8) is commonly conducted with a recursive algorithm. The algorithm aims to determine the optimal feedback matrix $\mathbf{K}(t)$ by adjusting $\mathbf{K}(t)$ to the nonlinearities of the system during runtime. The derivation of the optimal recursive algorithm is not the focus of the present work. For an in-depth explanation it is referred to [106, p.9]. The algorithm relies on the discretized state-space model derived from (6.7). The discretization is done with respect to the sampling instance n ²⁷ using the explicit Euler method with the assumption of a sufficiently small sampling interval. It yields:

$$\begin{aligned} \mathbf{x}[n] &= \underbrace{\mathbf{x}[n-1] + T_{\text{ctr}} \mathbf{f}(\mathbf{x}[n-1], \mathbf{u}[n-1])}_{=: \mathbf{f}_a[n-1]} + T_{\text{ctr}} \boldsymbol{\mu}[n-1] \\ \mathbf{y}[n] &= \mathbf{g}[n](\mathbf{x}[n], \mathbf{u}[n]) + \boldsymbol{\rho}[n] \end{aligned} \quad (6.9)$$

The main steps of the recursive algorithm are called “prediction” and “correction”. During the prediction step, a prediction is performed based on the previous estimation and the system’s dynamics without using currently available measurements. During the correction step, the feedback matrix \mathbf{K} is determined to correct the previous estimation from the prediction step. Based on the optimized Kalman gain \mathbf{K} , a new prediction is performed and used for the final estimation. These steps are repeatedly executed on the control platform. The pseudo-code of the recursive algorithm is depicted in Algorithm 1 and in accordance with [103]. The matrices not defined yet have the following properties $\mathbf{I} \in \mathbb{R}^{j \times j}$, $\mathbf{P}_{\text{EKF},x} \in \mathbb{R}^{j \times j}$ with $x \in \{p, c\}$, $\mathbf{Q}_{\text{EKF}} \in \mathbb{R}^{j \times j}$, $\mathbf{R}_{\text{EKF}} \in \mathbb{R}^{m \times m}$, $\mathbf{K} \in \mathbb{R}^{j \times m}$, $\mathbf{J}_{f,da} \in \mathbb{R}^{j \times j}$, $\mathbf{J}_g \in \mathbb{R}^{m \times j}$ where j is the number of states and $m \in \mathbb{N}$ the number of measurements. The same properties apply to the corresponding matrices used for the initialization indicated with a zero in the subscript. Thereby, $\mathbf{P}_{\text{EKF},x}$, \mathbf{Q}_{EKF} , and \mathbf{R}_{EKF} are the covariance matrices of the estimation error, the state (system) noise, and the measurement noise. The matrix \mathbf{J}_g is the Jacobian matrix of $\mathbf{g}(\mathbf{x}, \mathbf{u})$ with respect to the state vector \mathbf{x} of the prediction step and defined as follows:

$$\mathbf{J}_g[n] := \left. \frac{\partial \mathbf{g}}{\partial \mathbf{x}} \right|_{\mathbf{x}=\hat{\mathbf{x}}_p[n]} \quad (6.10)$$

²⁷The computational requirement of the EKF is too high to execute the algorithm for each sampling instance k with the control platform used.

Algorithm 1: Pseudo-code of the extended Kalman filter

```

1 // Initialize covariances
2  $\mathbf{Q}_{\text{EKF}} = \mathbf{Q}_{\text{EKF},0}; \mathbf{R}_{\text{EKF}} = \mathbf{R}_{\text{EKF},0}; \mathbf{P}_{\text{EKF},c} = \mathbf{P}_{\text{EKF},0};$ 

3 while 1 do
4   // Prediction
5    $\hat{\mathbf{x}}_p[n] = \hat{\mathbf{x}}_c[n-1] + \mathbf{f}(\hat{\mathbf{x}}_c[n-1], \mathbf{u}[n-1]) \mathbf{T}_{\text{ctr}};$ 
6    $\mathbf{P}_{\text{EKF},p}[n] = \mathbf{J}_{f,\text{da}}(\hat{\mathbf{x}}_c[n-1]) \mathbf{P}_{\text{EKF},c}[n-1] \mathbf{J}_{f,\text{da}}^\top(\hat{\mathbf{x}}_c[n-1]) + \mathbf{Q}_{\text{EKF}};$ 
7   // Correction
8    $\mathbf{K}[n] = \mathbf{P}_{\text{EKF},p}[n] \mathbf{J}_g[n]^\top (\mathbf{J}_g[n] \mathbf{P}_{\text{EKF},p}[n] \mathbf{J}_g[n]^\top + \mathbf{R}_{\text{EKF}})^{-1};$ 
9    $\mathbf{P}_{\text{EKF},c}[n] = (\mathbf{I} - \mathbf{K}[n] \mathbf{J}_g[n]) \mathbf{P}_{\text{EKF},p}[n];$ 
10   $\hat{\mathbf{x}}_c[n] = \hat{\mathbf{x}}_p[n] + \mathbf{K}[n] (\mathbf{y}[n] - \mathbf{g}(\hat{\mathbf{x}}_p[n]));$ 
11 end while

```

The matrix $\mathbf{J}_{f,\text{da}}$ constitutes the first-order Taylor approximation of the matrix exponential [103] resulting from the explicit Euler approximation and is defined as follows

$$\mathbf{J}_{f,\text{da}}[n] := \frac{\partial \mathbf{f}_d}{\partial \mathbf{x}} = \mathbf{I} + \mathbf{J}_f[n] \mathbf{T}_{\text{ctr}} \quad (6.11)$$

with the Jacobian matrix \mathbf{J}_f of the system vector function \mathbf{f} with respect to the state vector \mathbf{x} at the last correction step:

$$\mathbf{J}_f[n] := \left. \frac{\partial \mathbf{f}}{\partial \mathbf{x}} \right|_{\mathbf{x}=\hat{\mathbf{x}}_c[n-1]} \quad (6.12)$$

Note that the EKF requires that \mathbf{f} and \mathbf{g} are in the subspace of the one-time continuously differentiable vector functions $\mathbf{f} \in \mathcal{C}^1(\mathbb{R}^j; \mathbb{R}^j)$, $\mathbf{g} \in \mathcal{C}^1(\mathbb{R}^j; \mathbb{R}^j)$ of the state vector \mathbf{x} . This must be ensured by choosing an appropriate model for all contained parameters.

The covariance matrices $\mathbf{Q}_{\text{EKF},0}$, $\mathbf{P}_{\text{EKF},0}$, and $\mathbf{R}_{\text{EKF},0}$ of the algorithm are determined later in the derivation after calculating the Jacobian matrices \mathbf{J}_g and \mathbf{J}_f .

6.3.1 Jacobian matrices

The Jacobian matrices defined in (6.10) and (6.12) are determined more detailed in this subsection. The derivation requires the assumption that all inductances $\dot{L}_x, \forall x \in \{\text{dd}, \text{qq}, \text{dq}\}$ are in the subspace of the one-time continuously differentiable functions

$\dot{L}_x \in \mathcal{C}^1(\mathbb{R}; \mathbb{R})$ of the components of the current vector \mathbf{i}_s^r . Also, M_f must be in the subspace of the one-time continuously differentiable functions $M_f \in \mathcal{C}^1(\mathbb{R}; \mathbb{R})$ of the mechanical angular velocity ω_m . Hence, only the viscous friction torque (no coulomb friction) can be considered in the model of the friction torque to fulfill this requirement.

The determination of \mathbf{J}_g is simple. The Jacobian matrix is a row vector with one entry unequal to zero:

$$\mathbf{J}_g = \frac{\partial \mathbf{g}}{\partial \mathbf{x}} = \frac{\partial \omega_m}{\partial \mathbf{x}} = [0 \quad 0 \quad 1 \quad 0] \quad (6.13)$$

The derivation of \mathbf{J}_f used in (6.11) is more comprehensive. The matrix has the general form shown below, containing a few zero elements.

$$\mathbf{J}_f = \frac{\partial \mathbf{f}}{\partial \mathbf{x}} = \begin{bmatrix} j_{11} & j_{12} & j_{13} & 0 \\ j_{21} & j_{22} & j_{23} & 0 \\ j_{31} & j_{32} & j_{33} & j_{34} \\ 0 & 0 & 0 & 0 \end{bmatrix} \quad (6.14)$$

The detailed entries of the Jacobian \mathbf{J}_f are shown in (6.15). The comprehensive entries result from the current dependency of \mathbf{f} (magnetic saturation), which is considered throughout. Note that the current vector dependency of the parameters affected by magnetic saturation is not explicitly denoted to improve the readability of the equations. Also, the sampling instance n is not denoted for clarity.

$$\begin{aligned} j_{11} &= - \left(\dot{L}_{dd} \frac{\partial u_{d, \text{vsi}}}{\partial i_d} - \frac{\partial \dot{L}_{dd}}{\partial i_d} u_{d, \text{vsi}} + u_{d, \text{ctr.}} \frac{\partial \dot{L}_{dd}}{\partial i_d} + R_s \dot{L}_{dd} - R_s i_d \frac{\partial \dot{L}_{dd}}{\partial i_d} + \frac{di_q}{dt} \dot{L}_{dd} \frac{\partial \dot{L}_{dq}}{\partial i_d} \dots \right. \\ &\quad \left. \dots - \frac{di_q}{dt} \dot{L}_{dq} \frac{\partial \dot{L}_{dd}}{\partial i_d} - \omega_m p \dot{L}_{dd} \frac{\partial \psi_q}{\partial i_d} + \omega_m p \psi_q \frac{\partial \dot{L}_{dd}}{\partial i_d} \right) \frac{1}{\dot{L}_{dd}^2} \\ j_{12} &= - \left(\dot{L}_{dd} \frac{\partial u_{d, \text{vsi}}}{\partial i_q} - \frac{\partial \dot{L}_{dd}}{\partial i_q} u_{d, \text{vsi}} + u_{d, \text{ctr.}} \frac{\partial \dot{L}_{dd}}{\partial i_q} - R_s i_d \frac{\partial \dot{L}_{dd}}{\partial i_q} + \frac{di_q}{dt} \dot{L}_{dd} \frac{\partial \dot{L}_{dq}}{\partial i_q} \dots \right. \\ &\quad \left. \dots - \frac{di_q}{dt} \dot{L}_{dq} \frac{\partial \dot{L}_{dd}}{\partial i_q} - \omega_m p \dot{L}_{dd} \frac{\partial \psi_q}{\partial i_q} + \omega_m p \psi_q \frac{\partial \dot{L}_{dd}}{\partial i_q} \right) \frac{1}{\dot{L}_{dd}^2} \\ j_{13} &= \frac{p \psi_q}{\dot{L}_{dd}} \\ &\vdots \end{aligned}$$

$$\begin{aligned}
& \vdots \\
j_{21} &= - \left(\dot{L}_{\text{qq}} \frac{\partial u_{\text{q, vsi}}}{\partial i_{\text{d}}} - \frac{\partial \dot{L}_{\text{qq}}}{\partial i_{\text{d}}} u_{\text{q, vsi}} + u_{\text{q, ctr.}} \frac{\partial \dot{L}_{\text{qq}}}{\partial i_{\text{d}}} - R_{\text{s}} i_{\text{q}} \frac{\partial \dot{L}_{\text{qq}}}{\partial i_{\text{d}}} - \frac{di_{\text{d}}}{dt} \dot{L}_{\text{dq}} \frac{\partial \dot{L}_{\text{qq}}}{\partial i_{\text{d}}} \dots \right. \\
& \quad \left. \dots + \frac{di_{\text{d}}}{dt} \dot{L}_{\text{qq}} \frac{\partial \dot{L}_{\text{dq}}}{\partial i_{\text{d}}} + \omega_{\text{m}} p \dot{L}_{\text{qq}} \frac{\partial \psi_{\text{d}}}{\partial i_{\text{d}}} - \omega_{\text{m}} p \psi_{\text{d}} \frac{\partial \dot{L}_{\text{qq}}}{\partial i_{\text{d}}} \right) \frac{1}{\dot{L}_{\text{qq}}^2} \\
j_{22} &= - \left(\dot{L}_{\text{qq}} \frac{\partial u_{\text{q, vsi}}}{\partial i_{\text{q}}} - \frac{\partial \dot{L}_{\text{qq}}}{\partial i_{\text{q}}} u_{\text{q, vsi}} + u_{\text{q, ctr.}} \frac{\partial \dot{L}_{\text{qq}}}{\partial i_{\text{q}}} + R_{\text{s}} \dot{L}_{\text{qq}} - R_{\text{s}} i_{\text{q}} \frac{\partial \dot{L}_{\text{qq}}}{\partial i_{\text{q}}} - \frac{di_{\text{d}}}{dt} \dot{L}_{\text{dq}} \frac{\partial \dot{L}_{\text{qq}}}{\partial i_{\text{q}}} \dots \right. \\
& \quad \left. \dots + \frac{di_{\text{d}}}{dt} \dot{L}_{\text{qq}} \frac{\partial \dot{L}_{\text{dq}}}{\partial i_{\text{q}}} + \omega_{\text{m}} p \dot{L}_{\text{qq}} \frac{\partial \psi_{\text{d}}}{\partial i_{\text{q}}} - \omega_{\text{m}} p \psi_{\text{d}} \frac{\partial \dot{L}_{\text{qq}}}{\partial i_{\text{q}}} \right) \frac{1}{\dot{L}_{\text{qq}}^2} \\
j_{23} &= - \frac{p \psi_{\text{d}}}{\dot{L}_{\text{qq}}} \\
j_{31} &= -K_{\text{T}} \left(\psi_{\text{q}} + i_{\text{d}} \frac{\partial \psi_{\text{q}}}{\partial i_{\text{d}}} - i_{\text{q}} \frac{\partial \psi_{\text{d}}}{\partial i_{\text{d}}} \right) \\
j_{32} &= K_{\text{T}} \left(\psi_{\text{d}} - i_{\text{d}} \frac{\partial \psi_{\text{q}}}{\partial i_{\text{q}}} + i_{\text{q}} \frac{\partial \psi_{\text{d}}}{\partial i_{\text{q}}} \right) \\
j_{33} &= - \frac{1}{J} \frac{\partial M_{\text{f}}}{\partial \omega_{\text{m}}} \\
j_{34} &= - \frac{1}{J} \tag{6.15}
\end{aligned}$$

The partial derivatives of the flux linkages with respect to the currents can be substituted according to (2.22) and conform to the known differential inductances.

$$\frac{\partial \psi_{\text{d}}}{\partial i_{\text{d}}} = \dot{L}_{\text{dd}} \quad \frac{\partial \psi_{\text{q}}}{\partial i_{\text{q}}} = \dot{L}_{\text{qq}} \quad \frac{\partial \psi_{\text{d}}}{\partial i_{\text{q}}} = \frac{\partial \psi_{\text{q}}}{\partial i_{\text{d}}} = \dot{L}_{\text{dq}} \tag{6.16}$$

The partial derivatives of the differential inductances are substituted as follows,

$$\begin{aligned}
\frac{\partial \dot{L}_{\text{dd}}}{\partial i_{\text{d}}} &=: \zeta_{\text{ddd}} & \frac{\partial \dot{L}_{\text{qq}}}{\partial i_{\text{q}}} &=: \zeta_{\text{qqq}} \\
\frac{\partial \dot{L}_{\text{dd}}}{\partial i_{\text{q}}} &=: \zeta_{\text{ddq}} & \frac{\partial \dot{L}_{\text{qq}}}{\partial i_{\text{d}}} &=: \zeta_{\text{qqd}} \\
\frac{\partial \dot{L}_{\text{dq}}}{\partial i_{\text{d}}} &=: \zeta_{\text{dqd}} & \frac{\partial \dot{L}_{\text{dq}}}{\partial i_{\text{q}}} &=: \zeta_{\text{dqq}}
\end{aligned} \tag{6.17}$$

and named extended differential inductances in the following. The extended differential inductances can be derived from the measurements shown in Fig. 2.4. The results are depicted in Fig. 6.1. It can be seen that the extended differential inductances are primarily in the range of a few mVsA^{-2} , which is exploited later in the derivation process. According to the sentence of Hermann Amandus Schwarz (symmetry of second derivatives), the following must apply $\zeta_{dqd} = \zeta_{ddq}$, $\zeta_{qqd} = \zeta_{dqq}$. This is confirmed by the measurements of Fig. 6.1.

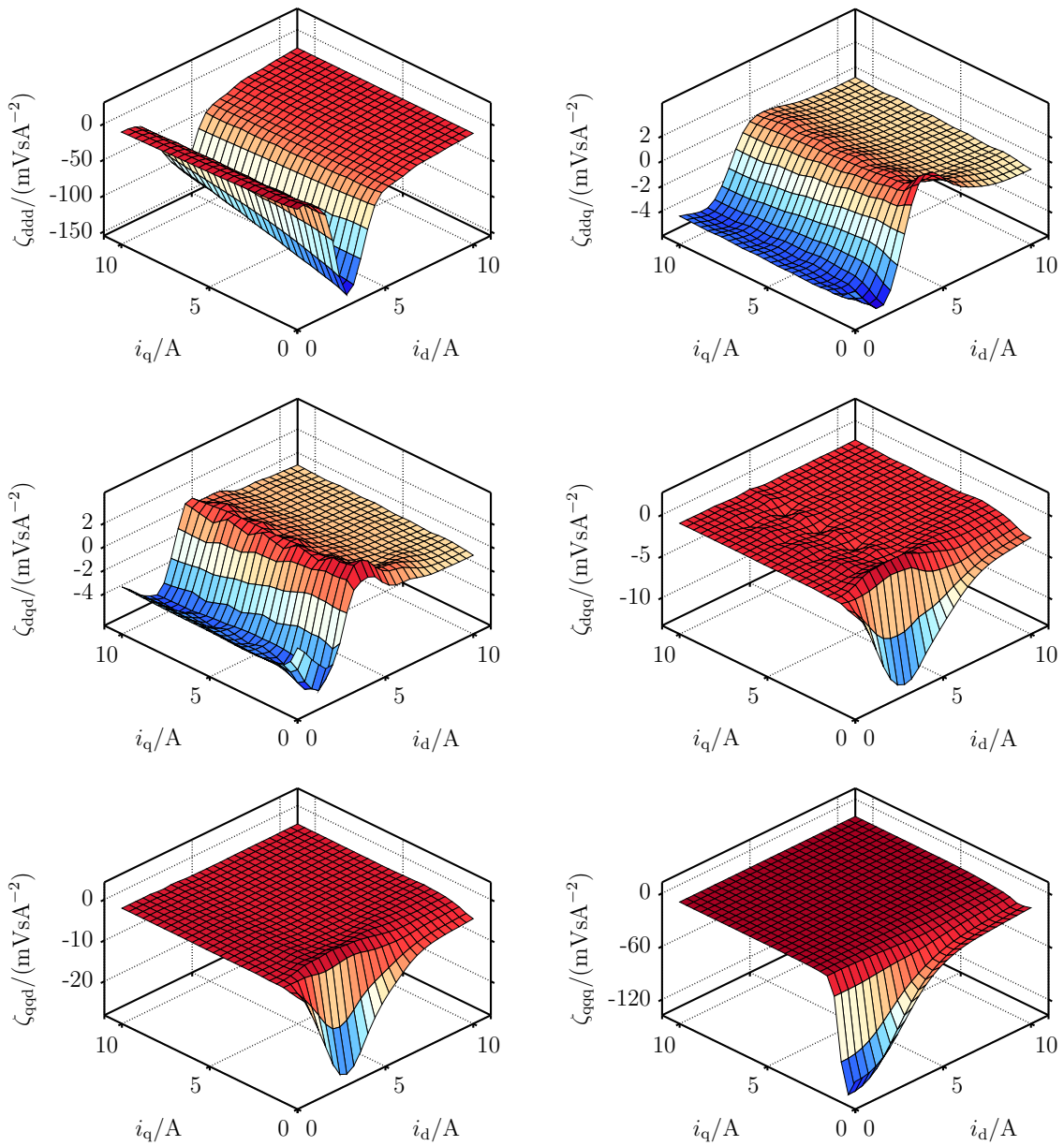


Figure 6.1: Extended differential inductances derived from the measured flux linkage maps (Fig. 2.4).

After the substitutions with (6.16) and (6.17), the entries of the Jacobian \mathbf{J}_f are as follows.

$$\begin{aligned}
j_{11} &= - \left(\dot{L}_{dd} \frac{\partial u_{d,\text{vsi}}}{\partial i_d} - \zeta_{ddd} u_{d,\text{vsi}} + u_{d,\text{ctr}} \zeta_{ddd} + R_s \dot{L}_{dd} - R_s i_d \zeta_{ddd} + \frac{di_q}{dt} \dot{L}_{dd} \zeta_{dq} \dots \right. \\
&\quad \left. \dots - \frac{di_q}{dt} \dot{L}_{dq} \zeta_{ddd} - \omega_m p \dot{L}_{dd} \dot{L}_{dq} + \omega_m p \psi_q \zeta_{ddd} \right) \frac{1}{\dot{L}_{dd}^2} \\
j_{12} &= - \left(\dot{L}_{dd} \frac{\partial u_{d,\text{vsi}}}{\partial i_q} - \zeta_{ddq} u_{d,\text{vsi}} + u_{d,\text{ctr}} \zeta_{ddq} - R_s i_d \zeta_{ddq} + \frac{di_q}{dt} \dot{L}_{dd} \zeta_{dq} \dots \right. \\
&\quad \left. \dots - \frac{di_q}{dt} \dot{L}_{dq} \zeta_{ddq} - \omega_m p \dot{L}_{dd} \dot{L}_{qq} + \omega_m p \psi_q \zeta_{ddq} \right) \frac{1}{\dot{L}_{dd}^2} \\
j_{13} &= \frac{p \psi_q}{\dot{L}_{dd}} \\
j_{21} &= - \left(\dot{L}_{qq} \frac{\partial u_{q,\text{vsi}}}{\partial i_d} - \zeta_{qqd} u_{q,\text{vsi}} + u_{q,\text{ctr}} \zeta_{qqd} - R_s i_q \zeta_{qqd} - \frac{di_d}{dt} \dot{L}_{dq} \zeta_{qqd} \dots \right. \\
&\quad \left. \dots + \frac{di_d}{dt} \dot{L}_{qq} \zeta_{dq} + \omega_m p \dot{L}_{qq} \dot{L}_{dd} - \omega_m p \psi_d \zeta_{qqd} \right) \frac{1}{\dot{L}_{qq}^2} \\
j_{22} &= - \left(\dot{L}_{qq} \frac{\partial u_{q,\text{vsi}}}{\partial i_q} - \zeta_{qqq} u_{q,\text{vsi}} + u_{q,\text{ctr}} \zeta_{qqq} + R_s \dot{L}_{qq} - R_s i_q \zeta_{qqq} - \frac{di_d}{dt} \dot{L}_{dq} \zeta_{qqq} \dots \right. \\
&\quad \left. \dots + \frac{di_d}{dt} \dot{L}_{qq} \zeta_{dq} + \omega_m p \dot{L}_{qq} \dot{L}_{dq} - \omega_m p \psi_d \zeta_{qqq} \right) \frac{1}{\dot{L}_{qq}^2} \\
j_{23} &= - \frac{p \psi_d}{\dot{L}_{qq}} \\
j_{31} &= -K_T (\psi_q + i_d \dot{L}_{dq} - i_q \dot{L}_{dd}) \\
j_{32} &= K_T (\psi_d - i_d \dot{L}_{qq} + i_q \dot{L}_{dq}) \\
j_{33} &= - \frac{1}{J} \frac{\partial M_f}{\partial \omega_m} \\
j_{34} &= - \frac{1}{J}
\end{aligned} \tag{6.18}$$

Some entries of (6.18) contain terms where differential inductances are multiplied with extended differential inductances. This can be exploited to introduce simplifications.

The simplifications decrease the high computational effort required in executing the full Jacobian with the entries of (6.18). The differential inductances are in the range of some hundredths of Henry if the machine is saturated (Fig. 2.4). Hence, the product of the differential inductances with the extended differential inductances is in the range of $10^{-6}\text{V}^2\text{s}^2\text{A}^{-3}$. Therefore, the respective terms are less influential, which allows for the simplifications shown next.

$$\begin{aligned}
\dot{L}_{dd}\zeta_{dqd} &\approx 0 \frac{\text{V}^2\text{s}^2}{\text{A}^3} & \dot{L}_{dq}\zeta_{ddd} &\approx 0 \frac{\text{V}^2\text{s}^2}{\text{A}^3} \\
\dot{L}_{dd}\zeta_{dqq} &\approx 0 \frac{\text{V}^2\text{s}^2}{\text{A}^3} & \dot{L}_{dq}\zeta_{ddq} &\approx 0 \frac{\text{V}^2\text{s}^2}{\text{A}^3} \\
\dot{L}_{dq}\zeta_{qqd} &\approx 0 \frac{\text{V}^2\text{s}^2}{\text{A}^3} & \dot{L}_{qq}\zeta_{dqd} &\approx 0 \frac{\text{V}^2\text{s}^2}{\text{A}^3} \\
\dot{L}_{dq}\zeta_{qqq} &\approx 0 \frac{\text{V}^2\text{s}^2}{\text{A}^3} & \dot{L}_{qq}\zeta_{dqq} &\approx 0 \frac{\text{V}^2\text{s}^2}{\text{A}^3}
\end{aligned} \tag{6.19}$$

The general description of the voltage drop across the VSI (6.2) was not replaced yet. The voltages $u_{d,\text{vsi}}$ and $u_{q,\text{vsi}}$ must be one-time continuously differentiable functions $u_{d,\text{vsi}}, u_{q,\text{vsi}} \in \mathcal{C}^1(\mathbb{R}; \mathbb{R})$ of the components of the current vector \mathbf{i}_s^r according to (6.18). This requirement is not fulfilled if the model of the inverter interlock time (2.46) is used. The signum function in the model (2.46) causes discontinuity and is, hence, inappropriate. Therefore, a new model is proposed in the following.

The in (2.46) introduced model of the VSI voltage drop outputs rectangular voltage waveforms in the case of sinusoidal steady-state of the currents. This rectangular voltage is primarily aimed to be approximated by the new model. However, in total, the model must fulfill three requirements which are defined as follows. First, it is not allowed to cause discontinuity to ensure differentiability. Secondly, it should approximate the model of equation (2.46) with the fundamental of its Fourier series during the sinusoidal steady-state of the currents. And thirdly, it must be able to follow the sign of the currents instantaneously during current transients. A model of the VSI voltage drop that fulfills these three requirements is proposed in (6.20).

$$\mathbf{u}_{\text{vsi}}^t := \begin{cases} \frac{4 u_{\text{DC}} t_{\text{dt}}}{\pi T_{\text{sw}} \|\mathbf{i}_s^r\|} \mathbf{i}_s^t & \|\mathbf{i}_s^r\| \neq 0 \\ \begin{bmatrix} 0 & 0 & 0 \end{bmatrix}^\top & \|\mathbf{i}_s^r\| = 0 \end{cases} \tag{6.20}$$

Factor 4 and π are according to the fundamental of the Fourier series of a rectangular

signal. The three currents are normalized and only used to provide the correct sign of the voltages by replacing the signum functions. The rest is inherited from equation (2.46). This model guarantees that the voltage drops are continuous functions. Furthermore, the model has the advantage that the voltages of $\mathbf{u}_{\text{vsi}}^t$ are sinusoidal if the currents are sinusoidal (if u_{DC} is assumed to be constant). Hence, the voltages of the rotor fixed reference frame $u_{\text{d,vsi}}$ and $u_{\text{q,vsi}}$ are constants during sinusoidal steady-state. This allows for the simplifications shown in (6.21), which further reduce the computational effort to calculate the Jacobian. However, the simplifications (6.21) might lead to estimation errors during current transients.

$$\begin{aligned} \frac{\partial u_{\text{d,vsi}}}{\partial i_{\text{d}}} &\approx 0 \Omega & \frac{\partial u_{\text{d,vsi}}}{\partial i_{\text{q}}} &\approx 0 \Omega \\ \frac{\partial u_{\text{q,vsi}}}{\partial i_{\text{d}}} &\approx 0 \Omega & \frac{\partial u_{\text{q,vsi}}}{\partial i_{\text{q}}} &\approx 0 \Omega \end{aligned} \quad (6.21)$$

The simplifications (6.19) and (6.21) are applied to (6.18) and result in the simplified Jacobian matrix $\mathbf{J}_{f,s}$. This simplified Jacobian matrix is used for the EKF algorithm and is defined analogously to (6.14):

$$\mathbf{J}_f \approx \mathbf{J}_{f,s} := \begin{bmatrix} \dot{j}_{11s} & \dot{j}_{12s} & \dot{j}_{13s} & 0 \\ \dot{j}_{21s} & \dot{j}_{22s} & \dot{j}_{23s} & 0 \\ \dot{j}_{31s} & \dot{j}_{32s} & \dot{j}_{33s} & \dot{j}_{34s} \\ 0 & 0 & 0 & 0 \end{bmatrix} \quad (6.22)$$

The entries of the simplified Jacobian are significantly reduced compared to their origin (6.15) and are given below.

$$\dot{j}_{11s} = \frac{\zeta_{\text{ddd}} u_{\text{d,vsi}} - u_{\text{d,ctr}} \zeta_{\text{ddd}} - R_s \dot{L}_{\text{dd}} + R_s i_{\text{d}} \zeta_{\text{ddd}} + \omega_m p \dot{L}_{\text{dd}} \dot{L}_{\text{dq}} - \omega_m p \psi_{\text{q}} \zeta_{\text{ddd}}}{\dot{L}_{\text{dd}}^2}$$

$$\dot{j}_{12s} = \frac{\zeta_{\text{ddq}} u_{\text{d,vsi}} - u_{\text{d,ctr}} \zeta_{\text{ddq}} + R_s i_{\text{d}} \zeta_{\text{ddq}} + \omega_m p \dot{L}_{\text{dd}} \dot{L}_{\text{dq}} - \omega_m p \psi_{\text{q}} \zeta_{\text{ddq}}}{\dot{L}_{\text{dd}}^2}$$

$$\dot{j}_{13s} = \frac{p \psi_{\text{q}}}{\dot{L}_{\text{dd}}}$$

⋮

$$\begin{aligned}
& \vdots \\
j_{21s} &= \frac{\zeta_{qqd} u_{q, \text{vsi}} - u_{q, \text{ctr.}} \zeta_{qqd} + R_s i_q \zeta_{qqd} - \omega_m p \dot{L}_{qq} \dot{L}_{dd} + \omega_m p \psi_d \zeta_{qqd}}{\dot{L}_{qq}^2} \\
j_{22s} &= \frac{\zeta_{qqq} u_{q, \text{vsi}} - u_{q, \text{ctr.}} \zeta_{qqq} - R_s \dot{L}_{qq} + R_s i_q \zeta_{qqq} - \omega_m p \dot{L}_{qq} \dot{L}_{dq} + \omega_m p \psi_d \zeta_{qqq}}{\dot{L}_{qq}^2} \\
j_{23s} &= -\frac{p \psi_d}{\dot{L}_{qq}} \\
j_{31s} &= -K_T (\psi_q + i_d \dot{L}_{dq} - i_q \dot{L}_{dd}) \\
j_{32s} &= K_T (\psi_d - i_d \dot{L}_{qq} + i_q \dot{L}_{dq}) \\
j_{33s} &= -\frac{1}{J} \frac{\partial M_f}{\partial \omega_m} \\
j_{34s} &= -\frac{1}{J} \tag{6.23}
\end{aligned}$$

6.3.2 Covariance tuning

The covariance matrices $\mathbf{Q}_{\text{EKF},0}$, $\mathbf{R}_{\text{EKF},0}$, and $\mathbf{P}_{\text{EKF},0}$ are to be determined for the algorithm of the [EKF](#). The determination process is briefly described in this subsection. The finding of the appropriate covariances is one of the challenges when applying a state estimation based on an [EKF](#). The determination is often conducted in an optimization procedure. The optimization faces a multidimensional nonlinear problem with an unknown number of local and global maxima and minima. Most analytical approaches are not suitable due to the complexity of the system and the noise properties, which are difficult to determine. The covariance of the measurement noise $\mathbf{R}_{\text{EKF},0}$ is often the only parameter that can be calculated analytically using the datasheet of the sensor. The matrices $\mathbf{Q}_{\text{EKF},0}$ and $\mathbf{P}_{\text{EKF},0}$ are mostly chosen based on experience or by the trial and error principle [104]. The setting of $\mathbf{Q}_{\text{EKF},0}$, which describes the state noise, has the most significant impact on the performance of the [EKF](#). The covariance matrix $\mathbf{P}_{\text{EKF},0}$, which describes the estimation error noise, is only used for initialization and is not that critical, therefore. The covariance matrices $\mathbf{P}_{\text{EKF},x} \forall x \in \{c, p\}$ are throughout calculated by the algorithm itself. Besides the tuning approach of trial and error [104], methods based on artificial intelligence are becoming more popular. Artificial

intelligence-based methods have the benefit that they can be applied to multidimensional nonlinear optimization problems without relying on an analytical description of the optimization problem, which is often not available for covariance optimization. For example, particle swarm optimization [107] or genetic algorithms (GAs) [108] can be used to optimize the covariances.

The covariance determination procedure used in this dissertation is based on a GA, similar to the procedure proposed in [108]. The GA-based covariance optimization is described in the following. The optimization was investigated within the master's thesis [109], which was supervised by the author of this dissertation. The optimization procedure is briefly described in the following, without discussing the topic of genetic algorithms.

The optimization was carried out in a simulation procedure using the ©MATLAB/Simulink model of the system. The simulation-based pre-tuning provides a high possibility that the EKF is stable on the actual test bench. The simulation process is conducted as follows. The test machine (for which the EKF is derived) is operated in open-loop current control mode using the measured currents. Hence, the estimations from the EKF are only used for optimization and not for control. The machine is operated on the speed profile shown in Fig. 6.2 and the reference torque is varied during the different speeds to cover various operating conditions.

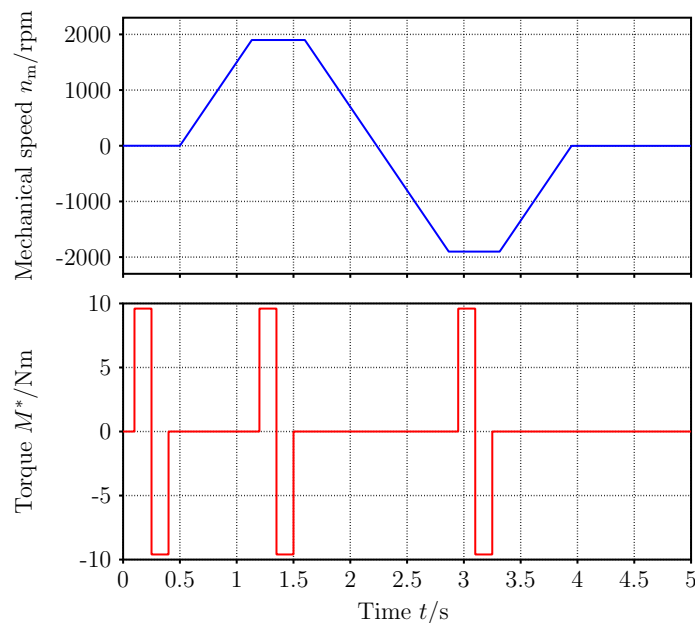


Figure 6.2: Simulated test drive for the covariance tuning in current control mode.

All state variables and their estimations are recorded over the test drive of Fig. 6.2.

The recordings are used to calculate the cost function, which is minimized by the genetic algorithm. The cost function used for the optimization is defined as follows

$$\bar{f}_{\text{rel,EKF}} := \frac{1}{i_{\text{max}}} \sum_{i=1}^{i_{\text{max}}} \left| \frac{\hat{i}_{\text{d},i} - i_{\text{d},i}}{i_{\text{d},i}} \right| + \left| \frac{\hat{i}_{\text{q},i} - i_{\text{q},i}}{i_{\text{q},i}} \right| + \left| \frac{\hat{\omega}_{\text{m},i} - \omega_{\text{m},i}}{\omega_{\text{m},i}} \right| + \left| \frac{\hat{M}_{\text{L},i} - M_{\text{L},i}}{M_{\text{L},i}} \right| \quad (6.24)$$

and constitutes the absolute mean relative error of all estimations. Here, i is one measurement, and i_{max} is the number of measurements taken over one test drive. The possible division by zero in the cost function is intercepted in the implementation. The cost function (6.24), often also called the fitness function in conjunction with genetic algorithms, is optimized by the GA. The ©MATLAB internal function $ga()$ is used to solve the optimization problem, which is defined as follows:

$$\min_{\mathbf{Q}_{\text{EKF},0}, \mathbf{R}_{\text{EKF},0}, \mathbf{P}_{\text{EKF},0}} \bar{f}_{\text{rel,EKF}}(\cdot) \quad (6.25)$$

The procedure is conducted recursively up to the maximum number of iterations. Thereby it is less important whether all entries of the matrices are used and optimized or only the diagonal entries. The difference is small, as shown in [109]. Hence, the covariance matrices are considered diagonal matrices to reduce the optimization effort. The use of diagonal matrices reduces the optimization problem to five dimensions. The setting of the initialization matrix $\mathbf{P}_{\text{EKF},0}$ shows less influence. Therefore, the matrix is arbitrarily set to the unity matrix.

$$\mathbf{P}_{\text{EKF},0} = \begin{bmatrix} 1 \text{ A}^2 & 0 \text{ A}^2 & 0 \text{ A rad s}^{-1} & 0 \text{ A Nm} \\ 0 \text{ A}^2 & 1 \text{ A}^2 & 0 \text{ A rad s}^{-1} & 0 \text{ A Nm} \\ 0 \text{ A rad s}^{-1} & 0 \text{ A rad s}^{-1} & 1 \text{ rad}^2 \text{ s}^{-2} & 0 \text{ Nm rad s}^{-1} \\ 0 \text{ A Nm} & 0 \text{ A Nm} & 0 \text{ Nm rad s}^{-1} & 1 (\text{Nm})^2 \end{bmatrix} \quad (6.26)$$

Therefore, only $\mathbf{Q}_{\text{EKF},0}$ and $\mathbf{R}_{\text{EKF},0}$ must be optimized by the GA, resulting in the five-dimensional optimization problem. The optimized covariance matrices were determined to be:

$$\mathbf{R}_{\text{EKF},0} = 0.625 \text{ rad}^2 \text{ s}^{-2} \quad (6.27)$$

$$\mathbf{Q}_{\text{EKF},0} = \begin{bmatrix} 0.75 \text{ A}^2 & 0 \text{ A}^2 & 0 \text{ A rad s}^{-1} & 0 \text{ A Nm} \\ 0 \text{ A}^2 & 0.81 \text{ A}^2 & 0 \text{ A rad s}^{-1} & 0 \text{ A Nm} \\ 0 \text{ A rad s}^{-1} & 0 \text{ A rad s}^{-1} & 2.50 \text{ rad}^2 \text{ s}^{-2} & 0 \text{ Nm rad s}^{-1} \\ 0 \text{ A Nm} & 0 \text{ A Nm} & 0 \text{ Nm rad s}^{-1} & 1.50 (\text{Nm})^2 \end{bmatrix} \quad (6.28)$$

A high value can be interpreted as low trust in the model or measurement. A low value consequently indicates high confidence. $\mathbf{Q}_{\text{EKF},0}$ has only eigenvalues greater than zero and is positive definite ($\mathbf{x}^\top \mathbf{Q}_{\text{EKF},0} \mathbf{x} > 0, \forall \mathbf{x} \in \mathbb{R}^4$). This property is in accordance with the general positive (semi) definiteness of covariance matrices [110, p. 1454] and confirms the optimization to be meaningful.

The simulation-aided optimization has several benefits and enables a conceptual procedure always aimed for in engineering. The time-consuming, manually conducted search (many dimensions and tuning possibilities) for a stable setting is not required. Furthermore, the actual system is not burdened with the risk of unstable operation, which risks the destruction of components. The possibility of finding the global minima of the cost function is greater than when tuning manually as more settings can be tested by the GA.

6.4 Empirical verification

The following section presents the measurement results of the EKF-based current sensorless control scheme. The functionality and reliability of the estimation are investigated by different tests. Besides the demonstration of functionality and reliability, the tests aim to determine the achievable accuracy required for implementing the sensor fault detection. Furthermore, a stability assessment of the method in deep magnetic saturation is required due to the use of current-dependent parameters (inductances, flux linkages). The current-dependent parameters of the EKF algorithm are estimations when operating current sensorless. The estimated parameters might lead to a similar stability issue (convergence issue), as it appeared for some of the encoderless control algorithms. The EKF algorithm is executed in Task 3 (Fig. 3.3) in parallel with the DC-link voltage estimator. The matrix operations are carried out element-wise to avoid computing the terms where multiplications with zero are contained.

All tests are conducted in current control mode, except one, which is performed in speed control mode to demonstrate the speed tracking performance. The current control mode is primarily chosen because it is more challenging, which becomes clear when interpreting the results. During speed control mode, the settings of the speed controller are the same as for encoderless control. The gain factors remain at $g_{p,n} = 0.1 \text{ Nm s rad}^{-1}$ and $g_{i,n} = 0.5 \text{ Nm rad}^{-1}$. The speed controller setting remains to ensure stability in the event of an encoder failure, resulting in a limited bandwidth of the speed control loop for all estimation methods. This could be improved by adapting the speed controller, dependent on the fault scenario. However, for simplicity this is

not implemented within the present work. Instead, the slowest required speed controller setting (encoderless control) is used for all other sensorless methods.

The current control loop time constants of the first-order elements (time constant of the machine is compensated operating-point-dependent [3, p. 933]) are adapted to $\tau_{cc} = 4$ ms for each axis. This is done with respect to the current-sensor-fault-detection proposed later, which requires a lower current controller bandwidth. However, it was experienced that the current sensorless control also works reliable with a time constant of $\tau_{cc} = 2$ ms.

Besides the currents, the **EKF** also estimates the rotor speed and load torque. However, the estimations of speed and load torque are not of interest and are not presented in the following. The estimation errors of the currents are presented and are defined as follows.

$$\Delta i_d := \hat{i}_d - i_d \quad (6.29)$$

$$\Delta i_q := \hat{i}_q - i_q \quad (6.30)$$

Fig. 6.3 shows the measurement results during current sensorless speed control mode. The speed reference tracking is comparable to the operation with sensors. The d-axis current is estimated more precisely than the q-axis current, which shows larger deviations of mean value and ripple when the rotor is rotating. The noise on the actual q-axis current can be explained by higher harmonics in the inductances, which are not considered in the state-space model. Hence, the **EKF** provides no current feedback related to higher harmonics as they appear in the actual machine. The neglect of higher harmonics leads subsequently to a current ripple in the actual currents.

At the beginning of this subsection, it was mentioned that the current control mode is more challenging than the speed control mode. This is because the speed control mode takes advantage of the angular velocity as additional feedback, which affects the current controllers via the speed controller. The speed controller adjusts the reference torque when the reference speed is not met due to torque deviations caused by current estimation errors. This explains the good speed-tracking without current sensors.

The advantage of speed control mode implies that current control mode is more challenging when operating current sensorless. In the current control mode, the feedback via the speed controller is not available and, hence, the estimation error-dependent adjustment of the reference torque omits. Therefore, the following tests are conducted in the more challenging current control mode.

Fig. 6.4 shows the test results for constant reference currents (torques) while the load

machine targets a particular speed profile. The d-axis current is estimated slightly more accurately than the q-axis current. The increased noise content in the estimation errors from Fig. 6.4 a) to Fig. 6.4 b) is due to higher harmonics in the actual inductances. The higher harmonics in the inductances become more intensive if the machine is saturated²⁸, leading to larger deviations in the model. However, the deviations are in an acceptable range with a maximum absolute deviation of about $\Delta \|\mathbf{i}_s^r\| = 0.55 \text{ A}$ ²⁹. Most important is that the measurements attest to a general stable behavior of the method.

Fig. 6.5 shows the measurements during a reference current step while the rotor of the machine is locked. The reference currents are calculated from a reference torque step to nominal torque. The test is conducted for two different rotor positions of $\theta_{el} = 0^\circ$ and $\theta_{el} = 90^\circ$. The settling times are in the expected range for the settings of the current control loops ($\tau_{cc} = 4 \text{ ms}$). The step response of the d-axis current follows that of a first-order element accurately. The shape of the q-axis step response deviates more from that expectation, which seems to be caused by a mechanical oscillation as the frequency is the same as in the measured torque. The oscillation in the measured torque signals is mainly due to the imperfectly stiff locking of the rotor and also appears with sensors. However, this effect was not further investigated. In general, the d-axis current shows minor deviations between the two rotor positions compared to the results of the q-axis current. This confirms the results from the previous tests, where the q-axis estimation was more rotor-position-dependent. However, the main aim of the current control loop is to achieve a mechanical torque close to the reference value. This aim is achieved very well for both rotor positions when the torque is in a steady state. The deviations in this test are again in an acceptable range with a maximum absolute deviation of about $\Delta \|\mathbf{i}_s^r\| = 0.36 \text{ A}$ (conforms $\pm 6\%$) in steady-state. The measurements attest to a general stable behavior of the method.

The results of the last test are depicted in Fig. 6.6. It shows the measurements during a ramp-shaped increase of the reference torque. This test is conducted to verify the stability of the method in deep magnetic saturation. A convergence issue as it was investigated for encoderless control is possible since the EKF also relies on estimated parameters (inductances, flux linkages) in closed loop operation. However, Fig. 6.6 shows that the convergence issue does not appear. The current sensorless scheme re-

²⁸The stator-fixed harmonic anisotropy caused by the winding arrangement becomes more intensive. The saturated stator teeth of the machine also have a slight impact.

²⁹The absolute deviation is defined as $\Delta \|\mathbf{i}_s^r\| := \sqrt{\Delta i_d^2 + \Delta i_q^2}$.

mains stable up to more than four-times rated torque with a minimum accuracy of about 5%.

The empirical verifications of this chapter confirmed the functionality and reliability of the [EKF](#)-based current sensorless control scheme. The control behaved stable across all the tests with acceptable accuracy. The absolute maximum deviations are in the range of $\Delta \|\hat{\mathbf{i}}_s^i\| = 0.7 \text{ A}$ (this conforms about $\pm 7\%$ ([Fig. 6.6](#))), which must be considered when implementing the sensor fault detection.

This chapter closes with some remarks regarding possible improvements. There are several possibilities to enhance the accuracy of the estimator. The Jacobian matrix of the system vector function was simplified to guarantee that it is executable on the microcontroller. The full Jacobian is expected to increase the accuracy. Another improvement could be an extended model of the [VSI](#) voltage drop, which was approximated by a simple Fourier expansion ([6.20](#)). The most significant improvement might be achieved by taking higher harmonics into account. An entirely different possibility is to test a different observer type, which might enhance the current estimation performance further. The unscented Kalman filter [[106](#), p. 36] might be appropriate as it does not rely on a linearization of the state-space model. Hence, the issue of differentiability omits, which allows for more flexibility when choosing the state-space model.

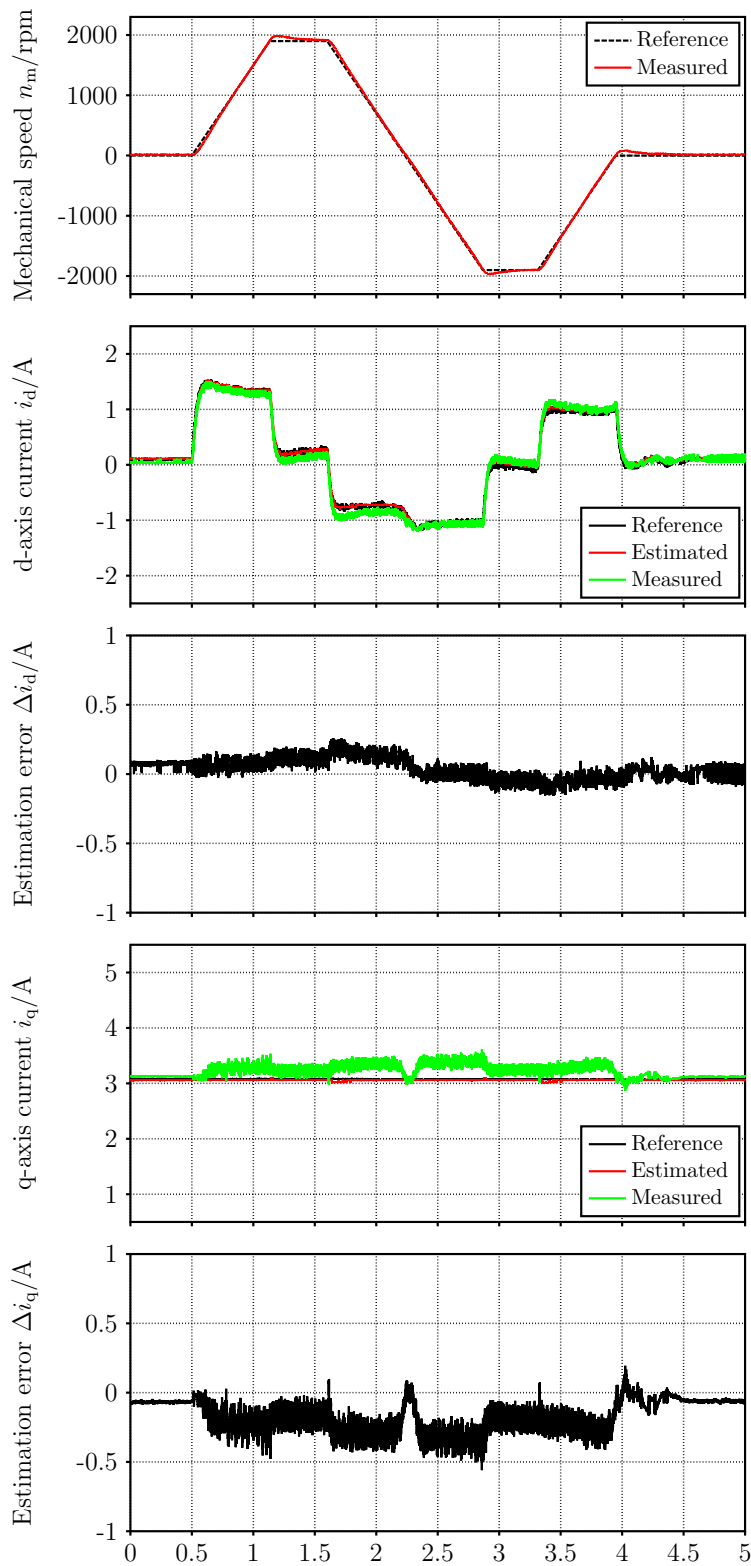
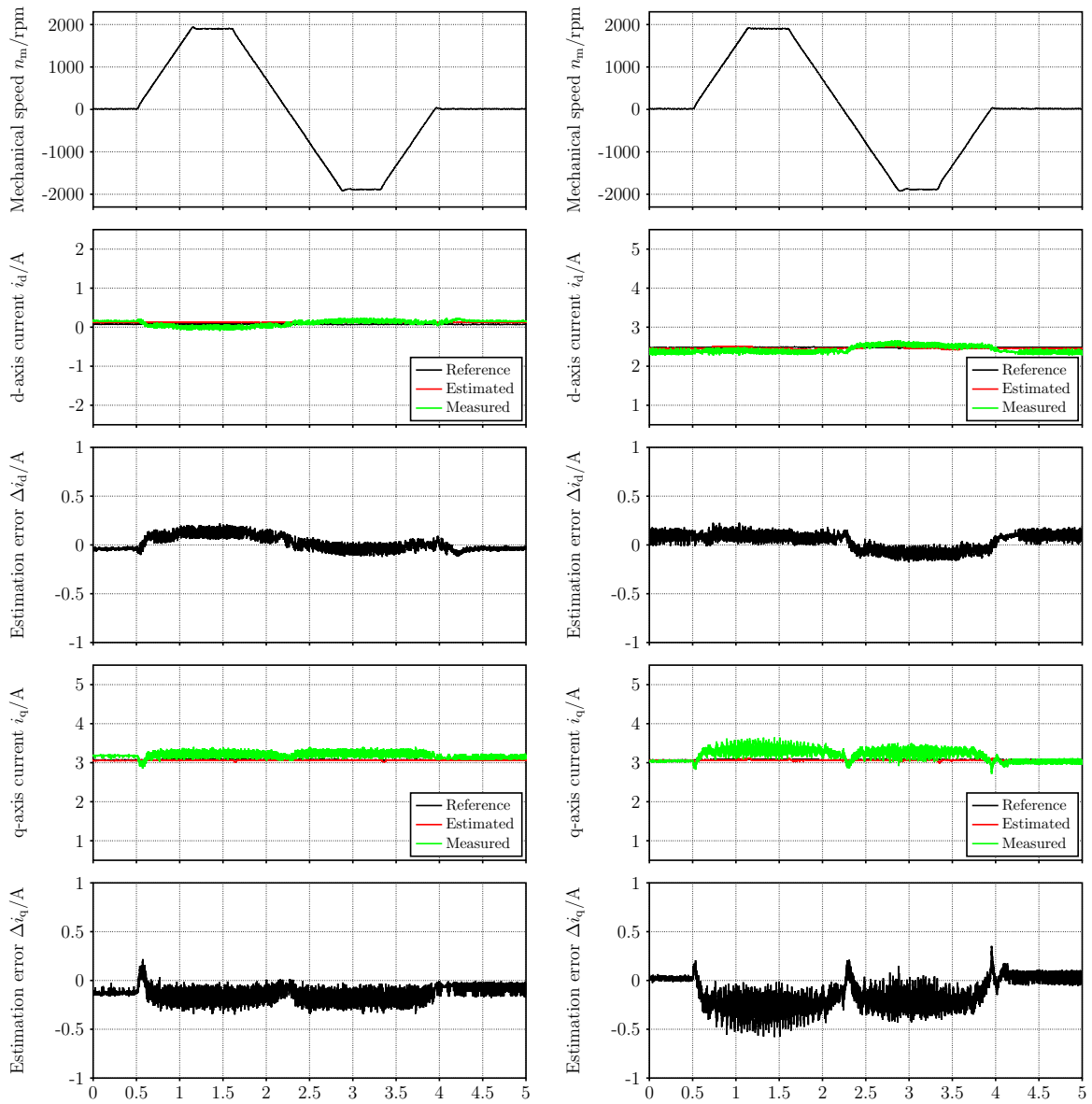


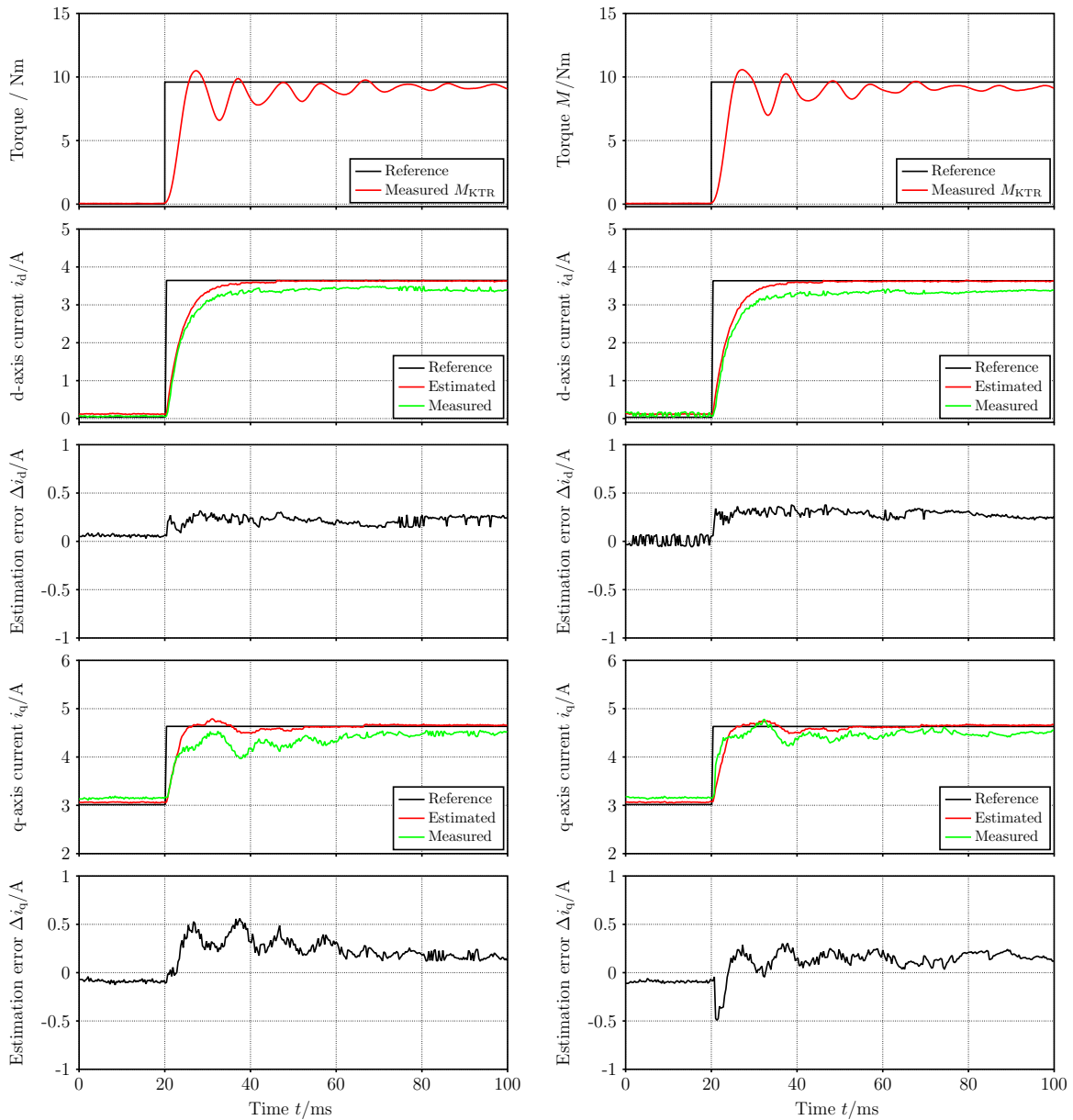
Figure 6.3: Current sensorless speed tracking performance.



a) At zero reference torque.

b) At a reference torque of 4 Nm.

Figure 6.4: Current sensorless current control during constant reference currents and changing speeds.



a) At rotor position $\theta_{el} = 0^\circ$.

b) At rotor position $\theta_{el} = 90^\circ$.

Figure 6.5: Current sensorless current step response to nominal torque.

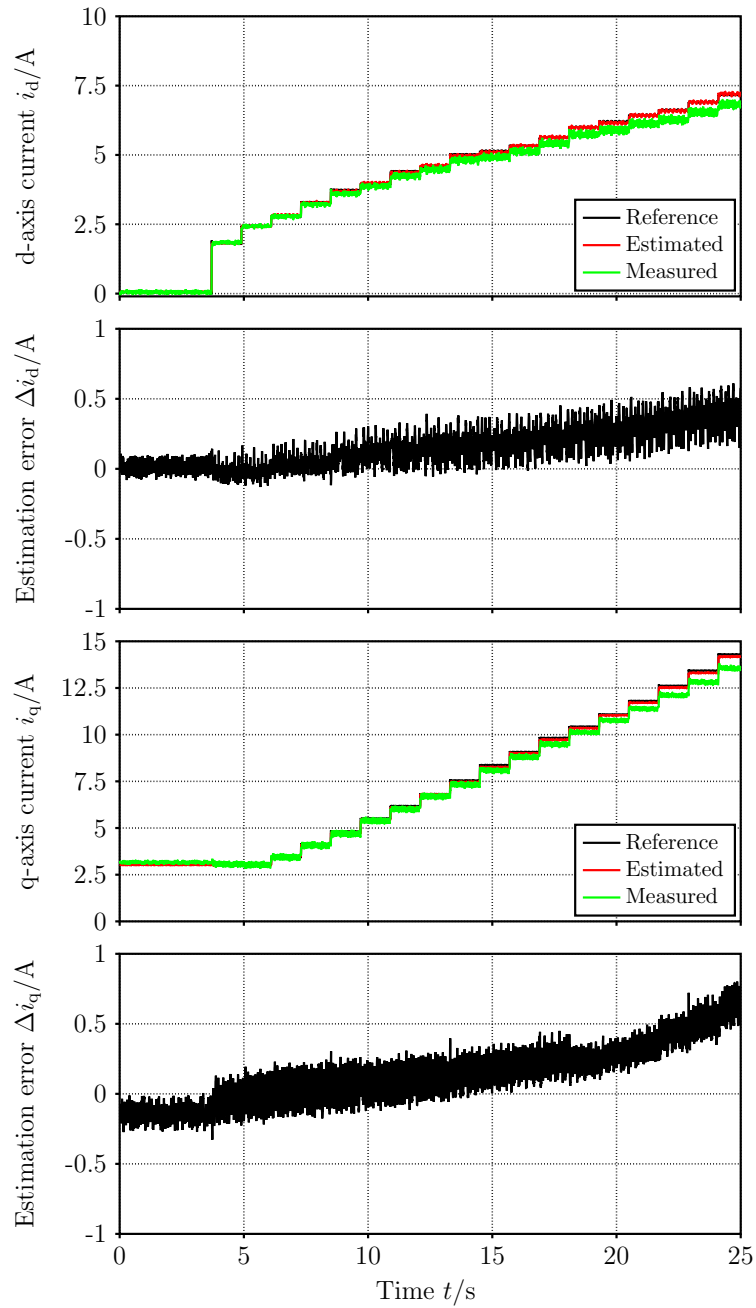


Figure 6.6: Stability investigation in deep magnetic saturation up to 40 Nm.

Chapter 7

Sensor fault-tolerant control approach

The previous chapters were dedicated to different sensorless control algorithms used to estimate the most important sensor data of the drive system. The algorithms were developed with the aim of detecting sensor faults³⁰ and then backing them up to increase the reliability of the drive system.

The number of possible sensor fault scenarios in a drive system is comprehensive as each sensor can fail in different ways. Considering the incremental encoder, for example, all three signals (A, B, and Z) can be affected by a fault. However, it is also possible that only one of the three signals is faulty. Thus, each fault scenario has a different effect on the drive system with a specific signal pattern and needs special attention in the fault detection algorithm. Not all of these possible fault scenarios can be discussed within this dissertation. This work primarily aims to propose reliable sensorless algorithms that can be employed for a sensor fault-tolerant control, whereas the actual detection is less in focus. However, this chapter demonstrates that the provided sensorless algorithms are very effective for sensor fault-tolerant control using a deterministic fault detection approach. This fault-tolerant approach does not aim to work for all possible fault scenarios but demonstrates the functionality of the sensorless algorithms for this application.

Without additional hardware installed for sensor fault-tolerant control, it is not possible to detect and back up multiple sensor fault categories³¹ simultaneously. Each

³⁰The terminology “sensor fault” is vicariously used for a measurement feedback fault in the following.

³¹The three sensor fault categories are incremental encoder fault, DC-link voltage sensor fault, and current sensor faults.

sensorless algorithm relies on two categories of sensors to estimate the signal of the third, which leads to this limitation. Hence, either the encoder, the DC-link voltage sensor, or the current sensors are assumed to fail but not two of these sensor categories at the same time. More than one sensor category failure could only be managed with additional hardware, which is to be avoided within the present work. Furthermore, it is assumed that no other possible fault scenario, e.g., an interrupted phase, is present so that only sensor faults are considered. The sensor fault scenario will be emulated by disconnecting the supply voltages of the sensors. The supply-voltage disconnections do not lead to a sudden change in the measured sensor signals, which are detectable comparably easy, but to a nonpredictable pattern in the measured sensor outputs. Such a fault scenario is more realistic and more difficult to interpret by the fault detection than an idealized software emulated fault.

The idea of a sensor fault-tolerant control is not novel; research has been conducted for about 20 years by a small number of researchers. Thus, it has not been investigated by a broad community as is the case for encoderless control. Fault-tolerant control algorithms rely on a fault detection structure. These fault detection algorithms are commonly categorized into two categories [111], signal-based and model-based. Signal-based methods try to identify a fault using the sensor signal itself. Model-based approaches estimate the sensor signals based on a model running on a control unit. The estimations are compared to the measured sensor signals to identify a sensor fault. Both categories are commonly applied separately and not in conjunction.

Many sensor fault-tolerant-related works are dedicated to IMs. The dissertation [112] gives a good overview of the topic with respect to IMs. The authors of [113, 114, 115, 116] considered only individual sensor faults in their implementation for IMs, but not all sensor fault categories simultaneously. In [117], all sensor fault categories are detected and isolated. However, no estimation of the sensor data is provided, which could be used to back up the control. The authors of [118] proposed a more advanced solution for the detection and compensation by providing estimations as well. However, their fault detection is based on a direct comparison between measurement and estimation, constituting a purely model-based approach. Such model-based methods for sensor fault detection should be treated with caution due to cross-interference [112, p. 16]. This effect is briefly demonstrated later and shows that purely model-based detections are ambiguous. The works mentioned in this paragraph are with respect to IMs, which differ significantly from RSMs in terms of the fundamental operating principle. Thus, the sensor data estimation approaches for IMs are not suitable for RSMs and SMs in general.

The authors of [119, 120] proposed methods for single sensor faults in **SMs**. In the case of [119, 120], they are either speed or current sensor faults. In [119], only speed sensor faults are considered and compensated with a so-called **EMF**-based encoderless method. However, the low-speed region of the machine is not taken into account. The current sensor fault detection of [120] is a purely signal-based approach without an estimation scheme and compensation structure. Hence, current sensor faults can only be detected but not compensated.

In [121], a sensor fault-tolerant control for a **PMSM** is proposed, intended for all sensor fault categories. The estimations are based on a sliding mode observer using a linear state-space model. The estimation of the encoder signals is based on the **EMF** and is not suitable around zero-speed. Furthermore, the **DC**-link voltage is not estimated, which allows no compensation of **DC**-link voltage sensor faults. Their sensor fault detection only employs the difference between measurement and estimation to detect a fault (model-based approach). Such a detection approach is fault-prone due to the mentioned effect of cross-interference. The functionality of the detection algorithm is tested by a sudden change of the measured signals in the software before feeding it to the fault detection. This is a less realistic scenario and comparably easy to detect due to the distinct change in the signals.

The approach of [91] is proposed for all sensor categories and was one of the first for **SMs** with a focus on **IPMSMs**. The approach has several limitations. The current sensor fault detection relies on interruption of the normal operation mode for about 25 ms and does not function continuously. Therefore, the current sensors are only tested at startup. This is a big drawback since faults might also appear during operation. The detection of a **DC**-link voltage sensor fault is based on a power balance calculation, which is not reliably working at low speeds and light loads due to a low **SNR**.

The authors of [122] proposed an **EKF**-based approach for the sensor fault detection in **IPMSMs**. Current and encoder signals are estimated. The approach does not provide a **DC**-link voltage estimation and detects such a fault with the measured and estimated current and encoder signals. However, the signal estimation of the encoder constitutes an **EMF**-based method, which does not work in the low-speed region. The fault indication signals require low-pass filtering (time constants of about 50 ms), which significantly delays detection. Furthermore, the effect of magnetic saturation is simplified in their underlying model, making this approach less appropriate if the machine is operated in deep magnetic saturation. Their overall sensor fault detection employs the difference between measurement and estimation (model-based approach). Again, such a detection approach is subject to cross-interference and does not pro-

vide an unambiguous detection. Also, here, the sensor faults were emulated by an instantaneous change of the sensor signals in the software, which does not constitute a realistic scenario. In conclusion, the control performance is quite limited compared to sensor-based control performance due to the simple estimation methods.

In [123], a sensor fault-tolerant control for a dual three-phase PMSM is proposed. A DC-link voltage sensor fault is detected by calculating the difference between two consecutive measurements. If the difference exceeds a certain threshold in a certain time, it is interpreted as a DC-link voltage sensor fault. However, this approach might be unreliable if the measured DC-link voltage fades out slowly after a fault. Only the speed signal is considered in the fault detection; the rotor position is neglected. The angular velocity of the flux linkage vector is equated to the rotor speed and used for the estimation. This speed estimation is expected to be inaccurate during current transients. A speed sensor fault is determined by comparing the speed estimation with the sensor signal (model-based approach). However, since the flux linkage estimation relies on the current measurements, this detection is not unambiguous.

The authors of [124] proposed a sliding-mode-observer-based approach for the sensor fault detection in five-phase PMSMs. The approach concerns current and speed sensor faults without addressing the position signal. However, most drive systems rely on a single sensor to measure rotor speed and position. Hence, it is not appropriate to assume that the position signal is faultless in the event of a speed sensor fault. The approach does not address DC-link voltage sensor faults, and the speed estimation approach constitutes a so-called EMF-based method, not appropriate around zero speed. Hence, the operation in the low-speed region is not ensured during a fault. The actual fault detection algorithm constitutes a purely model-based method, which is fault-prone due to the effect of cross-interference. The method is verified by simulation results with a step-shaped modification of the sensor signals in the software, which is a less realistic scenario.

For existing fault-tolerant control approaches, it can be concluded that the fault detection methods for SMs suffer several drawbacks, which can be briefly summarized as follows. Altogether, the approaches do not provide estimations of all sensor signals, and the ones that are provided are not capable of working at all possible operating points of the machine. However, this is required to achieve the highest possible functional safety of the drive system. For example, encoder faults cannot be backed up in deep magnetic saturation due to the use of conventional injection-based encoderless methods, as explained in Subsection 4.2.3. Furthermore, almost all approaches use EMF-based encoderless control only. Hence, detection and back up are not possible in the low-

speed region anyway. No appropriate DC-link voltage estimation scheme is provided, which could be used to compensate for DC-link voltage sensor faults. Furthermore, the approaches do not combine signal-based and model-based fault detection, which could enhance the reliability of the algorithm. Instead, measured and estimated signals are compared and directly used for detection (only model-based). Hence, the detections are subject to cross-interference and, subsequently, ambiguity. The empirical tests of existing detection methods were almost solely carried out by a sudden change of the measured signal in the software to emulate a sensor fault. However, this test scenario is different from a real sensor fault and less conclusive, therefore.

In general, the existing detection methods aimed to compensate for the simplified estimation methods with more comprehensive fault detection algorithms. Hence, the control performance after a detected fault is not comparable to that with sensors. The approach of the present work is different. This work aims to take advantage of the good estimation methods achieving better control performance and more reliable fault detection with less effort for the actual fault detection.

The estimation methods introduced in the previous chapters enable opportunities for improving fault-tolerant control. All signals can be estimated with reasonable accuracy in all possible operating conditions. This allows for the compensation for any sensor faults at any time, which is not possible with existing methods. The estimation methods also have the advantage that a combination of signal-based and model-based fault detection is always possible, resulting in more reliable detection. Furthermore, the machine can be operated with comparably high performance after detecting a sensor fault. These benefits from the estimation methods are taken advantage of in the following by proposing a simple but effective deterministic fault detection method.

The fault detection approach requires a distinction between the measured, possibly fault-affected, sensor signals $\theta_{\text{el,sens.}} \in \mathbb{R}$, $u_{\text{DC,sens.}} \in \mathbb{R}$, $\mathbf{i}_{\text{s,sens.}}^t \in \mathbb{R}^3$ and the estimations of the sensor signals $\hat{\theta}_{\text{el}} = \theta_{\text{el,PII}}$, \hat{u}_{DC} , $\hat{\mathbf{i}}_{\text{s}}^t$ from the sensorless algorithms depicted in Fig. 4.19, Fig. 5.2, and Algorithm 1. Whereas the estimated currents of the two-phase rotor fixed reference frame are transformed into three-phase stator fixed coordinates (7.1) before using them in the detection algorithm.

$$\hat{\mathbf{i}}_{\text{s}}^t := \mathbf{C}^+ \mathbf{P}^{-1} \hat{\mathbf{i}}_{\text{s}}^r \quad (7.1)$$

The three-phase stator fixed coordinates of the currents are useful to assign a detected current sensor fault to a specific current sensor.

From the incremental encoder, only the position signal is used for detection due

to the following. First, only the rotor position signal relies on all three incremental encoder signals (A, B, and Z). Thus, it is affected by each of the three possible signal faults. The measured speed signal relies on signals A and B, only. Secondly, the rotor position signal changes faster, except at a standstill, allowing faster fault detection than the speed signal.

The comparisons between estimations and measurements are a first possible fault indicator and are called the residua³². They are defined as follows.

$$\Delta\theta_{\text{el}} := \hat{\theta}_{\text{el}} - \theta_{\text{el,sens.}} \quad (7.2)$$

$$\Delta u_{\text{DC}} := \hat{u}_{\text{DC}} - u_{\text{DC,sens.}} \quad (7.3)$$

$$\Delta \mathbf{i}_{\text{s}}^{\text{t}} := \hat{\mathbf{i}}_{\text{s}}^{\text{t}} - \mathbf{i}_{\text{s,sens.}}^{\text{t}} \quad (7.4)$$

The fault detection algorithm uses the absolute values of these residua, which are defined and denoted next.

$$\mathcal{E}_{\theta_{\text{el}}} := |\Delta\theta_{\text{el}}| \quad (7.5)$$

$$\mathcal{E}_{u_{\text{DC}}} := |\Delta u_{\text{DC}}| \quad (7.6)$$

$$\mathcal{E}_{\mathbf{i}_{\text{abc}}} := \|\Delta \mathbf{i}_{\text{s}}^{\text{t}}\| = \sqrt{(\hat{i}_{\text{a}} - i_{\text{a,sens.}})^2 + (\hat{i}_{\text{b}} - i_{\text{b,sens.}})^2 + (\hat{i}_{\text{c}} - i_{\text{c,sens.}})^2} \quad (7.7)$$

These three absolute residua are a central element of fault detection. It seems evident to use these residua without additional information to detect a sensor fault. However, this is not recommended due to the mentioned effect of cross-interference, which is briefly demonstrated in the following section.

7.1 The ambiguity of residua

The impact of sensor deviations on $\mathcal{E}_{\theta_{\text{el}}}$, $\mathcal{E}_{u_{\text{DC}}}$, and $\mathcal{E}_{\mathbf{i}_{\text{abc}}}$ is briefly investigated in this section. It will be demonstrated why not to use the residua without additional information from the sensors for fault detection. The related issue is known as the mentioned effect of cross-interference [112, p. 16].

A test procedure is conducted for the investigation and is performed as follows. A constant value (deviation) is added to the sensor signals while operating sensor-based. Hence, the sensor signals plus the added deviation are used in the control, for the

³²The term residuum is common in sensor fault-tolerant related literature. It describes a sensor fault indicator based on a deviation between the measurements and estimations [112, p. 10].

estimations, and the calculation of $\mathcal{E}_{\theta_{el}}$, $\mathcal{E}_{u_{DC}}$, and $\mathcal{E}_{i_{abc}}$. The constant value added is varied over a certain range for each sensor category and the absolute residua are recorded throughout. This is repeated at different speeds to take the speed dependency of the hybrid estimation methods into account. The mean values of $\bar{\mathcal{E}}_{\theta_{el}}$, $\bar{\mathcal{E}}_{u_{DC}}$, and $\bar{\mathcal{E}}_{i_{abc}}$ are determined over one electrical period (except at a standstill) for each measurement.

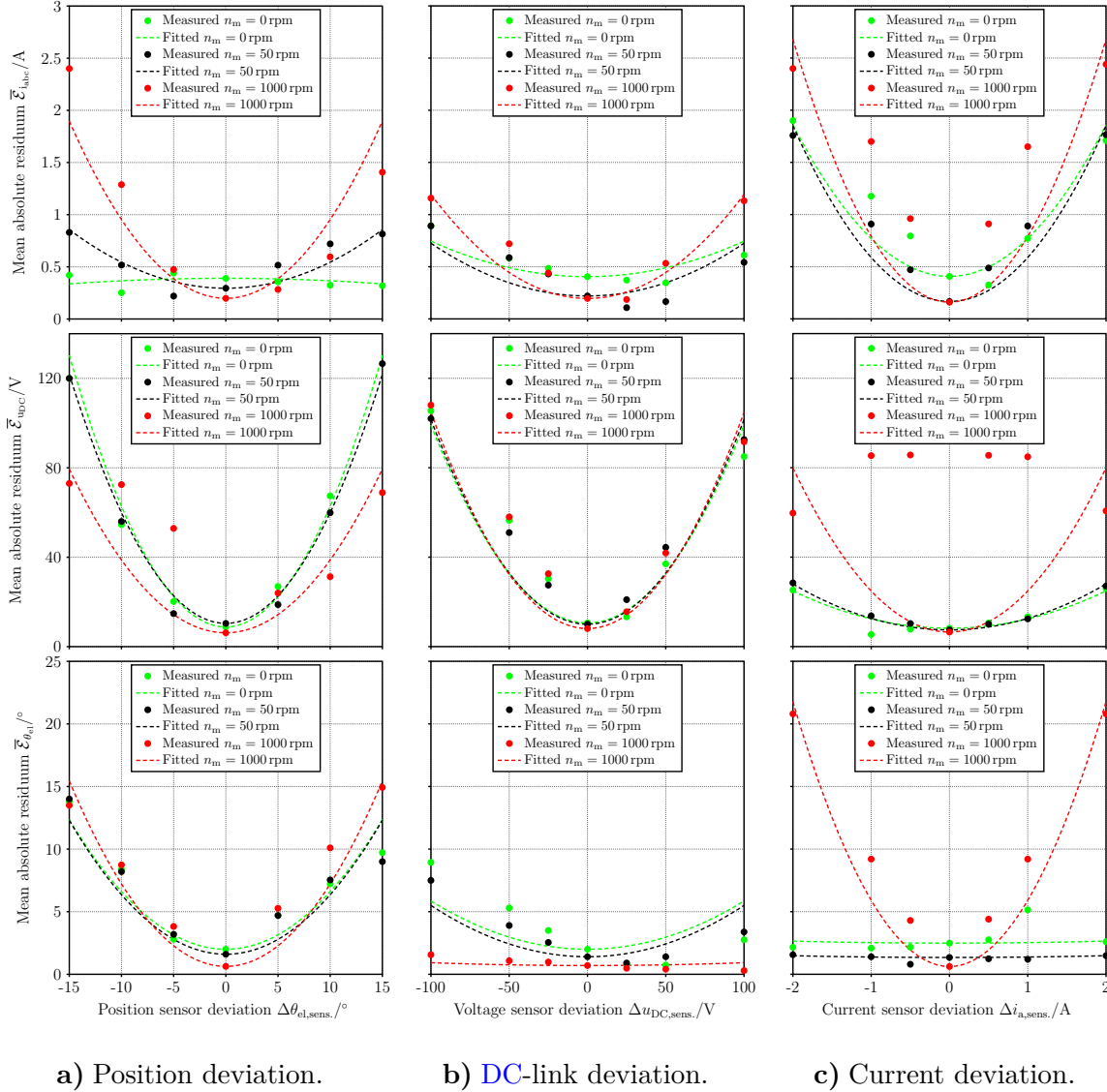


Figure 7.1: Effect of sensor deviations on the absolute mean residua.

For the current sensor category, the constant deviation $\Delta i_{a,sens.}$ is added vicariously to the measured current signal of phase a ($i_{a,sens.} + \Delta i_{a,sens.}$). In the case of the encoder, the constant deviation $\Delta \theta_{el,sens.}$ is added to the measured rotor position ($\theta_{el,sens.} + \Delta \theta_{el,sens.}$). The deviation $\Delta u_{DC,sens.}$ is added to the measured DC-link voltage

$(u_{\text{DC,sens.}} + \Delta u_{\text{DC,sens.}})$. The results are depicted in Fig. 7.1. A quadratic fit is included to indicate the tendency of $\bar{\mathcal{E}}_{\theta_{\text{el}}}$, $\bar{\mathcal{E}}_{u_{\text{DC}}}$, and $\bar{\mathcal{E}}_{i_{\text{abc}}}$ over the introduced deviations.

The comparison of the different quadratic fits reveals no (general holding across all speeds) absolutely unambiguous pattern in the absolute residua $\mathcal{E}_{\theta_{\text{el}}}$, $\mathcal{E}_{u_{\text{DC}}}$, and $\mathcal{E}_{i_{\text{abc}}}$ for each sensor deviation. Hence, these residua alone are not reliable indicators, which is caused by the following. Each sensorless method relies on two sensor categories to estimate the signals of the third category, which are then compared with the respective measured signals to achieve $\mathcal{E}_{\theta_{\text{el}}}$, $\mathcal{E}_{u_{\text{DC}}}$, or $\mathcal{E}_{i_{\text{abc}}}$. Hence, the deviation can be caused by each of the three sensor categories involved in the determination of the residua. It is, hence, important to verify the model-based detection with a signal-based approach.

7.2 Hybrid sensor fault detection

The approach presented in the following combines both detection categories, signal-based and model-based [111], which are commonly used independently. Due to the use of both detection categories, the approach is called hybrid sensor fault detection. The hybrid method helps to detect a sensor fault more reliably as both information can be verified against each other. When using fault detection, there is always the possibility that a fault is detected despite the system being healthy, or the wrong kind of fault is detected. Both scenarios decrease the reliability of the overall control and must be strictly avoided. The fusion of both fault detection categories, signal-based and model-based, decreases the probability of such an unintended scenario.

The hybrid fault detection of this work relies on the provided estimation methods. To avoid incorrect fault detection, the maximum estimation errors must be considered when setting fault indication thresholds. The maximum estimation errors during the empirical verifications were about $\pm 10^\circ$ for encoderless control, about $\pm 11\%$ relative error or roughly ± 60 V for DC-link-voltage-sensorless control, and about ± 0.7 A ($\pm 7\%$) for current sensorless control. These maximum deviations are taken into account in the sensor fault detection algorithm. The pseudo-code of the sensor fault detection is shown in Algorithm 2 and is explained in the following.

The detection of a DC-link voltage sensor fault is performed as follows. If the absolute deviation between the measurement and estimation $\mathcal{E}_{u_{\text{DC}}}$ exceeds a certain threshold $\mathcal{T}_{1,u_{\text{DC}}}$ and the measured signal $u_{\text{DC,sens.}}$ drops below a second threshold $\mathcal{T}_{2,u_{\text{DC}}}$ simultaneously, a DC-link voltage sensor fault is assumed. In this case, the sensor fault indication flag $\mathcal{F}_{\text{err}} \in \{0, 1, 2, 3\}$ is set to 3, and the control mode switches to DC-link-voltage-sensorless operation. Thereby, it is assumed that $u_{\text{DC,sens.}}$ drops during

the sensor fault. Here, the exceedance of the threshold by the residuum (model-based) is cross-checked with the sensor signal (signal-based). The detection approaches for the other sensor categories follow this example.

The detection of a current sensor fault is conducted as follows. If the absolute deviation between measurement and estimation $\mathcal{E}_{i_{abc}}$ exceeds a certain threshold $\mathcal{T}_{1,i_{abc}}$ and the sum of the three measured phase currents $i_{a,sens.} + i_{b,sens.} + i_{c,sens.}$ exceeds a second threshold $\mathcal{T}_{2,i_{abc}}$ simultaneously, a current sensor fault is assumed. In this case, the sensor fault indication flag \mathcal{F}_{err} is set to 2, and the control mode switches to current sensorless operation. This detection employs Kirchhoff's current law, which is applied to the circuitry of Fig. 2.2. The sum of the three currents must be zero in the idealized case, which is not fulfilled (at least in the beginning) in the event of current sensor faults (except zero current).

The detection of an incremental encoder fault works as follows. If the absolute deviation between the measurement and estimation $\mathcal{E}_{\theta_{el}}$ exceeds a certain threshold $\mathcal{T}_{\theta_{el}}$ and the difference between two consecutive measurements $\theta_{el,sens.}[n] - \theta_{el,sens.}[n-1]$ is equal to zero simultaneously, an encoder fault is assumed. In this case, the sensor fault indication flag \mathcal{F}_{err} is set to 1, and the control mode switches to encoderless operation. Thereby, it is employed that the signals of the incremental encoder (A, B, and Z) drop to zero in the event of a supply voltage fault, resulting in a frozen position signal. In conclusion, the encoder fault detection completely relies on $\mathcal{E}_{\theta_{el}}$ and its threshold at a standstill (purely model-based). However, the measured information (signal-based approach) comes into play once the rotor is rotating.

The thresholds, which are compared with the residua are set to $\mathcal{T}_{\theta_{el}} = 17^\circ$, $\mathcal{T}_{1,i_{abc}} = 2 \text{ A}$, and $\mathcal{T}_{1,u_{DC}} = 100 \text{ V}$. Thus, they are in the range of two times the maximum estimation errors. The remaining two thresholds for the signal-based verification were set to $\mathcal{T}_{2,i_{abc}} = 0.5 \text{ A}$, and $\mathcal{T}_{2,u_{DC}} = 480 \text{ V}$. The value of 480 V was chosen due to the B6 rectifier, in which the instantaneous value of the DC-link voltage can go down to about 488 V³³.

As mentioned at the beginning of this chapter, the aim of this work is to provide reliable sensorless control algorithms for sensor fault detection purposes. The actual sensor fault detection is less in focus and only included to demonstrate future possibilities using the proposed estimators. Hence, the thresholds were set intuitively without further investigations and not all possible fault scenarios are considered.

³³This applies in ideal European grid voltage conditions. Actually, the magnitudes of the grid voltages are allowed to vary 10%.

Algorithm 2: Sensor fault detection pseudo-code

```

1  $\mathcal{F}_{\text{err}} = 0$ ; // Initialize sensor fault detection flag
2 while  $\mathcal{F}_{\text{err}} = 0$  do
3   if  $\mathcal{E}_{\theta_{\text{el}}} > \mathcal{T}_{\theta_{\text{el}}}$  and  $(\theta_{\text{el,sens.}}[n] - \theta_{\text{el,sens.}}[n-1]) = 0$  then
4      $\mathcal{F}_{\text{err}} = 1$ ; // Set sensor fault detection flag for encoder fault
5     Switch to encoderless operation;
6   else if  $\mathcal{E}_{i_{\text{abc}}} > \mathcal{T}_{1,i_{\text{abc}}}$  and  $(i_{\text{a,sens.}} + i_{\text{b,sens.}} + i_{\text{c,sens.}}) > \mathcal{T}_{2,i_{\text{abc}}}$  then
7      $\mathcal{F}_{\text{err}} = 2$ ; // Set sensor fault detection flag for current sensor fault
8     Switch to current sensorless operation;
9   else if  $\mathcal{E}_{u_{\text{DC}}} > \mathcal{T}_{1,u_{\text{DC}}}$  and  $u_{\text{DC,sens.}} < \mathcal{T}_{2,u_{\text{DC}}}$  then
10     $\mathcal{F}_{\text{err}} = 3$ ; // Set sensor fault detection flag for DC-link voltage sensor
11    fault
12    Switch to DC-link-voltage-sensorless operation;
13   else
14     Continue operation with sensors; // No sensor fault detected
15   end if
16 end while

```

7.3 Empirical verification during supply voltage fault

The fault detection and compensation approach is verified within this section. The sensor fault is emulated by disconnecting the supply voltage of the sensors, which leads to an unpredictable pattern in the sensor outputs. Such a scenario is more realistic than emulating the sensor faults in the software. The disconnection of the supply voltage ends in a total fault of the specific sensor category.

All tests were conducted in the speed control mode of the test machine. The settings of the speed PI controller are oriented on the encoderless control algorithm and result, therefore, in a comparably low speed control bandwidth. The gain factors remain at $g_{p,n} = 0.1 \text{ Nm s rad}^{-1}$ and $g_{i,n} = 0.5 \text{ Nm rad}^{-1}$. Hence, a very fast adjustment of the speed is not expected. Each sensor fault category was investigated at low-speed and high-speed to ensure that the entire speed range is reliably covered by the hybrid sensorless methods. During all tests, the machine was loaded via the load machine with 4.5 Nm, which constitutes about 50% nominal torque.

Algorithm 2 is carried out in Task 1 (Fig. 3.3) and runs simultaneously to the FOC. Thus, the estimated sensor information from the different tasks are collected in Task 1 to feed the fault detection algorithm and to provide the estimations for the FOC.

There is one crucial circumstance to consider during the implementation. Each of the sensorless methods relies on model parameters, e.g., LUT-stored inductances. It is important that these parameters rely on their own estimations and not on the sensor data³⁴. Otherwise, the estimation is not independent of the sensor data. In this case, the fault detection will not work as intended, and no compensation by the sensorless algorithms is possible.

7.3.1 DC-link voltage sensor fault

The DC-link voltage sensor fault is investigated first. It is expected to be the least critical sensor fault as the impact on the currents is compensated automatically for if there is no large deviation in the signal. This is due to the current controllers, which adjust the reference voltages and duty cycles to meet the reference currents. This functions well as long as the measured faulty DC-link voltage does not deviate significantly from the actual signal.

For the test, the internal DC-link voltage measurement from the VSI (Fig. 3.2) is replaced by a differential probe shown in Fig. 7.2 a) as the internal measurement of the VSI is not accessible for mounting the fault emulating switch. Since each DC-link voltage measurement circuitry is slightly different, it is not falsifying to conduct the test with the differential probe. The fault detection algorithm must be adapted from system to system in any case. The schematic of the supply circuitry is shown in Fig. 7.2 b) for a better interpretation of the measurement results.

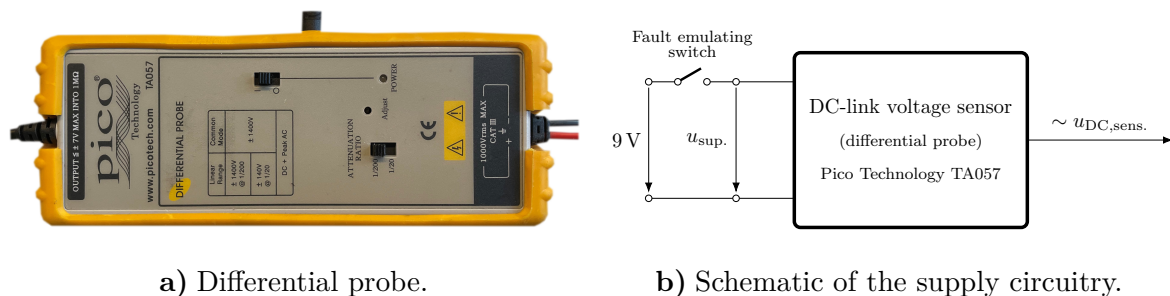
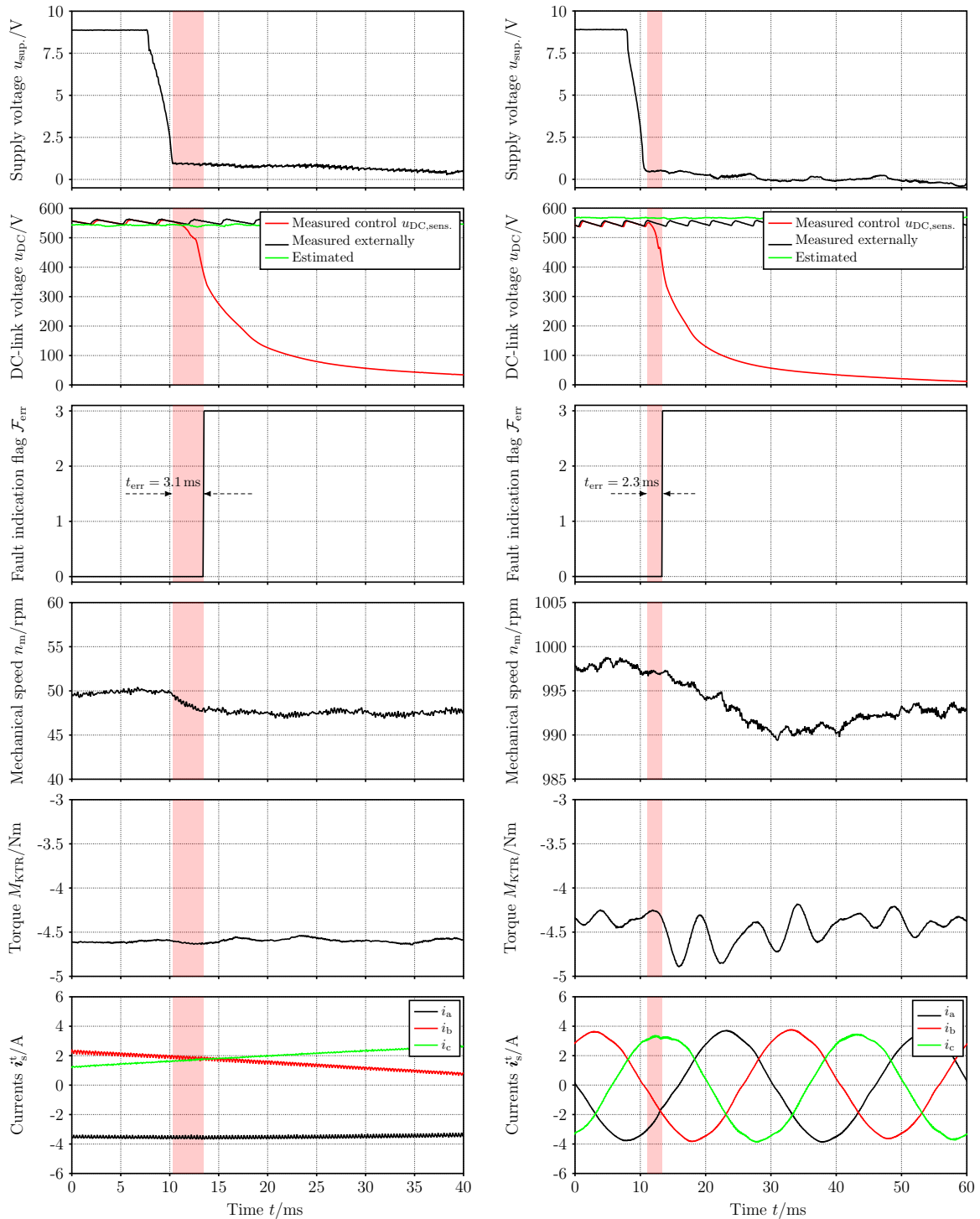


Figure 7.2: Overview of the DC-link voltage measurement.

The test results at different speeds are shown in Fig. 7.3. The time window t_{err} over which the fault affects the FOC is shaded in red. For the comparison with the estimation, the DC-link voltage is measured with a second external probe (depicted in black

³⁴For example, the LUTs used to store the inductances for current sensorless control must be fed with the estimated currents from the current sensorless control method.

in the respective plot).



a) At a speed of $n_m = 50$ rpm.

b) At a speed of $n_m = 1000$ rpm.

Figure 7.3: Fault detection and compensation during DC-link voltage sensor supply fault at about 50% nominal torque.

It can be noticed that the supply voltage fault does not immediately affect the sensor signal $u_{\text{DC},\text{sens.}}$. There is a certain delay due to energy storage inside the differential probe. Once the supply fault affects the sensor signal, the measurement drops exponentially and not step-shaped as emulated in many related publications. The time to detect the faults is fast and similar for both speeds with $t_{\text{err}} = 3.1$ ms and $t_{\text{err}} = 2.3$ ms. The speed and currents are only slightly affected by the fault for both measurements. However, the measured torque signal in Fig. 7.3 b) shows a stronger oscillation. The oscillation is caused by the mechanical coupling of the machines, which is briefly excited by the effect of the sensor fault. However, the fault detection and compensation work reliably, and the control capability can be maintained during the DC-link voltage sensor fault. It is important to mention that without such a compensation structure, all duty cycles would aspire to a value of one as the faulty DC-link voltage signal approaches zero. This would lead to a loss of the control capability of the machine. The tests were repeated several times, which confirmed the results above.

7.3.2 Incremental encoder fault

In the following section, the incremental encoder fault is investigated. Encoder faults are very critical and result quickly in the loss of the control capability without a compensation structure. The incremental encoder is supplied by the microcontroller board shown in Fig. 3.2. The schematic of the supply circuitry, including the fault emulating switch, is shown in Fig. 7.4.

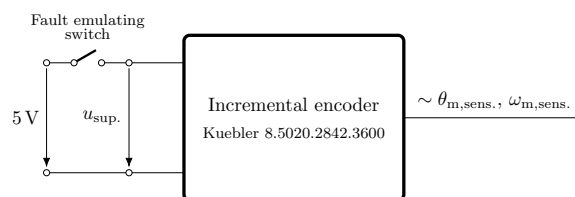
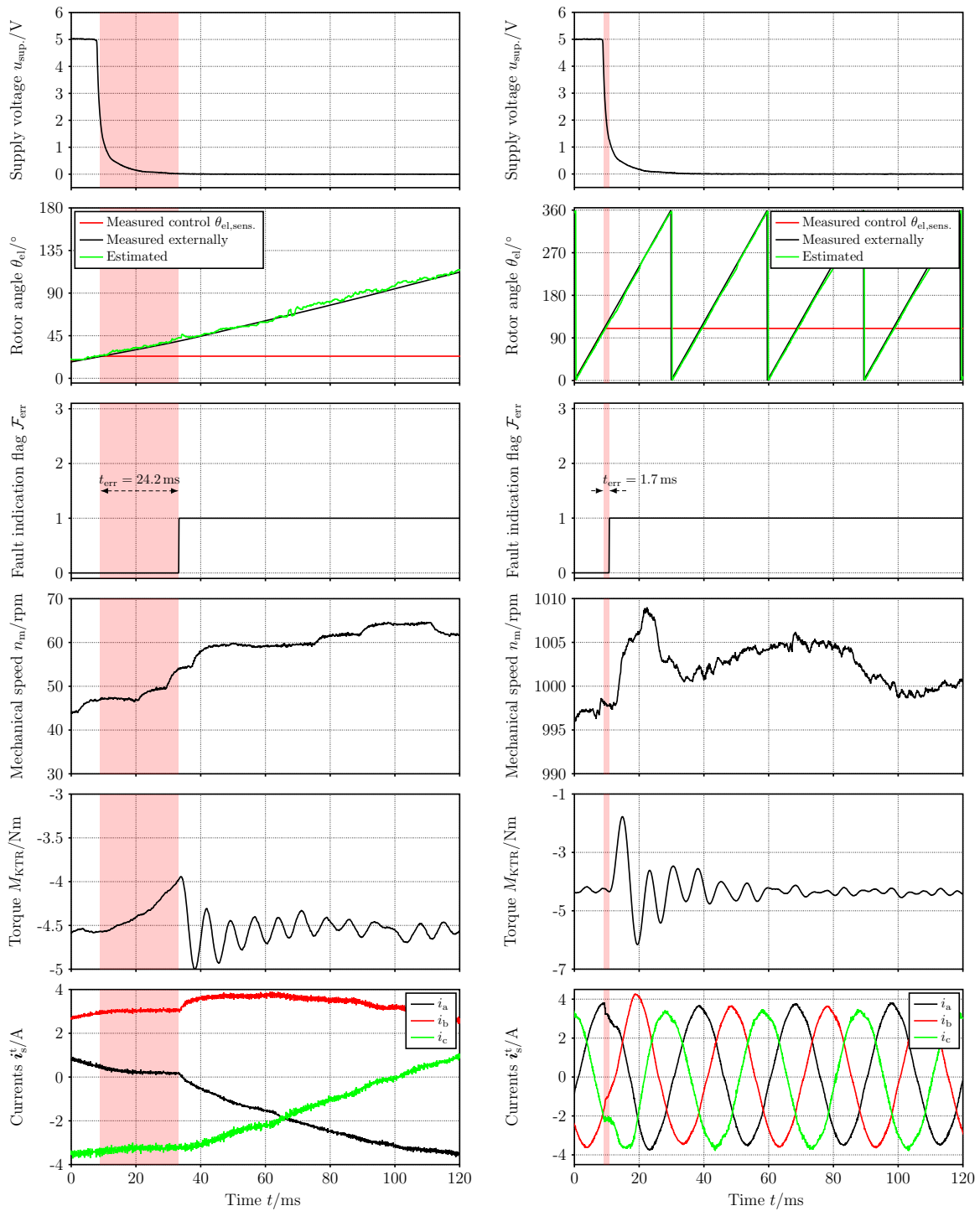


Figure 7.4: Schematic of the incremental encoder supply circuitry.

The test results at different speeds are shown in Fig. 7.5. For the comparison with the estimations, position and speed are measured with an additional encoder (second and fourth plot from the top). The measurements from the additional encoder are shown in black in the respective plots. The position signal freezes quickly after the supply voltage fault. This behavior is reasonable since the microcontroller evaluates high- and low-level from the incremental encoder signals.



a) At a speed of $n_m = 50$ rpm.

b) At a speed of $n_m = 1000$ rpm.

Figure 7.5: Fault detection and compensation during incremental encoder supply voltage fault at about 50% nominal torque.

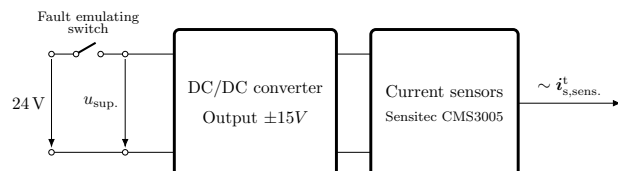
The evaluation fails abruptly once the logic thresholds cannot be maintained due to insufficient supply voltage. The fault detection times $t_{\text{err}} = 24.2 \text{ ms}$ and $t_{\text{err}} = 1.7 \text{ ms}$ differ in this case. This is due to the fixed threshold for the residuum, which must be exceeded. If the rotor is spinning fast and the fault appears, the threshold is also exceeded quickly. The effect, however, remains the same for both speeds since the maximum position error is equal. The impact of the fault on speed, torque, and currents is clearly visible. In the case of Fig. 7.5 b) the speed remains close to its reference value due to the inertia of the rotor. In the case of Fig. 7.5 a) the speed is affected more. The speed in Fig. 7.5 a) does not recover in the illustrated time. This is due to the slow settings of the speed PI controller and could be improved by adjusting the speed controller settings depending on the fault scenario. The current control instead takes only a short time to recover once the fault is detected. It can be concluded that the incremental encoder fault detection works very satisfactorily and can be used to maintain control during encoder faults. The tests were repeated several times and showed high reproducibility.

7.3.3 Fault of the current sensors

Current sensor faults are the last scenario investigated. A current sensor fault is expected to be at least as critical as an encoder fault. The control cannot be maintained in such an event without a compensation algorithm. Furthermore, a fault could trigger over-current fault detection, commonly implemented for safety reasons in the microcontroller. Therefore, sensor fault detection must detect such a fault quickly before the faulty current measurement exceeds the over-current threshold. The current measurement printed circuit board (PCB) used for the measurement is shown in Fig. 7.6 a). The current sensors require $\pm 15 \text{ V}$, provided by the DC/DC converter on the PCB (right side). The fault emulating switch is placed in the input branch of this DC/DC converter as shown in the schematic of the supply circuitry Fig. 7.6 b). The actuation of the switch leads to a fault in all three current sensors.



a) Current measurement PCB.



b) Schematic of the supply circuitry.

Figure 7.6: Overview of the current measurement.

The time constants of the current control loop (first-order elements; time constant of the machine is compensated operating-point-dependent [3, p. 933]) are changed to $\tau_{cc} = 4$ ms for both axes. This is required to avoid the current controllers reacting too quickly to the current deviation in the first phase of the fault, which could lead to over currents and subsequently instability. The test results are shown in Fig. 7.7 and Fig. 7.8 for two different speeds. For the comparison with the estimations, the currents are measured a second time ($i_{a,ext.}$, $i_{b,ext.}$, $i_{c,ext.}$) with external probes. These measurements are illustrated in the third plot from the top in the same diagram as the estimations.

The DC/DC converter on the PCB maintains the operation for about 25 ms after the disconnection. Hence, the effect on the current sensor signals is delayed as well. Once the sensor outputs are affected, the signals behave unpredictable before falling towards zero. This behavior is far from the step-shaped scenario investigated by many related publications. It becomes evident why the signal-based approach (validation with Kirchhoff's current law) is used to verify the model-based detection. The signal-based verification condition is not fulfilled during the first phase of the fault. However, it must be ensured that the fault is detected quickly. Otherwise, the condition is fulfilled even in the presence of the fault (all currents become zero without supply voltage sooner or later). The detection times are slightly different, with $t_{err} = 3.9$ ms and $t_{err} = 3.1$ ms and depend on the instantaneous current values at which the fault appears. The speed control recovers slowly again due to the slow settings of the speed PI controller (encoderless control settings). Again, this could be improved by adjusting the speed controller settings depending on the fault scenario.

The current sensors fault has caused the biggest disturbance of all sensor faults on the drive system. Nevertheless, it has been confirmed that the algorithm can detect and compensate for current sensor faults. This allows control to be maintained in the event of such a worst-case scenario. The tests were repeated several times and have shown high reproducibility.

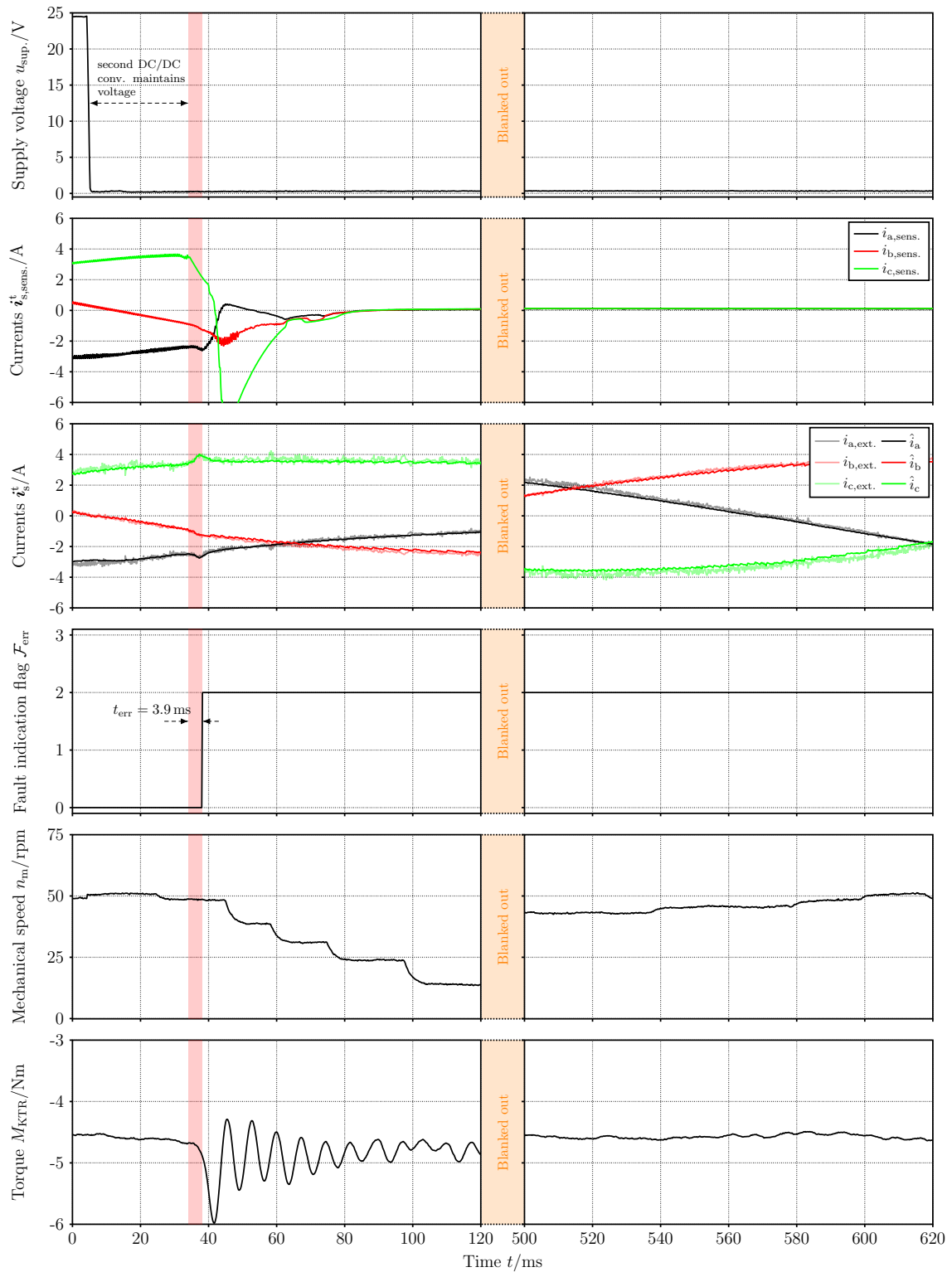


Figure 7.7: Fault detection and compensation during current sensors supply voltage fault at $n_m = 50$ rpm, and about 50% nominal torque.

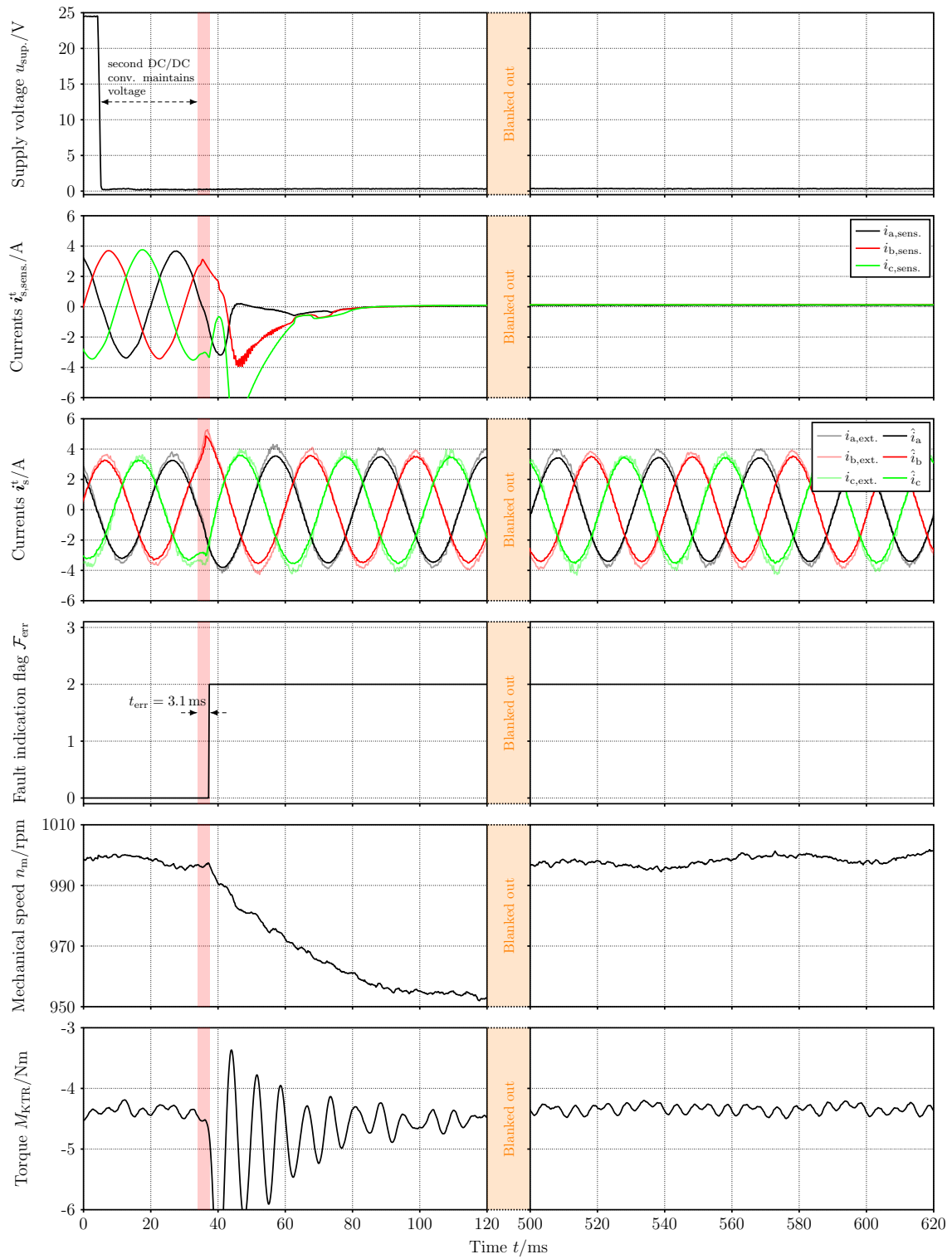


Figure 7.8: Fault detection and compensation during current sensors supply voltage fault at $n_m = 1000$ rpm, and about 50 % nominal torque.

7.4 Conclusion to fault-tolerant control

A combination of signal and model-based sensor fault detection was proposed in this chapter and was called hybrid sensor fault detection. The fault detection employs the high-quality estimation methods introduced in the previous chapters.

The development and investigation of the estimation methods is the actual aim of this thesis. Fault detection is secondary. However, the simple but effective detection algorithm demonstrated the advantage of the estimation methods for fault-tolerant control. More detailed research in the field of sensor fault-tolerant control is beyond the scope of this work. In combination with the new estimation methods, the field of sensor fault-tolerant control provides enough possibilities for extensive research. Hence, the effectiveness of the estimation methods for sensor fault detection was only demonstrated and could be enhanced by future works.

As a brief outlook, it should be mentioned that deterministic sensor fault detection approaches have one drawback – their generality. That means they need to be adapted (thresholds) from system to system and are not a plug-and-play solution. Furthermore, it is difficult to cover all possible sensor fault scenarios with a deterministic approach. Thereby, decision-making is one of the great challenges of this field, besides the supply of suitable estimation methods for back up purposes. However, suitable estimation methods were provided within this work. For the decision-making, it is prospectively reasonable to test approaches based on artificial intelligence (AI) or probabilistic methods. The AI could be trained with many fault scenarios, which is likely impossible for a deterministic approach.

Chapter 8

Conclusion

The present work investigated existing and developed new estimation methods for sensor fault-tolerant control with the primary aim of contributing to a more safe and more reliable drive system. In the area of encoderless control, the work contributed to the investigation of the convergence issue, also known as the overload capability issue. It has been shown that the structure of the algorithm causes the restriction in the achievable current magnitude. This drawback has been present for a long time in the field of encoderless control and has been researched increasingly in the last years. In the area of current sensorless control, this work has contributed with a novel estimation approach, which considers the effect of magnetic saturation in detail and employs remaining feedback from the speed sensor. Furthermore, a DC-link voltage estimation method for a drive system has been proposed, enabling the detection and compensation of DC-link voltage feedback errors. The sensor data estimation algorithms allow sensor fault compensation over the entire operating range of the machine, which significantly increases the drive system's reliability. Finally, the potential of the estimation methods for fault-detection was demonstrated by a deterministic sensor fault-detection approach. The sensor fault-tolerant approach was verified by realistic sensor supply voltage faults, leading to a total malfunction of the sensors. It can be concluded that this work forms a foundation for enhancing the reliability of drive systems prospectively. The methods are applicable in all safety-critical applications where high reliability is required.

The work faced the restriction of using limited computational resources and no additional hardware. However, it has been shown that the algorithms can be executed simultaneously on a standard industrial microcontroller without high computational power or the need for additional hardware. The limited computational power of the TI Microcontroller type TMS320F2837xS was sufficient. The typical execution times

for the algorithms are shown in Tab. 8.1.

Algorithm	Execution time
FOC + fault detection	37.6 μ s
Encoderless	33.2 μ s
Current sensorless	28.3 μ s
DC-link-voltage-sensorless	25.3 μ s

Table 8.1: Typical execution times of the algorithms on the TMS320F2837xS.

8.1 Summary

The most important findings, investigations, and contributions are repeated in more detail in the following for each of the four topics described in the introduction. The parenthesized numbers refer to the open issues stated in the introduction chapter.

Encoderless control

The focus in the area of encoderless control was on the investigation of the convergence issue (2), which describes the stability issues when operating encoderlessly in deep magnetic saturation. The convergence issue was investigated for a selection of so-called injection-based algorithms. However, the findings should also apply to EMF-based methods and estimation algorithms in general. The injection-based algorithms have been investigated concerning their behavior in deep magnetic saturation. The structural diagrams of the investigated algorithms are different, which was the key to revealing the cause of the convergence issue through comparison. The investigations were based on a novel convergence criterion and empirical tests. The convergence criterion assesses the impact of an incorrect current vector angle, used to derive magnetic-saturation-dependent model parameters, on the rotor position estimation error. The empirical tests confirmed the prediction of the convergence area with the novel criterion and, hence, the assumptions made during the derivation of the criterion. Thus, it can be deduced that the convergence issue is caused by the way the magnetic-saturation-dependent model parameters are stored. As long as the model parameters are stored according to an unknown reference frame during encoderless operation, the stability issue will appear at some point. To overcome the convergence issue, the injection-based model must fully rely on model parameters that are stored according to the components of an always-known reference frame. In the field of encoderless control,

it has long been assumed that the machine properties mainly cause the convergence issue. However, this assumption has not been confirmed within this work. Indeed, the behavior can be improved (not solved) by optimizing the electrical machine, but the approach published in the patent [74] makes this optimization unnecessary. Hence, it can be deduced that the convergence issue is mainly a property of the injection-based algorithm.

The extended electromotive force (EEMF) method was used to operate the machine in the medium to high-speed range. The EEMF model was extended by the effect of cross-saturation, which might explain reported estimation errors during torque transients. However, a further investigation of this effect was not conducted within this work.

The low-speed and high-speed methods were combined in a hybrid approach called IFPLL. The hybrid method was empirically tested and is suitable for fault-tolerant control.

Current sensorless control

A novel current sensorless method has been proposed to operate the machine without a current sensor. The estimation is based on EKF-based state estimation. The model was developed with precise consideration of magnetic saturation to address subject (3) and to improve estimation for highly nonlinear machines. Furthermore, the EKF employs the speed as one of the remaining control feedback signals (5). This establishes a link between the estimation algorithm and the actual physical system.

Local observability of the nonlinear state-space system has been assessed and confirmed in the investigated operating points. The well-known issue of covariance tuning was considered with a genetic algorithm (GA)-based optimization. The GA solves the multidimensional optimization problem in a simulation procedure to improve the estimation and find a stable parametrization. This allows for a structured approach without the need for the trial-and-error principle. It was possible to use the covariance settings achieved by the simulation procedure without adaption on the test bench. The Jacobian matrices of the EKF were simplified by neglecting less influential terms to reduce the computational effort without significantly decreasing the estimation quality.

The current sensorless approach was tested empirically in different test scenarios and demonstrated its suitability for sensor fault-tolerant control purposes or other applications. A test in deep magnetic saturation has shown that the control is stable up to the current limitation of the test bench, which conforms to a multiple of the nominal

machine current.

DC-link voltage sensorless control

The first DC-link voltage estimation scheme for a drive system has been introduced to solve subject (6). The new method estimates the DC-link voltage and allows for DC-link-voltage-sensorless control. Comparable schemes have not been published thus far.

The approach of most encoderless schemes, combining a low-speed and a high-speed method, was inherited for this purpose. Both DC-link voltage estimation methods employ knowledge of a current-based machine model with knowledge of the switching states of the VSI to estimate the DC-link voltage. The high-speed method works without additional voltage injection and considers the impact of the VSI interlock time. The low-speed method is injection-based. The same injection sequence as for encoderless control is applied and employed to estimate the unknown voltage drop of the VSI online. In the process, it is taken advantage of the multiple current measurements available during one estimation cycle. This allows estimation of the VSI voltage drop and DC-link voltage by solving a system of equations.

The DC-link-voltage-sensorless approach was empirically verified in different test scenarios. It was demonstrated that it is suitable for fault-tolerant control or other applications.

Sensor fault-tolerant control

Sensor fault-tolerant control commonly consists of two stages. The first stage is called fault detection, which aims to detect sensor or control feedback faults. The second stage is the compensation, in which an alternative signal is used for control in the event of a failure. The compensation stage is significantly improved within this work due to the reliable estimation methods discussed. These estimation methods can be used for the compensation of all sensor faults in various operating conditions. Hence, the compensation stage is no longer limited and the restrictions due to limited estimation methods, discussed in subject (8), are no longer an issue. For the fault detection stage, a simple but effective deterministic approach has been introduced. The approach combines signal-based and model-based detection and was, therefore, referred to as a hybrid method. The hybrid method is more reliable than purely signal-based, or model-based approaches as both detection principles are verified against each other. It is worth mentioning once more that this work focused on the estimation methods.

The approach presented should be considered a first attempt and aims to demonstrate the capability of the new estimation methods for fault-tolerant control. Hence, the approach has restrictions and allows for future improvements.

The fault-tolerant control approach was tested by a realistic voltage supply fault for all sensor categories. The tests revealed that the faults are detected reliably and fast. Subsequently, the estimation methods enable adequate compensation.

8.2 Limitations and outlook

Throughout this dissertation, estimation algorithms employed to estimate control feedback were developed, investigated, and applied for sensor fault-tolerant control. The aim was to contribute to a more reliable drive system in the future. However, the provided algorithms can also be used to reduce the costs and space of the system.

The findings of this thesis could form a base for future works. However, comprehensive research works actually always include open issues, open up new possibilities, or leave space for improvements in the future. This also applies to the present work. Therefore, this thesis closes by summarizing the limitations and giving an outlook for future improvements and ideas.

Encoderless control

The field of encoderless control has faced several big challenges over a long period. Namely, they are the acoustic noise due to voltage injection, the convergence issue, and the accuracy of the methods. Approaches to overcome acoustic noise were proposed several years ago. The convergence issue was investigated within this thesis for injection-based algorithms. The cause of the convergence issue was found, and it has been shown that one of the existing injection-based methods can overcome it. Hence, the convergence issue is solved, even if the respective method is protected by a patent at the date of this dissertation. It is expected that the so-called [EMF](#)-based methods suffer the same convergence issue as injection-based algorithms, but this remains to be confirmed. The accuracy of the methods is the remaining challenge in the field of encoderless control. However, it is not expected that the accuracy of the methods will reach those of high-resolution encoders in the near future. This expectation is explainable by the dependency on other sensors with inaccuracies and the highly complex system to model. However, the accuracy is sufficient for many applications.

It can be concluded that the field of encoderless control, in general, has been researched very comprehensively.

Current sensorless control

The field of current sensorless control still provides enough possibilities for future improvements and developments. The **EKF**-based method in this work has shown sufficient estimation accuracy. The estimation accuracy is expected to be improved by a more comprehensive model of the **VSI** voltage drop. However, the state-space system must be continuously differentiable one-time to apply the **EKF**. This limits the possibilities in modeling the **VSI**. Hence, it might be appropriate to investigate other observers especially developed for nonlinear systems, e.g., the unscented Kalman filter. Besides this, the estimation quality can be enhanced by computing the full Jacobian matrices, which was not conducted within this work to save computational resources.

Issue number (4) must be solved in the future to enable current sensorless control for machines with strong harmonic anisotropies. This might be possible by taking the rotor position dependency of the involved parameters into account.

DC-link-voltage-sensorless control

This thesis proposed the first **DC-link** voltage estimation scheme for a drive system. The method worked well, and the accuracy was sufficient for the purposes of this work. Nevertheless, the accuracy can be improved. A more detailed model of the **VSI** voltage drop is expected to improve the estimation quality, at least for the high-speed method. For the low-speed method, a higher sampling rate k might bring an advantage in the online estimation of the **VSI** voltage drop. The higher sampling rate enables the approximation of the **VSI** voltage drop by a higher-degree polynomial. In turn, this could improve the estimation of the **DC-link** voltage.

Sensor fault-tolerant control

It has been demonstrated that the full compensation functionality of fault-tolerant control is achieved with the provided estimation methods. However, the fault-detection properties are still to be improved. The generality (7) must be enhanced so that the schemes work without great adaption for all drive systems. Furthermore, the fault decision-making properties must be extended and improved. This might be possible by employing approaches based on **AI** or probabilistic methods, which replace the commonly used deterministic detections.

It is worth mentioning that the estimation methods might be helpful in detecting other faults in the system, e.g., disruption of a phase or faults in the power electronics.

However, this remains to be investigated in the future.

Appendix

A.1 Abbreviations

AC	alternating current
ADC	analog-to-digital converter
AI	artificial intelligence
BNC	Bayonet Neill-Concelman
DAC	digital-to-analog converter
DC	direct current
EEMF	extended electromotive force
EKF	extended Kalman filter
EMF	electromotive-force
FEM	finite element method
FOC	field-oriented control
FPGA	field-programmable gate array
FW	field weakening
GA	genetic algorithm
HF	high-frequency
IFPLL	information-fusion-phase-locked-loop
IGBT	insulated-gate-bipolar-transistor
IM	induction machine
INFORM	indirect flux detection by online reactance measurement
IPMSM	interior permanent magnet synchronous machine
KF	Kalman filter
KSB	KSB SE & Co. KGaA
LPF	low-pass filter
LUT	lookup table
MTPA	maximum torque per ampere
MTPV	maximum torque per voltage
PC	personal computer
PCB	printed circuit board
PF	power factor
PI	proportional integral
PLL	phase-locked loop
PM	permanent magnet

PMSM	permanent magnet synchronous machine
PV	photovoltaic
PWM	pulse width modulation
RSM	synchronous reluctance machine
SCS	synchronous current sampling
SEW	SEW-Eurodrive GmbH & Co KG
SM	synchronous machine
SNR	signal-to-noise ratio
TI	Texas Instruments
UARP	method of the unique assignment of the admittance or inductivity to the rotor location
VSI	voltage source inverter

A.2 List of publications

The following list includes the publications that have arisen during this Ph.D. project. The self-citations of the author can be recognized by the letters in brackets following the citation number, e.g., [Number][LWK].

- [33][LWK] M. Laumann, C. Weiner and R. Kennel, "Convergence Investigation of Injection-Based Encoderless Control Algorithms for RSMs in Deep Magnetic Saturation," *IEEE Access (Volume: 10)*, 10.03.2022, pp. 30091-30108, doi: 10.1109/ACCESS.2022.3158662.
- [94][LWK] M. Laumann, C. Weiner and R. Kennel, "Current sensorless field oriented control of a RSM by Extended-Kalman-Filter based state estimation," *2019 IEEE 10th International Symposium on Sensorless Control for Electrical Drives (SLED)*, 2019, pp. 1-6, doi: 10.1109/SLED.2019.8896343.
- [125][LKWK] M. Laumann, M. J. Kamper, C. Weiner and R. Kennel, "FEM based analysis of the impact of temperature on the stability range of anisotropy based encoderless control schemes," *2019 IEEE International Conference on Industrial Technology (ICIT)*, 2019, pp. 261-266, doi: 10.1109/ICIT.2019.8754910.
- [126][LWK] M. Laumann, C. Weiner and R. Kennel, "Arbitrary injection based sensorless control with a defined high frequency current ripple and reduced current and sound level harmonics," *2017 IEEE International Symposium on Sensorless Control for Electrical Drives (SLED)*, 2017, pp. 103-108, doi: 10.1109/SL-ED.2017.8078438.

A.3 Determination of the phase inductances

The inductive behavior of the machine can be divided into an isotropic and anisotropic part. Hence, the superposition of the isotropic with the anisotropic part results in the full inductive behavior of the machine. To better understand the inductance determination, the anisotropic and isotropic behavior is separately determined. Note that the determination is done vicariously for certain inductances; the other inductances can then be derived analogously. Hence, the determination should be seen as a short introduction. For a detailed view, it is referred to the extensive literature.

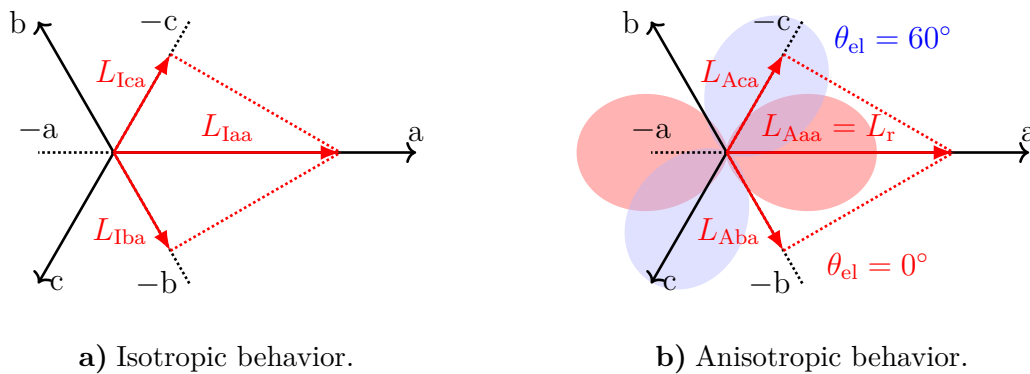


Figure A.1: Illustration of the isotropic and anisotropic behavior of phase a.

Firstly, the isotropic behavior is determined and explained vicariously on phase a, as shown in Fig. A.1 a). The isotropic inductance of phase a (L_{Iaa}) projects to the negative axes of phases b and c. This isotropic behavior is described by one self and two mutual inductances, which are modeled as follows³⁵:

$$L_{Iaa} = \frac{2}{3}L_{\Sigma} \quad L_{Iba} = -\cos(60^\circ) \cdot \frac{2}{3}L_{\Sigma} = -\frac{1}{2} \cdot \frac{2}{3}L_{\Sigma}$$

Fig. A.1 b) shows the anisotropic behavior at a rotor angle of $\theta_{el} = 0^\circ$. The inductance L_r is considered to be aligned with the rotor angle. In this case, the highest inductance of phase a appears at $\theta_{el} = 0^\circ$ and L_{Aaa} changes sinusoidally with the rotor position (ideal sinusoidal arrangement assumed). However, the rotor-related inductance also projects to phases b and c with the highest shared inductive path of phase a and b appearing at a rotor angle of $\theta_{el} = 60^\circ$. Therefore, the self- and mutual inductances are modeled as follows:

$$L_{Aaa} = \frac{2}{3}L_{\Delta} \cos(2\theta_{el}) \quad L_{Aba} = \frac{2}{3}L_{\Delta} \cos(2\theta_{el} - 120^\circ)$$

³⁵The factor 2/3 is introduced to simplify the derivation later on and cancels out after the Clarke transformation.

List of Figures

1.1	System overview with control feedback measurements.	2
2.1	Examples of a stator with one pole pair.	13
2.2	Star-connected three-phase machine.	14
2.3	Reluctance synchronous machine with one pole pair.	15
2.4	Measured magnetic quantities of the RSM.	18
2.5	Schematic of the fundamental simulation model.	24
2.6	Effect of the VSI interlock time.	25
3.1	Test bench.	28
3.2	VSI with microcontroller.	28
3.3	Setup of the timing structure.	30
3.4	Schematic of the control structure.	31
3.5	Geometry of the RSM.	33
4.1	Schematic of the disturbance observer with compensation for the in- verter's interlock time.	40
4.2	Illustration of the low-frequency current difference when a linear change over two consecutive sampling periods of the current difference is assumed.	44
4.3	Schematic of the Arbitrary Injection Δ^2 -scheme.	48
4.4	Voltage injection sequence of the Arbitrary Injection.	49
4.5	Measured misalignment angle with MTPA trajectory in green.	50
4.6	PLL combined with the rotor position assignment.	51
4.7	Simplified structural diagrams of conventional Arbitrary Injection.	57
4.8	Simplified structural diagram of the Alternating Injection.	59
4.9	Simplified structural diagram of the HF-EEMF method.	61

4.10	Measured trajectories at $\ \mathbf{i}_s^s\ = 8$ A. The current angle in the alpha-beta reference was fixed at $\theta_{i,\alpha\beta} = 90^\circ$. The trajectory for a constant current vector in the rotor fixed reference frame is depicted in green and the trajectory for a stator fixed current vector in blue. The linearization approach is depicted in red.	63
4.11	Illustration of the vector projection.	65
4.12	Measured coefficients of the UARP approach.	66
4.13	Simplified structural diagram of the UARP method according to [74].	67
4.14	Overload test with reference torque ramp at current control mode and $n_m = 50$ rpm [33][LWK].	69
4.15	Relationship between rotor position estimation error and current angle deviation; exemplarily for a dq rotating reference frame.	72
4.16	Current trajectories for the measurement of the convergence criterion.	74
4.17	Measurement results for the verification of the convergence criterion.  convergence factor.  test bench maximum reached.  mean unstable points.  sample standard deviation of $\ \mathbf{i}_s^s\ _{\max}$	78
4.18	Coefficients for the hybrid encoderless control scheme.	81
4.19	Schematic of the information-fusion-phase-locked-loop (IFPLL).	82
4.20	Reference tracking during encoderless speed control.	84
4.21	Disturbance rejection during encoderless speed control at a standstill.	85
4.22	Disturbance rejection during encoderless speed control at $n_m = 1000$ rpm.	86
5.1	Two-level VSI.	89
5.2	Hybrid DC-link-voltage-sensorless scheme.	96
5.3	Steady-state measurements at a load torque of 5 Nm.	99
5.4	Reference speed tracking during DC-link-voltage-sensorless control.	100
5.5	Test drive into the voltage saturation of the VSI.	101
6.1	Extended differential inductances derived from the measured flux linkage maps (Fig. 2.4).	117
6.2	Simulated test drive for the covariance tuning in current control mode.	122
6.3	Current sensorless speed tracking performance.	128
6.4	Current sensorless current control during constant reference currents and changing speeds.	129
6.5	Current sensorless current step response to nominal torque.	130
6.6	Stability investigation in deep magnetic saturation up to 40 Nm.	131

7.1	Effect of sensor deviations on the absolute mean residua.	139
7.2	Overview of the DC-link voltage measurement.	143
7.3	Fault detection and compensation during DC-link voltage sensor supply fault at about 50 % nominal torque.	144
7.4	Schematic of the incremental encoder supply circuitry.	145
7.5	Fault detection and compensation during incremental encoder supply voltage fault at about 50 % nominal torque.	146
7.6	Overview of the current measurement.	147
7.7	Fault detection and compensation during current sensors supply voltage fault at $n_m = 50$ rpm, and about 50 % nominal torque.	149
7.8	Fault detection and compensation during current sensors supply voltage fault at $n_m = 1000$ rpm, and about 50 % nominal torque.	150
A.1	Illustration of the isotropic and anisotropic behavior of phase a	164

List of Tables

2.1	Nomenclature for different dimensions.	10
2.2	Nomenclature of time-variant and invariant symbols.	10
2.3	List of the most used superscripts.	11
2.4	Frequently used subscripts.	11
2.5	List of accents.	12
3.1	SEW inverter data.	28
3.2	Parameters of the KSB test machine.	33
6.1	Possible ranges of values of the parameters and states.	108
6.2	Constellations where the criterion for local observability is not fulfilled (part 1).	110
6.3	Constellations where the criterion for local observability is not fulfilled (part 2).	111
8.1	Typical execution times of the algorithms on the TMS320F2837xS. . .	154

List of Symbols

a_{SO}	Adjustable coefficient of the symmetrical optimum (speed control loop).
$\Delta a_{d,i}, \Delta a_{q,i}$	Polynomial coefficients of the d- and q-axis voltage deviation vector (DC-link sensorless).
\mathbf{C}, \mathbf{C}^+	Clarke and pseudoinverse Clarke transformation.
$\mathbf{e}_{s,EEMF}^s$	Extended electromotive force EEMF .
$\mathbf{e}_{s,AI}^s$	Prediction error vector (Arbitrary injection).
$\mathbf{e}_{dem,EEMF}^s$	Demodulation signal (HF-EEMF).
e_{EEMF}	Amplitude of the EEMF voltage.
$\hat{e}_{\alpha,EEMF}, \hat{e}_{\beta,EEMF}$	Estimated components of the EEMF vector $\hat{\mathbf{e}}_{s,EEMF}^s$.
$e_{\alpha,AI}, e_{\beta,AI}$	Alpha and beta component of the prediction error (Arbitrary injection).
$\mathcal{E}_{\theta_{el}}, \mathcal{E}_{u_{DC}}, \mathcal{E}_{i_{abc}}$	Absolute residua (fault detection).
\mathbf{f}	System vector function of the nonlinear state-space system (current sensorless).
\mathbf{f}_d	System vector function of the discretized nonlinear state-space system (current sensorless).
f_{cl}	Clock frequency of the microcontroller.
$f_{sw}, f_{sp,ctr}, f_{ctr}$	Switching, sampling/PWM, and control frequency.
$f(u_{DC})$	Relative estimation error of the DC-link voltage.
$\bar{f}_{rel,EKF}$	Cost (fit) function for the optimization of the covariance matrices (current sensorless).
\mathcal{F}_{err}	Sensor fault indication flag (fault detection).
\mathbf{g}	Output vector function of the state-space system (current sensorless).
g_p, g_i	Proportional and integral gain of the PLL .
$g_{p,n}, g_{i,n}$	Proportional and integral gain of the speed PI controller.
Γ	Convergence factor of the convergence criterion (encoderless).

$\mathbf{i}_{\text{car}}^{\text{a}}$	HF current response vector (Alternating inj.).
$\mathbf{i}_{\text{car,EEMF}}^{\text{r}}$	Injected current vector (HF-EEMF).
$\ \mathbf{i}_{\text{s}}^{\text{s}}\ _{\text{max}}$	Maximum achieved current magnitude (encoderless).
$\mathbf{i}_{\text{s,sens.}}^{\text{t}}, \Delta\mathbf{i}_{\text{s}}^{\text{t}}$	Measured stator phase current vector and its deviation compared to the estimation (fault detection).
$\mathbf{i}_{\text{s}}^{\text{t}}$	Stator phase current vector in three-phase stator fixed coordinates.
$\mathbf{i}_{\text{s}}^{\text{s}}$	Stator phase current vector in $\alpha\beta$ coordinates.
$\mathbf{i}_{\text{s}}^{\text{r}}$	Stator phase current vector in dq coordinates.
$\Delta\mathbf{i}_{\text{s}}^{\text{s}}, \Delta^2\mathbf{i}_{\text{s}}^{\text{s}}$	Current difference and “squared” current difference.
$\Delta\mathbf{i}_{\text{s,HF}}^{\text{s}}, \Delta\mathbf{i}_{\text{s,LF}}^{\text{s}}$	“High-frequency” and “low-frequency” current difference.
$\Delta^2\mathbf{i}_{\text{s,\Sigma}}^{\text{s}}, \Delta^2\mathbf{i}_{\text{s,\Delta}}^{\text{s}}$	“Squared” isotropic and anisotropic current difference.
$\hat{i}_{\text{A,d}}, \hat{i}_{\text{A,q}}$	Components of the current response vector (Alternating inj.).
$i_{\text{A,q,PLL}}$	Error signal for the PLL (Alternating inj.).
$i_{\text{car,EEMF}}$	Amplitude of the injected current (HF-EEMF).
$i_{\text{cd}}, i_{\text{cq}}$	Components of the injected current vector (HF-EEMF).
$\Delta i_{\text{d}}, \Delta i_{\text{q}}$	Estimation errors of d- and q-axis current (current sensorless).
$i_{\text{a,sens.}}, i_{\text{b,sens.}}, i_{\text{c,sens.}}$	Measured phase currents (fault detection).
$i_{\text{a}}, i_{\text{b}}, i_{\text{c}}$	Stator phase current vector components in three-phase representation.
$I_{\text{vsi}}, I_{\text{n}}$	Nominal current of VSI and RSM.
$\Delta^2 i_{\alpha,\Delta}, \Delta^2 i_{\beta,\Delta}$	Components of the anisotropic “squared” current difference vector.
\mathbf{J}	Rotational matrix (rotation by 90°).
$\mathbf{J}_{\text{g}}, \mathbf{J}_{\text{f}}, \mathbf{J}_{\text{f,da}}, \mathbf{J}_{\text{f,s}}$	Jacobian matrices (current sensorless).
J	Mass moment of inertia.
j_{11} to j_{34}	Entries of Jacobian matrix \mathbf{J}_{f} (current sensorless).
$j_{11\text{s}}$ to $j_{34\text{s}}$	Entries of the simplified Jacobian matrix $\mathbf{J}_{\text{f,s}}$ (current sensorless).
\mathbf{K}	Kalman-gain matrix (current sensorless).
k	Sampling and PWM instance.
k_{ani}	Weighting coefficient of the IFPLL and for the hybrid methods.
k_{inj}	Weighting coefficient (scales the voltage injection amplitude speed dependent).
K_{T}	Constant factor (6.4) (current sensorless).
$\hat{\mathbf{L}}_{\text{s}}^{\text{a}}$	Differential inductance matrix in anisotropy coordinates.

L_s^t	Absolute inductance matrix in three-phase stator fixed coordinates.
L_s^s	Absolute inductance matrix in $\alpha\beta$ coordinates.
L_s^r	Absolute inductance matrix in dq coordinates.
\dot{L}_s^s	Differential inductance matrix in $\alpha\beta$ coordinates.
\dot{L}_s^r	Differential inductance matrix in dq coordinates.
$\dot{L}_{s,EEMF}^r, \dot{L}_{s,EEMF}^s$	Differential inductance matrices of the EEMF model.
$L_{s,EEMF}^r, L_{s,EEMF}^s$	Absolute inductance matrices of the EEMF model.
$\dot{L}_{\alpha\alpha}, \dot{L}_{\beta\beta}$	Differential self-inductances of the alpha and beta axes.
$\dot{L}_{\alpha\beta}, \dot{L}_{\beta\alpha}$	Differential mutual inductances of the alpha and beta axes.
$\dot{L}_\Sigma, \dot{L}_\Delta$	Differential mean and delta inductance.
\dot{L}_A	Differential anisotropy inductance.
L_Σ, L_Δ	Absolute mean and delta inductance.
L_d, L_q	Absolute inductances of the d- and q-axis.
$\dot{L}_{dd}, \dot{L}_{qq}$	Differential self-inductances of d- and q-axis.
$\dot{L}_{dq}, \dot{L}_{qd}$	Differential mutual inductances of d- and q-axis.
$\dot{L}_{HF,EEMF}$	Inductance factor (HF-EEMF).
$L_{k,A}, L_{k,B}$	Inductance coefficients of the UARP approach.
\mathbf{m}	Slope vector of the linearized admittance vector (UARP).
$M_{el}, M_m, M_{m,n}$	Electromechanical, mechanical, and nominal mechanical torque.
M_L, M_f	Load and friction torque.
m_A, m_B	Entries of the slope vector (UARP).
$M_{L,s}$	Step-shaped load torque (current sensorless).
M_{KTR}	Torque measurement from the KTR torque transducer.
$\boldsymbol{\mu}$	Noise process vector of the states (current sensorless).
$n_m, n_{m,n}$	Mechanical and nominal mechanical speed of the machine.
N_{teeth}	Number of stator teeth.
n	Control/algorithm repetition instance.
ω_{el}, ω_m	Angular velocity in electrical and mechanical units.
ω_{car}	Angular frequency of the injected voltage (Alternating inj.).
$\omega_{g,LP}$	Cut-off frequency of a low-pass filter.
$\omega_{car,EEMF}$	Angular frequency of the injected current (HF-EEMF).
$\mathbf{P}_{EKF,c}, \mathbf{P}_{EKF,0}$	Estimation error noise covariance matrices (current sensorless).
$\mathbf{P}, \mathbf{P}^{-1}$	Park and inverse Park transformation.
$P_m, P_{m,n}$	Mechanical and nominal mechanical power of the RSM .
p	Number of pole pairs.

P_{vsi}	Nominal power of the VSI .
p_{deg}	Polynomial order of the voltage deviation vector (DC-link sensorless).
ψ_s^t	Flux linkage vector in three-phase stator fixed coordinates.
ψ_s^s	Flux linkage vector in $\alpha\beta$ coordinates.
ψ_s^r	Flux linkage vector in dq coordinates.
ψ_{car}^a	HF flux linkage vector in anisotropy coordinates (Alternating inj.).
ψ_a, ψ_b, ψ_c	Components of the flux linkage vector in three-phase stator fixed coordinates.
$\mathbf{Q}_{\text{EKF}}, \mathbf{Q}_{\text{EKF},0}$	State noise covariance matrices (current sensorless).
$\mathbf{R}_{\text{EKF}}, \mathbf{R}_{\text{EKF},0}$	Measurement noise covariance matrices (current sensorless).
R_s	Resistance of the stator windings.
ρ	Measurement noise process vector (current sensorless).
$\mathbf{S}(x)$	Rotational matrix.
$\bar{\mathbf{s}}$	Mean switching state vector in three-phase stator fixed coordinates.
$\bar{\mathbf{s}}_{\text{dt}}$	Mean switching state deviation vector caused by the interlock time in three-phase stator fixed coordinates.
$\bar{\mathbf{s}}^r$	Mean switching state vector in two-phase rotor fixed coordinates.
S_{tot}	Total apparent power of the electrical machine.
$s_{a,\text{ctr}}, s_{b,\text{ctr}}, s_{c,\text{ctr}}$	Controller related switching functions of the three inverter legs.
s	Complex frequency parameter.
$s_{\ i_s^*\ _{\text{max}}}$	Sample standard deviation of the maximum achieved current magnitude.
\mathbf{T}	Coefficient matrix (DC-link sensorless).
\mathbf{T}^+	Pseudoinverse coefficient matrix (DC-link sensorless).
$t_{x,\text{ON},\text{ctr}}$	ON times of the VSI high side switches over one switching period with $x \in \{a, b, c\}$.
$\mathcal{T}_{1,\text{uDC}}, \mathcal{T}_{2,\text{uDC}}$	Fault thresholds (DC-link voltage sensor fault detection).
$\mathcal{T}_{1,i_{\text{abc}}}, \mathcal{T}_{2,i_{\text{abc}}}$	Fault thresholds (current sensor fault detection).
$\mathcal{T}_{\theta_{\text{el}}}$	Fault threshold (encoder fault detection).
t_{dt}	Interlock time of the VSI .
$T_{\text{sw}}, T_{\text{sw},\text{ctr}}$	Switching period and controller defined switching period.
$t_{\text{dt},\text{vsi}}$	Interlock time of the VSI .
$T_{\text{ctr}}, T_{\text{sp},\text{ctr}}$	Repetition period of the control algorithms and sampling period.

$\theta_{A,comp}$	Anisotropy angle resulting from $\theta_{\delta,comp}$.
$\Delta\theta_A$	Estimation error of the anisotropy angle.
$\theta_{i,\alpha\beta}$	Current angle related to $\alpha\beta$ coordinates.
θ_{inters}	Position of intersection between both trajectories (UARP).
θ_L	Position of the linearized admittance vector $\theta_L = \theta_{el} - \theta_{inters}$. (UARP).
θ_0	Position coefficient of the UARP approach.
θ_i	Current angle with respect to a rotating reference frame that is rotating in coherence with the rotor angle.
$\Delta\theta_i$	Current angle deviation with respect to a rotating reference frame that is rotating in coherence with the rotor angle.
$\Delta\theta_{el,init}$	Initial position estimation error.
$\theta_{i,MTPA}$	Current angle with respect to the MTPA trajectory.
θ_{el}, θ_m	Rotor angle in electrical and mechanical units.
$\hat{\theta}_{el,UARP}$	Estimated rotor position from the UARP model.
$\hat{\theta}_{el,EEMF}$	Estimated rotor position from the EEMF model.
$\theta_{el,sens}$	Measured electrical rotor position (fault detection).
θ_A	Anisotropy angle.
θ_δ	Misalignment angle due to magnetic saturation.
$\theta_{\delta,comp}$	Implemented compensation term for the misalignment angle.
τ_{cc}	Time constant of the current control loop.
$\mathbf{U}_t, \mathbf{U}_t^+$	Transformation and pseudoinverse transformation matrix (DC-link sensorless).
\mathbf{U}	Transformation matrix (switching states to machine voltages, DC-link sensorless).
$\hat{\mathbf{u}}_{s,mod}^s$	Part of the machine voltage vector estimated by the EEMF model.
\mathbf{u}_{car}^a	Injected HF voltage vector (Alternating inj.).
$\bar{\mathbf{u}}_{S246}$	Mean voltage vector across the VSI bottom switches in three-phase stator fixed coordinates.
\mathbf{u}_s^t	Voltage vector in three-phase stator fixed coordinates.
\mathbf{u}	Input vector of the state-space system (current sensorless).
$\mathbf{u}_{vsi}^t, \mathbf{u}_{vsi}^r$	Voltage drop across the VSI in three-phase stator fixed and two-phase rotor fixed coordinates (current sensorless).
\mathbf{u}_s^s	Machine voltage vector in $\alpha\beta$ coordinates.
\mathbf{u}_s^r	Machine voltage vector in dq coordinates.

$\mathbf{u}_{dt}^t, \mathbf{u}_{dt}^s, \mathbf{u}_{dt}^r$	Voltage deviation due to the VSI interlock time for the different reference frames.
$\mathbf{u}_{ctr}^t, \mathbf{u}_{ctr}^s, \mathbf{u}_{ctr}^r$	Idealized controller output voltages for the different reference frames.
$\Delta^2 \mathbf{u}_s^s$	“Squared” voltage difference in two-phase stator fixed coordinates.
$\Delta^2 u_\alpha, \Delta^2 u_\beta$	Alpha and beta component of the “squared” voltage difference.
u_{car}	Amplitude of the injected voltage (Alternating inj.).
$ u_{inj} $	Injection amplitude of Arbitrary injection.
$\hat{u}_{DC, speed}$	DC-link voltage estimated by the medium to high-speed method.
$\hat{u}_{DC, inj}$	DC-link voltage estimated by the injection method.
$\ \mathbf{u}_s^{r*}\ $	Magnitude of the current controller output voltage vector.
$\ \mathbf{u}_s^{r*}\ _{max}$	Maximum allowed controller output voltage vector magnitude (sinusoidally modulated three-phase system).
$u_{d, vsi}, u_{q, vsi}$	Components of the voltage drop vector across the VSI in two-phase rotor fixed coordinates (current sensorless).
$u_{DC, sens.}, \Delta u_{DC}$	Measured DC-link voltage and its deviation compared to the estimation (fault detection).
u_{S2}, u_{S4}, u_{S6}	Voltages across the VSI bottom switches.
u_a, u_b, u_c	Components of the machine voltage vector in three-phase representation.
u_{DC}	DC-link voltage.
$U_{DC, vsi}$	Idealized DC-link voltage from a B6 rectifier.
\mathbf{v}	Vector that indicates the shortest distance between $\mathbf{y}_{L,0}^s$ and $\hat{\mathbf{y}}_s^s$.
\mathbf{x}	State vector of the state-space system (current sensorless).
ξ_s^r	Vector of unknowns in two-phase rotor fixed coordinates (DC-link sensorless).
$\hat{\mathbf{Y}}_s^s$	Admittance matrix in two-phase stator fixed coordinates.
\mathbf{y}_s^s	Admittance vector in $\alpha\beta$ coordinates.
\mathbf{y}_L^s	Linearized admittance vector (UARP).
$\mathbf{y}_{L,0}^s$	Admittance vector in the point of intersection (UARP).
\mathbf{y}	Output vector of the state-space system (current sensorless).
$\hat{Y}_\Sigma, \hat{Y}_A$	Mean and anisotropy admittance.
$\hat{Y}_{\alpha\alpha}, \hat{Y}_{\beta\beta}, \hat{Y}_{\alpha\beta}, \hat{Y}_{\beta\alpha}$	Entries of the admittance matrix in $\alpha\beta$ coordinates.
y_A, y_B	Entries of the admittance vector.
$y_{A,0}, y_{B,0}$	Entries of the admittance vector in the point of intersection (UARP).

ζ_{ddd} to ζ_{qqq} Extended differential inductances (current sensorless).

Bibliography

- [1] Bundesministerium für Umwelt, Naturschutz und nukleare Sicherheit, “Klimaschutzbericht 2021,” 2021.
- [2] T.-M. I. Băjenescu, “Zuverlässige Bauelemente für elektronische Systeme: Fehlerphysik, Ausfallmechanismen, Prüffeldpraxis, Qualitätsüberwachung,” *Springer Fachmedien Wiesbaden*, 2020.
- [3] D. Schröder and J. Böcker, “Elektrische Antriebe – Regelung von Antriebssystemen,” *Springer-Verlag GmbH*, Heidelberg, 2021.
- [4] P. Landsmann, “Sensorless Control of Synchronous Machines by Linear Approximation of Oversampled Current,” *Dissertation*, Technical University Munich, 2014.
- [5] C. Edith, “Circuit Analysis Of AC Power Systems Vol I,” *John Wiley and Sons*, 1943.
- [6] R. de Doncker, D. W. Pülle, and A. Veltman, “Advanced Electrical Drives: Analysis, Modeling, Control,” *Springer Netherlands*, 2011.
- [7] N. P. Quang and J.-A. Dittrich, “Vector control of three-phase AC machines: System development in the practice,” *Springer-Verlag GmbH*, Heidelberg, 2008.
- [8] A. Binder, “Elektrische Maschinen und Antriebe: Grundlagen, Betriebsverhalten,” *Springer-Verlag GmbH*, Heidelberg, 2017.
- [9] A. Glumineau and J. de León Morales, “Sensorless AC Electric Motor Control: Robust Advanced Design Techniques and Applications,” *Springer International Publishing*, Heidelberg, 2015.
- [10] I. N. Bronshtein, K. A. Semendyayev, G. Musiol, and H. Mühlig, “Handbook of Mathematics,” *Springer-Verlag GmbH*, Heidelberg, 2015.

-
- [11] R. H. Park, "Two-reaction theory of synchronous machines: Generalized method of analysis-part I," *Transactions of the American Institute of Electrical Engineers*, vol. 48, no. 3, pp. 716–727, 1929.
- [12] P. C. Krause, O. Wasynczuk, and S. D. Sudhoff, "Analysis of electric machinery and drive systems," *IEEE Press Wiley-Interscience; IEEE Xplore*, vol. 3, 2002.
- [13] D. Mingardi, M. Morandini, S. Bolognani, and N. Bianchi, "On the Proprieties of the Differential Cross-Saturation Inductance in Synchronous Machines," *IEEE Transactions on Industry Applications*, vol. 53, no. 2, pp. 991–1000, 2017.
- [14] S. Kim, "Moment of Inertia and Friction Torque Coefficient Identification in a Servo Drive System," *IEEE Transactions on Industrial Electronics*, vol. 66, no. 1, pp. 60–70, 2019.
- [15] G. Si, Z. Shen, Z. Zhang, and R. Kennel, "Investigation of the limiting factors of the dead time minimization in a H-bridge IGBT inverter," in *2016 IEEE 2nd Annual Southern Power Electronics Conference (SPEC)*, pp. 1–6, IEEE, 05.12.2016 - 08.12.2016.
- [16] N. Bedetti, S. Calligaro, and R. Petrella, "Self-Commissioning of Inverter Dead-Time Compensation by Multiple Linear Regression Based on a Physical Model," *IEEE Transactions on Industry Applications*, vol. 51, no. 5, pp. 3954–3964, 2015.
- [17] T. Fukumoto, H. Hamane, and Y. Hayashi, "Performance Improvement of the IPMSM Position Sensorless Vector Control System by the Online Motor Parameter Error Compensation and the Practical Dead-time Compensation," *2007 Power Conversion Conference - Nagoya*, pp. 314–321, 2007.
- [18] S. Morimoto, M. Sanada, and Y. Takeda, "High-performance current-sensorless drive for PMSM and synRM with only low-resolution position sensor," *IEEE Transactions on Industry Applications*, vol. 39, no. 3, pp. 792–801, 2003.
- [19] Y. Zhao, W. Qiao, and L. Wu, "Dead-Time Effect Analysis and Compensation for a Sliding-Mode Position Observer-Based Sensorless IPMSM Control System," *IEEE Transactions on Industry Applications*, vol. 51, no. 3, pp. 2528–2535, 2015.
- [20] P. Landsmann, J. Jung, M. Kramkowski, P. Stolze, D. Paulus, and R. Kennel, "Lowering injection amplitude in sensorless control by means of current oversam-

- pling,” in *3rd IEEE International Symposium on Sensorless Control for Electrical Drives (SLED 2012)*, pp. 1–6, IEEE, 21.09.2012 - 22.09.2012.
- [21] F. Briz, D. Diaz-Reigosa, M. W. Degner, P. Garcia, and J. M. Guerrero, “Current sampling and measurement in PWM operated AC drives and power converters,” in *The 2010 International Power Electronics Conference - ECCE ASIA*, pp. 2753–2760, IEEE, 21.06.2010 - 24.06.2010.
- [22] M. Roetzer, U. Vollmer, and R. M. Kennel, “Demodulation Approach for Slowly Sampled Sensorless Field-Oriented Control Systems Enabling Multiple-Frequency Injections,” *IEEE Transactions on Industry Applications*, vol. 54, no. 1, pp. 732–744, 2018.
- [23] Atmel, “AVR121: Enhancing ADC resolution by oversampling: Application Note,” accessed 18.02.2022.
- [24] K. Hasse, “Zur Dynamik drehzahl geregelter Antriebe und stromrichterspeisten Asynchronkurzschlussläufermaschinen,” *Dissertation*, Technische Hochschule Darmstadt, 1969.
- [25] F. Blaschke and K. Böhm, “Verfahren der Felderfassung bei der Regelung stromrichtergespeister Asynchronmaschinen,” *IFAC Proceedings Volumes*, vol. 7, no. 2, pp. 635–649, 1974.
- [26] P. Niazi, H. A. Toliyat, and A. Goodarzi, “Robust Maximum Torque per Ampere (MTPA) Control of PM-Assisted SynRM for Traction Applications,” *IEEE Transactions on Vehicular Technology*, vol. 56, no. 4, pp. 1538–1545, 2007.
- [27] J. K. Kostko, “Polyphase reaction synchronous motors,” *Journal of the American Institute of Electrical Engineers*, vol. 42, no. 11, pp. 1162–1168, 1923.
- [28] Sven Ludwig Kellner, “Parameteridentifikation bei permanenterregten Synchronmaschinen,” *Dissertation*, Universität Erlangen-Nürnberg, 2012.
- [29] J. Richter, “Modellbildung, Parameteridentifikation und Regelung hoch ausgenutzter Synchronmaschinen,” *Dissertation*, Karlsruher Institut für Technologie, 2016.
- [30] S. Morimoto, K. Kawamoto, M. Sanada, and Y. Takeda, “Sensorless control strategy for salient-pole PMSM based on extended EMF in rotating reference

- frame,” *IEEE Transactions on Industry Applications*, vol. 38, no. 4, pp. 1054–1061, 2002.
- [31] S. Morimoto, K. Kawamoto, M. Sanada, and Y. Takeda, “Sensorless control strategy for salient-pole PMSM based on extended EMF in rotating reference frame,” in *Conference Record of the 2001 IEEE Industry Applications Conference. 36th IAS Annual Meeting (Cat. No.01CH37248)*, pp. 2637–2644, IEEE, 30 Sept.–4 Oct. 2001.
- [32] Z. Chen, M. Tomita, S. Doki, and S. Okuma, “An extended electromotive force model for sensorless control of interior permanent-magnet synchronous motors,” *IEEE Transactions on Industrial Electronics*, vol. 50, no. 2, pp. 288–295, 2003.
- [33] M. Laumann, C. Weiner, and R. M. Kennel, “Convergence Investigation of Injection-Based Encoderless Control Algorithms for RSMs in Deep Magnetic Saturation,” *IEEE Access*, vol. 10, pp. 30091–30108, 2022.
- [34] Z. Q. Zhu, Y. Li, D. Howe, C. M. Bingham and D. Stone, “Influence of Machine Topology and Cross-Coupling Magnetic Saturation on Rotor Position Estimation Accuracy in Extended Back-EMF Based Sensorless PM Brushless AC Drives,” *2007 IEEE Industry Applications Annual Meeting*, pp. 2378–2385, 2007.
- [35] Y. Li, Z. Q. Zhu, D. Howe, and C. M. Bingham, “Improved Rotor Position Estimation in Extended Back-EMF Based Sensorless PM Brushless AC Drives with Magnetic Saliency,” *2007 IEEE International Electric Machines & Drives Conference*, pp. 214–219, 2007.
- [36] K. Kato, M. Tomita, M. Hasegawa, S. Doki, S. Okuma, and S. Kato, “Position and velocity sensorless control of synchronous reluctance motor at low speed using disturbance observer for high-frequency extended EMF,” in *IECON 2011 - 37th Annual Conference of the IEEE Industrial Electronics Society*, pp. 1971–1976, IEEE, 07.11.2011 - 10.11.2011.
- [37] Ayame Makimura, Yuta Nomura, Shota Kondo, Mutuwo Tomita, Masaru Hasegawa, Shinji Doki, and Shinji Kato, “Study of influence of inductance variation of position sensorless control of SynRM at low speeds by estimating high-frequency extended EMF caused by superimposed current,” *2016 IEEE 2nd Annual Southern Power Electronics Conference (SPEC)*, pp. 1–6, 2016.

- [38] S. Kondo, M. Tomita, M. Hasegawa, S. Doki, and S. Kato, "Position sensorless control of SynRM at low speeds by estimating high-frequency extended EMF using disturbance observer," in *2015 IEEE 2nd International Future Energy Electronics Conference (IFEEEC)*, pp. 1–5, IEEE, 01.11.2015 - 04.11.2015.
- [39] Y. Zhao, W. Qiao, and L. Wu, "Estimated-speed-aided stabilizers for sensorless control of interior permanent magnet synchronous machines," in *2012 IEEE Energy Conversion Congress and Exposition (ECCE)*, pp. 2631–2638, IEEE, 15.09.2012 - 20.09.2012.
- [40] K. A. D. Lee, "The Study on Transient Performance Improvement of Position Sensorless Control Algorithm for IPMSM," *Conference proceedings : 2017 International Symposium on Sensorless Control for Electrical Drives : 18th-19th September 2017, Catania, Italy : 8th Symposium*, pp. 67–72, 2017.
- [41] Y. Zhao, W. Qiao, and L. Wu, "Stability and dynamic performance improvement of a sensorless IPMSM drive via adaptive estimated-speed-assisted position prediction and current quality evaluation," in *2013 IEEE Energy Conversion Congress and Exposition*, pp. 3473–3480, IEEE, 15.09.2013 - 19.09.2013.
- [42] L. Euler, "Institutiones Calculi Integralis," 1792.
- [43] J. Holtz and J. Quan, "Sensorless vector control of induction motors at very low speed using a nonlinear inverter model and parameter identification," *IEEE Transactions on Industry Applications*, vol. 38, no. 4, pp. 1087–1095, 2002.
- [44] M. Hinkkanen and J. Luomi, "Modified integrator for voltage model flux estimation of induction motors," *IEEE Transactions on Industrial Electronics*, vol. 50, no. 4, pp. 818–820, 2003.
- [45] P. Landsmann, D. Paulus, P. Stolze, and R. Kennel, "Saliency based encoderless Predictive Torque Control without signal injection for a reluctance synchronous machine," in *Proceedings of 14th International Power Electronics and Motion Control Conference EPE-PEMC 2010*, IEEE, 06.09.2010 - 08.09.2010.
- [46] D. Paulus, P. Landsmann, and R. Kennel, "General arbitrary injection approach for synchronous machines," in *2013 IEEE International Symposium on Sensorless Control for Electrical Drives and Predictive Control of Electrical Drives and Power Electronics (SLED/PRECEDE)*, pp. 1–6, IEEE, 17.10.2013 - 19.10.2013.

- [47] D. Paulus, "Beliebige Injektion für permanent erregte Synchronmaschinen," *Dissertation*, Technische Universität München, 2015.
- [48] P. L. Jansen and R. D. Lorenz, "Transducerless position and velocity estimation in induction and salient AC machines," *IEEE Transactions on Industry Applications*, vol. 31, no. 2, pp. 240–247, 1995.
- [49] M. J. Corley and R. D. Lorenz, "Rotor position and velocity estimation for a salient-pole permanent magnet synchronous machine at standstill and high speeds," *IEEE Transactions on Industry Applications*, vol. 34, no. 4, pp. 784–789, 1998.
- [50] M. Linke, R. Kennel, and J. Holtz, "Sensorless position control of permanent magnet synchronous machines without limitation at zero speed," in *IEEE 2002 28th Annual Conference of the Industrial Electronics Society. IECON 02*, pp. 674–679, IEEE, 5–8 Nov. 2002.
- [51] M. Schrödl, E. Robeischl, "Sensorlose Drehzahl- und Lageregelung von Permanentmagnet-Synchronmaschinen auf Basis des INFORM-Verfahrens," *e&i Elektrotechnik und Informationstechnik*, 2000.
- [52] P. Landsmann, D. Paulus, and R. Kennel, "Silent and parameter independent hybrid sensorless control for SPMSM based on current oversampling," in *2013 IEEE International Symposium on Sensorless Control for Electrical Drives and Predictive Control of Electrical Drives and Power Electronics (SLED/PRECEDE)*, pp. 1–8, IEEE, 17.10.2013 - 19.10.2013.
- [53] P. Landsmann, C. M. Hackl, and R. Kennel, "Eliminating all machine parameters in Encoderless Predictive Torque Control without signal injection," in *2011 IEEE International Electric Machines & Drives Conference (IEMDC)*, pp. 1259–1264, IEEE, 15.05.2011 - 18.05.2011.
- [54] S. Kim, Y.-C. Kwon, S.-K. Sul, J. Park, and S.-M. Kim, "Position sensorless operation of IPMSM with near PWM switching frequency signal injection," in *8th International Conference on Power Electronics - ECCE Asia*, pp. 1660–1665, IEEE, 30.05.2011 - 03.06.2011.
- [55] Manfred Schroedl, "Sensorless Control of AC Machines at Low Speed and Standstill Based on the "INFORM" Method," *Conference record of the 1996 IEEE In-*

- dustry Applications Conference : Thirty-first IAS Annual Meeting, October 6-10, 1996, San Diego, California, 1996.*
- [56] D. Paulus, P. Landsmann, S. Kuehl, and R. Kennel, "Arbitrary injection for permanent magnet synchronous machines with multiple saliencies," in *2013 IEEE Energy Conversion Congress and Exposition*, pp. 511–517, IEEE, 15.09.2013 - 19.09.2013.
- [57] P. Landsmann and R. K. Kennel, "Saliency-based sensorless predictive torque control with reduced torque ripple," *IEEE Transactions on Power Electronics*, vol. 27, no. 10, pp. 4311–4320, 2012.
- [58] E. Capecchi, P. Guglielmi, M. Pastorelli, and A. Vagati, "Position sensorless control of transverse-laminated synchronous reluctance motors," in *Conference Record of the 2000 IEEE Industry Applications Conference. Thirty-Fifth IAS Annual Meeting and World Conference on Industrial Applications of Electrical Energy (Cat. No.00CH37129)*, pp. 1766–1773, IEEE, 2000.
- [59] M. W. Degner and R. D. Lorenz, "Using multiple saliencies for the estimation of flux, position, and velocity in AC machines," *IEEE Transactions on Industry Applications*, vol. 34, no. 5, pp. 1097–1104, 1998.
- [60] R. Raute, "Sensorless Control of AC Machines for Low and Zero Speed Operation without Additional Test Signal Injection," *Dissertation*, University of Nottingham, 2009.
- [61] N. Bianchi and S. Bolognani, "Influence of rotor geometry of an interior PM motor on sensorless control feasibility," *Fourtieth IAS Annual Meeting. Conference Record of the 2005 Industry Applications Conference*, pp. 2553–2560, 2005.
- [62] N. Bianchi, E. Fornasiero, and S. Bolognani, "Effect of Stator and Rotor Saturation on Sensorless Rotor Position Detection," *IEEE Transactions on Industry Applications*, vol. 49, no. 3, pp. 1333–1342, 2013.
- [63] Al Kassem Jebai, "Sensorless control of synchronous permanent magnet motors by signal injection," *Dissertation*, Mines ParisTech, 2013.
- [64] M. Barcaro, M. Morandini, T. Pradella, N. Bianchi, and I. Furlan, "Iron Saturation Impact on High-Frequency Sensorless Control of Synchronous Permanent-

- Magnet Motor,” *IEEE Transactions on Industry Applications*, vol. 53, no. 6, pp. 5470–5478, 2017.
- [65] M. Berto, L. Alberti, V. Manzoloni, and S. Bolognani, “Computation of Self-Sensing Capabilities of Synchronous Machines for Rotating High Frequency Voltage Injection Sensorless Control,” *IEEE Transactions on Industrial Electronics*, vol. 69, no. 4, pp. 3324–3333, 2022.
- [66] Giacomo Bacco, Silverio Bolognani, Nicola Bianchi, and Virginia Manzoloni, “Self-Sensing-Oriented Optimization of Synchronous Reluctance Machine Design,” *2019 IEEE 10th International Symposium on Sensorless Control for Electrical Drives (SLED)*, pp. 1–6, 2019.
- [67] L. Chen, M. Roetzer, G. Goetting, I. Hahn, “Design of Highly-Saturated Permanent Magnet Synchronous Machines for Torque Ripple Optimized Self-Sensing Control,” *2017 IEEE International Symposium on Sensorless Control for Electrical Drives (SLED)*, pp. 1–6, 2017.
- [68] W. Hammel, P. Landsmann, and R. M. Kennel, “Operating point dependent anisotropies and assessment for position-sensorless control,” in *2016 18th European Conference on Power Electronics and Applications (EPE'16 ECCE Europe)*, pp. 1–10, IEEE, 2016.
- [69] Yong-Cheol Kwon, Joo Hyun Lee, Seung-Ki Sul, “Full Torque-Range Low-Speed Sensorless Drive for Heavily Saturated IPMSMs by Manipulation of Convergence Point,” *2017 IEEE Energy Conversion Congress and Exposition (ECCE)*, pp. 865–872, 2017.
- [70] M. Rötzer, “Anisotropy-Based Position Estimation for Highly-Saturated Permanent Magnet Synchronous Machines in Slowly-Sampled Control Systems,” *2017 19th European Conference on Power Electronics and Applications (EPE'17 ECCE Europe)*, pp. P.1–P.10, 2017.
- [71] Kum - Kang Huh, Di Pan, “System and method for sensorless control of electric machines using magnetic alignment signatures,” *Patent US 9,948,224 B1*, General electric company, publication date: 17.04.2018.
- [72] Y.-C. Kwon, J. Lee, and S.-K. Sul, “Extending Operational Limit of IPMSM in Signal-Injection Sensorless Control by Manipulation of Convergence Point,” *IEEE Transactions on Industry Applications*, vol. 55, no. 2, pp. 1574–1586, 2019.

-
- [73] V. Manzoloni and S. Bolognani, "On the Rotor Position Self-sensing Capability of Reluctance and IPM Synchronous Motors," *IEEE Transactions on Industry Applications*, p. 1, 2020.
- [74] P. Landsmann, D. Paulus, and S. Kuehl, "Verfahren und Vorrichtung zur Regelung eines Synchronmotors ohne Lagegeber mittels eindeutiger Zuordnung der Admittanz oder Induktivität zur Rotorlage," *Patent - DE 10 2018 006 657 A1*, KOSTAL Drives Technology GmbH, publication date: 20.02.2020.
- [75] W. Hammel and H. Wolf, "Method for determining a rotor position of a three-phase machine without using a rotary encoder, and device for controlling a three-phase motor without using a rotary encoder," *Patent - WO2019120617A1*, SEW-Eurodrive GmbH & Co. KG, Date of registration: 11.12.2018.
- [76] W. T. Villet, M. J. Kamper, P. Landsmann, and R. Kennel, "Hybrid position sensorless vector control of a reluctance synchronous machine through the entire speed range," *15th International Power Electronics and Motion Control Conference, 2012*, 2012.
- [77] F. J. W. Barnard, W. T. Villet, and M. J. Kamper, "Hybrid Active-Flux and Arbitrary Injection Position Sensorless Control of Reluctance Synchronous Machines," *IEEE Transactions on Industry Applications*, vol. 51, no. 5, pp. 3899–3906, 2015.
- [78] O. Wallmark and L. Harnefors, "Sensorless Control of Salient PMSM Drives in the Transition Region," *IEEE Transactions on Industrial Electronics*, vol. 53, no. 4, pp. 1179–1187, 2006.
- [79] H. Zhang, W. Liu, Z. Chen, S. Mao, T. Meng, J. Peng, and N. Jiao, "A Time-Delay Compensation Method for IPMSM Hybrid Sensorless Drives in Rail Transit Applications," *IEEE Transactions on Industrial Electronics*, vol. 66, no. 9, pp. 6715–6726, 2019.
- [80] M. Seilmeier and B. Piepenbreier, "Sensorless Control of PMSM for the Whole Speed Range Using Two-Degree-of-Freedom Current Control and HF Test Current Injection for Low-Speed Range," *IEEE Transactions on Power Electronics*, vol. 30, no. 8, pp. 4394–4403, 2015.

-
- [81] C. Silva, G. M. Asher, and M. Sumner, “Hybrid rotor position observer for wide speed-range sensorless PM motor drives including zero speed,” *IEEE Transactions on Industrial Electronics*, vol. 53, no. 2, pp. 373–378, 2006.
- [82] K. Ide, H. Iura, and M. Inazumi, “Hybrid sensorless control of IPMSM Combining high frequency injection method and back EMF method,” in *IECON 2010 - 36th Annual Conference on IEEE Industrial Electronics Society*, pp. 2236–2241, IEEE, 07.11.2010 - 10.11.2010.
- [83] N. E. Zakzouk, A. K. Abdelsalam, A. A. Helal, and B. W. Williams, “PV Single-Phase Grid-Connected Converter: DC-Link Voltage Sensorless Prospective,” *IEEE Journal of Emerging and Selected Topics in Power Electronics*, vol. 5, no. 1, pp. 526–546, 2017.
- [84] M. Ahmed, M. Abdelrahem, A. Farhan, I. Harbi, and R. Kennel, “DC-link sensorless control strategy for grid-connected PV systems,” *Electrical Engineering*, vol. 103, no. 5, pp. 2345–2355, 2021.
- [85] A. Mallik and A. Khaligh, “DC link voltage sensorless control of a three-phase boost power factor correction rectifier,” in *2016 IEEE Transportation Electrification Conference and Expo (ITEC)*, pp. 1–6, IEEE, 2016.
- [86] W. Dahmen and A. Reusken, “Numerik für Ingenieure und Naturwissenschaftler,” *Springer-Verlag GmbH*, Heidelberg, 2006.
- [87] H. Kim and T. M. Jahns, “Phase Current Reconstruction for AC Motor Drives Using a DC Link Single Current Sensor and Measurement Voltage Vectors,” *IEEE Transactions on Power Electronics*, vol. 21, no. 5, pp. 1413–1419, 2006.
- [88] Y. Cho, T. LaBella, and J.-S. Lai, “A Three-Phase Current Reconstruction Strategy With Online Current Offset Compensation Using a Single Current Sensor,” *IEEE Transactions on Industrial Electronics*, vol. 59, no. 7, pp. 2924–2933, 2012.
- [89] T. Matsuo and T. A. Lipo, “Current sensorless field oriented control of synchronous reluctance motor,” in *Conference Record of the 1993 IEEE Industry Applications Conference Twenty-Eighth IAS Annual Meeting*, pp. 672–678, IEEE, 1993.

-
- [90] S. Morimoto, M. Sanada, and Y. Takeda, “High-performance current-sensorless drive for PMSM and synRM with only low-resolution position sensor,” *IEEE Transactions on Industry Applications*, vol. 39, no. 3, pp. 792–801, 2003.
- [91] Y.-s. Jeong, S.-K. Sul, S. E. Schulz, and N. R. Patel, “Fault detection and fault-tolerant control of interior permanent-magnet motor drive system for electric vehicle,” *IEEE Transactions on Industry Applications*, vol. 41, no. 1, pp. 46–51, 2005.
- [92] Sang Dang Ho, Pavel Brandstetter, Petr Palacky, Martin Kuchar, Bach Hoang Dinh, Cuong Dinh Tran, “Current sensorless method based on field-oriented control in induction motor drive,” *Journal of Electrical Systems*, pp. 62–76, Paris, 2021.
- [93] Y. Li, M. Yang, J. Long, Z. Liu and D. Xu, “Current sensorless predictive control based on extended Kalman filter for pmsm drives,” *2017 IEEE Transportation Electrification Conference and Expo, Asia-Pacific (ITEC Asia-Pacific)*, pp. 1–6, 2017.
- [94] M. Laumann, C. Weiner, and R. Kennel, “Current sensorless field oriented control of a RSM by Extended-Kalman-Filter based state estimation,” *2019 IEEE 10th International Symposium on Sensorless Control for Electrical Drives (SLED)*, pp. 1–6, 2019.
- [95] J. Adamy, “Nichtlineare Systeme und Regelungen,” *Springer-Verlag GmbH*, Heidelberg, 2018.
- [96] J. Lunze, “Regelungstechnik 2: Mehrgrößensysteme, Digitale Regelung,” *Springer-Verlag GmbH*, Heidelberg, 2020.
- [97] H. W. Knobloch, “Observability of nonlinear systems,” *Mathematica Bohemica*, vol. 131, no. 4, pp. 411–418, 2006.
- [98] S.-W. Su, C. M. Hackl, and R. Kennel, “Analytical Prototype Functions for Flux Linkage Approximation in Synchronous Machines,” *IEEE Open Journal of the Industrial Electronics Society*, vol. 3, pp. 265–282, 2022.
- [99] R. E. Kalman, “A New Approach to Linear Filtering and Prediction Problems,” *Journal of Basic Engineering*, pp. 35–45, 1960.

-
- [100] D. G. Luenberger, "Observing the State of a Linear System," *IEEE Transactions on Military Electronics*, vol. 8, no. 2, pp. 74–80, 1964.
- [101] J. F. Bellantoni and K. W. Dodge, "A square root formulation of the Kalman-Schmidt filter," *AIAA 5th Aerospace Sciences Meeting*, New York, 1967.
- [102] J. F. Bellantoni and K. W. Dodge, "A square root formulation of the Kalman-Schmidt filter," *AIAA Journal*, vol. 5, no. 7, pp. 1309–1314, 1967.
- [103] R. M. Dressler and D. W. Ross, "Real-time implementation of the Kalman filter for trajectory estimation," Stanford Research Institute Menlo Park CA, 1968.
- [104] S. Bolognani, R. Oboe, and M. Zigliotto, "Sensorless full-digital PMSM drive with EKF estimation of speed and rotor position," *IEEE Transactions on Industrial Electronics*, vol. 46, no. 1, pp. 184–191, 1999.
- [105] Z. Xu and M. F. Rahman, "Comparison of a Sliding Observer and a Kalman Filter for Direct-Torque-Controlled IPM Synchronous Motor Drives," *IEEE Transactions on Industrial Electronics*, vol. 59, no. 11, pp. 4179–4188, 2012.
- [106] P. Hilgers, "Verteilte Zustandsschätzung nichtlinearer Systeme," *Universitätsverlag Ilmenau*, 2012.
- [107] Y. Laamari, K. Chafaa, and B. Athamena, "Particle swarm optimization of an extended Kalman filter for speed and rotor flux estimation of an induction motor drive," *Electrical Engineering*, vol. 97, no. 2, pp. 129–138, 2015.
- [108] K. L. Shi, T. F. Chan, Y. K. Wong, and S. L. Ho, "Speed Estimation of an Induction Motor Drive Using an Optimized Extended Kalman Filter," *IEEE Transactions on Industrial Electronics*, vol. 49, pp. 124–133, 2002.
- [109] P. H. Narayana, "Covariance Determination by Evolutionary Algorithm," *Master Thesis, Supervisors: Christof Klesen, Matthias Laumann*, Darmstadt University of Applied Sciences, 2020.
- [110] T. Arens, F. Hettlich, C. Karpfinger, U. Kockelkorn, K. Lichtenegger, and H. Stachel, "Mathematik," *Springer-Verlag GmbH*, Heidelberg, 2018.
- [111] Z. Gao, C. Cecati, and S. X. Ding, "A Survey of Fault Diagnosis and Fault-Tolerant Techniques—Part I: Fault Diagnosis With Model-Based and Signal-Based Approaches," *IEEE Transactions on Industrial Electronics*, vol. 62, no. 6, pp. 3757–3767, 2015.

-
- [112] K. Rothenhagen, “Fehlertolerante Regelung der doppeltgespeisten Asynchronmaschine bei Sensorfehlern,” *Dissertation*, Christian-Albrechts-Universität zu Kiel, 2011.
- [113] M. E. H. Benbouzid, D. Diallo, and M. Zeraoulia, “Advanced Fault-Tolerant Control of Induction-Motor Drives for EV/HEV Traction Applications: From Conventional to Modern and Intelligent Control Techniques,” *IEEE Transactions on Vehicular Technology*, vol. 56, no. 2, pp. 519–528, 2007.
- [114] S. Karimi, A. Gaillard, P. Poure, and S. Saadate, “Current Sensor Fault-Tolerant Control for WECS With DFIG,” *IEEE Transactions on Industrial Electronics*, vol. 56, no. 11, pp. 4660–4670, 2009.
- [115] K. Rothenhagen and F. W. Fuchs, “Current Sensor Fault Detection, Isolation, and Reconfiguration for Doubly Fed Induction Generators,” *IEEE Transactions on Industrial Electronics*, vol. 56, no. 10, pp. 4239–4245, 2009.
- [116] H. Berriri, M. W. Naouar, and I. Slama-Belkhodja, “Easy and Fast Sensor Fault Detection and Isolation Algorithm for Electrical Drives,” *IEEE Transactions on Power Electronics*, vol. 27, no. 2, pp. 490–499, 2012.
- [117] T. A. Najafabadi, F. R. Salmasi, and P. Jabehdar-Maralani, “Detection and Isolation of Speed-, DC-Link Voltage-, and Current-Sensor Faults Based on an Adaptive Observer in Induction-Motor Drives,” *IEEE Transactions on Industrial Electronics*, vol. 58, no. 5, pp. 1662–1672, 2011.
- [118] K. Rothenhagen and F. W. Fuchs, “Doubly Fed Induction Generator Model-Based Sensor Fault Detection and Control Loop Reconfiguration,” *IEEE Transactions on Industrial Electronics*, vol. 56, no. 10, pp. 4229–4238, 2009.
- [119] S. K. Kommuri, M. Defoort, H. R. Karimi, and K. C. Veluvolu, “A Robust Observer-Based Sensor Fault-Tolerant Control for PMSM in Electric Vehicles,” *IEEE Transactions on Industrial Electronics*, vol. 63, no. 12, pp. 7671–7681, 2016.
- [120] K. Jankowska and M. Dybkowski, “Design and Analysis of Current Sensor Fault Detection Mechanisms for PMSM Drives Based on Neural Networks,” *MDPI designs*, vol. 6, no. 1, 2022.

-
- [121] S. K. Kommuri, S. B. Lee, and K. C. Veluvolu, “Robust Sensors-Fault-Tolerance With Sliding Mode Estimation and Control for PMSM Drives,” *IEEE/ASME Transactions on Mechatronics*, vol. 23, no. 1, pp. 17–28, 2018.
- [122] G. H. B. Foo, X. Zhang, and D. M. Vilathgamuwa, “A Sensor Fault Detection and Isolation Method in Interior Permanent-Magnet Synchronous Motor Drives Based on an Extended Kalman Filter,” *IEEE Transactions on Industrial Electronics*, vol. 60, no. 8, pp. 3485–3495, 2013.
- [123] X. Wang, Z. Wang, Z. Xu, M. Cheng, W. Wang, and Y. Hu, “Comprehensive Diagnosis and Tolerance Strategies for Electrical Faults and Sensor Faults in Dual Three-Phase PMSM Drives,” *IEEE Transactions on Power Electronics*, vol. 34, no. 7, pp. 6669–6684, 2019.
- [124] Y. Bensalem, A. Kouzou, R. Abbassi, H. Jerbi, R. Kennel, and M. Abdelrahem, “Sliding-Mode-Based Current and Speed Sensors Fault Diagnosis for Five-Phase PMSM,” *MDPI Energies*, vol. 15, no. 1, pp. 1–26, 2022.
- [125] M. Laumann, M. J. Kamper, C. Weiner, and R. Kennel, “FEM based analysis of the impact of temperature on the stability range of anisotropy based encoderless control schemes,” *2019 IEEE International Conference on Industrial Technology (ICIT)*, pp. 261–266, 2019.
- [126] M. Laumann, C. Weiner, and R. Kennel, “Arbitrary Injection based sensorless control with a defined high frequency current ripple and reduced current and sound level harmonics,” *2017 IEEE International Symposium on Sensorless Control for Electrical Drives (SLED)*, pp. 103–108, 2017.